Employing Electroanalysis as a Diagnostic Tool to Enable Carbon-free Energy Supply

by

Tejal Sawant

Bachelor in Chemical Engineering, Institute of Chemical Technology, 2016

Submitted to the Graduate Faculty of
the Swanson School of Engineering in partial fulfillment
of the requirements for the degree of

Doctor of Philosophy

University of Pittsburgh

2021

UNIVERSITY OF PITTSBURGH

SWANSON SCHOOL OF ENGINEERING

This dissertation was presented

by

Tejal Sawant

It was defended on

December 7, 2020

and approved by

Dr. James McKone, Ph.D., Assistant Professor, Department of Chemical and Petroleum Engineering

Dr. Susan Fullerton, Ph.D., Associate Professor, Department of Chemical and Petroleum Engineering, Department of Electrical and Computer Engineering

Dr. Götz Veser, Ph.D., Professor, Department of Chemical and Petroleum Engineering

Dr. Lei Li, Ph.D., Associate Professor, Department of Chemical and Petroleum Engineering

Dissertation Director: Dr. James McKone, Ph.D., Assistant Professor, Department of Chemical and Petroleum Engineering

Employing Electroanalysis as a Diagnostic Tool to Enable Carbon-free Energy Supply

Tejal Sawant, PhD

University of Pittsburgh, 2021

Fossil fuel-based energy has been instrumental over the last century to satisfy the socio-economic welfare of humankind. However, the continuous increase in population and resource consumption places a significant strain on the limited supply of fossil fuels available in the world. Moreover, fossil fuel consumption gives rise to negative environmental impacts, particularly greenhouse gas emissions that contribute to global climate change. Thus, there is a clear and pressing need for the development of carbon-free energy technologies as alternatives to fossil fuels. This dissertation focuses on leveraging the tools of applied electroanalysis to advance the development of a carbon-free energy supply. The work described herein encompasses two overarching research objectives:

1. to improve the energy efficiency of Redox Flow Batteries (RFBs) by developing highly catalytic, robust electrodes for the associated electron-transfer reactions.
2. to increase the long-term stability of nuclear reactors by mitigating the effects of Zircaloy corrosion under the unique photochemical conditions of nuclear fission.

In the field of RFBs, we developed an electroanalytical platform for precise and accurate characterization of interfacial electron transfer kinetics at technologically relevant flow battery conditions. Additionally, we modulated the surface chemistry of carbon and established pretreatment strategies that resulted in ten times faster kinetics for the Fe redox chemistry. In the nuclear energy domain, we confirmed that the passivating oxides that form on Zr under nuclear reactor conditions behave as semiconductor photoanodes, which influences the corrosion performance of Zr-based cladding materials. We further developed a mechanistic understanding of the degradation of Zr oxides under these conditions of high energy radiation. Overall, this work demonstrated the importance of electrochemical catalysis in the design of RFBs and provided an impetus to develop more corrosion resistant alloys for use in nuclear reactors, thus advancing the path toward a carbon-free energy supply.

Table of Contents

Preface . . . xvii

1.0 Introduction . . . 1

1.1 Purpose and Scope . . . 1

1.2 Background . . . 2

1.2.1 The Need for a Carbon-free Energy Supply . . . 2

1.2.2 Efforts toward Renewable Energy Storage . . . 5

1.2.3 Progress in the Nuclear Energy Domain . . . 11

2.0 Electrocatalysis in Redox Flow Batteries . . . 14

2.1 What are Redox Flow Batteries? . . . 14

2.2 Effect of Interfacial Electron Transfer Kinetics on RFB Performance Parameters . . . 17

2.3 Developing an Electroanalytical Platform for Accurate Characterization of Flow Battery Kinetics . . . 22

2.3.1 The Challenge of Making Good Measurements . . . 22

2.3.2 Electroanalytical Techniques for Characterizing RFB Kinetics 27

2.3.3 Critically Assessing Rotating Disk Electrode (RDE) Voltammetry as a Characterization Tool . . . 29

2.3.4 A Novel Flow-based Microelectrode Platform for Analytical Measurements . . . 38

2.3.5 Adapting the Flow Cell for Flat Electrode Geometries . . . 45

2.3.6 Recommended Future Work: Online Kinetics Measurements 47

2.4 Modulating Carbon Surface Chemistry for Efficient and Robust Electrocatalysis . . . 51

2.4.1 Evaluating the Effect of Surface Oxidation of Carbon on Kinetics of $Fe^{3+/2+}$ Electrolyte . . . 52

2.4.2 Testing the Hypothesis that C=O Functionalities enhance Fe Redox Kinetics Irrespective of the Type of Carbon 64
2.4.3 Future Outlook for Developing Flow Batteries–Opportunities to Leverage Catalysis Science 68
2.5 Summary, Impact and Recommended Future Work 70
3.0 Dynamics of Zircaloy Corrosion in Nuclear Reactors 71
3.1 Significance of Zircaloy corrosion 71
3.2 Assessing the Semiconducting Behavior of Zr and Zircaloy Surface Oxides 76
3.2.1 Identifying the Effect of Illumination on Photoelectrochemical Behavior of the Oxides 77
3.2.2 Elucidating the Semiconducting Properties using Band Energy Diagrams 85
3.3 Conditions of Oxide Growth/Dissolution 98
3.3.1 Efforts to Induce Oxide Growth/Dissolution under Lab-scale Conditions 98
3.4 Summary, Impact and Recommended Future Work 113
4.0 Summary and Conclusions 114
Appendix A Electrocatalysis in Redox Flow Batteries. 115
A.1 Simulation Details for Figure 9 115
A.2 Simulation Details for Figure 10 117
A.3 Analytical Protocol for Measurement of Kinetics using Ultramicroelectrodes (UMEs) 118
A.4 Simulation Details for Figure 21 121
Bibliography 124

List of Tables

1 Compiled kinetics data for aqueous RFB redox couples at various types of carbon electrodes 23

2 Electron transfer kinetics data for oxidation and reduction of $Fe^{3+/2+}$ at Pt microelectrode 43

3 Kinetics of iron oxidation and reduction at pre-treated carbon electrodes (n=5) 56

4 Typical operating conditions in light water nuclear reactors (Individual data-points extracted from Allen et al. [275]) 72

5 Typical compositions of four Zr-based alloys (via Stanford Advanced Materials) 73

6 Composition details and naming convention for various Zr oxides samples . 89

7 Parameters used for simulating the effect of electron-transfer kinetics on voltage and coulombic efficiencies, Figures 9 and 10 respectively. 116

List of Figures

1 Bar graph depicting the number of people with and without access to electricity over the last three decades. (Based on data obtained from Sustainable Energy for All (SE4ALL) Database [2]. Graphical representation of the figure was inspired by https://ourworldindata.org/energy-access, Creative Commons License) 3

2 Plot depicting growing energy consumption with an increase in population from 1800 to 2019 alongside projected data for 2050. (Based on data obtained from Energy Transitions (2017) and BP Statistical Review of World Energy [5, 6]) 4

3 Cost of energy production (USD/kWh) using various renewable and non-renewable energy sources alongside the global average cost in 2019 and compared to cost of energy production using fossil fuels. (Based on data obtained from International Renewable Energy Agency [11].) 6

4 Pie chart depicting the contributions of various energy sources to the total energy consumption of the United States in 2019. Note that the sum of all components is not 100% due to individual rounding. (Based on data obtained from US Energy Information Administration, April 2020 [20]) 7

5 Normalized energy demand, solar irradiance and wind power over a 3-day span in a region near Bend, Oregon, USA. Data is normalized to the respective maxima. (Based on data obtained from US Energy Information Administration, April 2019 and National Solar Radiation Data Base [10, 25]) 9

6 Energy storage systems categorized into various types based on the mechanism of operation. (Based on data obtained from Cho et al. [26]) 10

7 A map of United States of America depicting contribution of nuclear energy in various states (Reproduced from US Department of Energy, Office of Nuclear Energy [38]) 12

8 Schematic representation of a redox flow battery alongside the components of an RFB stack. 15

9 Simulated charge/discharge curve for a prototypical VRFB depicting the contributions of kinetics, resistance, and mass transport to the total overpotential losses during charge and discharge. (b) Simulated VRFB polarization curves at 50 % state of charge encompassing the expected range of electron-transfer rate constants for sluggish versus facile charge transfer processes. (c) Simulated voltage efficiency vs. power density plot for a VRFB like that shown in panel (a) highlighting the theoretical maximum performance (infinitely fast kinetics and zero electrical resistance) and four cases of progressively decreasing electron-transfer rates. 18

10 (a) Simulated polarization curves for the oxidation of a hypothetical RFB positive electrolyte, where the desired oxidization is followed by an undesired over-oxidation reaction that results in irreversible decomposition. (b) Simulated capacity retention data for three cases: the "base case" corresponding to the parameters depicted in (a); thermodynamic stabilization, where the equilibrium potential for the decomposition reaction was shifted positive by 0.1 V; and kinetic stabilization, where k^0 for the decomposition reaction was decreased by a factor of 10. 21

11 Simulated charge-discharge performance, overpotential as a function of % state of charge (SOC), of $Fe^{3+/2+}$ RFB electrolyte. The heterogeneous electron transfer rate constant, k^0, was varied from 10^{-2} to 10^{-5} cm/s corresponding to the upper and lower limits of reported kinetics at Au electrodes. 25

12 Schematic representation of a scientific/engineering workflow that describes ongoing work on RFB systems. 26

13 Schematic (left) and photograph (right) of the RDE experimental setup. Components labeled in the schematic are as follows: (a) glass cell, (b) Teflon cap, (c) nitrogen purge tube, (d) vent, (e) RDE motor, (f) RDE shaft, (g) electrolyte solution, (h) working electrode, (i) counter electrode, (j) stopcock, (k) electrolyte bridge, (l) reference electrode, and (m) reference electrode compartment. 30

14 Data collected in 5 mM $FeCl_2$ and 5 mM $FeCl_3$ in 0.5 M HCl(aq) at polycrystalline Pt electrode. (a) Representative current density versus potential data for RDE voltammetry between 100 and 2500 rpm, (b) Koutecky-Levich analysis depicting inverse current versus inverse square root of rotation rate data for iron oxidation, (c) Koutecky-Levich analysis depicting inverse current versus inverse square root of rotation rate data for iron reduction and (d) Transport-free polarization data. 32

15 Data collected in 5 mM $FeCl_2$ and 5 mM $FeCl_3$ in 0.5 M HCl(aq) at polycrystalline Au electrode. (a) Representative current density versus potential data for RDE voltammetry between 100 and 2500 rpm, (b) Koutecky-Levich analysis depicting inverse current versus inverse square root of rotation rate data for iron oxidation, (c) Koutecky-Levich analysis depicting inverse current versus inverse square root of rotation rate data for iron reduction and (d) Transport-free polarization data. 34

16 (a) RDE current density versus potential data using a Pt electrode in 5 mM $FeCl_2$ and 5 mM $FeCl_3$ in 0.5 M HCl obtained by omitting cleaning steps between different rotation rates. (b) Current density versus rotation rate at 375 mV versus Ag/AgCl with and without cleaning steps alongside theoretical data. Numbered dotted lines represent the order in which RDE measurements were performed. 35

17 (a) RDE current density versus potential data for a $Fe^{3+/2+}$ RFB electrolyte containing 0.5 M $FeCl_2$ and 0.5 M $FeCl_3$ in 2 M HCl(aq). The inset shows the same data without compensating for series resistance (4 ohms). (b) The corresponding transport free polarization data, where the equilibrium potential, E_{eq} was taken to be 425 mV vs. Ag/ AgCl. 36

18 Transport-free polarization data for (a) a 5 mm diameter Pt rotating-disk electrode and (b) a 10-micron diameter Pt electrode in 10 mM total Fe in 0.5 M HCl electrolyte. 39

19 Schematic (top) and photograph (bottom) of experimental setup; Components labeled in the schematic are as follows: (a) inlet pump tubing, (b) o-ring, (c) flow channel, (d) reference electrode (Ag/AgCl), (e) working electrode (Pt microelectrode), (f) counter electrode (graphite), (g) teflon threaded plugs, (h) leur valve, (i) flow cell and (j) outlet pump tubing. 41

20 (a) Linear and (b) semilog current density vs. potential data for a Pt microelectrode under static (0 mL/min) and flowing (10 mL/min) conditions in 10 mM total Fe in 0.5 M HCl electrolyte. 42

21 Simulated current density vs. potential data for (a) rotating disk electrode (using DigiElch) and (b) microelectrode flow cell platform (using COMSOL) for $Fe^{3+/2+}$ electrolyte. 44

22 Schematic representation (top) and photograph (bottom) of modified flow cell platform for incorporating flat electrode geometries. Components labeled in the schematic are as follows: (a) inlet pump tubing, (b) leur valve, (c) flow channel, (d) bottom piece of the flow cell, (e) teflon threaded plug, (f) reference electrode (Ag/AgCl), (g) screw, (h) top piece of the flow cell, (i) gasket, (j) working electrode (Pt deposited on microscope slide), (k) counter electrode (graphite), (l) o-ring, (m) outlet pump tubing. 46

23 Representative cyclic voltammogram in 5 mM $FeCl_2$ and 5 mM $FeCl_3$ in 0.5 M HCl electrolyte on a platinum electrode deposited on microscope slide. . 48

24 Conceptual schematic of a set of real-time analytical capabilities based on ultramicroelectrode voltammetry (top) and spectroelectrochemistry (right) that can be directly interfaced with an operating RFB cell (lower left). 50

25 Current density vs. potential data at a scan rate of 200 mV/s for solvent treated GC, electrochemically treated GC, and peroxide treated GC in 5 mM $FeCl_2$ and 5 mM $FeCl_3$ in 0.5 M HCl. 53

26 Data collected in 5 mM $FeCl_2$ and 5 mM $FeCl_3$ in 0.5 M HCl(aq). RDE current density vs. potential data for (a) solvent treated GC, (b) electrochemically treated GC, and (c) peroxide treated GC; Tafel plots and corresponding fits for $Fe^{3+/2+}$ oxidation and reduction at (d) solvent treated GC, (e) electrochemically treated GC, and (f) peroxide treated GC. 55

27 XPS survey scan data for solvent treated, electrochemically treated, and peroxide treated GC electrodes. Peaks corresponding to the O 1s and C 1s regions are noted along with the associated O/C ratios. 57

28 Normalized Raman data for solvent treated, electrochemically treated, and peroxide treated GC electrodes in the region corresponding to the characteristic features of graphitic carbon: D band at 1330 cm^{-1} and G band at 1590 cm^{-1}. The intensities are normalized to the maximum intensity of the G band for each electrode type. 58

29 Scanning electron micrographs of (a) solvent treated GC, (b) electrochemically treated GC and (c) peroxide treated GC and atomic force micrographs of (d) solvent treated GC, (e) electrochemically treated GC and (f) peroxide treated GC. 60

30 (a) Bar chart of various functional groups present in solvent treated, electrochemically treated, and peroxide treated GC electrodes obtained from C 1s peak deconvolution using XPS. Reported data are the mean of five replicates. (b) Schematic representation of the possible mechanistic rationale for enhanced electron transfer kinetics mediated by surface bound Fe species on –C=O functionalities. 61

31 Schematic representation of carbon layers from n=0 to n=33 ($\sim 3\lambda_{eff}$), each separated by an average distance of 2.2 A°, along with the diminishing probabilities of electron escape in each layer. 63

32 Data collected on electrochemically treated carbon fiber microelectrode in 5 mM $FeCl_2$ and 5 mM $FeCl_3$ in 0.5 M HCl electrolyte at 10 mL/min flow rate; (a) Representative cyclic voltammetry data and (b) associated BV fit. . . . 65

33 Exchange current densities obtained on solvent and electrochemically treated carbon under static (0 mL/min) and flowing conditions (10 mL/min) of the electrolyte (5 mM $FeCl_2$ and 5 mM $FeCl_3$ in 0.5 M HCl). 67

34 Schematic representation of corrosion rates of Zircaloy. Variables k_c and k_l represent cubic and linear rate constants for the pre- and post-transition regions, respectively. (Adapted from Hillner et al. [45]) 74

35 (a) SEM micrograph of a representative Zr sample after thermal oxidation in air at 400 ^{o}C for 5 min; Plot of potential vs. current density obtained in pH 13 LiOH using linear polarization method for (b) Zr and (c) Zr heat treated to obtain 240 nm of oxide thickness. Blue lines represent the experimental data and red lines indicate tangents drawn at open circuit conditions. 78

36 Schematic (top) and photograph (bottom) of the experimental setup used for photoelectrochemistry measurements. Components labeled in the schematic are as follows: (a) stand, (b) o-ring, (c) electrolyte, (d) counter electrode (platinum), (e) light guide, (f) reference electrode (Ag/AgCl), (g) quartz glass cell, (h) sample, (i) teflon housing and (j) brass pin for back contact. . . . 80

37 Electrochemical measurements taken on a representative Zr—ZrO_x sample over a range of electrolyte and illumination conditions. (a) Open circuit potential in pH 10 LiOH (aq.), (b) linear sweep voltammetry in pH 10 LiOH (aq.), (c) open circuit potential in pH 13 LiOH (aq.), (d) linear sweep voltammetry in pH 13 LiOH (aq.), (e) open circuit potential in 0.5 M Na_2SO_3(aq.) and (f) linear sweep voltammetry in 0.5 M Na_2SO_3(aq.). 81

38 Electrochemical measurements taken on a representative Zircaloy-4 sample over a range of electrolyte and illumination conditions. Open circuit potential measurements in (a) pH 10 LiOH (aq.), (b) pH 13 LiOH (aq.) and (c) 0.5 M Na_2SO_3(aq.); Linear sweep voltammetry measurements in (d) pH 10 LiOH (aq.), (e) pH 13 LiOH (aq.) and (f) 0.5 M Na_2SO_3(aq.). 84

39 Mott Schottky plot depicting C^{-2} vs. E for (a) TiO_2 single crystal electrode and (b) pure Zr oxide electrode in pH 13 electrolyte. 86

40 Schematic representation of the band energy diagram of an n-type semiconductor under vacuum, depletion, flatband and accumulation conditions. . . 88

41 Transient photocurrent response in pH 10 LiOH saturated with air on pure Zr sample heat treated to obtain 240 nm of oxide thickness. (V_{fb} = -1.05 V vs. Ag/AgCl). 90

42 Bar chart presenting the flatband potentials referenced to (a) Ag/AgCl and (b)RHE scales obtained in various electrolytic conditions on different Zr samples [Zr240, Zircaloy-4 (Zry-4), Zr sponge (Z1), Zr-0.1%Cr (C1), Zr-0.2%Sn (S1), Zr-0.4%Sn (S2) and Zr-0.2%Fe (F1)]. 91

43 Bar chart presenting the open circuit potential shift obtained in various electrolytic conditions on different Zr samples [Zr240, Zircaloy-4 (Zry-4), Zr sponge (Z1), Zr-0.1%Cr (C1), Zr-0.2%Sn (S1), Zr-0.4%Sn (S2) and Zr-0.2%Fe (F1)]. 92

44 Plot depicting the doping density for various Zr samples [Zr240, Zircaloy-4 (Zry-4), Zr sponge (Z1), Zr-0.1%Cr (C1), Zr-0.2%Sn (S1), Zr-0.4%Sn (S2) and Zr-0.2%Fe (F1)]. 95

45 Representative plot depicting the correlation between flatband potential, doping density and photovoltages obtained in air saturated pH 13 LiOH electrolyte. 97

46 SEM micrographs of Zr samples with 240 nm of oxide thickness subjected to 48 hours of UV illumination in DI water; (a) non-illuminated region, (b) illuminated region of the sample. 100

47 Schematic (top) and photograph (bottom) of the 'all quartz' experimental setup. Components labeled in the schematic are as follows: (a) quartz petri dish, (b) quartz plate, (c) light guide, (d) aluminum foil, (e) electrolyte and (f) sample. 101

48 SEM micrographs of Zr samples with 240 nm of oxide thickness subjected to 48 hours of UV illumination in 100 ppm LiF in DI water; (a) non-illuminated region, (b) illuminated region of the sample. 102

49 Simulated pH as a function of current density for water oxidation reaction occurring on the surface of Zr oxide sample. Bulk electrolyte was assumed to be 10^{-4} M and the diffusion boundary layer thickness was set to 100 μm. . 104

50 SEM micrographs of Zr samples with 240 nm of oxide thickness subjected to 24 hours of UV illumination in pH 4 $HClO_4$ electrolyte; (a) non-illuminated region, (b) illuminated region of the sample. 105

51 SEM micrographs of Zr samples with 240 nm of oxide thickness subjected to 24 hours of UV illumination in DI water; (a) non-illuminated region, (b) illuminated region of the sample. 106

52 Plot of contact angle vs. time for pure Zr sample in DI water under (a) illuminated and (b) non-illuminated conditions. Error bars are reported at 95% confidence interval over a set of 6 measurements at each time point. . 107

53 Plot of contact angle vs. time for Zry-4 sample in DI water under (a) illuminated and (b) non-illuminated conditions. Error bars are reported at 95% confidence interval over a set of 6 measurements at each time point; SEM micrographs of Zry-4 subjected to 24 hours in DI water under (c) illuminated and (d) non-illuminated conditions. 109

54 Schematic representation of the metal-oxide bond breaking process occurring on the surface of the oxide. 110

55 Schematic representation of postulated photo-chemical processes under open-circuit conditions in n-type Zr oxide. 111

56 Simulated exchange current density as a function of overpotential range used in Butler-Volmer fit where the transport limited current density was 2.5 mA/cm^2. Inset represents the same data over a narrow overpotential range and filled black markers indicate the maximum overpotential range that can be used to obtain j_0 with an error less than 3%. Hypothetical k^0 values are extracted using a concentration of 5 mM. 120

57 Representative image of the geometry used in COMSOL to simulate cyclic voltammograms in our microelectrode flow platform. 123

Preface

First, I want to express my gratitude to my advisor, Dr. James R. McKone for giving me the opportunity to work with him over the last four years. Your enthusiasm and knowledge in science and engineering has been instrumental in helping me drive my doctoral work to completion. Your constant support, guidance and mentorship has helped me shape myself into an independent researcher. You have been an amazing advisor and a great friend, and it was an honor and a privilege to learn from you. Special acknowledgement to your three year old daughter, Matilda for scheduling video calls and putting a smile on my face during the '2020 pandemic' thesis writing process.

Next, I would like to acknowledge my committee members, Dr. Susan Fullerton, Dr. Götz Veser and Dr. Lei Li whose advice, feedback and insights have helped expand the breadth of my doctoral work. I would also like to thank my collaborators at NNL for introducing me to the challenge of corrosion in nuclear reactors and for their constant feedback. I further express my gratitude to all undergraduate and graduate students who I have had a chance to work with in the last four years. Special thanks to my RFB team–Carissa Yim, Thomas Henry and Dean Miller–for contributing to our efforts in the field of flow batteries and for making BEH 921 incredibly fun.

I cannot go without acknowledging the 'Lunch' group – Rituja Patil, Shubham Awate, Sanjana Karpe, Riddhesh Patel and Ritesh Pawar. The times we spent in our grad lounge will always remain the most memorable parts of my PhD journey. I would also like to acknowledge all my friends who have made Pittsburgh–a new home away from home.

I would further like to acknowledge my parents, Vidya Sawant and Vijay Sawant for first providing the education and resources required to start this PhD journey and for their constant love, understanding and motivation despite living on the other side of the world. I would also like to express my gratitude to my sister, Rashmi Sawant. You have always been a constant source of encouragement and have provided innumerable instances of laughter and humor, and have picked me up during the difficult times of this journey. Finally, I would like to acknowledge Rishabh Shah for celebrating the small victories of good experimental results,

for helping me debug codes when simulations won't run and for providing inspirational ways to look at the same research challenges. I could not have done this without your love and support through the last four years.

1.0 Introduction

1.1 Purpose and Scope

This dissertation describes my research efforts in the field of sustainable energy since the fall of 2016. I hope that it serves as a helpful document for researchers who aim to make a difference in the clean energy domain. The primary purpose of this work was to leverage the tools of electrochemistry to contribute to the development of a carbon-free energy supply by improving our ability to store and produce clean energy. With that in mind, the remainder of this chapter is intended to introduce the reader to challenges with the current energy system and the need for a carbon-free energy supply, with specifics about my efforts in the renewable and nuclear energy fields.

Chapter 2 describes the complete body of work directed towards the development of electrocatalysis in redox flow batteries (RFBs). It begins with a background of RFBs to familiarize the reader with this technology and then discusses the efforts I made towards the development of electroanalytical techniques and electrode materials to improve the performance of RFBs. Chapter 3 summarizes my studies of Zr alloy corrosion in nuclear reactors. It starts by introducing the need to understand mechanisms of Zr oxide corrosion and goes on to lay out the work I undertook to address this need. Chapters 2 and 3 conclude with the impact that my work was able to create in these field and recommendations for future research directions. Chapter 4 summarizes and contextualizes the key findings and concludes this dissertation. Appendix A provides simulation details and experimental protocols for the RFB portion of the work.

I hope that this document will be useful as a comprehensive resource for someone who is looking to expand on my work, and I encourage the reader to gather additional information from the published articles if they intend to reproduce it. Finally, I hope that this document can encourage others to dream and work towards a sustainable energy future.

1.2 Background

1.2.1 The Need for a Carbon-free Energy Supply

Energy is one of the most crucial resources of the world; it impacts all day-to-day activities of humans from food to shelter to transportation and beyond [1]. Nonetheless, a substantial proportion of the world still lacks access to a reliable energy supply [2]. Figure 1 depicts a bar graph of the number of people with and without access to electricity over the last three decades, showing that as of 2016 nearly 1 in 7 people suffer from a lack of electricity. While the percentage of population without access to electricity has decreased substantially over this time period, efforts still need to be made to achieve United Nation's sustainable development target of "global electricity access by 2030" [3]. Moreover, the steadily increasing population puts additional strain on the available energy resources to satisfy the energy demand. In 2018, the Census Bureau's International Database reported a total world population of 7.5 billion, a factor of seven rise compared to the early 1800s [4]. The rapid growth in world population alongside the need for socio-economic welfare has resulted in an increase in the energy demand 30-fold, from 5000 TWh to 150,000 TWh, over the same time period (Figure 2) [5,6]. Moreover, a 50% rise in the total world energy consumption is predicted by the U.S. Energy Information Administration by the end of 2050 [7]. This historical increase in energy demand places further demands on the global energy supply and has rendered our current systems of energy production and consumption unsustainable.

Fossil fuel-based technologies have been the most prevalent forms of energy production worldwide [8,9]. As of 2018, coal, petroleum and natural gas together accounted to about 85% of the total energy supply in the world [10]. The massive technological advancements made in this field have led to the generation of remarkably low cost electricity and combustible fuels. Figure 3 presents a 2019 snapshot of the relative cost for electricity generation using various resources [11]. Owing in part to their ready availability and low cost, fossil-based sources will remain major contributors in satisfying energy needs in the next few decades. However, the advantages of low cost are reaped at the expense of environmental damage. Burning of fossil fuels releases large quantities of greenhouse gases like carbon dioxide, methane, nitrous oxide

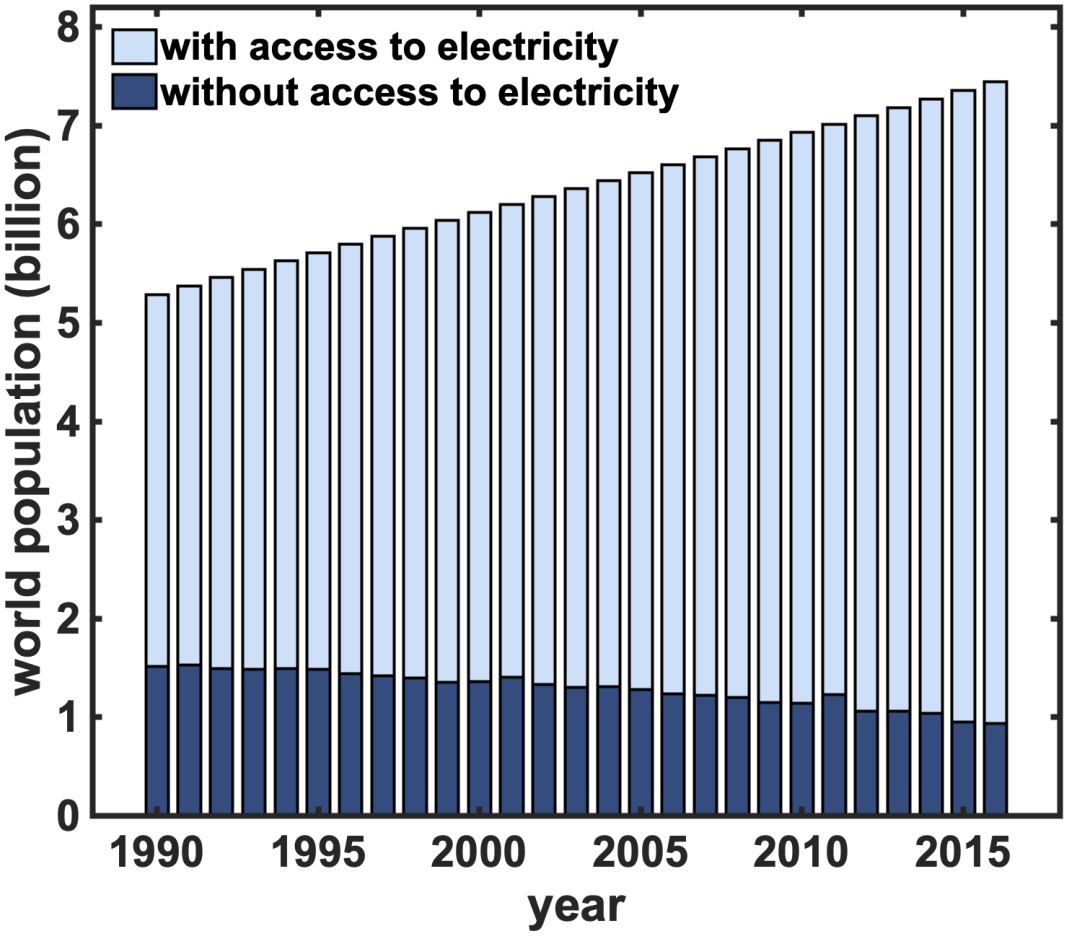

Figure 1: Bar graph depicting the number of people with and without access to electricity over the last three decades. (Based on data obtained from Sustainable Energy for All (SE4ALL) Database [2]. Graphical representation of the figure was inspired by https://ourworldindata.org/energy-access, Creative Commons License)

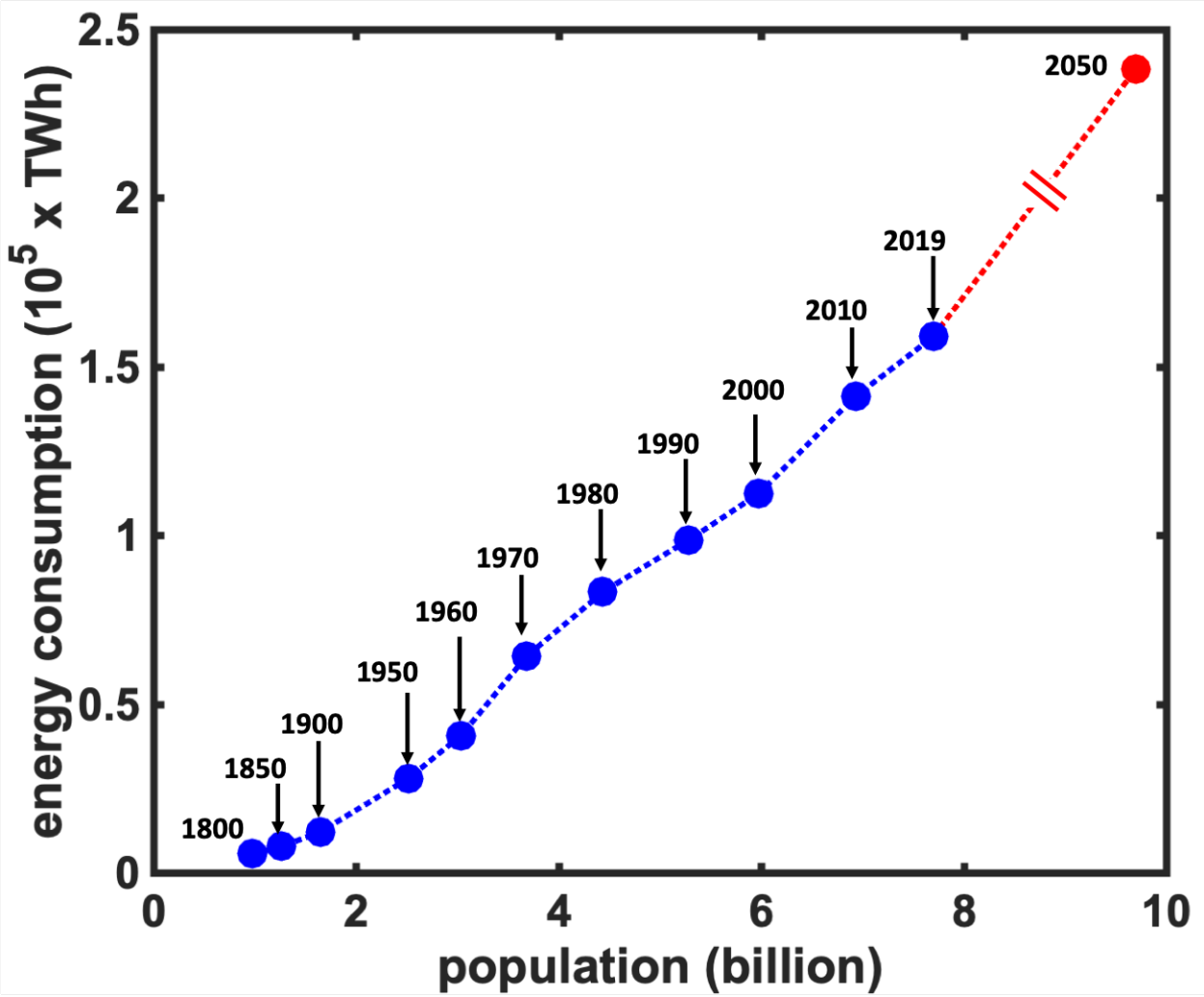

Figure 2: Plot depicting growing energy consumption with an increase in population from 1800 to 2019 alongside projected data for 2050. (Based on data obtained from Energy Transitions (2017) and BP Statistical Review of World Energy [5, 6])

as well as other environmental pollutants like SOx and NOx that pose a major cause of health concern [12, 13]. Thus, leaders in many countries are now prioritizing sustainability and are promoting the development of alternative electricity production methods [14,15]. Renewable and nuclear power sources have both garnered attention due to their ability to produce electric power without continuous carbon emissions [16, 17]. Moreover, the increasingly competitive cost of energy generation from renewables like wind and solar, as well as nuclear fission, make these alternative energy technologies promising for future electricity production [18].

This dissertation is aimed at pursuing the vision of a sustainable energy future by employing the tools of electrochemical analysis to improve our ability to produce and store carbon-free electricity via multiple research avenues. The two research objectives of the work described herein were:

1. To improve the energy efficiency of redox flow batteries (RFBs) by developing highly catalytic, robust electrodes for the associated electron-transfer reactions.
2. To increase the long-term stability of nuclear reactors by mitigating the effects of Zircaloy corrosion under the unique photochemical conditions of nuclear fission.

I addressed these two objectives as parallel research projects that were linked by a common set of skills and tools associated with analytical electrochemistry and the broader pursuit of a sustainable energy future.

1.2.2 Efforts toward Renewable Energy Storage

To reduce carbon intensity of our electricity production and thereby improve environmental sustainability, there exists a pressing need to harness renewable energy on a large scale [19]. In 2019, renewable energy resources contributed to ∼11% of total energy production in the United States (See Figure 4) [20]. In comparison, the contribution from renewable resources in 2010 was only 8% [21]. These low contributions result from the massive gap between the potential capacity of these resources and the relatively low maturity of the associated energy capture technologies. Another key aspect that needs to be considered in developing a stable electric grid based predominantly on solar and wind power is the spatial

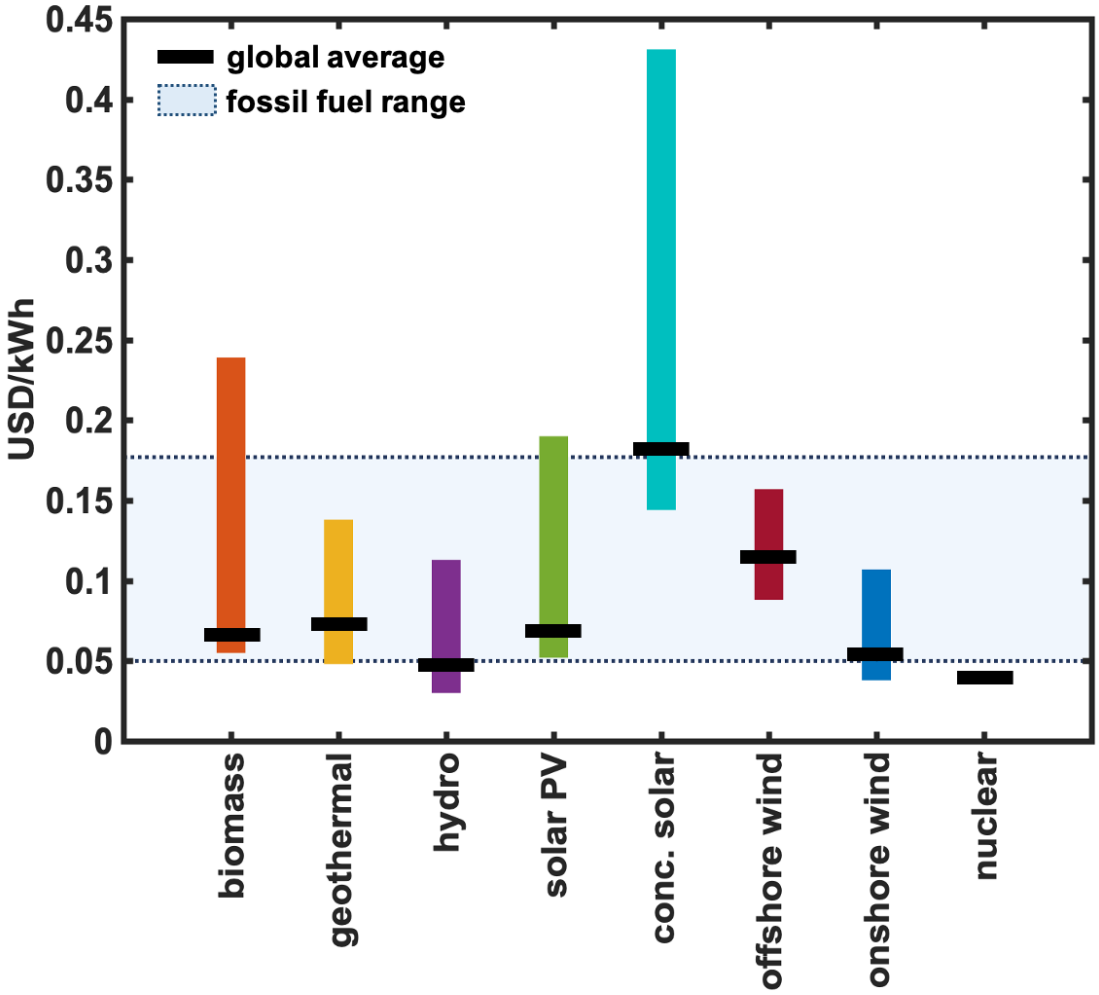

Figure 3: Cost of energy production (USD/kWh) using various renewable and non-renewable energy sources alongside the global average cost in 2019 and compared to cost of energy production using fossil fuels. (Based on data obtained from International Renewable Energy Agency [11].)

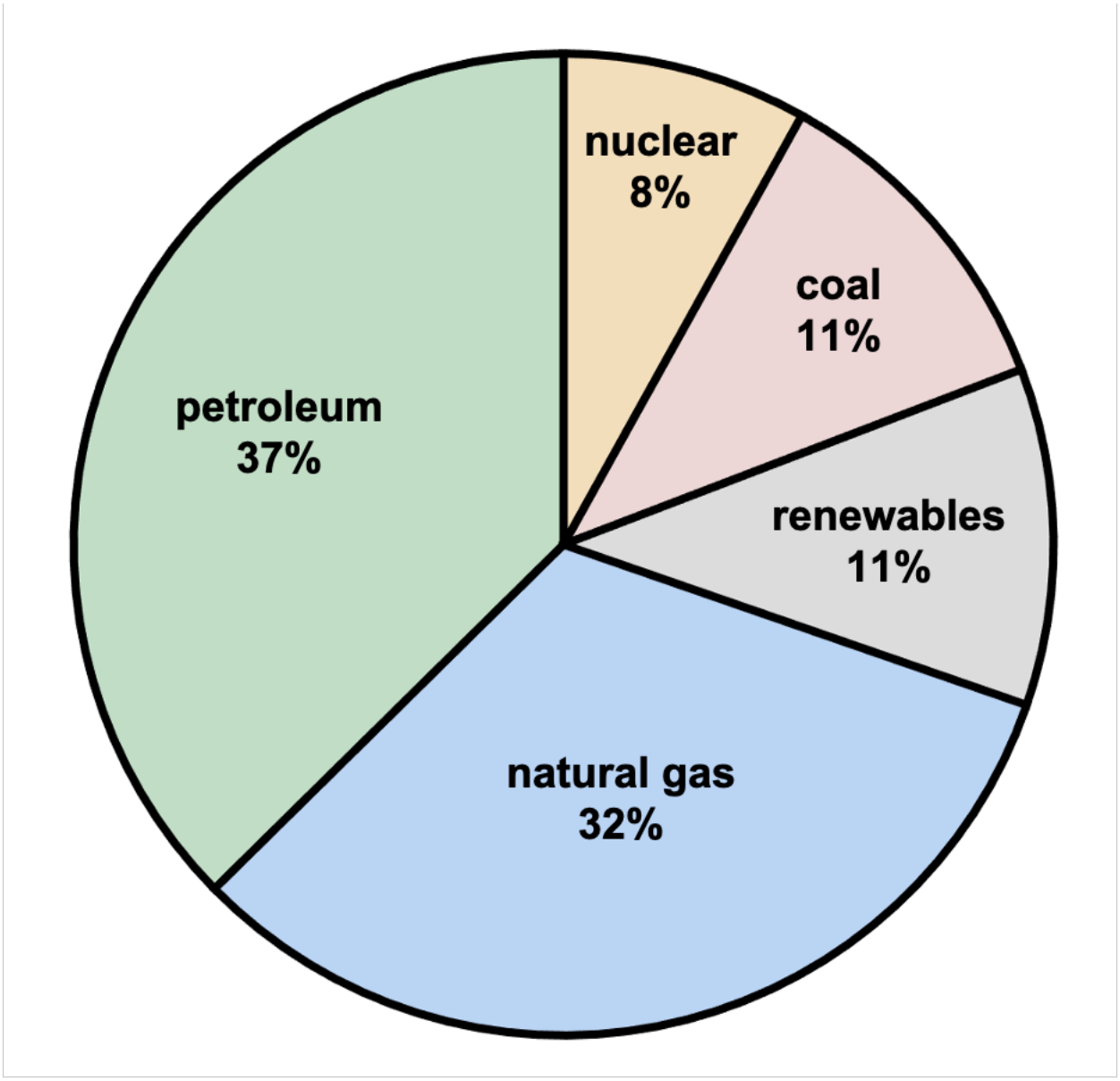

Figure 4: Pie chart depicting the contributions of various energy sources to the total energy consumption of the United States in 2019. Note that the sum of all components is not 100% due to individual rounding. (Based on data obtained from US Energy Information Administration, April 2020 [20])

and temporal intermittency of renewables [22–24]. To illustrate, Figure 5 presents the comparative energy demand and supply data over a period of three consecutive days in a region near Bend, Oregon [10, 25]. These data clearly demonstrate the intermittent nature of renewables, in that the energy supply from these resources does not coincide with the demand in energy. Thus, there is a pressing need for the development of cost effective technologies that can store large quantities of renewable electricity on a continuous basis.

Stationary energy storage technologies are generally classified into thermal, kinetic, electrochemical, electrical, potential and chemical categories [26, 27]. Examples of each of these types are presented in Figure 6. Pumped hydroelectric storage (PHS), compressed air storage (CAS) and flywheel technologies are few of the widely commercialized systems for grid scale applications [28–32]. PHS and CAS are high energy, high power systems but require a high degree of geographic favorability and large capital and maintenance costs. Flywheels, on the other hand, are touted for their long lifetimes and high power ratings but also require high capital investment. Electrochemical energy storage technologies such as batteries offer a unique advantage in that they are energy efficient and can be easily scaled from the kWh to MWh energy range [26, 33–35]. A Redox Flow Battery (RFB) is one electrochemical energy storage device that is specifically designed for use on the grid-scale [36, 37].

My doctoral research on Redox Flow Batteries (RFBs) was focused on improving their energy efficiency by developing robust, catalytic electrodes for the associated electron-transfer reactions. While RFBs have been the subject of considerable interest for grid-scale energy storage, slow-electron transfer kinetics resulting from poor catalysis is a major limiting factor in commercializing RFB technologies. Since flow battery chemistries are often inhibited by slow interfacial electron transfer rate, understanding electrocatalysis is crucial to develop efficient and stable systems. Thus, our specific objectives for this work were:

1. Developing an experimental platform for accurate characterization of interfacial electron transfer kinetics of RFB electrolytes.
2. Modulating the surface chemistry of carbon electrodes to enable efficient and robust electrocatalysis.

Complete details of this work can be found in Chapter 2.

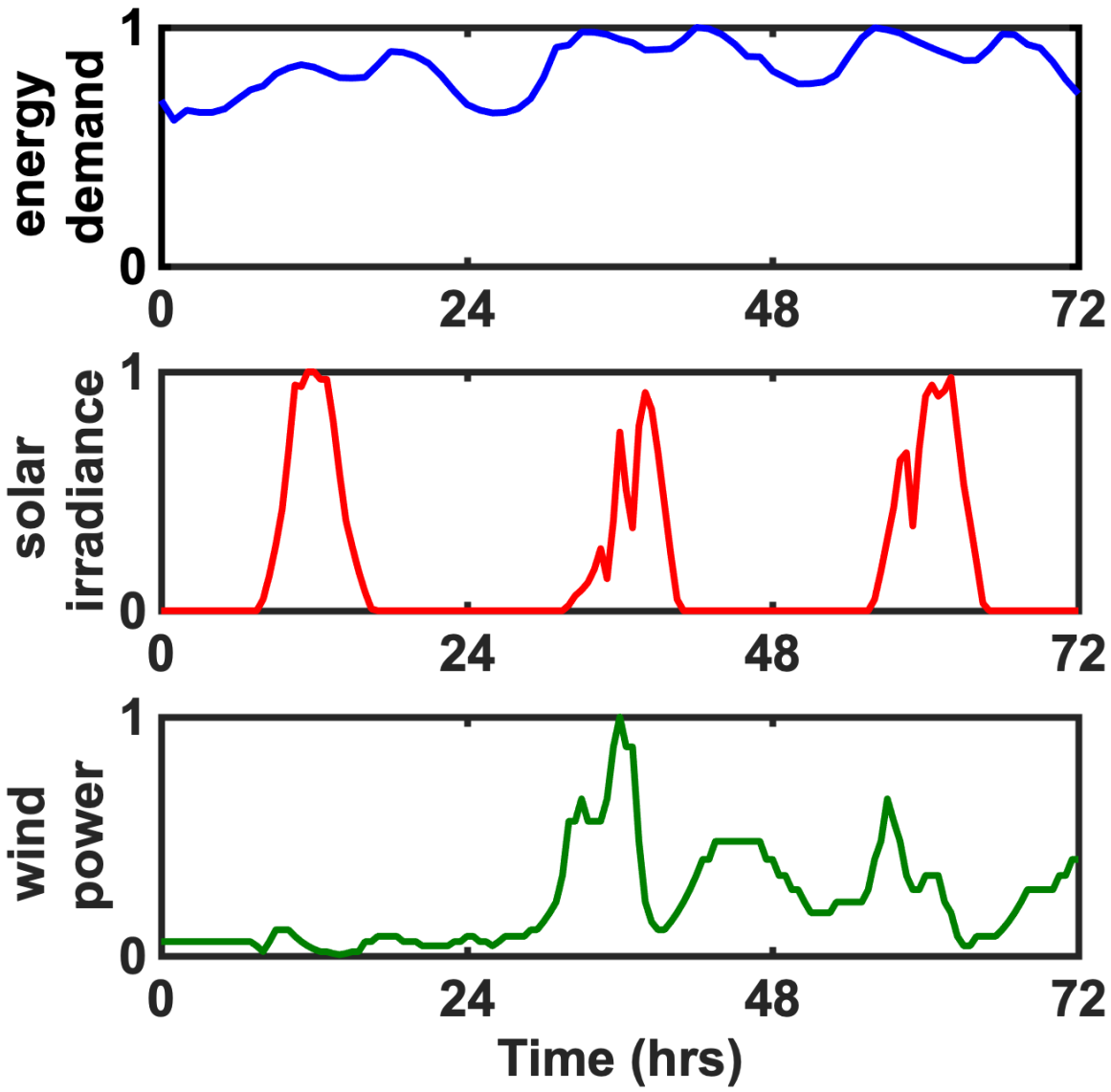

Figure 5: Normalized energy demand, solar irradiance and wind power over a 3-day span in a region near Bend, Oregon, USA. Data is normalized to the respective maxima. (Based on data obtained from US Energy Information Administration, April 2019 and National Solar Radiation Data Base [10, 25])

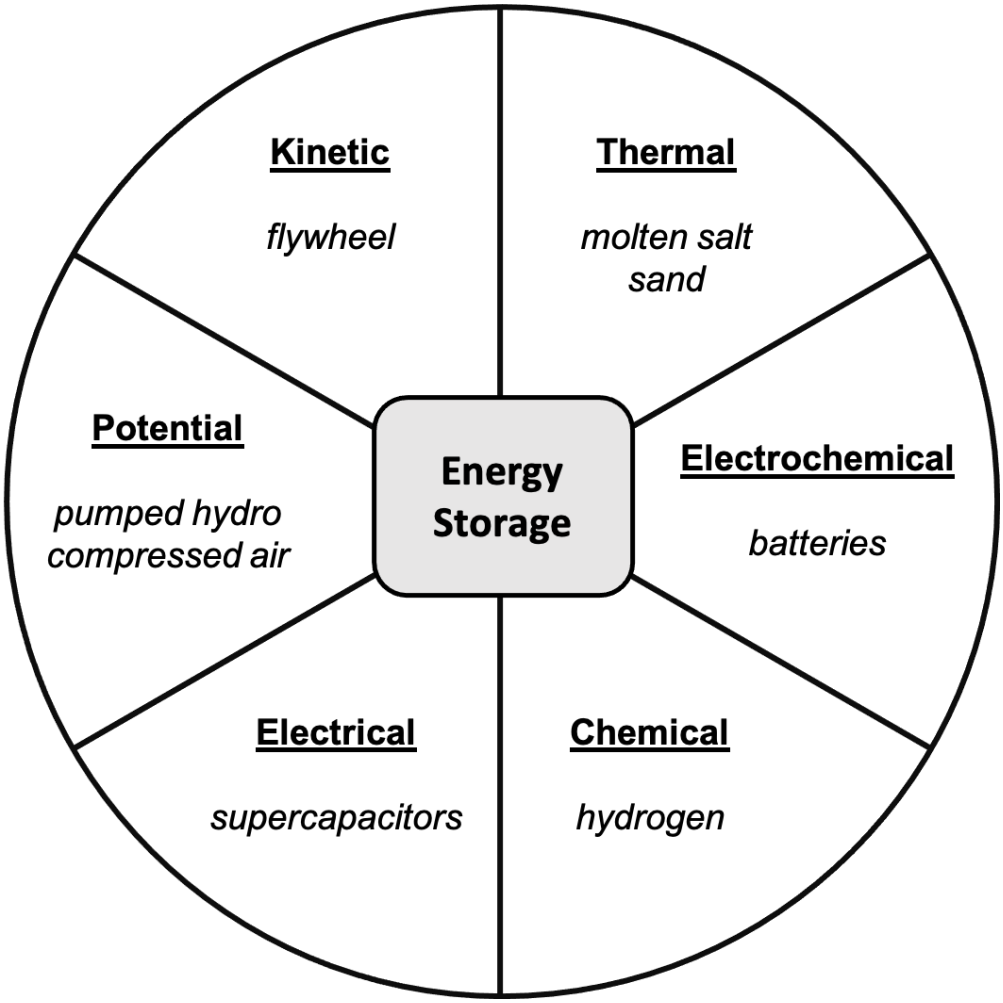

Figure 6: Energy storage systems categorized into various types based on the mechanism of operation. (Based on data obtained from Cho et al. [26])

1.2.3 Progress in the Nuclear Energy Domain

In the pursuit of a carbon-free energy supply, nuclear energy is an attractive alternative and compliment to renewables like wind and solar. In 2018, nuclear energy was used to contribute to the total energy supply for 30 US states, as shown in Figure 7 [38]. Nuclear fission can provide a stable base-load power supply, whereas wind and solar need to be combined with advanced storage technologies to address demand fluctuations owing to their intermittent nature. These power plants are generally operated at $> 90\%$ capacity factor, which means that nuclear reactors deliver at full capacity on average 328 days of the year [39]. As a comparison, solar farms only operate at $\sim$25% capacity factor because they produce zero power at night and diminished peak power output during the winter months relative to the summer [40]. Additionally, the low cost of energy production from nuclear sources make them a particularly valuable resource (See Figure 3) [41].

Despite these advantages, in 2018, the contribution of nuclear energy to the United States energy consumption was only $\sim$8% (See Figure 4) [20]. This low degree of nuclear energy penetration can be generally attributed to the perception that nuclear reactors are unsafe, in part as a result of several prominent nuclear emergencies like Chernobyl, 3-Mile Island, and most recently Fukushima. Moreover, the storage and disposal of spent nuclear fuel is challenging due to the inherent radioactivity hazard as well as public perceptions that make it difficult to build new nuclear waste storage facilities [42]. Finally, the high capital cost associated with nuclear reactors necessitates their use for multiple decades with minimum off-grid time [41]. Nuclear reactors are generally shut down for $\sim$10% of the year for maintenance requirements and thus, an important consideration in the continuous operation of these reactors is the long-term stability of cladding materials that encapsulate the fissile material in a nuclear reactor.

We are working to understand corrosion dynamics of a specific class of zirconium alloys called Zircaloys, which are used as cladding materials to hold the fuel in a nuclear reactor [43]. Corrosion of Zircaloy cladding material is a key factor in dictating the maintenance requirements and ultimate lifetime of a nuclear energy facility [44, 45]. The challenge exists in the lack of understanding of mechanisms of Zircaloy corrosion unclear nuclear operat-

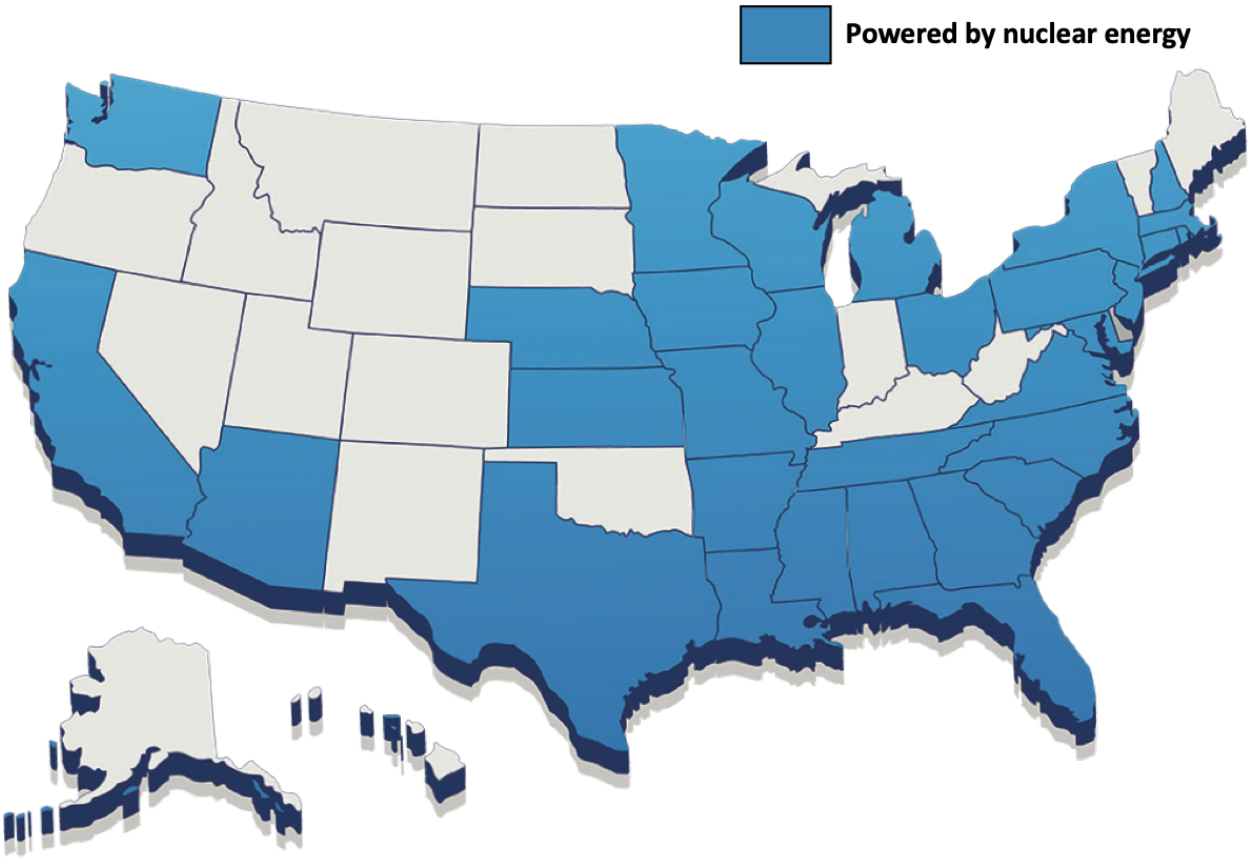

Figure 7: A map of United States of America depicting contribution of nuclear energy in various states (Reproduced from US Department of Energy, Office of Nuclear Energy [38])

ing conditions; this in turn greatly inhibits our ability to design more corrosion resistant cladding materials. We specifically hypothesized that corrosion of Zircaloy is enhanced by high intensity γ-radiation in the reactor, which destabilizes its protective oxide coating via photo-electrochemical oxidation reactions [46, 47]. Thus, my doctoral work in the nuclear energy domain was focused on

1. Assessing the semiconducting behavior of Zr and Zircaloy surface oxides under high energy radiation.
2. Identifying the conditions under which the oxide growth and dissolution processes are accelerated.

Full details of this work can be found in Chapter 3.

2.0 Electrocatalysis in Redox Flow Batteries

2.1 What are Redox Flow Batteries?

Grid-scale electrochemical energy storage (EES) devices can provide a robust solution by deploying renewable energy when and where it is needed [48,49]. Recently, EES technologies have grown in importance to modern society to act as buffers between the demand and supply of energy [50, 51]. While primary and secondary batteries have been available for more than a century, the most recent phase of rapid growth in EES technologies began with the development of the Li-ion battery, which was first commercialized by Sony in 1991 [52–54]. The continued development of Li-ion batteries was primarily driven in the portable electronics and transportation electrification sectors, but more recently, a newly emerging growth area for EES involves the use of secondary batteries for incorporation of renewables into the electric grid [55–57].

The redox flow battery (RFB, schematized in Figure 8) is promising as an alternative to Li-ion and other secondary batteries for grid-scale EES [58–61]. A typical RFB charges and discharges through reversible oxidation and reductions reactions between two sets of liquid-phase redox couples. These electroactive materials flow over a centralized electrode assembly, referred to as the stack, to interconvert between chemical and electrical energy. Several such stacks can be coupled together to increase the output power, voltage and cell capacity of the battery. The liquid phase electrolytes are stored in external reservoirs of arbitrary size and pumped through the stack for charging/discharging the battery. These stacks and the tanks for storing electrolytes can be independently sized, which decouples the power and energy density in the system. Moreover, the stack, tanks and pumps are packaged separately which enables easy service and replacement, thereby reducing the operation and maintenance costs compared to conventional secondary batteries which are completely integrated.

RFBs have seen significant technological development since their invention in the 1970s [62]. Some of the earliest work on RFBs was done by the National Aeronautics and Space Administration (NASA) using transition metal compounds of iron, chromium and titanium

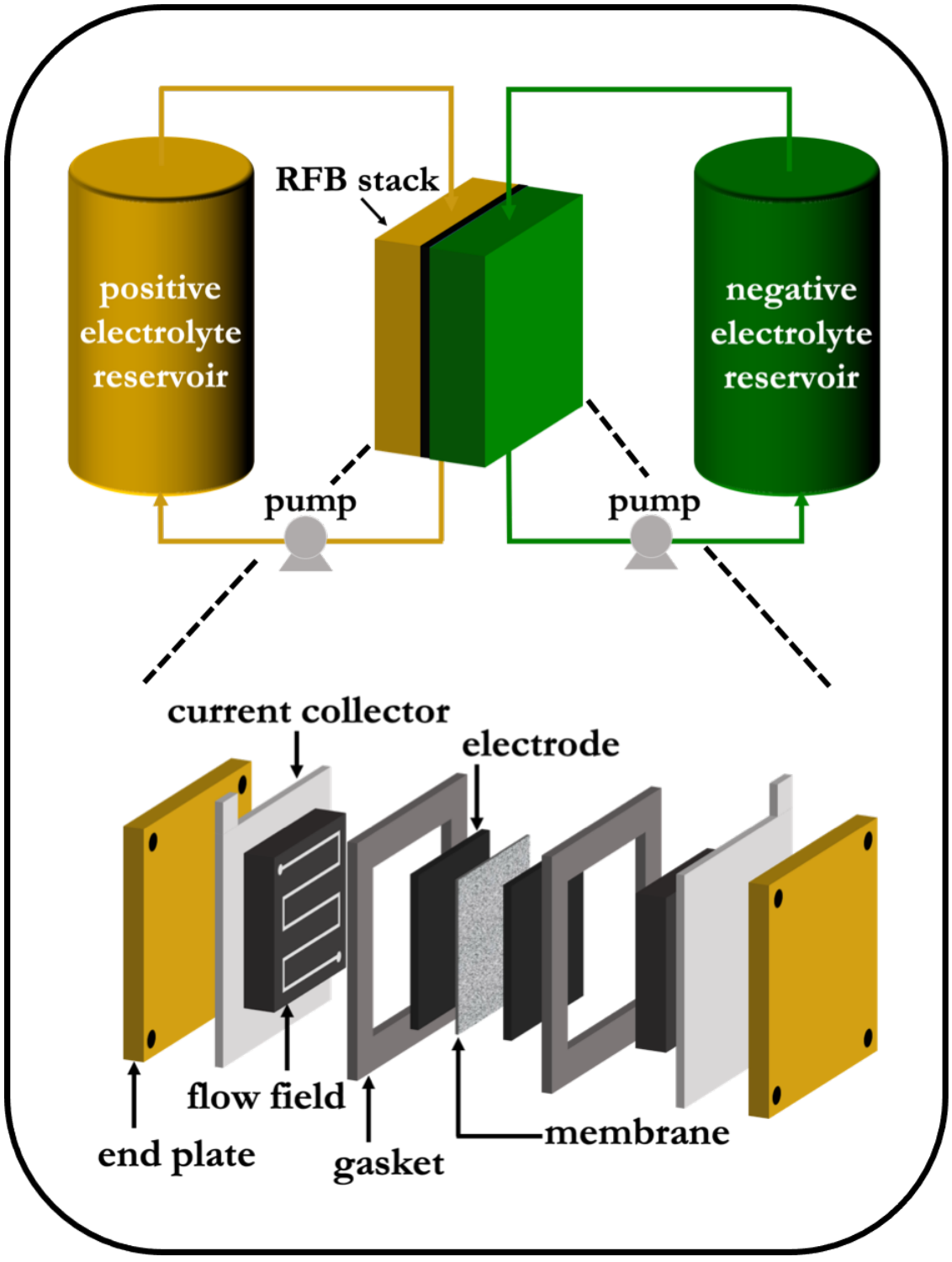

Figure 8: Schematic representation of a redox flow battery alongside the components of an RFB stack.

as the active components of the battery electrolytes [63–65]. However, problems associated with crossover of dissimilar reactive species across the membrane soon led to the development of the all-vanadium redox flow battery (VRFB), which uses a set of interconvertible aqueous vanadium complexes as the positive and negative electrolytes in the two half cells [66–71]. While aqueous electrolytes remain the subject of major commercial interest, considerable work is now focused on the development of non-aqueous RFB active materials, particularly centered around organic and organometallic redox couples which offer the advantage of extended stability from the use of organic solvents leading to high cell voltages ($\sim$3 V compared to 1.23 V achievable in aqueous electrolytes) [72–79]. Moreover, these electrolytes are touted for their ability to tune key physicochemical properties like solubility and reduction potentials and have shown excellent promise in lab-scale devices.

The practical performance of RFBs can be described using an interplay between the parameters of efficiency, lifetime and cost. The overall efficiency of a battery is a ratio of the total energy that can be extracted from the cell to the energy required to charge it. RFBs generally exhibit up to $\sim$70% overall energy efficiencies, which is significantly smaller than the typically achieved $>$ 90% efficiencies of conventional Li-ion batteries [80–86]. However, RFBs are expected to significantly exceed solid-state batteries in device longevity, owing to their ability to access both high and low states of charge without degrading the active components [58,87]. Moreover, RFBs can be completely depleted of the electrolyte when the system is not under operation [61,88]. This results in suppression of degradation occurring from unwanted side reactions when the electrode and electrolyte are in contact. Additionally, the ability to perform maintenance on electrolyte and stack components separately offer key advantages to achieve higher lifetimes as compared to the traditional batteries which need to be disassembled for service. Finally, RFBs provide lower system costs compared to traditional Li-ion batteries because increasing the capacity of the system only requires increasing the electrolyte volumes [89–92]. Nonetheless, these cost advantages have not yet materialized in practical devices; instead, RFBs still suffer from relatively high electrolyte and stack costs, which limits their commercial attractiveness even for "early adopters" of clean energy technologies [93–98].

A major challenge associated with the design and implementation of RFBs is to minimize the efficiency losses emerging from slow electron transfer in the positive and negative half cells of the battery. Thus, a critical need associated with the continued development of this technology involves the design of electrode-electrolyte interfaces that exhibit rapid and stable electron-transfer kinetics. Current research in RFBs is aimed at developing redox couples that exhibit intrinsically fast reaction rates and at employing several electrode modifications in an attempt to enhance the electron transfer kinetics [70, 71, 99, 100]. Our interest resides in understanding and elucidating the key characteristics of electrodes and electrolytes that lead to accelerated electron transfer behavior.

2.2 Effect of Interfacial Electron Transfer Kinetics on RFB Performance Parameters

Interfacial electron transfer kinetics impacts several key RFB performance parameters. For instance, electron transfer kinetics play a major role in determining the voltage efficiency of a battery. RFBs suffer from characteristically low energy conversion efficiencies as compared to solid-state batteries due to reduced voltage efficiencies [82, 83]. The voltage efficiency of an RFB, which is the ratio of discharge to charge voltage, $\frac{V_{discharge}}{V_{charge}}$, is primarily influenced by kinetics, resistance and mass transport losses in the system [101, 102]. Ohmic losses occur from current collectors and porous electrodes and can be minimized by using specific cell architectures; however those occurring from membranes still pose a significant challenge [103, 104]. Additionally, mass transport losses can be overcome with increased convective fluid velocity, which depend on parameters such as diffusivity, state-of-charge, solubility of active species and flow fields [105–108]. Finally, charge transfer losses result from sluggish electron transfer kinetics on the electrode of interest. These losses collectively result in an overpotential (potential required in excess of thermodynamic potential) to drive the oxidation and reduction reactions during charge and discharge.

To exemplify the effect of electron transfer kinetics on the voltage efficiency of an RFB, Figure 9 presents the simulated charge-discharge curves for a prototypical VRFB. Parame-

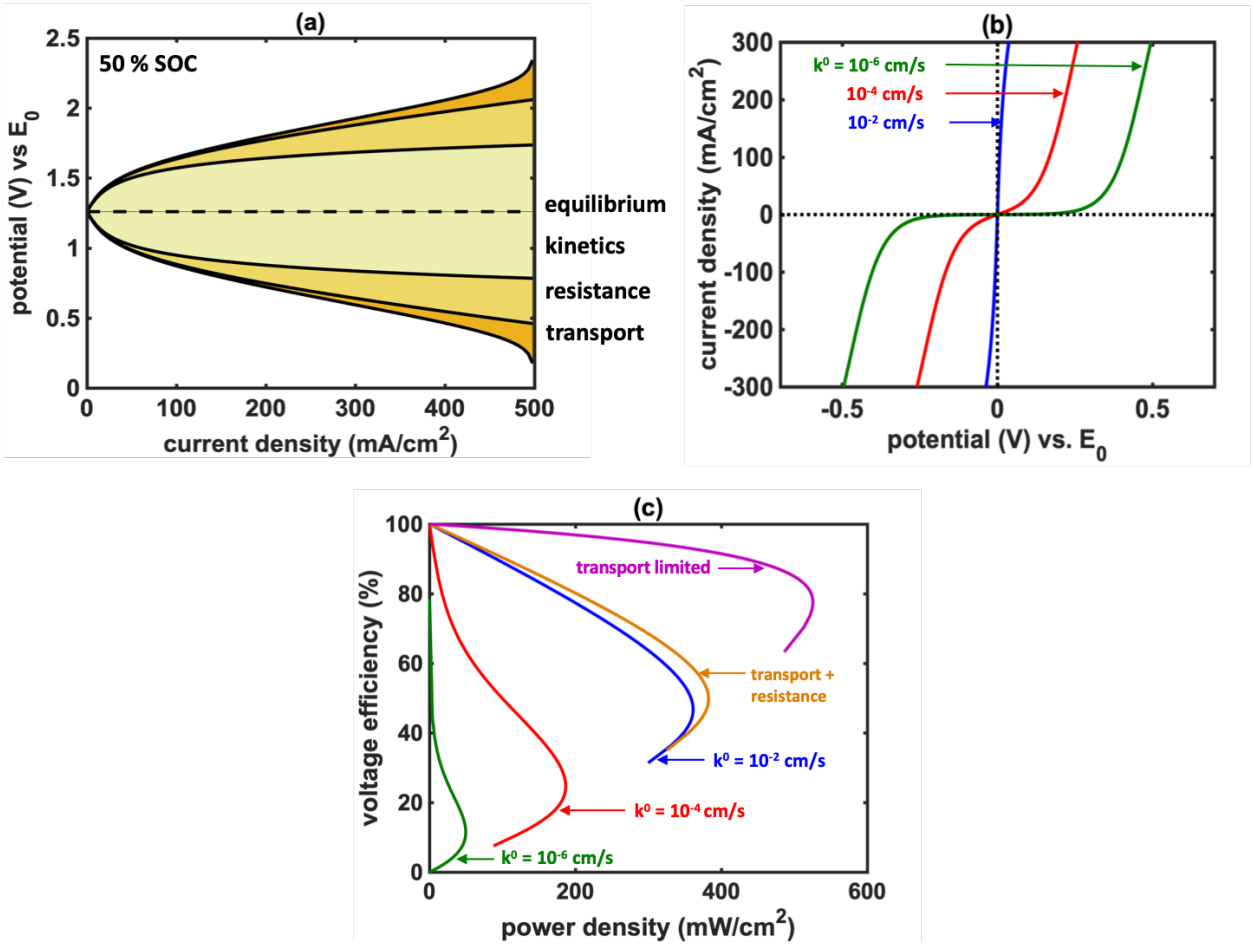

Figure 9: Simulated charge/discharge curve for a prototypical VRFB depicting the contributions of kinetics, resistance, and mass transport to the total overpotential losses during charge and discharge. (b) Simulated VRFB polarization curves at 50 % state of charge encompassing the expected range of electron-transfer rate constants for sluggish versus facile charge transfer processes. (c) Simulated voltage efficiency vs. power density plot for a VRFB like that shown in panel (a) highlighting the theoretical maximum performance (infinitely fast kinetics and zero electrical resistance) and four cases of progressively decreasing electron-transfer rates.

ters used for these simulations were adopted from recent reports on VRFB cells and modified to reflect practical RFB conditions [101, 103, 104, 109]. Complete simulation details are provided in the Appendix A.1. Figure 9(a) clearly shows that the overpotentials associated with kinetics dominate the charge/discharge curves upto several tens of mA/cm^2 current densities. At larger current densities, resistance and mass transport limitations further contribute to the overpotential losses. These overpotential losses can be clearly visualized in Figure 9(b), where the onset of polarization curves depict the overpotential required to drive the oxidation and reduction reactions. These simulations show that for RFBs operating at current densities of several hundred mA/cm^2, the effective heterogeneous electron transfer rate constant, k^0_{eff}, should be at least 10^{-2} cm/s to eliminate contribution of kinetics to overpotential. These values are characteristic of rapid "outer-sphere" electron transfer reactions or "inner-sphere" reactions that are efficiently catalyzed at the electrode surface [110, 111]. In this context, one of the easiest ways to increase k^0_{eff} is to increase the surface area of the battery electrode by using porous or nanostructured materials; however, surface area alone cannot be expected to generate greater than 10-100 fold increase in kinetics without introducing additional transport losses [103, 104]. Accordingly, we propose establishing as a general benchmark, a k^0 value of 10^{-4} cm/s as a "minimum viable electron-transfer rate" for highly efficient RFB systems. Figure 9(c) depicts the simulated voltage efficiency of the VRFB as a function of the power density. The maximum achievable power density at a target voltage efficiency increases with an increase in the heterogeneous electron transfer rate constant. This in turn contributes to the overall cost since increasing the power density enables the use of smaller stack components, which constitutes the most expensive hardware of the system.

Interfacial electron transfer kinetics also play a key role in influencing the couloumbic efficiency (CE) of RFBs. CE is the ratio of total charge (Q) that can be extracted from the battery to the total charge that is stored in it, $\frac{Q_{discharge}}{Q_{charge}}$. Self-discharge and unwanted side reactions are primary contributors to CE losses in RFBs [112–115]. Self-discharge occurs when redox active species from one half cell diffuses across the semipermeable membrane to the other half cell leading to direct charge transfer between molecules. This results in loss of energy as heat rather than useful electric power. While self-discharge was found to

be one of the main issues in the early demonstrations of RFBs, the magnitude of CE fade associated with self-discharge has greatly reduced as a result of the availability of ion-selective membranes [116–119].

While self-discharge is mainly governed by transport of the active components, side reactions are primarily influenced by the thermodynamics and the associated electron transfer kinetics. Side reactions generally comprise redox reactions of the impurities in the electrolyte or over-oxidation/over-reduction of the active species of the electrolyte. In many cases, these parasitic reactions can lead to irreversible degradation of the electrolyte alongside CE and capacity fade in the RFB. Thus, to visualize the effect of the thermodynamics and kinetics of the over-oxidation process on the CE and capacity of an RFB, we simulated the current-voltage behavior of a hypothetical battery that undergoes an over-oxidation of the product as shown in Figure 10. In this case, we simulated the desired oxidation to occur at $E_1^0 = 0$ V (vs. an arbitrary reference potential) followed by an irreversible second oxidation step at $E_2^0 = 0.3$ V that results in rapid decomposition. Complete simulation details are provided in Appendix A.2.

While the equilibrium potential of the over-oxidation reaction is far more positive than that of the desired oxidation, the contribution of the undesirable over-oxidation reaction to the operating current density remains non-zero throughout the onset of the desired oxidation reaction. This results from the Nernst equilibrium relationship $E_{eq} = E^\circ - \frac{RT}{nF} \ln \frac{[\text{red}]}{[\text{ox}]}$ which suggests that oxidative decomposition will proceed far negative of its equilibrium potential since the product concentration remains small. Thus, in spite of operating under "safe" current densities, irreversible degradation associated with over-oxidation can occur in an RFB. Indeed, this process of over-oxidation has been reported to fundamentally limit the cycle life of quinone based RFB redox couples [120–122].

One way to enhance the long-term stability of RFB electrolytes is to shift the equilibrium potential of the undesired reaction more positive, which will destabilize the over-oxidized product, resulting in a decrease in the contribution to the total operating current density. This is represented as the strategy in Figure 10(b). Another strategy involves "kinetic stabilization", also shown in Figure 10(b), where the electron transfer rate constant for the parasitic reaction can be suppressed by designing stable and selective electrocatalysts for this

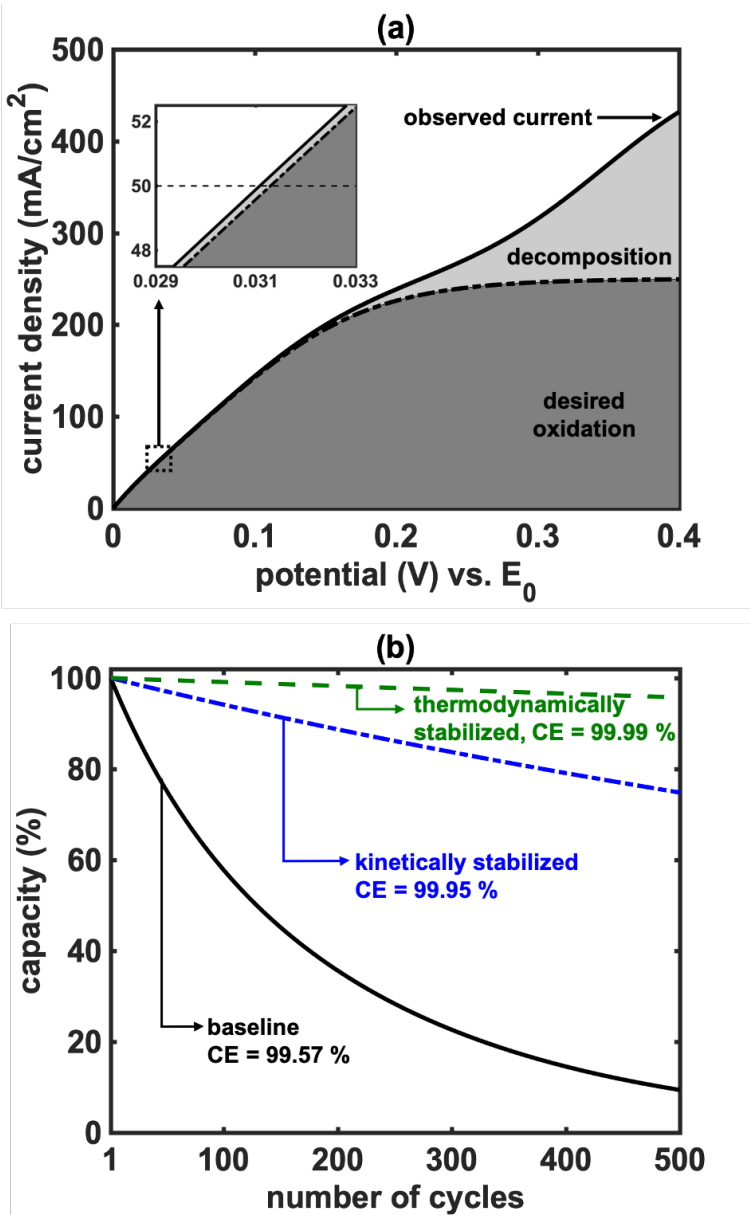

Figure 10: (a) Simulated polarization curves for the oxidation of a hypothetical RFB positive electrolyte, where the desired oxidization is followed by an undesired over-oxidation reaction that results in irreversible decomposition. (b) Simulated capacity retention data for three cases: the "base case" corresponding to the parameters depicted in (a); thermodynamic stabilization, where the equilibrium potential for the decomposition reaction was shifted positive by 0.1 V; and kinetic stabilization, where k^0 for the decomposition reaction was decreased by a factor of 10.

system where the rate constant for the undesired decomposition reaction is reduced relative to that of the desired one. This type of kinetic selectivity is the hallmark of well-designed catalyst materials.

2.3 Developing an Electroanalytical Platform for Accurate Characterization of Flow Battery Kinetics

2.3.1 The Challenge of Making Good Measurements

Considerable prior work has been undertaken to understand the dynamics of electron transfer to/from RFB redox couples [111, 123–127]. However, these studies are generally conducted under conditions that present a contrast to the operating conditions in an RFB. For instance, flow batteries are generally operated at high active and supporting electrolyte concentrations – typically greater than 1 M. By contrast, analytical experiments are carried out in the mM range or lower [29, 128]. Moreover, these analytical studies are generally performed using planar model electrode materials such as platinum, gold and glassy carbon under well defined hydrodynamic conditions [129, 130]. However, practical RFBs operate with high surface area porous carbon electrodes under forced convection in turbulent flow [100, 131]. Moreover, for redox couples whose electron-transfer mechanisms involve explicit interactions with the electrode, it can also be difficult to relate kinetics data collected from model electrodes like glassy carbon to porous electrodes like carbon felt, which are not guaranteed to exhibit the same surface chemistry. This methodological disconnect leads to one of the biggest challenges in this field: how to design and interpret electroanalytical measurements that can be readily translated to practical RFB conditions?

To illustrate the need to perform high-quality analytical measurements, Table 1 presents a representative set of interfacial electron transfer kinetics reported in the literature for four popular RFB electrolytes at various carbon electrodes. These data were collected from some studies that were directed at RFB operation and others that were directed at the fundamental chemistry and physics of interfacial electron-transfer. Accordingly, only a subset

Table 1: Compiled kinetics data for aqueous RFB redox couples at various types of carbon electrodes

redox couple	**electrode material**	**rate constant, k^0 (cm/s)**	**measurement technique**	**supporting electrolyte**	**concentration of active species**	**Ref.**
$Fe^{3+/2+}$	glassy carbon	7.3 x 10^{-5}	RDE	2 M H_2SO_4	1 M	Yang [132]
	glassy carbon	2.3 x 10^{-3}	RDE	0.2 M $HClO_4$	5 mM	McDermott [133]
	glassy carbon	1 x 10^{-3}	RDE	0.3 M HCl	1 mM	Stulikova [134]
	pyrolytic graphite	5.2 x 10^{-4}	RDE	4 M HCl	0.1 M	Ateya [135]
	pyrolytic graphite	1.0 x 10^{-3}	CV	1.5 M HCl	1 M	Hollax [136]
$V^{3+/2+}$	glassy carbon	1.0 x 10^{-6}	potentiostatic polarization	4.2 M H_2SO_4	1.6 M	Oriji [129]
	glassy carbon	1.4 x 10^{-4}	EIS	4.5 M H_2SO_4	1.5 M	Bourke [137]
	electrochemically activated graphite	1.1 x 10^{-6}	CV	2 M H_2SO_4	2 M	Liu [29]
	carbon felt	1.4 x 10^{-6}	LSV	0.1 M H_2SO_4	150 mM	Li [138]
	carbon felt	1.5 x 10^{-5}	CV	1 M H_2SO_4	50 mM	Agar [139]
	carbon paper	1.1 x 10^{-3}	CV	1 M H_2SO_4	50 mM	Wu [127]
VO^{2+}/VO_2^+	glassy carbon	2.2 x 10^{-6}	potentiostatic polarization	4.2 M H_2SO_4	1.6 M	Oriji [129]
	glassy carbon	4.5 x 10^{-5}	EIS	4.5 M H_2SO_4	1.5 M	Bourke [137]
	electrochemically activated graphite	8.2 x 10^{-4}	CV	2 M H_2SO_4	2 M	Liu [29]
	carbon nanotubes	1.8 x 10^{-6}	CV	1 M H_2SO_4	100 mM	Friedl [140]
	carbon paper	1.0 x 10^{-3}	CV	1 M H_2SO_4	50 mM	Wu [127]
	carbon–polymer composite	8.5 x 10^{-4}	CV	1 M H_2SO_4	50 mM	Yamamura [141]
AQDS/AQS	glassy carbon	7.2 x 10^{-3}	RDE	1 M H_2SO_4	1 mM	Huskinson [72]
	glassy carbon	1.5 x 10^{-4}	RDE	1 M H_2SO_4	1 mM	Yang [142]
	glassy carbon	4.8 x 10^{-4}	CV	1 M H_2SO_4	10 mM	Lantz [143]
	glassy carbon	1.5 x 10^{-4}	RDE	2 M H_2SO_4	1 M	Yang [132]

of these values include accompanying measurements of RFB figures of merit [72, 132, 138, 139, 142, 143], which in turn makes it challenging to contextualize differences in kinetics in terms of device-level performance. The large spread in these data clearly indicates that electron-transfer processes remain poorly understood even in well-established RFB active materials. While some of this ambiguity results from the use of different conditions for these studies like electrolyte concentrations, measurement techniques and electrode pretreatment procedures, differences in interfacial electron transfer kinetics of up to 10-fold are reported even under similar experimental conditions. This presents a unique challenge since the use of the interfacial electron transfer rate constant (k^0) as the primary kinetic desrciptor implies a direct knowledge of the electron-transfer process and the associated mechanisms, which should remain constant for a particular electrode-electrolyte pair.

To further capture the effect of electron-transfer kinetics on RFB performance, Figure 11 presents a simulated charge-discharge curve for a hypothetical RFB where the heterogeneous electron transfer constant was varied over 10^{-2} to 10^{-5} cm/s, which corresponds the outer bounds of reported kinetics in $Fe^{3+/2+}$ electrolyte at polycrystalline Au electrodes [144, 145]. The difference in the applied and the equilibrium potential at any given state-of-charge presents the overpotential loss in the system. For instance, at 90 % state-of-charge, the overpotentials associated with $k^0 = 10^{-2}$ and 10^{-5} cm/s are 50 and 300 mV respectively. This implies a 6-fold greater efficiency loss for the RFB with the slowest reported kinetics compared to the fastest case. This high level of variability in reported reaction rates makes it essentially impossible to perform appropriate engineering design on RFB systems. Thus, there remains a clear need to develop and validate robust characterization methods that can be readily deployed for established and emerging RFB active materials.

To further contextualize our work in this area, Figure 12 summarizes a conceptual workflow of the ongoing RFB research which can be categorized into the following three domains: (1) materials discovery, (2) applied electroanalysis and (3) device design. It is evident from the literature reports that most of the research performed in the past several decades is targeted at either the materials discovery or the device design phases with comparatively little progress in the area of applied electroanalysis [37, 58, 59]. Initial discovery and characterization of redox active molecules and electrodes is often carried out under "analytical"

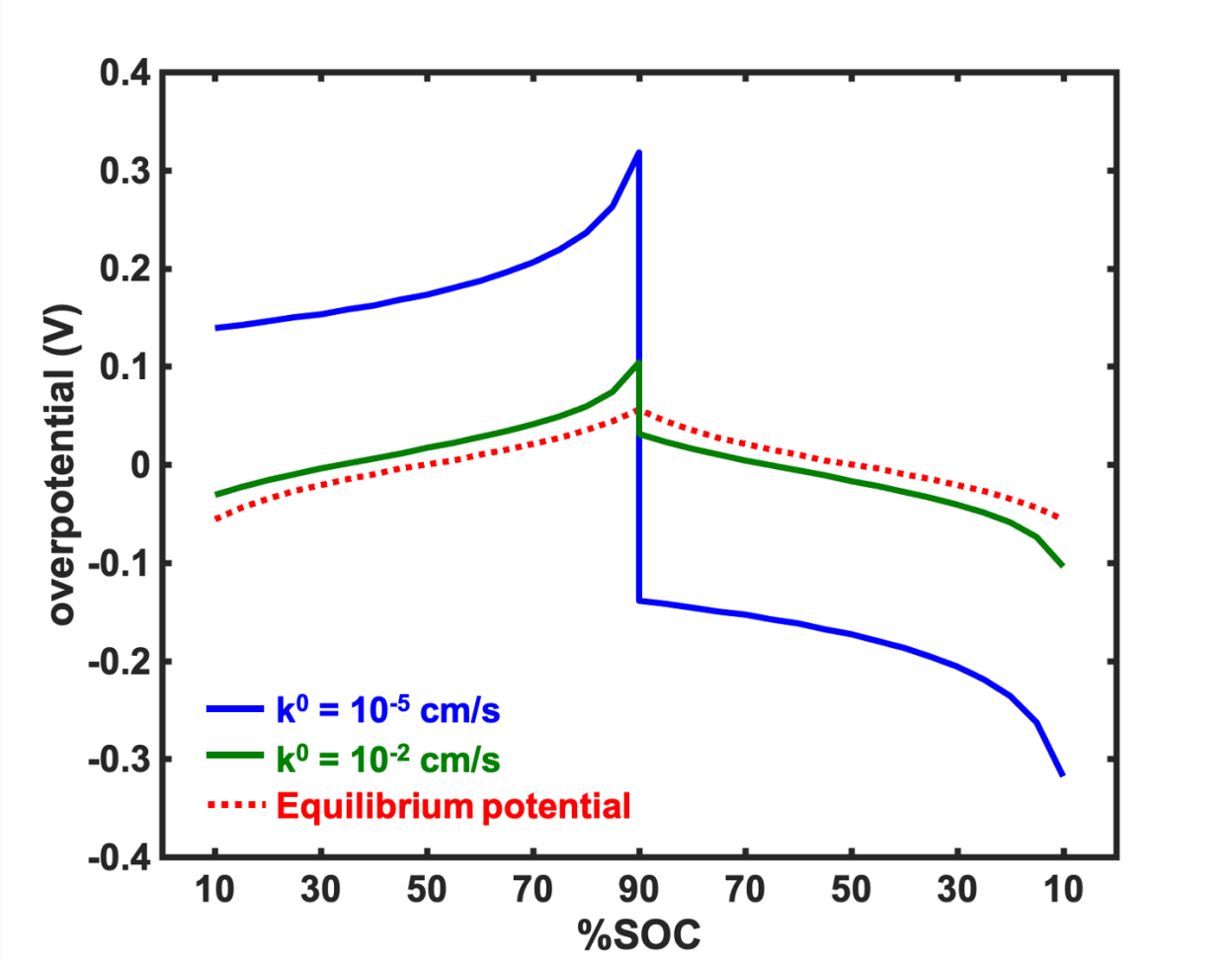

Figure 11: Simulated charge-discharge performance, overpotential as a function of % state of charge (SOC), of $Fe^{3+/2+}$ RFB electrolyte. The heterogeneous electron transfer rate constant, k^0, was varied from 10^{-2} to 10^{-5} cm/s corresponding to the upper and lower limits of reported kinetics at Au electrodes.

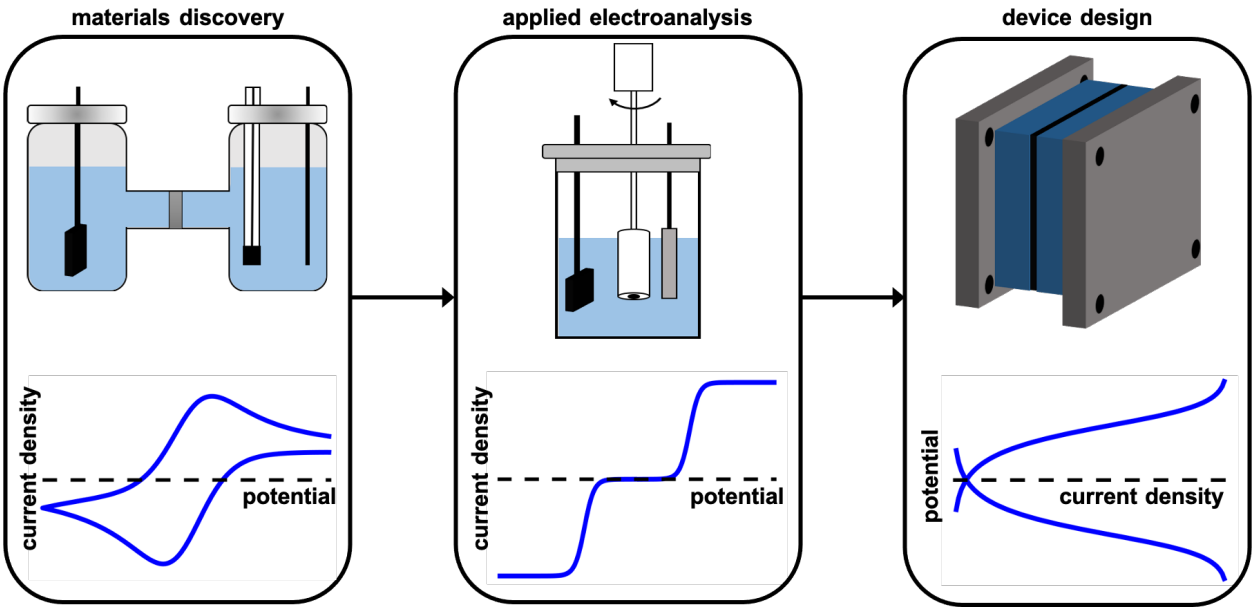

Figure 12: Schematic representation of a scientific/engineering workflow that describes ongoing work on RFB systems.

conditions (low electrolyte concentrations, planar electrodes, quiescent electrolyte) [146–156], and the most promising redox couples are then immediately deployed into lab-scale batteries to establish performance parameters [131, 157–166]. However, a lack of progress in applied electroanalysis makes it difficult to translate from discovery of new materials to the directed design of improved batteries.

Understanding and ultimately controlling electron-transfer kinetics in RFBs inherently depends on our ability to accurately measure the reaction rates and to interpret the result in the context of RFB operation. To that end, Section 2.3 describes our work over the last several years to develop an electroanalytical platform to accurately characterize flow battery kinetics. Early work on this effort was started in 2016 when I first joined the McKone Lab. After two years of my work on this project, I transitioned to managing a team of three undergraduate researchers to continue research efforts on RFBs.

2.3.2 Electroanalytical Techniques for Characterizing RFB Kinetics

At least three different types of electroanalytical techniques are currently used to understand electron-transfer in flow battery systems. The first comprises classical analytical electrochemistry methods like static and hydrodynamic voltammetry, potential and current-step techniques, and electrochemical impedance spectroscopy [129,137,167–170]. These techniques can be further adapted for electrodes and electrolytes resembling those used in RFBs—e.g., by using high electrolyte concentrations or technologically relevant electrode materials. As an illustrative example, Savinell et al. reported a series of studies using rotating-disk electrode voltammetry to understand the influence of carbon electrode composition and surface preparation on the kinetics of VRFB active materials [137, 150, 171]. Wang et al. also recently offered a perspective describing proper (and improper) applications of voltammetry techniques for the determination of RFB kinetics [172]. The advantage of these electroanalytical techniques is the ability to obtain credible estimates of electron-transfer rates using equipment and supplies that are readily available in most electrochemistry laboratories. However, the main drawback of these methods is their dissimilarity to practical RFB operation [173–179]. Moreover, it is challenging to execute these types of measurements

under simulated RFB cycling conditions, which would require ancillary equipment to charge and discharge the electrolyte of interest while maintaining minimal interference from the counter electrode. Accordingly, classical electroanalytical methods are excellent for making precise measurements of several key physicochemical properties of RFB active materials—including key kinetic parameters like k^0—but care must be taken when using these data to make specific inferences about the performance of a particular electrode or electrolyte in a battery.

A second general category of RFB analytical measurements comprises those that are executed using fully functional flow cells. This type of measurement can be accomplished using a small scale RFB stack with electrodes and electrolytes that are otherwise identical to those used in a practical device. Additional analytical precision can be obtained by incorporating a reference electrode to isolate the behavior of only one half cell at a time. Zawodzinski et al. made excellent use of this type of lab-scale RFB to understand the influence of electrode pretreatments on overpotential losses and coulombic effiency losses in VRFBs [104, 180, 181]. Similarly, Brushett and co-workers have used small-scale flow cells to execute analytical measurements on aqueous and nonaqueous RFB active materials. The main benefit of this approach is the ability to use the results to directly inform the design of larger RFB prototypes [97, 108, 179, 182, 183]. However, these measurements are difficult to execute since they require specialized equipment that is not as readily available nor as well standardized as most analytical electrochemistry tools. It can also be difficult to extract quantitative information about the properties of interest (e.g., electron-transfer rate constants) from full RFB cell measurements since the data often include significant contributions from complex diffusion/convection behavior, membrane crossover, heterogeneous current distributions across porous electrodes, and other convoluting factors. Nonetheless, full device measurements should be considered the gold standard for validating specific hypotheses about the effects of electron-transfer kinetics on the practical behavior of RFBs.

A third category of analytical methods comprises electrochemical tools that are dissimilar to practical flow battery configurations but offer unique advantages for understanding interfacial electron-transfer behavior. Perhaps the most popular of these are micro- and nanoelectrochemical techniques [184–186]. Ultra-microelectrode (UME) voltammery, for example,

offers the ability to measure electron-transfer kinetics even at very high current densities due to the reduced influence of mass-transfer limitations and series resistance losses [187–189]. Specifically, as the dimension of a working electrode approach the sub-mm scale, the mass transport of electroactive species changes from linear to hemispherical diffusion, which allows significantly enhanced mass transfer even under quiescent conditions [190–192]. Moreover, current densities at UMEs are characterically smaller than at macroelectrodes, which significantly decreases measurement errors associated with uncompensated solution resistance [193,194]. Hence, UMEs have been used to good effect to measure the electron transfer kinetics of both aqueous and non-aqueous RFB electrolytes [195–197]. Furthermore, Butler-Volmer analysis can be used to extract electron-transfer rates from UME voltammetry just as with RDE voltammetry, except that the UMEs exhibit characteristically larger mass transfer rates making it easier to operate under pure kinetic control. Scanning electrochemical microscopy (SECM) takes this a step further by offering the ability to control mass transport conditions using feedback mechanisms and to spatially resolve variable electron-transfer rates across an electrode surface [198,199]. Accordingly, this technique has been used to excellent effect to evaluate electron transfer kinetics for newly emerging RFB redox couples [200–202].

2.3.3 Critically Assessing Rotating Disk Electrode (RDE) Voltammetry as a Characterization Tool

We worked to accurately characterize the interfacial electron transfer kinetics of RFB electrode-electrolyte combinations using well-established electroanalytical tools in the interest of resolving ambiguity regarding electrode kinetics and ultimately improving our ability to design efficient devices. Thus, we employed rotating disk electrode (RDE) voltammetry—schematized in Figure 13—as an electroanalytical platform to obtain reproducible electron transfer kinetics for a popular flow battery electrolyte based on the aqueous $Fe^{3+/2+}$ redox couple. As noted above, RDE voltammetry is attractive for measurement of kinetics since it is already well established as an analytical tool in recent studies of RFB active materials and is commonly used in the electrocatalysis field [203–206]. As a result, instrumentation and expertise is readily translatable between these two areas. Nevertheless, it remains unclear

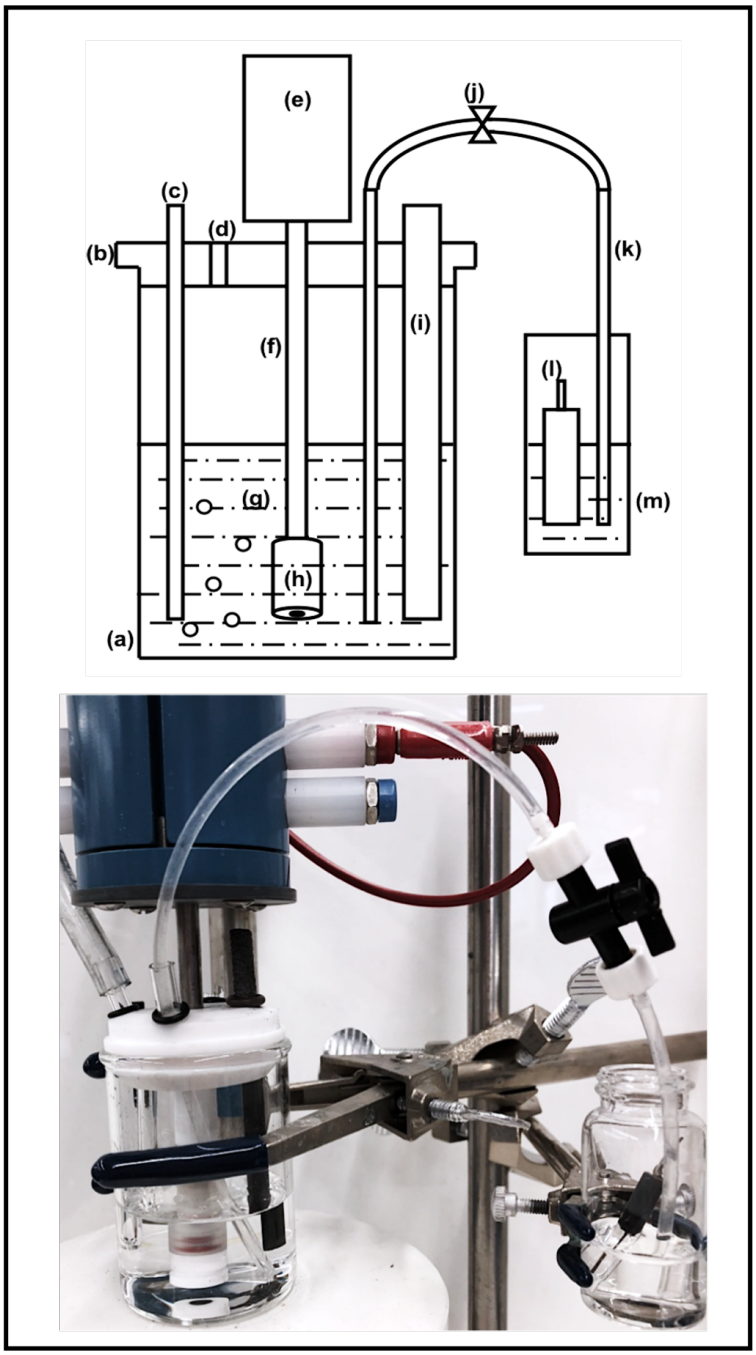

Figure 13: Schematic (left) and photograph (right) of the RDE experimental setup. Components labeled in the schematic are as follows: (a) glass cell, (b) Teflon cap, (c) nitrogen purge tube, (d) vent, (e) RDE motor, (f) RDE shaft, (g) electrolyte solution, (h) working electrode, (i) counter electrode, (j) stopcock, (k) electrolyte bridge, (l) reference electrode, and (m) reference electrode compartment.

whether this analytical method can be convincingly used to predict or explain the behavior of functional RFB devices. Thus, our study was aimed at critically analyzing the use of RDE voltammetry for accurate characterization of interfacial electron transfer kinetics under battery relevant conditions. To that end, we report herein a detailed description and critical analysis of this platform as applied to the well established $Fe^{3+/2+}$ chemistry at noble metal electrodes of Pt and Au. A detailed description of the analytical protocol can be found in our work published in *ACS Applied Energy Materials* [207].

Our experimental approach comprised an effort to balance between the goals of mimicking functional flow battery behavior while also maintaining suitable analytical precision. Thus, we employed equimolar concentrations of Fe salts to replicate the state-of-charge of a functional battery. Further, we used Fe chloride salts in HCl supporting electrolyte to resemble the composition of the positive electrolyte in an Fe/Cr battery. However, to avoid the confounding effects arising out of electrical resistance in the system, we primarily deployed the active Fe species at low concentrations of 10 mM total. Although Pt and Au are seldom used as electrode materials in practical devices due to their high costs, they were chosen for this study because there exists well developed preparation and cleaning protocols for these electrodes.

Figure 14(a) presents representative background subtracted RDE current density vs potential (j–V) data from 100 to 2500 rpm at polycrystalline platinum electrode. Current density, both in the oxidative and reductive directions, increased monotonically in magnitude with increasing rotation rates, as is expected for progressively diminishing transport limitations. Based on common practice in the analytical electrochemistry literature, we employed Koutecky-Levich (KL) analysis and Butler-Volmer (BV) fits to extract diffusivity and electron transfer kinetics respectively. The KL equation (Eq. 2.1) expresses the relationship between current density and rotation rate in an RDE experiment and the BV equation (Eq. 2.2) allows for the determination of exchange current density, j_0 where the exchange current density can be expressed as a function of reactant concentration and the heterogeneous electron transfer rate constant, k^0, according to Equation 2.3.

$$\frac{1}{j} = \frac{1}{j_k} + \frac{1}{0.620nFCD^{2/3}\nu^{-1/6}}\omega^{-0.5} \tag{2.1}$$

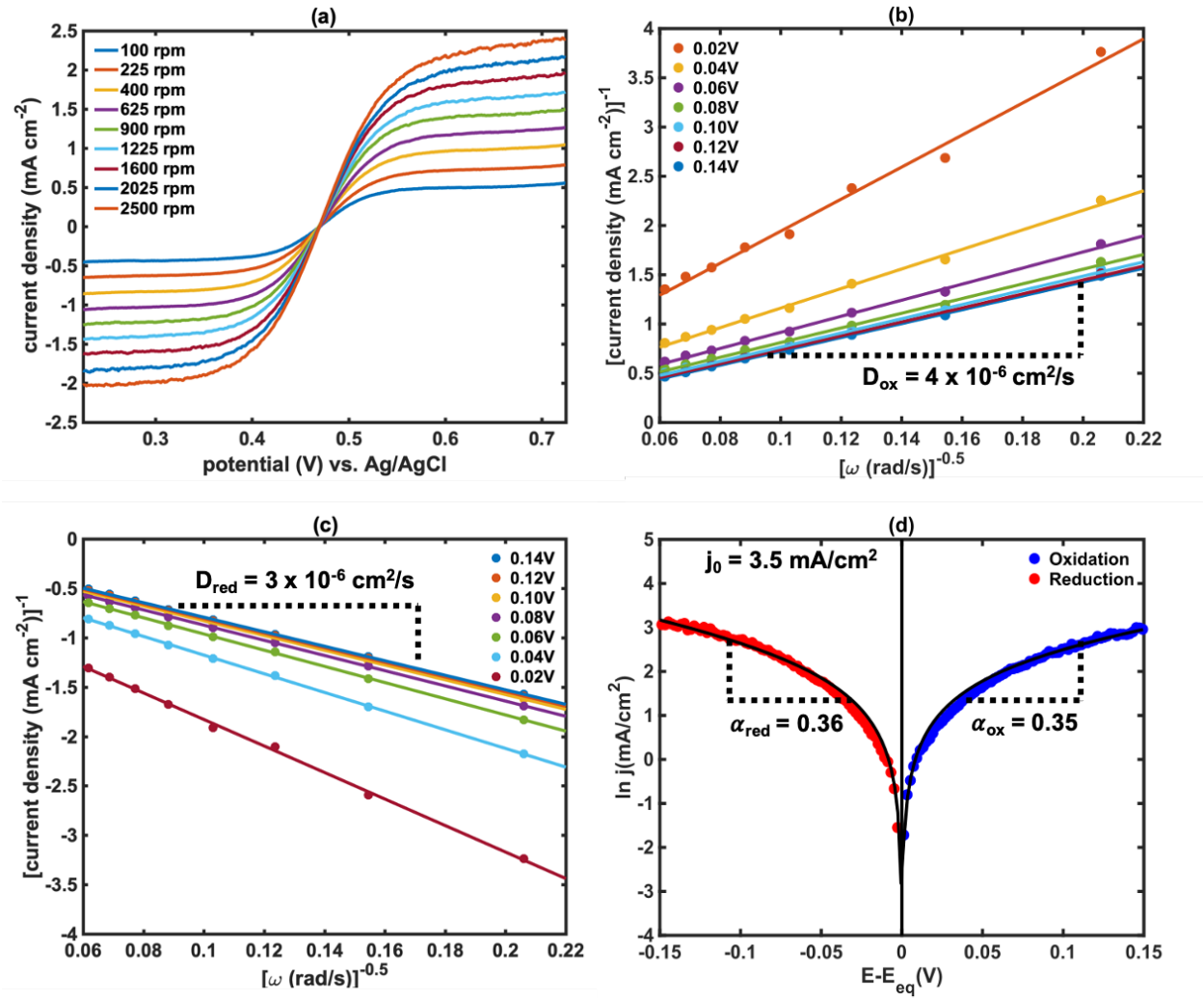

Figure 14: Data collected in 5 mM $FeCl_2$ and 5 mM $FeCl_3$ in 0.5 M HCl(aq) at polycrystalline Pt electrode. (a) Representative current density versus potential data for RDE voltammetry between 100 and 2500 rpm, (b) Koutecky-Levich analysis depicting inverse current versus inverse square root of rotation rate data for iron oxidation, (c) Koutecky-Levich analysis depicting inverse current versus inverse square root of rotation rate data for iron reduction and (d) Transport-free polarization data.

$$j_k = j_0 \left[exp\left(\frac{\alpha_{ox} n F \eta}{RT}\right) - exp\left(\frac{-\alpha_{red} n F \eta}{RT}\right) \right] \tag{2.2}$$

$$j_0 = nFCk^0 \tag{2.3}$$

where j is the measured current density, j_k is kinetic current density, n is number of electrons transferred (1 in the case of $Fe^{3+/2+}$), F is Faraday's constant (96485 C/mol), C is bulk reactant concentration, D is diffusivity, ν is kinematic viscosity (taken as 0.01 cm^2 s^{-1} for aqueous solutions at room temperature), ω is rotation rate in radians/second, α_{ox} and α_{red} are the symmetry factors, R is the universal gas constant, T is temperature, and $\eta = E - E_{eq}$ is the overpotential where E_{eq} is the empirically measured equilibrium potential of the system. Figures 14(b)–(d) present the KL and BV plots obtained at polycrystalline Pt electrode. We found the exchange current density to be 3.7 ±0.43 mA/cm^2 for platinum and 1.3 ±0.17 mA/cm^2 for gold (the data for Au are presented in Figure 15) where the error bounds are reported at a 95% confidence interval obtained over n=5 set of experiments for each electrode. Thus, we successfully demonstrated that our analytical protocol could be used to find reproducible electron transfer kinetics for RFB electrolytes.

The RDE analytical protocol that we developed involved a large number of tedious electrode preparation and cleaning steps, but we found that every step of the analytical protocol was necessary to obtain reproducible results. To illustrate, Figure 16 shows the results of RDE voltammetry experiments where one step–the electrochemical cleaning step implemented between different measurements was omitted. This resulted in a clear progressive decrease in the current response which we attribute to fouling of the electrode surface. While cleaning steps like these can be routinely employed in the course of lab-scale electroanalysis, analogous procedures cannot be readily implemented in a functional flow battery. Thus, optimal kinetics resulting from electrode pretreatments cannot be expected to last over extended battery operation.

To further assess the utility of our approach for measuring kinetics under practical flow battery conditions, we employed our analytical approach to reactor relevant concentrations of 1 M total Fe (0.5 M $FeCl_2$ and 0.5 M $FeCl_3$) in 2 M HCl electrolyte. Figure 17 presents the associated j–V and transport free polarization data in this electrolyte at the surface

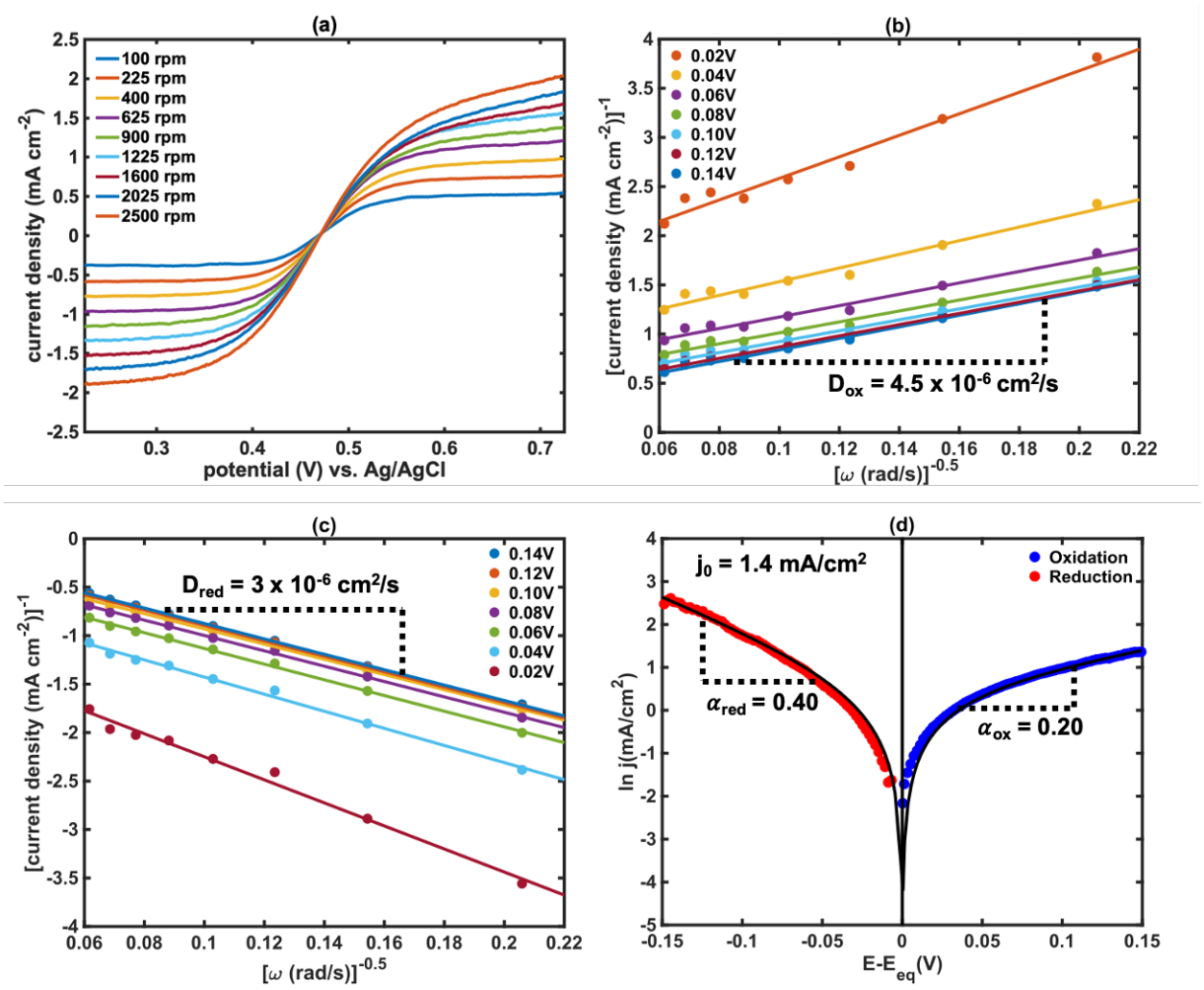

Figure 15: Data collected in 5 mM $FeCl_2$ and 5 mM $FeCl_3$ in 0.5 M HCl(aq) at polycrystalline Au electrode. (a) Representative current density versus potential data for RDE voltammetry between 100 and 2500 rpm, (b) Koutecky-Levich analysis depicting inverse current versus inverse square root of rotation rate data for iron oxidation, (c) Koutecky-Levich analysis depicting inverse current versus inverse square root of rotation rate data for iron reduction and (d) Transport-free polarization data.

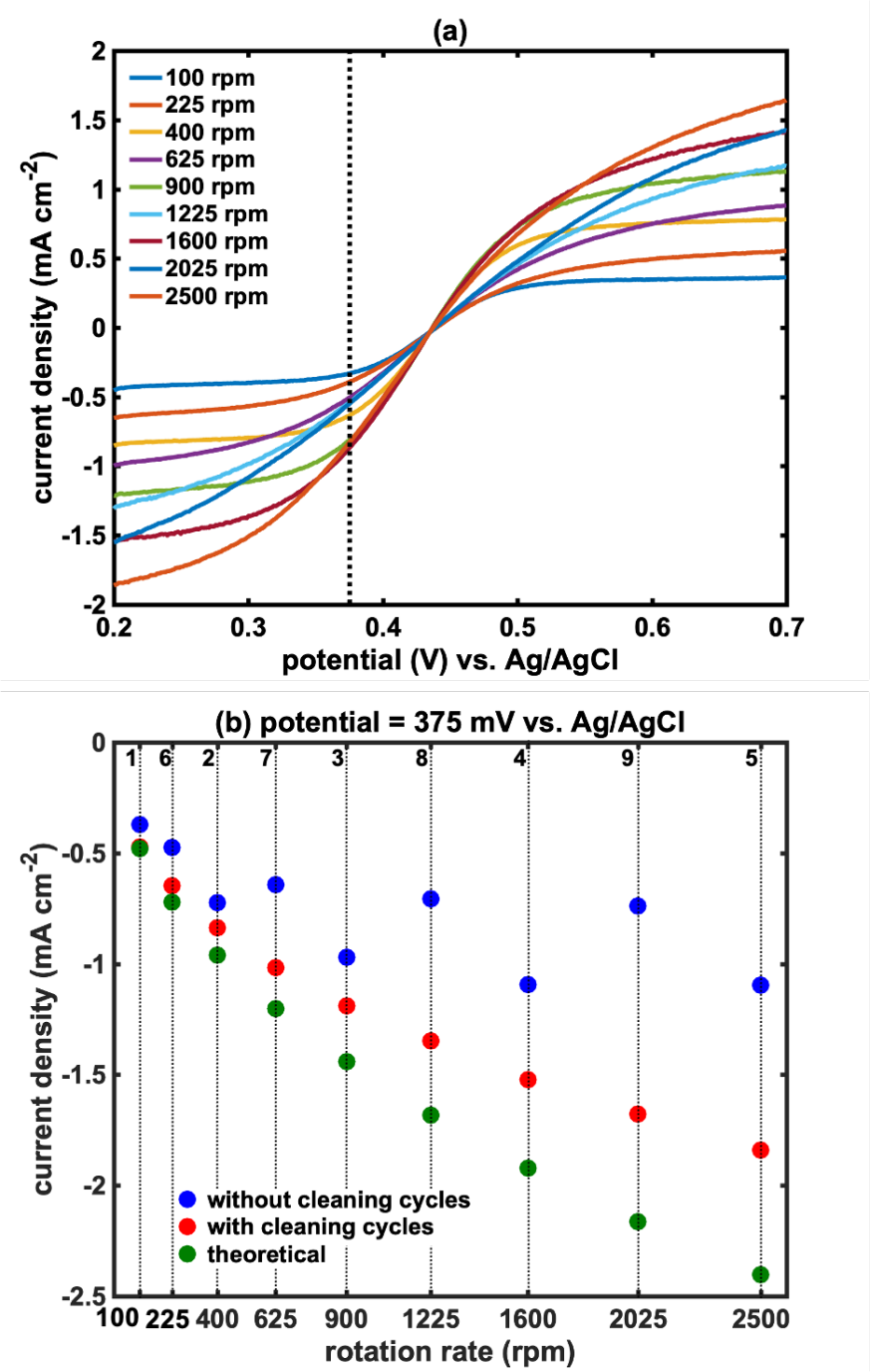

Figure 16: (a) RDE current density versus potential data using a Pt electrode in 5 mM $FeCl_2$ and 5 mM $FeCl_3$ in 0.5 M HCl obtained by omitting cleaning steps between different rotation rates. (b) Current density versus rotation rate at 375 mV versus Ag/AgCl with and without cleaning steps alongside theoretical data. Numbered dotted lines represent the order in which RDE measurements were performed.

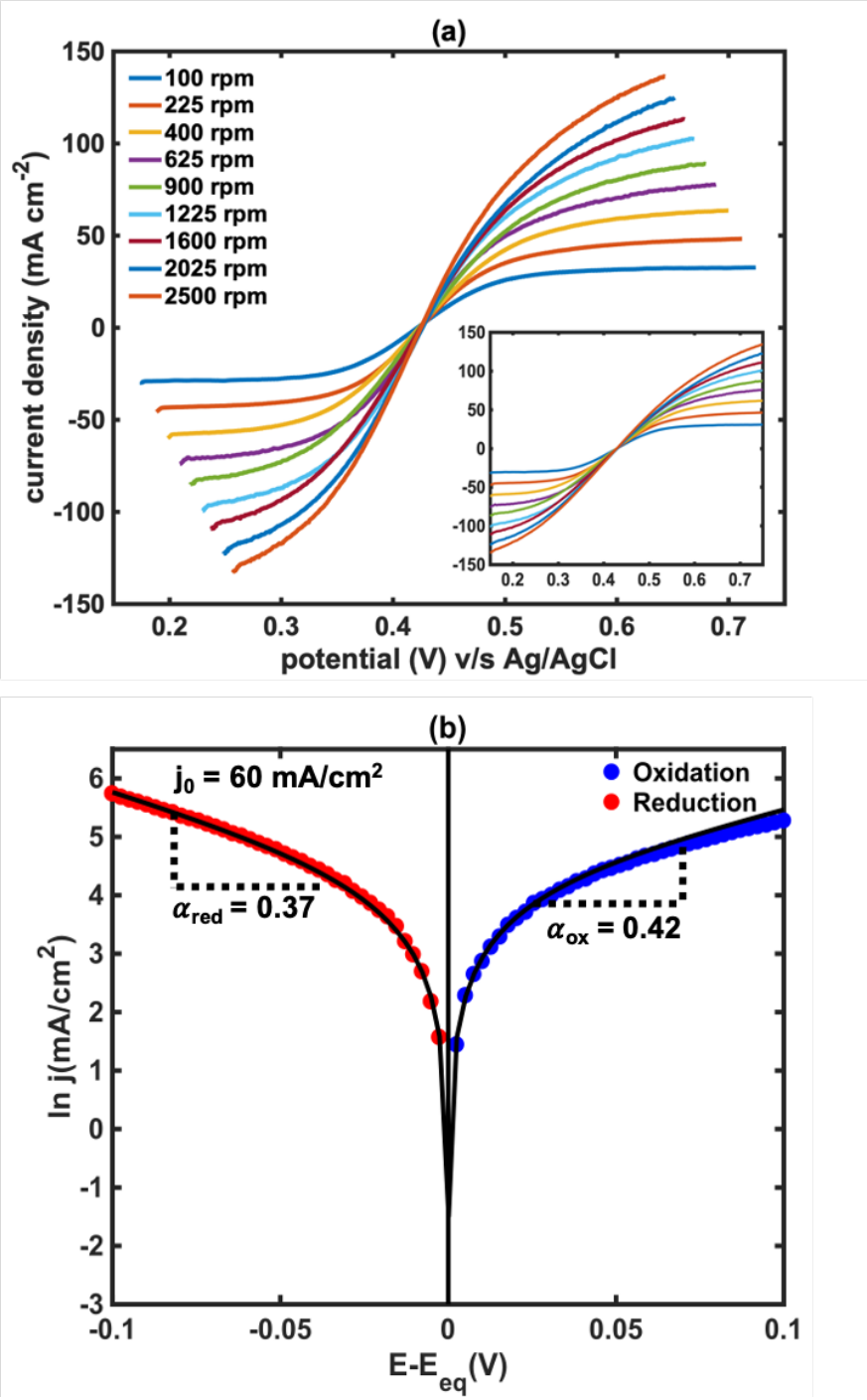

Figure 17: (a) RDE current density versus potential data for a $Fe^{3+/2+}$ RFB electrolyte containing 0.5 M $FeCl_2$ and 0.5 M $FeCl_3$ in 2 M HCl(aq). The inset shows the same data without compensating for series resistance (4 ohms). (b) The corresponding transport free polarization data, where the equilibrium potential, E_{eq} was taken to be 425 mV vs. Ag/ AgCl.

of a Pt electrode. We found the analysis of these data to be sensitive to the specifics of series resistance compensation; for several data sets, compensation at the experimentally measured value of 4 Ω resulted in unphysical results in KL analysis, while omitting the resistance compensation entirely resulted in j_0 values that were lower by approximately a factor of 2. While we expected the exchange current density to be 370 ±43 mA/cm^2–obtained from a simple extrapolation of lower concentration measurements using a first order rate expression–the observed exchange current density was ∼6 fold lower (60 mA/cm^2). Based on these results, we conclude that Fe-based RFB electrolytes do not exhibit simple kinetics. Our results are broadly consistent with a multi-step electron transfer mechanism where the electrode surface plays a catalytic role. This is evidenced by the fact that the Pt and Au electrodes exhibit different electron transfer kinetics and that even at Pt, the observed kinetics for $Fe^{3+/2+}$ were considerably slower than routinely observed from outer sphere single electron transfer redox couples like ferrocene [208]. Thus, our results clearly indicate that the electrode surface plays a role, which is consistent with prior electroanalytical work showing that adsorbed anions catalyze Fe redox chemistry [209–212].

While it is common to report k^0 as the descriptor of electron transfer rate constant in studies of electrochemical kinetics, we recommend against the use of k^0 to describe RFB electron-transfer kinetics unless the electrode surface is highly uniform in chemical composition and structure, such as when using single crystals. This is because unlike homogeneous reactions in which the reacting species are highly uniform in composition and structure, polycrystalline electrode surfaces exhibit considerable surface site heterogeneity. Thus, for reactions in which the electrode surface acts as a catalyst, each site likely exhibits a different characteristic k^0, and these may vary widely. This helps explain why consistent electrode surface preparation is so important to obtain reproducible kinetics data. We recommend instead reporting j_0 values, which are also commonly used in electrocatalysis research and clearly depend on extensive properties of the electrode (surface area, density of active sites) and the electrolyte (reactant concentration).

We further conclude that RDE voltammetry cannot be used to obtain the "true" electron transfer kinetics of most RFB electrolytes under practical operating conditions. Thus, new experimental protocols are needed to better approximate the conditions of operating

flow batteries. Hence, these results provided considerable impetus for further work to understand the differences in kinetics of RFB electrolytes under analytical (low concentration) and practical (high concentration) conditions.

2.3.4 A Novel Flow-based Microelectrode Platform for Analytical Measurements

While conventional hydrodynamic methods based on RDE are routinely employed in analytical studies, we found that these methods fail to approximate the electron-transfer behavior of RFB redox couples under practical conditions. Thus, there is a need to develop robust analytical platforms to elucidate the true electron-transfer kinetics of RFB redox couples under operating flow battery conditions. One such well-developed category of analytical tools for understanding electron transfer behavior are the micro- and nano-electrochemical techniques. Microelectrodes are desirable since they result in very high-transport limited current densities (in the range of 0.1-10 A/cm^2) but small absolute currents (in the range of tens of nA), which enable us to avoid the confounding effects of mass transport and electrical resistance in these systems [184,185]. This allows for the use of more relevant concentrations of the electrolyte for analytical measurements. Thus, our initial efforts to design and implement a new experimental platform for characterization of kinetics was based on the use of microelectrodes.

We first evaluated the viability of using microcopic electrodes by comparing the electrochemical behavior of Pt ultramicroelectrodes with that of a macroscopic RDE. We separately developed an analytical protocol tailored to microelectrode measurements that was used to obtain the associated exchange current densities. Complete details of this analytical protocol can be found in Appendix A.3. Figure 18 depicts representative results which compiles the transport free polarization data of a 5 mm diameter rotating-disk electrode versus that of a 10-micron diameter Pt microelectrode. As seen from the figure, the electrochemical responses in 10 mM $Fe^{3+/2+}$ electrolyte were qualitatively similar in each case, and the resulting kinetic analysis yielded similar apparent reaction rate constants.

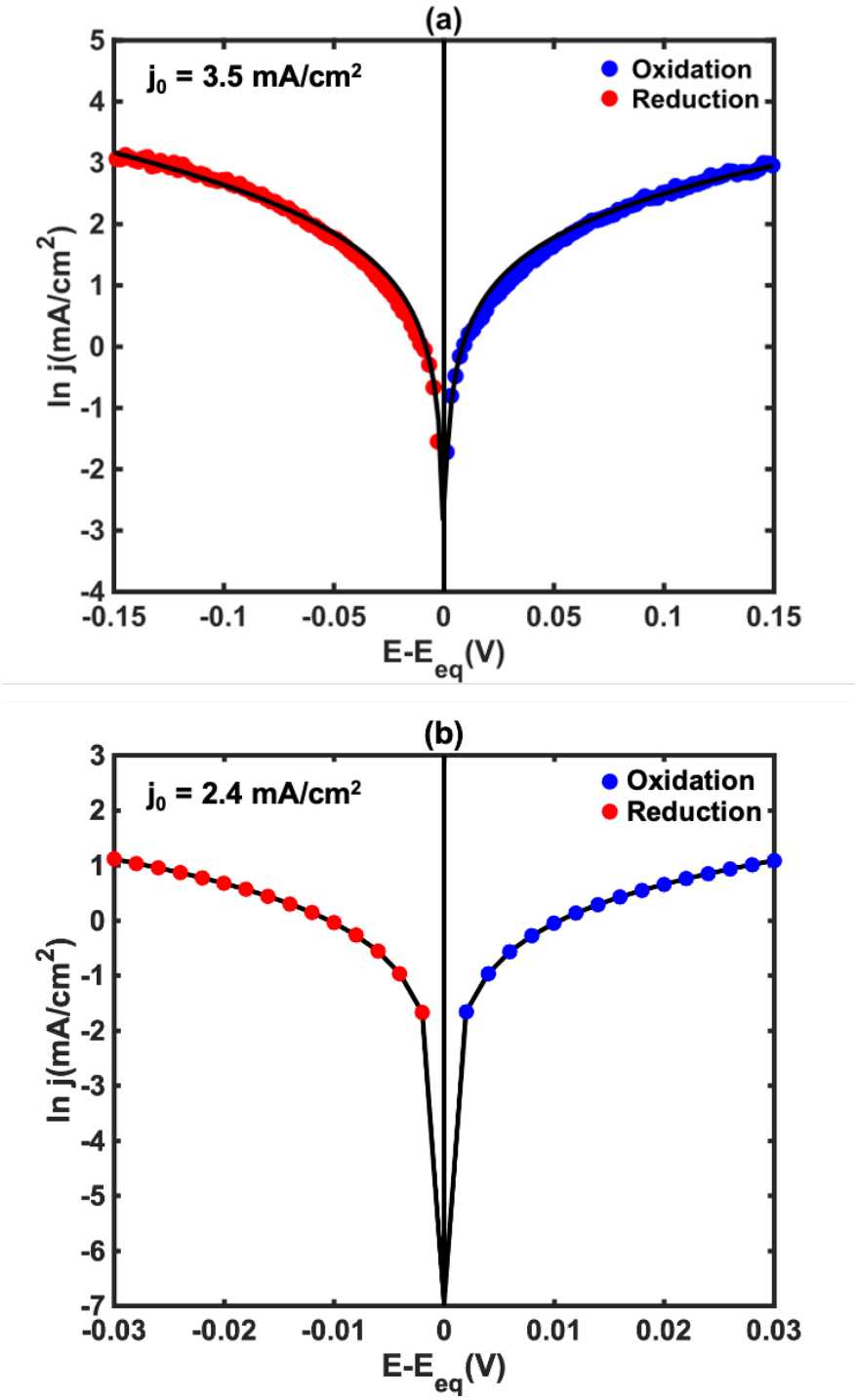

Figure 18: Transport-free polarization data for (a) a 5 mm diameter Pt rotating-disk electrode and (b) a 10-micron diameter Pt electrode in 10 mM total Fe in 0.5 M HCl electrolyte.

To further bridge the gap between analytical experiments and practical flow battery conditions, we employed our microelectrodes in a customized flow cell that directly mimics the dimensions of a popular lab-scale RFB device [107]. Our flow platform—depicted in Figure 19—is a 3D printed acrylic cell which encompasses a flow channel with the dimensions 40 x 1 x 0.5 mm^3, which enables linear velocities of tens of cm/s at volumetric flow rates as low as a few mL/min. Threaded sockets in the flow cell enable the use of commercially available ultramicroelectrodes along with reference and counter electrodes. We established a rigorous protocol of elucidating kinetics using our flow based platform, similar to that accomplished for RDE (See Appendix A.3).

Using the method described above, we tested the electrochemical performance of 10 mM $Fe^{3+/2+}$ electrolyte using a 10-micron diameter Pt microelectrode in the flow cell under static and flowing conditions. Figure 20 presents the associated j–V curves. The data clearly show an increase in the achievable current density under flow, which translates into faster apparent reaction kinetics. This result is clear evidence that the observed reaction rate for oxidation and reduction of $Fe^{3+/2+}$ at a clean Pt electrode is at least partially limited by mass transport and not electron-transfer kinetics. Accordingly, the value at 10 mL/min should be taken as a lower bound estimate of kinetics of the system. We further evaluated the kinetics of $Fe^{3+/2+}$ at varying electrolyte concentrations using our microelectrode flow platform and compared it to the kinetics obtained in a standard electrochemical cell. Table 2 compiles complete kinetics data for the same Pt microelectrode in a standard electrochemical and the flow cell over a range of electrolyte concentrations. We generally found that the apparent reaction rates were similar in the standard electrochemical cell and under static conditions in the flow cell. Moreover, in the flow configuration the reaction rate constants were approximately twice as fast as for the static experiments which we attributed to improved mass transport in the system. While the electron transfer rate constants should not vary with mass transfer rates, the difference obtained in the exchange current densities indicate that our system is at least partially mass transport limited. We separately evaluated that to completely eliminate transport effects in this system, we would need to increase the flow velocity by at least an order of magnitude. Thus, for each redox couple of interest, the flow rate could be tuned to completely eliminate the mass transfer effects and assess the true kinetics of the system.

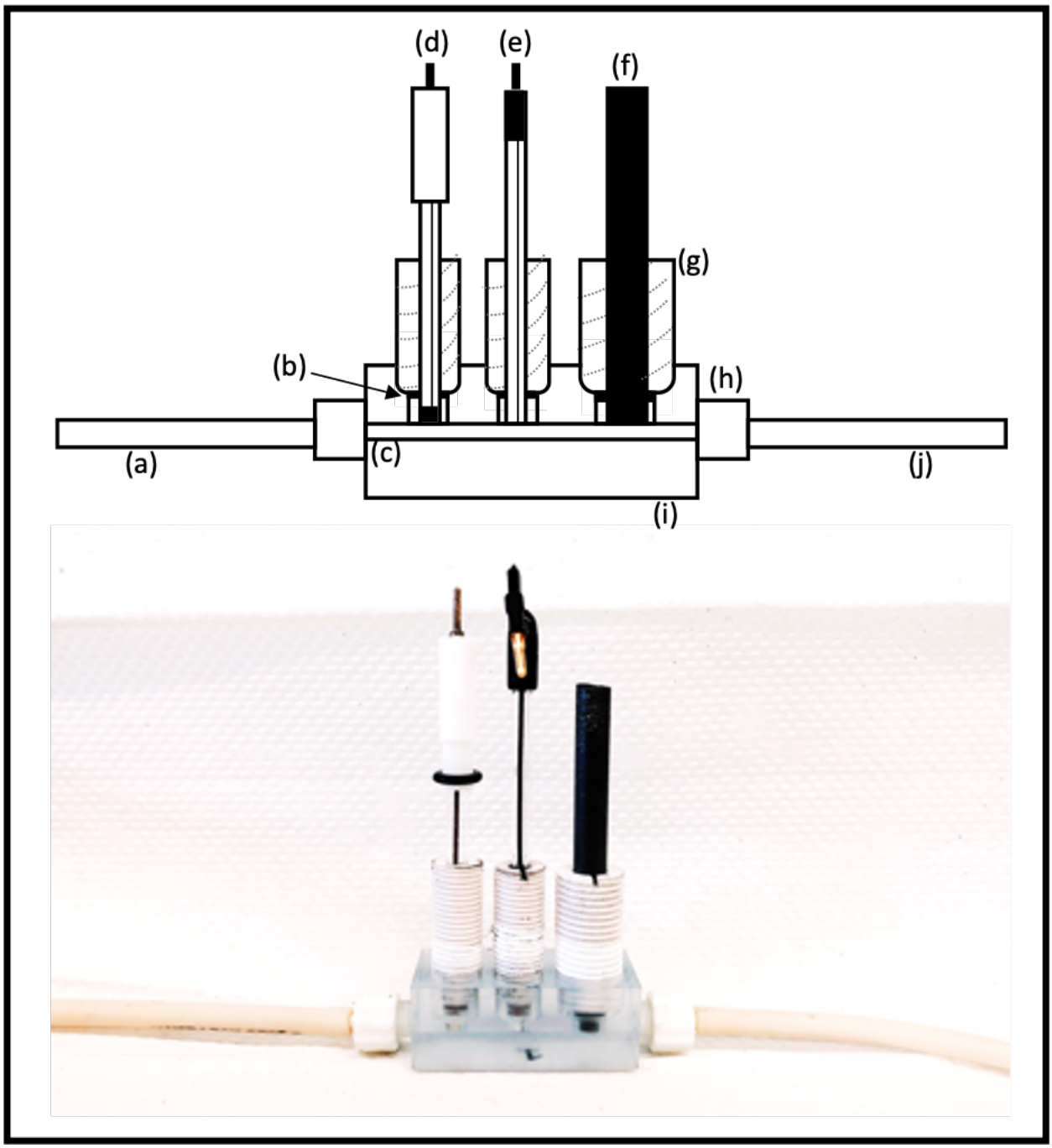

Figure 19: Schematic (top) and photograph (bottom) of experimental setup; Components labeled in the schematic are as follows: (a) inlet pump tubing, (b) o-ring, (c) flow channel, (d) reference electrode (Ag/AgCl), (e) working electrode (Pt microelectrode), (f) counter electrode (graphite), (g) teflon threaded plugs, (h) leur valve, (i) flow cell and (j) outlet pump tubing.

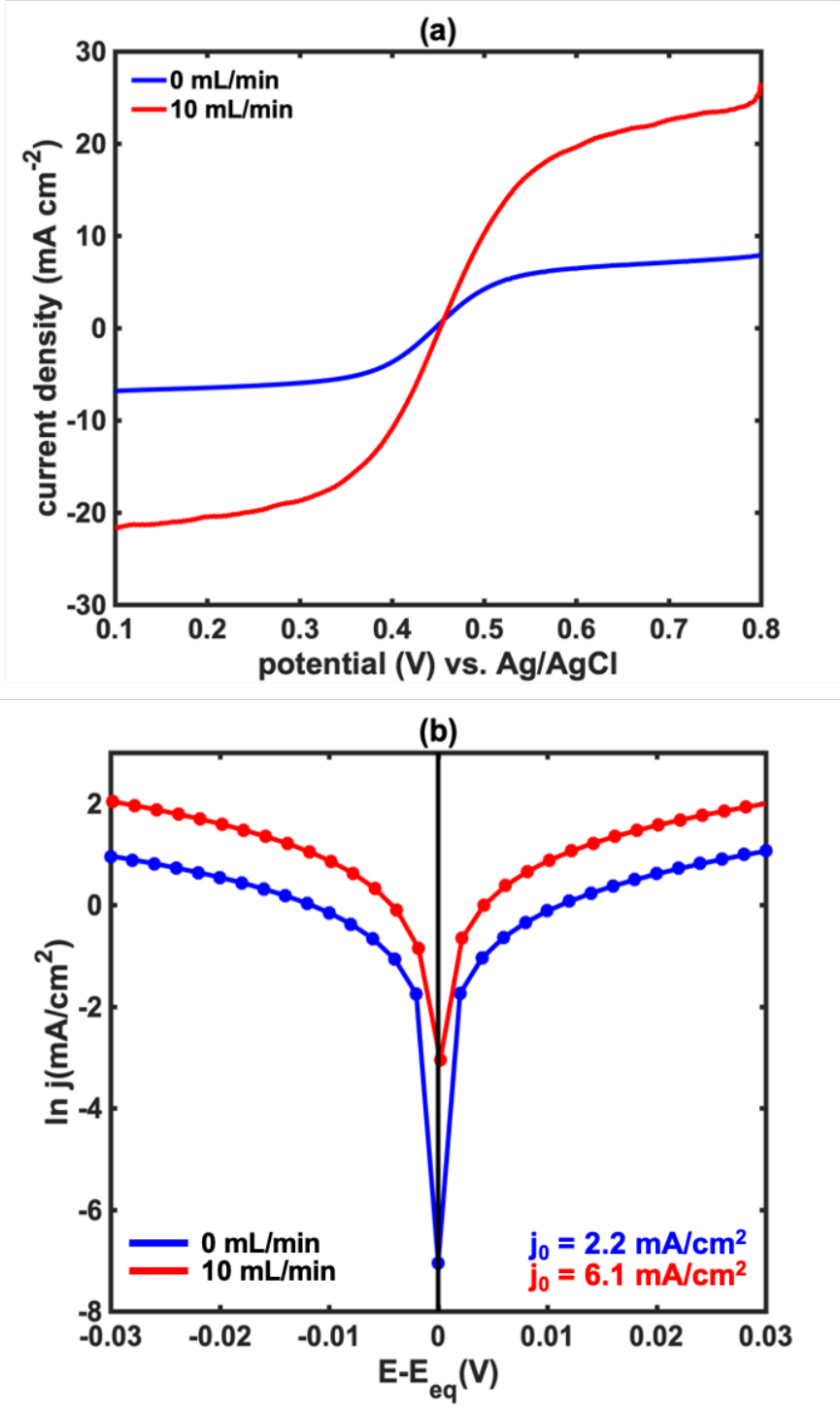

Figure 20: (a) Linear and (b) semilog current density vs. potential data for a Pt microelectrode under static (0 mL/min) and flowing (10 mL/min) conditions in 10 mM total Fe in 0.5 M HCl electrolyte.

Table 2: Electron transfer kinetics data for oxidation and reduction of $Fe^{3+/2+}$ at Pt microelectrode

Total Fe concentration (mM)	**Concentration of HCl (M)**	**Exchange current density (mA/cm^2)**		
		Standard electrochemical cell	**Static conditions in flow setup**	**Flow cell**
10	0.5	2.4	2.2	6.1
20	0.5	5	5.2	10.7
40	0.5	9	10	23.8
100	2	22	22.5	41.9
1000	2	136	144	255.2

Our microelectrode flow platform also offers several key advantages over RDE for kinetics measurements. For instance, elucidating kinetics from the microelectrode platform required only a single current-voltage measurement, whereas the data from Pt macroelectrode required a series of mathematical extrapolations over a set of 9 measurements. This significantly reduces the timescale of experimentation. Additionally, the use of microelectrodes lead to reduced mass transfer limitations owing to the presence of hemispherical diffusion layers as compared to linear diffusion obtained on macroelectrodes [192]. Moreover, when the electrolyte concentration was increased to 1M, the rotating disk electrode response became dominated by electrical resistance associated with the passage of large currents via ionic transport in the system as seen in Figure 17(a). By contrast, microelectrode flow platform gave current-voltage data that required no corrections for electrical resistance. These data clearly illustrate the significant advantages of shrinking the electrode size. Thus, we conclude that our flow based microelectrode platform can serve as an excellent analytical tool to elucidate electron transfer kinetics of RFB redox couples.

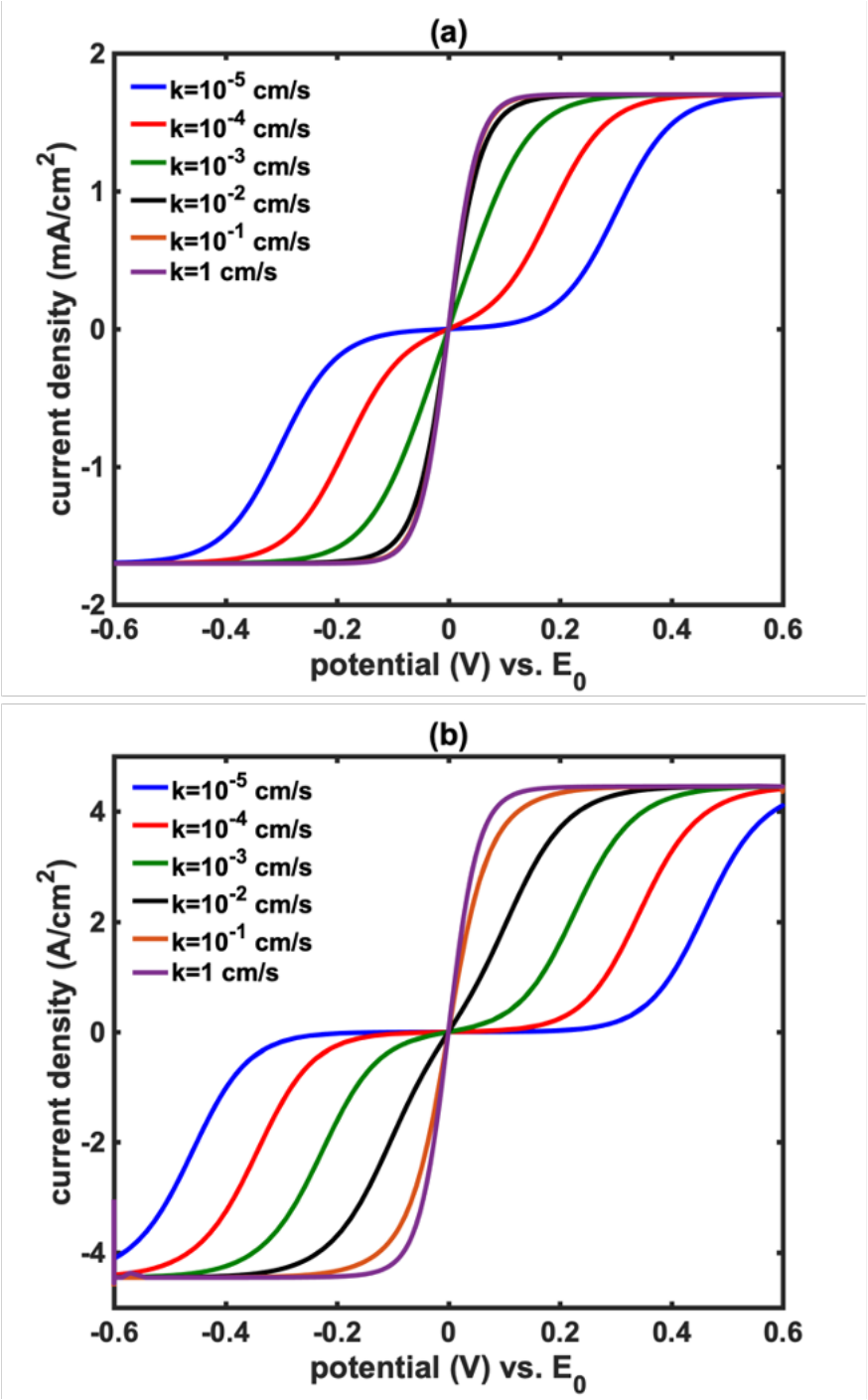

Figure 21: Simulated current density vs. potential data for (a) rotating disk electrode (using DigiElch) and (b) microelectrode flow cell platform (using COMSOL) for $Fe^{3+/2+}$ electrolyte.

Another advantage offered by our flow based platform is accurate prediction of electron transfer behavior over a wide range of reaction rate constants. To illustrate, we simulated the steady state voltammetry data for RDE and microelectrode flow platforms over a range of rate constants from 1 to 10^{-5} cm/s—depicted in Figure 21. Parameters used for these simulations closely resembled the laboratory conditions of our RDE and flow cell platforms. Complete simulations details are provided in Appendix A.4. As seen from the figure, the steady-state voltammograms obtained for RDE at 1600 rpm are indistinguishable above an intrinsic reaction rate constant of 0.01 cm/s; whereas for the microelectrodes, at a flow rate of 10 mL/min, we found that the data can be distinguished at least up to 0.1 cm/s. Thus, our microelectrode flow-based platform can be used to measure at least an order of magnitude faster kinetics as compared to RDE. Additionally, our "target" intrinsic reaction rate constant is $\sim$0.01 cm/s, at which RDE based methods are near the upper limit of their measurement potential. Thus, our microelectrode flow platform should be able to provide more accurate kinetics measurements in this range than RDE methods. This is especially important for characterizing new emerging redox couples that exhibit intrinsically fast reaction rates. Future work should be directed at further improving the mass transfer rate in the flow platform and evaluating its effect on the obtained electron transfer kinetics.

2.3.5 Adapting the Flow Cell for Flat Electrode Geometries

While we demonstrated our ability to measure reproducible electron-transfer kinetics using the flow cell platform, several modifications were necessary to make this system more broadly useful in RFB characterization. One such modification was to make it adaptable to flat electrode geometries. Flat electrodes are desirable due to their resemblance to electrodes in practical RFBs as well as their ability to be used with several characterization techniques, such as scanning electron microscopy and x-ray photoelectron spectroscopy, that cannot be used with commercial cylindrical disk-shaped ultramicroelectrodes. Thus, we redesigned the existing flow cell platform to accommodate flat electrode geometries. Our design is based on inverting the flat electrode over a flow channel (dimensions 75 x 1 x 2 mm^3), as shown in Figure 22.

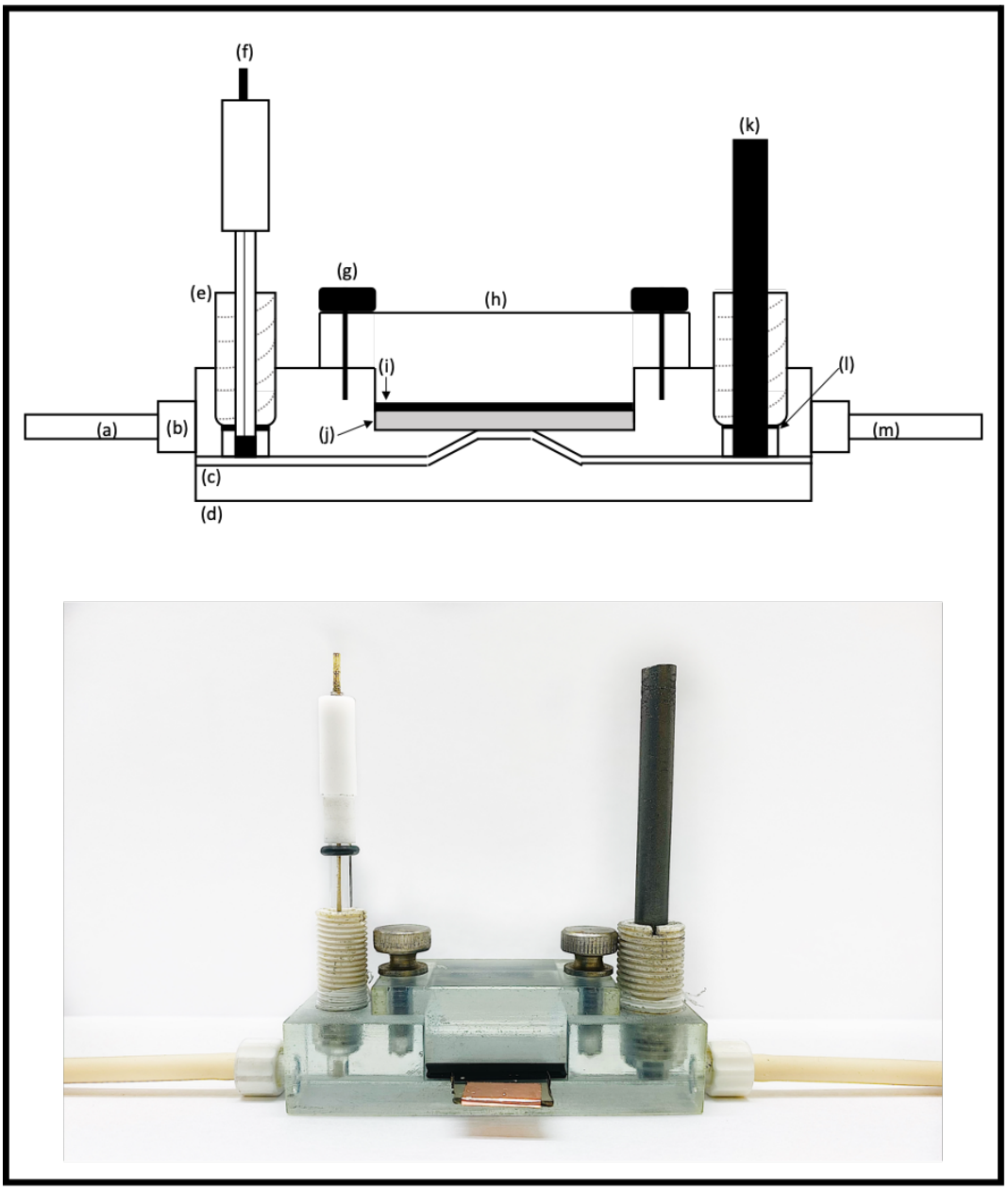

Figure 22: Schematic representation (top) and photograph (bottom) of modified flow cell platform for incorporating flat electrode geometries. Components labeled in the schematic are as follows: (a) inlet pump tubing, (b) leur valve, (c) flow channel, (d) bottom piece of the flow cell, (e) teflon threaded plug, (f) reference electrode (Ag/AgCl), (g) screw, (h) top piece of the flow cell, (i) gasket, (j) working electrode (Pt deposited on microscope slide), (k) counter electrode (graphite), (l) o-ring, (m) outlet pump tubing.

We evaluated the viability of this sandwich flow cell by performing control experiments on a platinum film deposited on a microscope slide using physical vapor deposition. 10 mM total Fe in 0.5 M HCl was used as the electrolyte with graphite counter and Ag/AgCl reference electrodes. Figure 23 presents a representative cyclic voltammogram obtained in this electrolyte on the flat Pt electrode. The characteristic "duck-shaped" hysteresis in the CV data obtained on Pt demonstrates the viability of our flat electrode flow cell platform.

Thus, future work on this effort should focus on evaluating and comparing the electron transfer kinetics of Fe redox chemistry using flat Pt electrodes as a control experiment. Further work should then be targeted towards evaluating electron transfer kinetics of vanadium chemistry using several electrode materials such as Pt, Au, Ru, Ir and others that can be deposited as thin films. This work can provide considerable opportunities to develop industrially relevant carbon electrodes with trace quantities of noble metals to improve electrocatalysis for vanadium redox chemistry. This work will also benefit from performing a techno-economic analysis to evaluate if the increase in cost associated with incorporating noble metals in carbon is offset by the improvement in performance.

2.3.6 Recommended Future Work: Online Kinetics Measurements

To develop a more robust and reliable platform for determination of kinetics and to further bridge the gap between fundamental and practical RFB conditions, we are also interested in adapting our microelectrode flow platform into a functioning RFB system. Figure 24 presents a conceptual schematic of a micro-electrode flow cell and an online optical spectrophotometer integrated into the flow loop of a functional RFB half cell. Recent work has demonstrated the value of executing in-situ measurements of RFB materials. Several methods, such as conductivity measurements, spectroscopic monitoring, and cell potential measurements have been used to measure the state of charge of redox flow batteries during operation [213–217]. Spectroscopic techniques are especially useful for studying RFB active materials because changes in the oxidation state very often give rise to characteristic changes in their optical absorption spectra [215, 218–222]. The particular benefits of optical spectroscopy include high precision—high quality spectrophotometers can detect absorbance

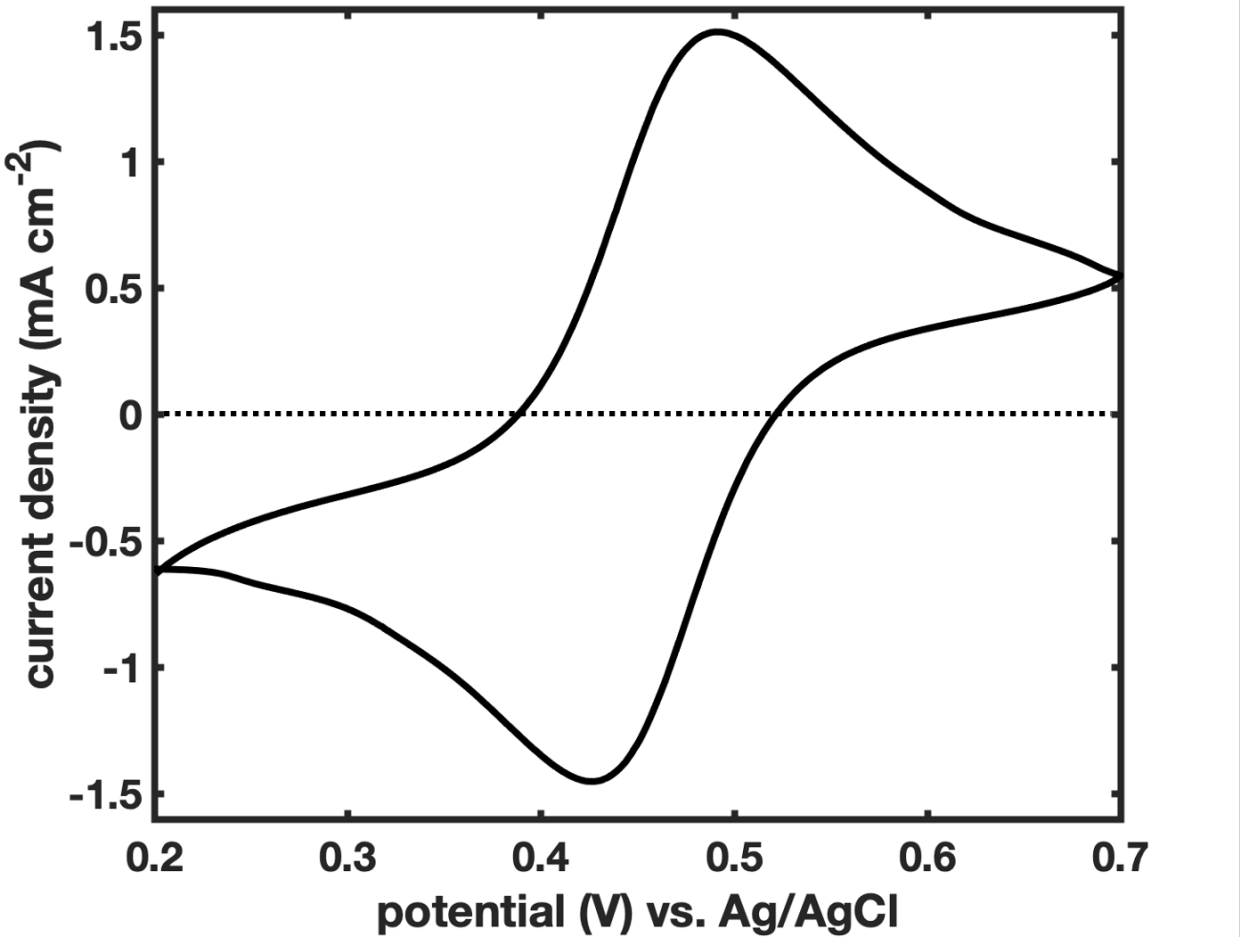

Figure 23: Representative cyclic voltammogram in 5 mM $FeCl_2$ and 5 mM $FeCl_3$ in 0.5 M HCl electrolyte on a platinum electrode deposited on microscope slide.

changes on the order of $< 0.1\%$ or less over long timescales—and the ability to measure the state of charge without directly perturbing the oxidation state of the active species.

While UME and spectroscopic techniques cannot be used to directly predict the practical performance of a fully-scaled RFB system, they may offer additional valuable insights via deployment as in-situ analytical tools for flow battery metrology. This type of tool could be used to measure key parameters like state-of-charge, electrolyte degradation, and perhaps even temporal changes in reaction kinetics (if the analytical electrode could be designed to adequately resemble the actual RFB electrode), all at modest cost and with minimal perturbation of the associated RFB device. Thus, micro-electrochemical methods present an excellent opportunity to advance battery design and operation by "sensorizing" RFB devices.

To this end, future work should be directed at building a lab-scale model of a functional flow battery device and incorporating our microelectrode platform into the flow loop. An Fe-based cell with equimolar concentrations of $FeCl_2$ and $FeCl_3$ in both positive and negative chambers can serve as a useful electrolyte for control experiments. Using the same electrolyte in both half cells can help eliminate the problems associated with electrolyte imbalance due to ion migration. At least two different concentrations of $Fe^{3+/2+}$ electrolyte should then be tested with a Pt microelectrode at a flow rate of 10 mL/min and the kinetics should be compared with those obtained in our flow channel as shown in Table 2. If this online kinetics measurement platform works well, then we should expect to observe comparable exchange current densities as obtained using only the flow platform. Once the viability of this technique is verified, efforts should be directed towards testing various electrode materials to improve the catalysis of vanadium redox chemistry and other slow redox couples. It can then be used to determine the effect of state-of-charge on the kinetics of the system as well as to determine the stability of electrode surfaces over multiple charge-discharge cycles. We believe that this work will open a new direction into fundamental RFB research by making it much easier to characterize the kinetics of these systems under practical operating conditions in the overall pursuit of developing improved electrocatalysts and designing efficient batteries.

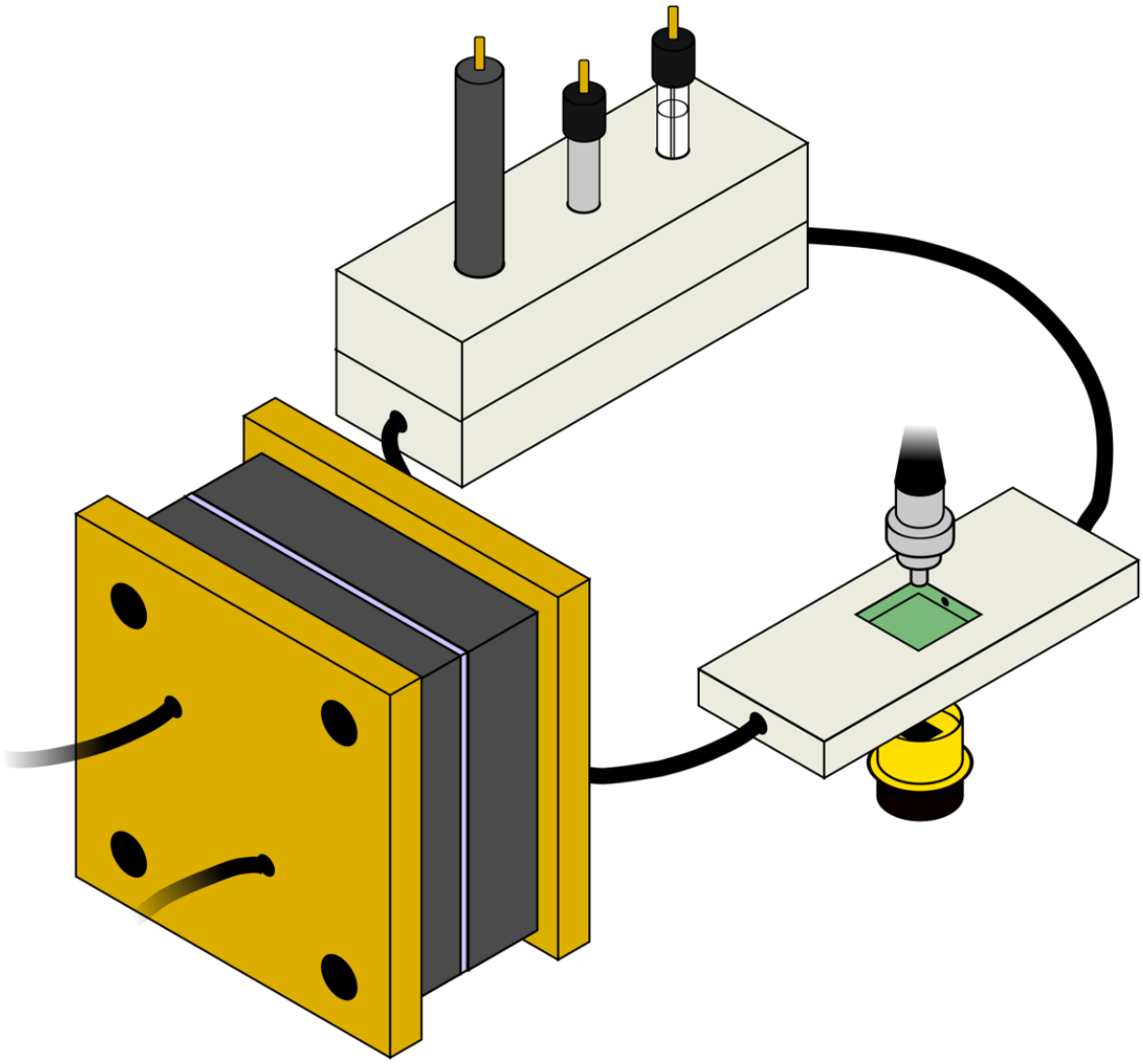

Figure 24: Conceptual schematic of a set of real-time analytical capabilities based on ultra-microelectrode voltammetry (top) and spectroelectrochemistry (right) that can be directly interfaced with an operating RFB cell (lower left).

2.4 Modulating Carbon Surface Chemistry for Efficient and Robust Electrocatalysis

While most analytical experiments are conducted with noble metal electrodes, carbon is the electrode of choice for commercial RFBs owing to its low cost [153, 223, 224]. Generally, graphitic carbon is processed into foam, paper or felt to produce high surface area porous electrodes for RFB operation [80, 225]. These electrodes are similar in composition to glassy carbon (GC) or pyrolytic graphite which are commonly used for electroanalytical studies [133, 226, 227]. However, the use of carbon electrodes pose an additional challenge since they are less straightforward to clean compared to noble metals due to their surface redox reactivity. In the context of electroanalysis, a variety of preparation protocols are generally employed on carbon surfaces in an effort to improve their catalytic properties [228, 229]. Generally, these procedures include polishing the electrodes on water-alumina slurries to remove surface impurities followed by various treatments. Some of these treatments include thermal oxidation [230–232], chemical oxidation [233,234], electrochemical cycling in aqueous acids [133, 235] and incubating in organic solvents [125, 236]. Thermal oxidation is generally conducted under vacuum or reducing environments to remove surface oxygen functional groups, whereas chemical oxidants are generally known to generate surface oxygen species. Electrochemical cycling techniques are known to remove surface impurities and usually result in partially oxidized carbon surface. And finally, incubating in organic solvents are known to decrease the amount of oxidized carbon, but are generally less effective compared to thermal treatments.

Although many of these cleaning or "activation" treatments are known to influence the electron transfer behavior between carbon materials and RFB redox couples, the mechanistic basis of these enhancements remain rather poorly understood. Several groups have argued that the enhancement in kinetics result from the presence of a higher degree of surface oxygen functionalities, while others argue that the enhancement results from a greater ratio of edge vs. basal sites on carbon [196, 237–239]. Recent work on vanadium chemistry shows that both oxidative and reductive treatments can result in enhancement of electron transfer kinetics [150]. These widely variable arguments present a key challenge of understanding

electron transfer kinetics on carbon electrodes and resolving these ambiguities would greatly improve our understanding of carbon-based electrocatalysis and help drive the development of strategies to control the associated catalysis for a range of carbon materials and electrolyte compositions.

2.4.1 Evaluating the Effect of Surface Oxidation of Carbon on Kinetics of $Fe^{3+/2+}$ Electrolyte

Our work in this area focused on evaluating the influence of various surface modifications of carbon on the electron transfer behavior of an aqueous Fe-based RFB redox couple. To that end, we pre-treated glassy carbon electrodes using three techniques to induce different degrees of surface oxidation. These are referred to hereafter as solvent treated, electrochemically treated, and peroxide treated GC electrodes, respectively. Solvent treatment involved incubation of polished GC electrode into a solution of activated carbon and isopropanol to remove surface oxidation. Electrochemical treatment consisted of the solvent treatment step followed by electrochemical cycling in aqueous H_2SO_4 solution. The peroxide treatment involved the solvent treatment step followed by incubating the electrode in a solution of hydrogen peroxide. Both electrochemical and peroxide treatments were performed to introduce oxidative functionalities on the surface of the electrode. We then characterized the resulting rates of electron transfer towards aqueous $Fe^{3+/2+}$ electrolyte using RDE voltammetry. Detailed experimental protocol and analysis can be found in our work published in the *Journal of Physical Chemistry C* [240].

A qualitative picture of the relative rates of electron transfer between the three electrode treatments is apparent from the cyclic voltammetry data presented in Figure 25. The peak to peak separation values, which varies inversely with reaction kinetics, were considerably smaller for electrochemical treatment (140 mV) compared to the solvent (420 mV) and peroxide (510 mV) treatments. Thus, it was immediately evident that the electron transfer kinetics were considerably faster at electrochemically treated glassy carbon as compared to the others.

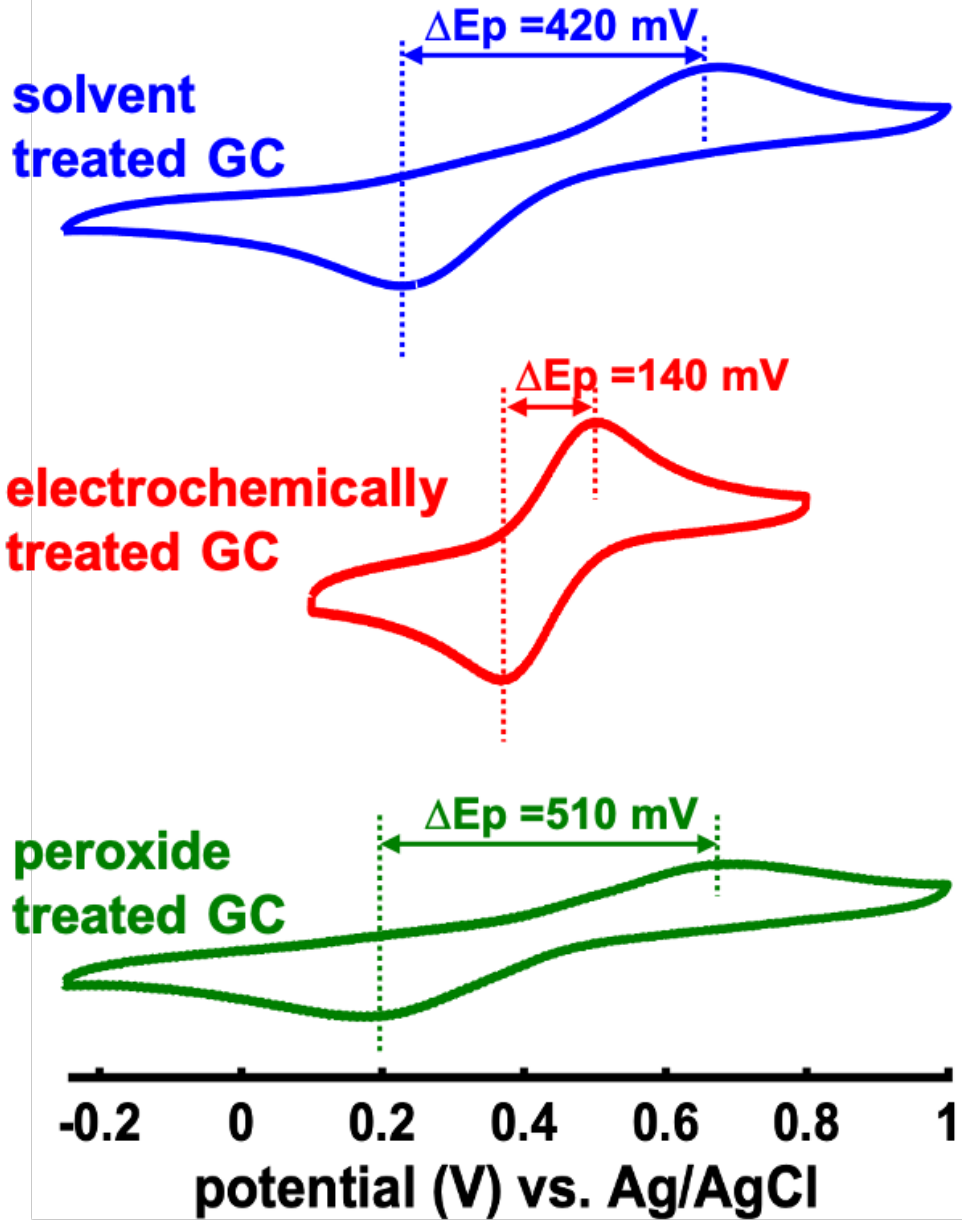

Figure 25: Current density vs. potential data at a scan rate of 200 mV/s for solvent treated GC, electrochemically treated GC, and peroxide treated GC in 5 mM $FeCl_2$ and 5 mM $FeCl_3$ in 0.5 M HCl.

Figure 26 (a)-(c) presents the current density vs. potential curves obtained using RDE voltammetry over a range of rotation rates from 0 to 2500 rpm. The equilibrium potential value for all datasets was found to be 0.45 V vs. Ag/AgCl (0.68 V vs. NHE), which is close to the standard reported value of 0.7 V vs. NHE in 1 M HCl electrolyte [241]. It is important to note that electrochemically treated GC exhibited well-differentiated j–V response over the entire potential range, whereas the solvent and peroxide treated GC resulted in an overlapping j–V response over a range of at least 100 mV near equilibrium, which is indicative of kinetic limitations. Figure 26 (d)-(f) present representative sets of Tafel plots for the three electrode treatments. The exchange current densities obtained at pre-treated glassy carbon rotating disk electrodes are summarized in Table 3. Uncertainty values represent error bounds at a 95% confidence interval obtained over a set of n=5 replicates for each electrode.

Prior precedent in the literature suggests that an increase in the degree of oxidation of carbon results in increase in electron transfer rates [237, 242–244]. Accordingly, we expected to observe an acceleration in reaction kinetics from both electrochemically and peroxide treated carbon electrodes relative to the solvent treatment, which was intended simply to clean the electrode surface of adventitious contaminants. However, only electrochemically treated GC resulted in appreciable increase in reaction kinetics, whereas the peroxide treatment resulted in indistinguishable kinetics compared to the solvent-treated GC. Thus, we explored the surface chemistry of carbon in a greater detail using a variety of techniques to identify the cause of acceleration in kinetics. First, we quantified the degree of oxidation of carbon using x-ray photoelectron spectroscopy (XPS). Figure 27 presents the XPS survey scans depicting the relative proportions of oxygen to carbon for all three electrode types. The oxygen to carbon ratio (O/C) was found to be comparable for all electrode types with a slight increase in oxidation from solvent treated to electrochemically treated and peroxide treated GC. However, the O/C ratio was not found to correlate with the relative rates of electron transfer for $Fe^{3+/2+}$ chemistry. Thus, the overall degree of surface oxidation was not found to be a good metric to explain the observed differences in electron transfer kinetics.

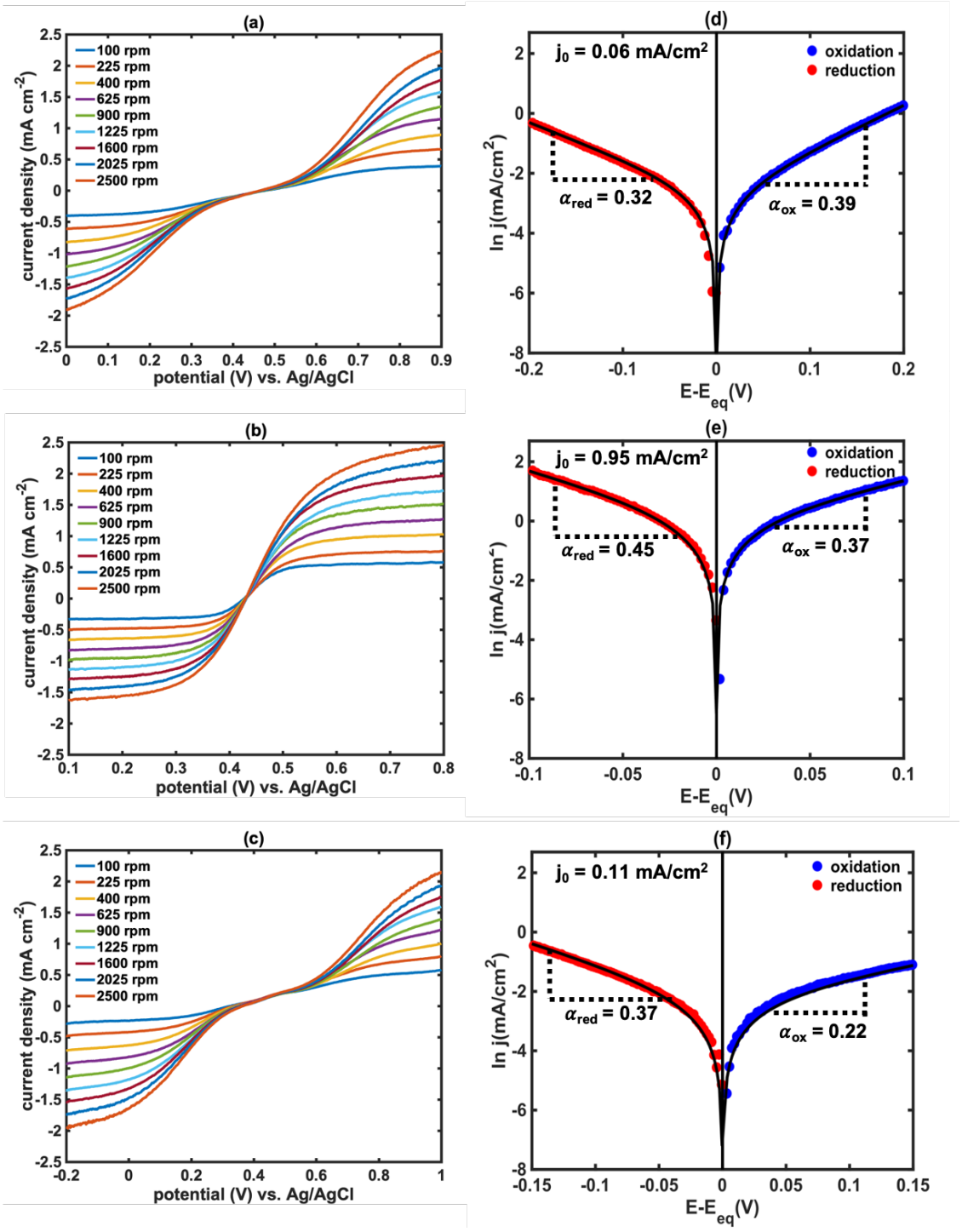

Figure 26: Data collected in 5 mM $FeCl_2$ and 5 mM $FeCl_3$ in 0.5 M HCl(aq). RDE current density vs. potential data for (a) solvent treated GC, (b) electrochemically treated GC, and (c) peroxide treated GC; Tafel plots and corresponding fits for $Fe^{3+/2+}$ oxidation and reduction at (d) solvent treated GC, (e) electrochemically treated GC, and (f) peroxide treated GC.

Table 3: Kinetics of iron oxidation and reduction at pre-treated carbon electrodes (n=5)

Electrode	**Exchange current density (mA/cm^2)**
solvent treated GC	0.07 ± 0.008
electrochemically treated GC	0.90 ± 0.06
peroxide treated GC	0.08 ± 0.035

Several literature reports on carbon surface chemistry suggest that an increase in the edge sites on carbon can result in enhanced kinetics performance [235, 238, 239]. Thus, we performed Raman microscopy on the pre-treated electrodes to evaluate the effect of edge vs. basal sites on the electron transfer kinetics of $Fe^{3+/2+}$ electrolyte. Figure 28 presents the data collected immediately after completing the surface preparation protocols. Two characteristic peaks of carbon at 1590 cm^{-1}, G band corresponding to presence of graphitic carbon, and 1360 cm^{-1}, D band corresponding to presence of structural defects, were observed in all three treatments [245–247]. Increasing the ratio of intensity of D band to that of G band, I_D/I_G is known to correlate with a decrease in the graphitic crystallite size, which also corresponds to the increase in the edge plane density and enhanced electron transfer kinetics. However, the I_D/I_G ratio was found to be similar (1.7 for electrochemical treatment and 2.1 for solvent and peroxide treatments) for all three carbons. These data also indicate the presence of a highly defective graphitic carbon (I_D/I_G ratio > 1) in all cases. We attribute this result to the inherent structure of a glassy carbon electrode, which is comprised of randomly oriented graphitic or fullerene-like nanocrystallites [248, 249]. Thus, Raman data do not provide a clear evidence for correlating enhanced electron transfer rates to an increase in the edge sites for our GC electrodes.

Another potential explanation for improved electron transfer kinetics is that electrochemically treating the carbon electrode introduces additional roughness leading to an increase in surface area, which in turn can lead to an increase in the geometric current densities. Thus, we evaluated the surface properties of the three electrode types using SEM and AFM

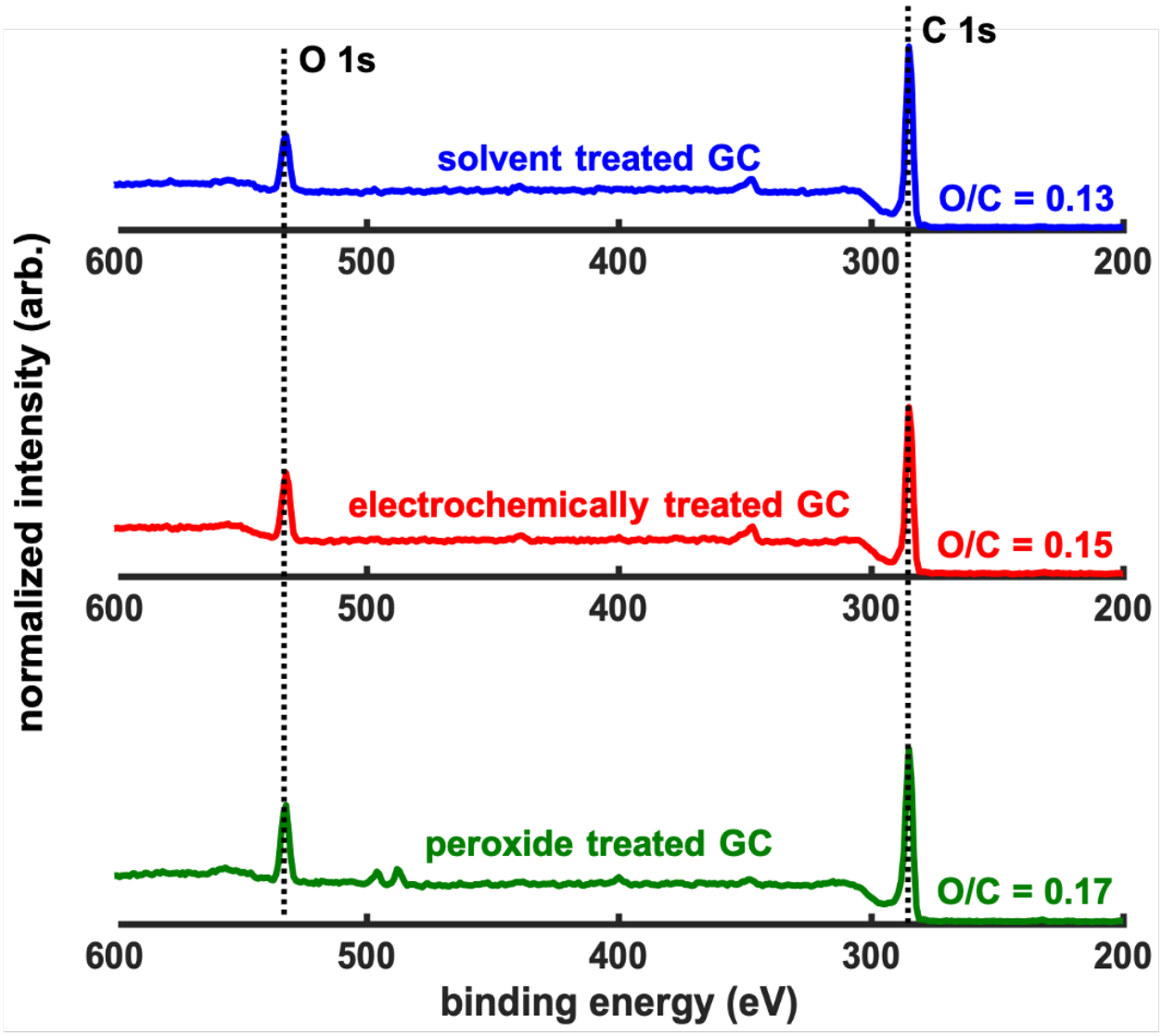

Figure 27: XPS survey scan data for solvent treated, electrochemically treated, and peroxide treated GC electrodes. Peaks corresponding to the O 1s and C 1s regions are noted along with the associated O/C ratios.

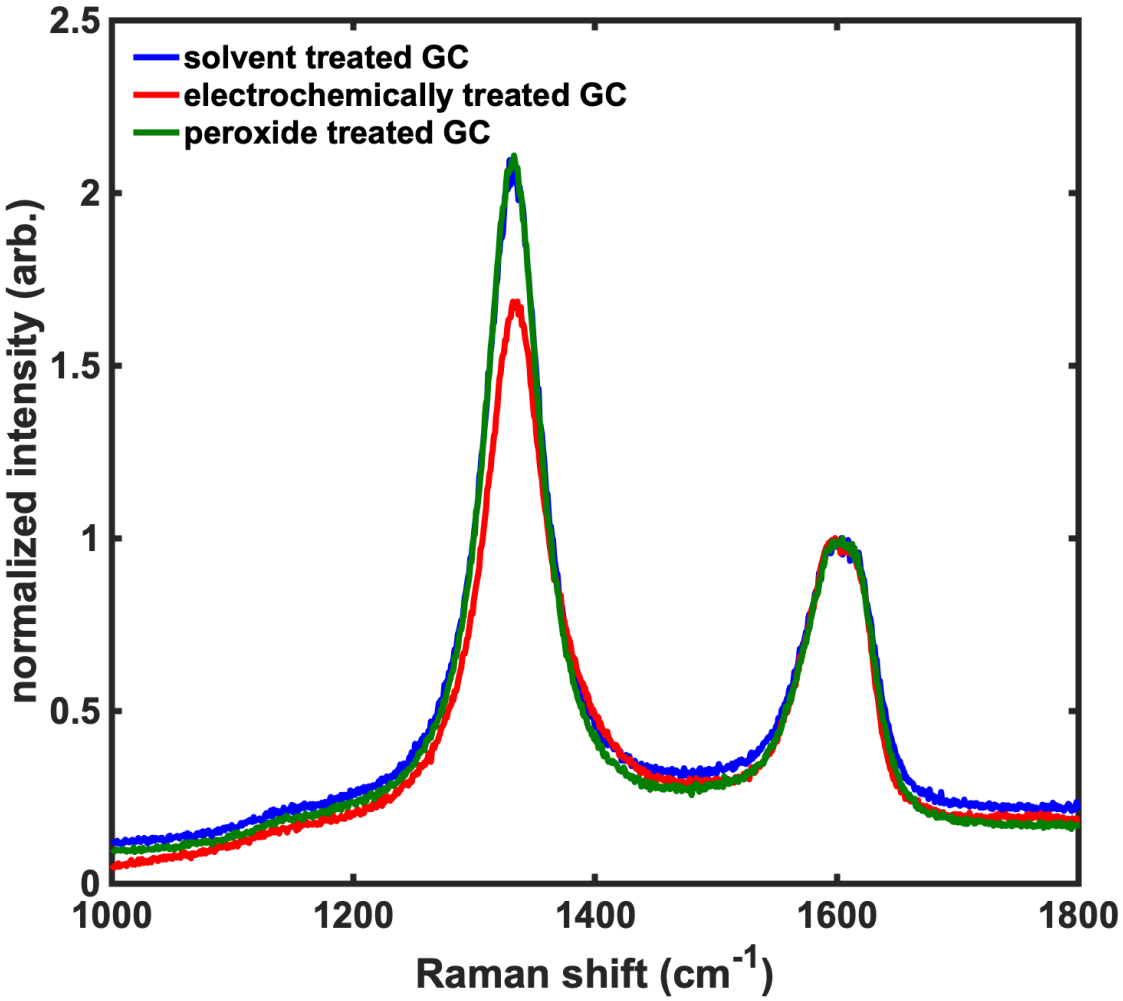

Figure 28: Normalized Raman data for solvent treated, electrochemically treated, and peroxide treated GC electrodes in the region corresponding to the characteristic features of graphitic carbon: D band at 1330 cm^{-1} and G band at 1590 cm^{-1}. The intensities are normalized to the maximum intensity of the G band for each electrode type.

measurements. Figure 29 presents the scanning electron micrographs and atomic force micrographs of the three electrodes after completing their pre-treatment protocols. However, qualitative comparisons of the three scanning electron micrographs showed similar morphologies, as well as the RMS roughness values obtained from AFM imaging for all three electrodes were ∼5 nm. Thus, we conclude that surface area effects were not responsible for the increase in electron transfer kinetics for electrochemically treated carbon.

Finally, we hypothesized that one or more chemical functionalities present on carbon is responsible for catalyzing the $Fe^{3+/2+}$ redox chemistry. To that end, we measured the relative amounts of oxidized surface species on carbon by collecting high resolution XPS spectra. These data were fit to find the relative proportions of graphitic (284.6 eV), alcoholic (286 eV), carbonyl (287 eV), and carboxylic functional groups (288.6 eV). Figure 30(a) collects the results from all three surface treatments into bar charts depicting fractional ratios for each type of functional group. The primary component in each case was graphitic carbon, which is unsurprising since XPS measurements probe several nanometers of sample depth, whereas only surface sites are susceptible to oxidation. Considering the distribution of the surface oxygen functional groups in solvent-treated GC as the baseline, we found an increase in the surface coverage by carbonyl and carboxylic groups upon electrochemical treatment and an increase in the alcoholic and carboxylic groups upon peroxide treatment.

Often the XPS probe depth is assumed to be a few nm so that the data can be treated as qualitatively indicative of the surface composition of a sample. However, because we observed only small changes in apparent oxidation after treating GC surfaces, we were interested in a more quantitative estimate of the degree of surface oxidation that would result in a particular increase in XPS signal corresponding to oxidized carbon. Thus, we estimated an XPS probe depth not in terms of distance, but in terms of the total number of carbon atoms in GC that are sampled by an XPS measurement. To do so, we used Equation 2.4, which describes the probability P(d) of a photoelectron escaping from a depth d within a solid as

$$P(d) = exp(\frac{-d}{\lambda cos\theta}) \tag{2.4}$$

where λ is the material and energy-dependent inelastic mean free path of the electron (31.06 A° at electron energy of 1196 eV in this case [250]) and θ is the angle between the detector

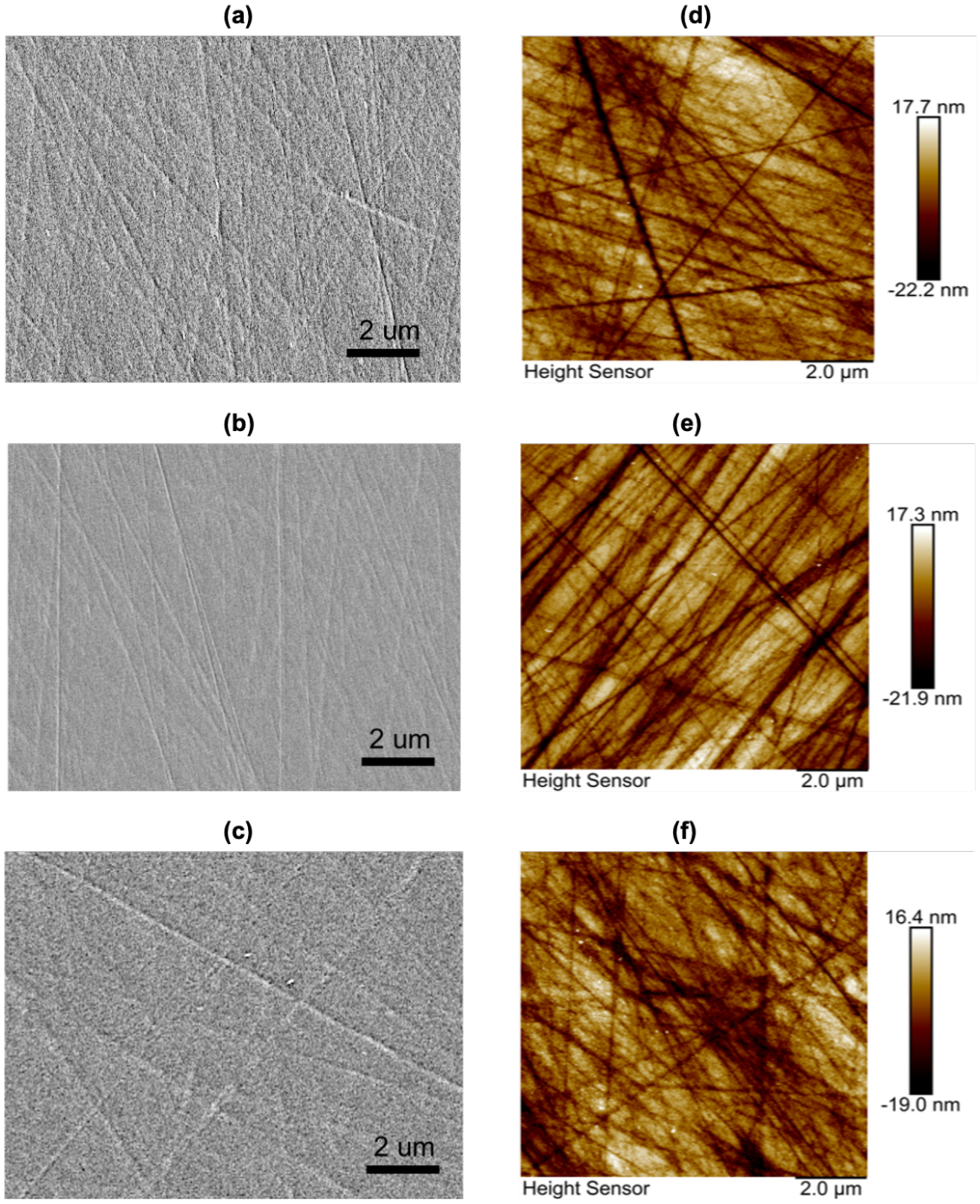

Figure 29: Scanning electron micrographs of (a) solvent treated GC, (b) electrochemically treated GC and (c) peroxide treated GC and atomic force micrographs of (d) solvent treated GC, (e) electrochemically treated GC and (f) peroxide treated GC.

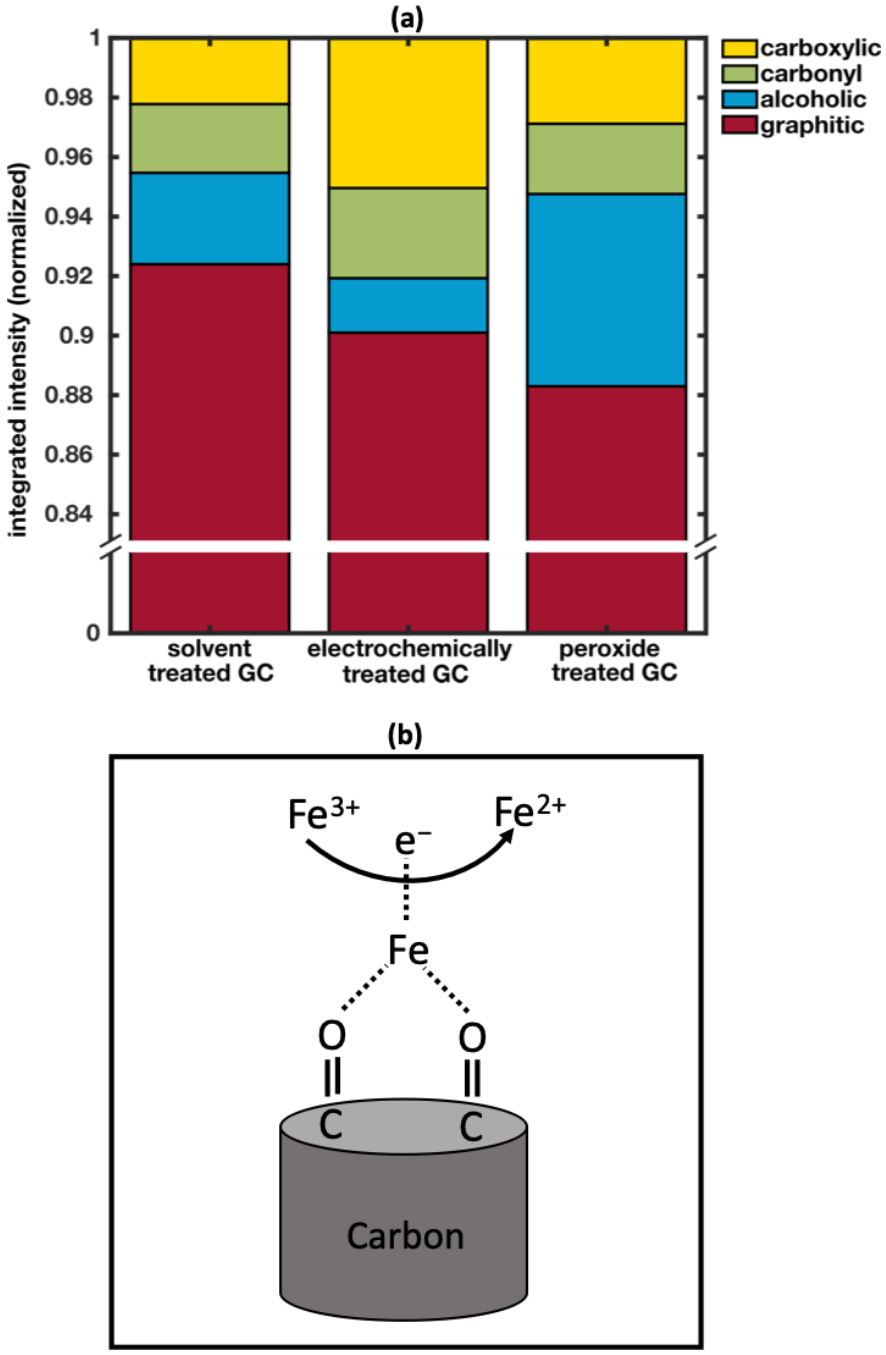

Figure 30: (a) Bar chart of various functional groups present in solvent treated, electrochemically treated, and peroxide treated GC electrodes obtained from C 1s peak deconvolution using XPS. Reported data are the mean of five replicates. (b) Schematic representation of the possible mechanistic rationale for enhanced electron transfer kinetics mediated by surface bound Fe species on –C=O functionalities.

and normal to the sample (40° in this case). Thus, the term $\lambda\cos(\theta)$ is an effective mean free path where $\lambda_{eff} = 23.8$ A° that takes into account the acceptance angle of the detector in the XPS measurement.

Next we approximated the GC near the surface region as a bulk solid comprised of essentially parallel layers separated by an average C-C distance of 2.2 A°, which is the arithmetic mean of three covalent bond lengths (1.42 A°) and two Van der Waals bond lengths (3.41 A°) in graphite as shown in Figure 31. This allowed us to approximate the total number of carbon atoms sampled by the XPS measurement in the z direction (normal to the surface) as the number of C-C distances required to reach a depth of 3 effective mean free paths (3 x 23.8/2.2 $\sim$ 33) weighted by the probability of electron escape at the depth of each individual layer, as in Equation 2.5.

$$C = \sum_{n=0}^{33} P(n \cdot 2.2) \tag{2.5}$$

where n refers simply to a layer index beginning at the surface (n=0) and ending at a depth equal to $3\lambda_{eff}$ (n=33). In this way, we found C to be 10.7, which implies that a GC sample with zero bulk oxygen content and monolayer surface coverage of oxygen would correspond to an apparent fraction of oxidized carbon on the order of 9 % by XPS. Thus, our estimation suggests that complete oxidation of a smooth GC surface where every surface carbon atom is bound to oxygen, would only give rise to $\sim$9% fraction of oxidized carbon by XPS. Interestingly, the solvent treated carbon surface already exhibited nearly this level of oxidation, which can be attributed to several factors such as (a) solvent treatments did not entirely remove oxidized surface functionalities, (b) our carbon surfaces were not completely smooth, (c) there may have been oxygen in the subsurface of our GC electrodes, and (d) some adventitious oxygen-bearing impurities may have been present in our XPS samples. If we treat the distribution of functional groups in the solvent treated carbon as a control, then the observed increases in oxidation for the electrochemical and peroxide treatments correspond to tens of percent of a monolayer equivalent. Thus, we conclude that C=O groups are primarily responsible for catalyzing the electron transfer for $Fe^{3+/2+}$ chemistry.

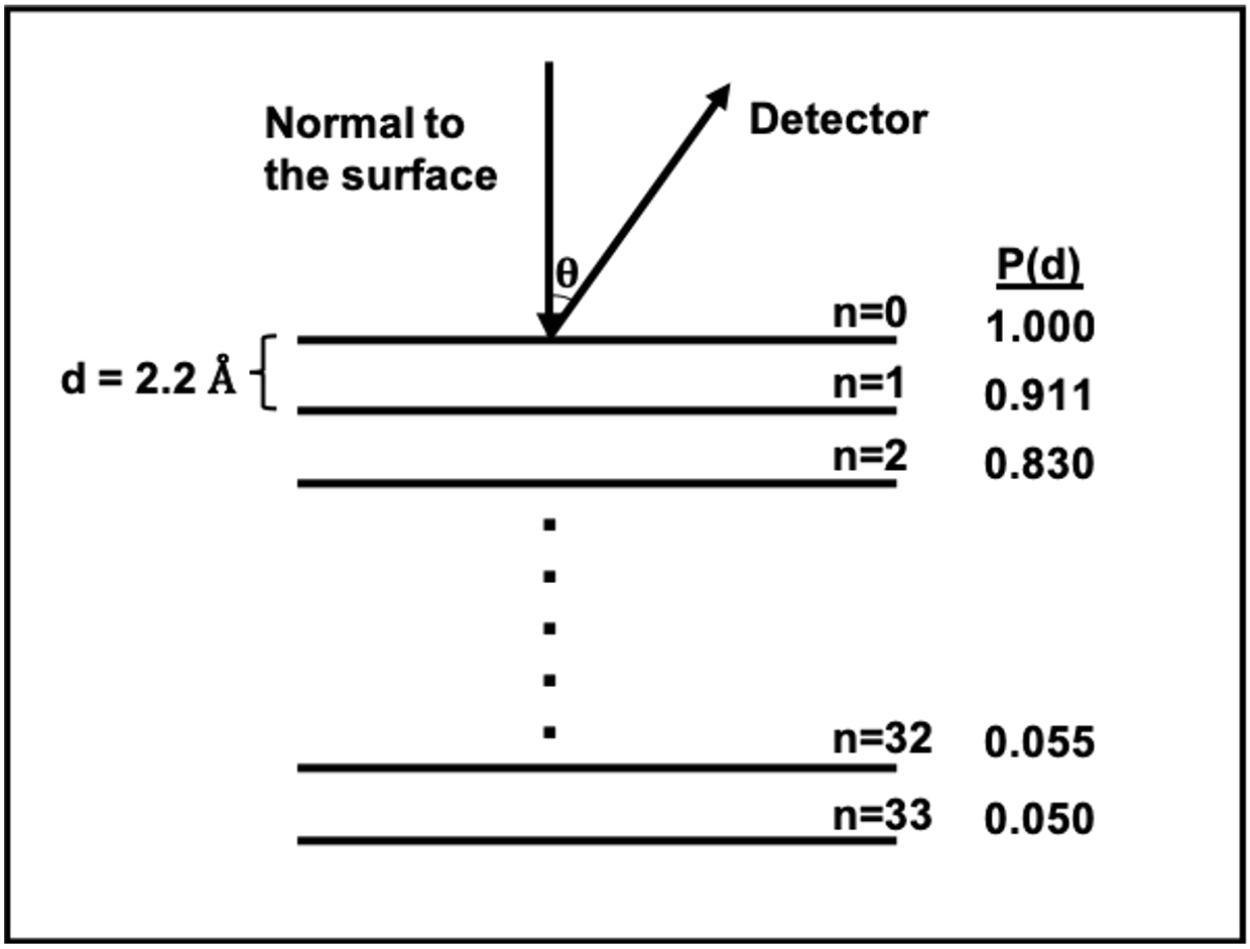

Figure 31: Schematic representation of carbon layers from n=0 to n=33 ($\sim 3\lambda_{eff}$), each separated by an average distance of 2.2 A°, along with the diminishing probabilities of electron escape in each layer.

Our results agree with several prior studies in which the catalytic activity of carbon electrodes toward transition metal aquo complexes was found to correlate with carbonyl coverage [125, 126, 227]. One possible mechanistic rationale for this enhancement involves the formation of Fe-bound surface adsorbates that are mediated by C=O functionalities, as schematized in Figure 30(b). This is comparable to Fe redox chemistry on noble metal electrodes, where halide-based bridging complexes are found to accelerate the rate of electron transfer [144,145,211,212]. We speculate that the predominant mechanism may involve rapid electron transfer from electrode to surface-bound Fe, followed by the exchange of electron from surface-bound Fe to solution phase Fe species, which would be the rate determining step. This mechanism is also reminiscent of "self-catalysis" by quinones bound to carbon surfaces through π stacking [236]. Thus, in the context of RFB device engineering, it is apparent that transition metal aquo complexes exhibit complex interfacial redox chemistry and do not behave as simple outer-sphere electron transfer reactions.

2.4.2 Testing the Hypothesis that C=O Functionalities enhance Fe Redox Kinetics Irrespective of the Type of Carbon

To explore the replicability of our surface treatments, we also evaluated the kinetics of $Fe^{3+/2+}$ electrolyte on carbon fiber electrodes using our flow platform. To conduct these experiments, we used commercially available carbon fiber microelectrodes embedded in cylindrical glass casing and employed them in the flow platform shown in Figure 19. We focused our efforts on electrochemically treated carbon to evaluate the enhancement in kinetics and compared the results with a solvent treated control. We performed the two treatments on carbon fiber microelectrodes using the same procedure as that used for glassy carbon RDE electrodes. Figure 32 presents representative cyclic voltammetry data and the associated Butler-Volmer fit for the electrochemically treated carbon fiber electrode in 5 mM $FeCl_2$ and 5 mM $FeCl_3$ in 0.5 M HCl electrolyte obtained using our flow based platform at a flow rate of 10 mL/min. We found that the exchange current density obtained at solvent treated carbon was 0.11 ± 0.01 mA/cm^2 and that obtained at electrochemically treated carbon was 0.83 ± 0.18 mA/cm^2. These results were comparable to the exchange current densities obtained at

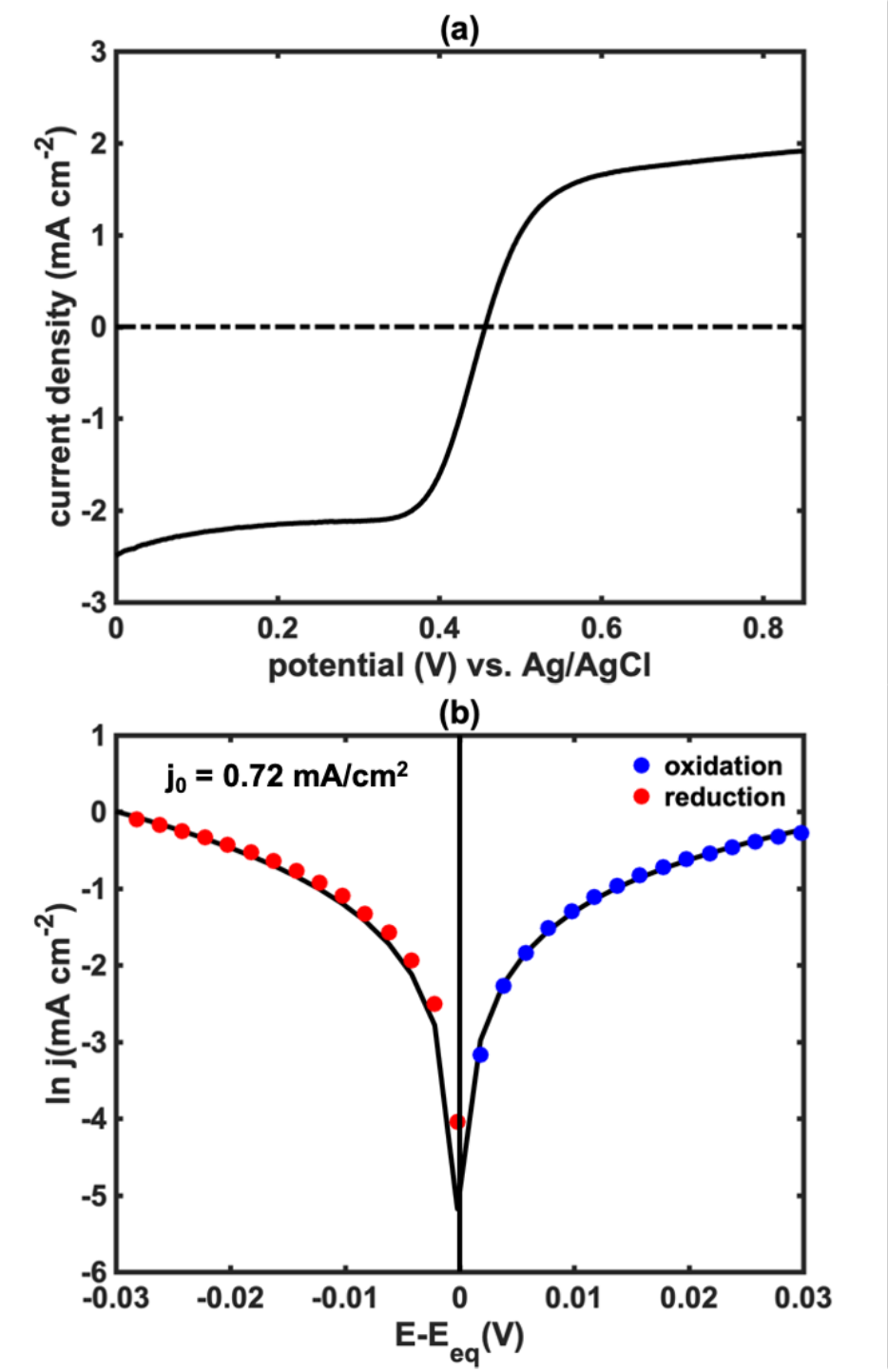

Figure 32: Data collected on electrochemically treated carbon fiber microelectrode in 5 mM $FeCl_2$ and 5 mM $FeCl_3$ in 0.5 M HCl electrolyte at 10 mL/min flow rate; (a) Representative cyclic voltammetry data and (b) associated BV fit.

glassy carbon RDE electrodes (see Table 3). Moreover, the observed enhancement in kinetics upon electrochemical treatment concludes that C=O functionalities enhance the electron transfer kinetics for $Fe^{3+/2+}$ electrolyte irrespective of the type of carbon.

We further performed these measurements at battery relevant concentrations of 1 M total Fe in 2 M HCl electrolyte and compared the kinetics to the expected results for a 100 fold increase in concentration. The exchange current density was found to be 16 $\pm$ 2.5 mA/cm^2 for the solvent treated carbon and 26.5 $\pm$ 4 mA/cm^2 for electrochemically treated carbon. While the solvent treated carbon resulted in similar exchange current density as compared to the expected value of 11 mA/cm^2, the j_0 obtained at electrochemically treated carbon was smaller by roughly a factor of 3 as compared to the expected value. These results suggest that electron transfer process at the surface of an electrochemically treated carbon is not completely kinetically limited. To confirm, we separately carried out a series of experiments on solvent and electrochemically treated carbon to evaluate the effect of increasing mass transport. Figure 33 presents a comparison of the exchange current densities obtained under static (0 mL/min) and flowing conditions (10 mL/min) of the electrolyte. As seen from the figure, the solvent treated carbon resulted in similar kinetics for both static and flowing experiments, whereas the electrochemically treated carbon showed enhanced kinetics upon flowing. This result is strong evidence that the solvent treated carbon surfaces are fully kinetically limited and thus, increasing mass transport has no effect on the apparent rate of electron transfer whereas electrochemically treated carbon are at least partially mass transport limited. Overall, this study provides considerable impetus to design more active and stable electrocatalysts for RFBs by selectively increasing the surface coverage of C=O functionalities on the surface of carbon. To that end, future work should be directed towards developing and optimizing the process of selectively adsorbing C=O functionalities on carbon electrodes. Additionally, the stability of these pretreatments should be evaluated as a function of charge/discharge cycles using our online measurement platform. And finally, the generality of improved kinetics using C=O functionalities should be tested for several electrolyte materials such as vanadium, anthraquinone and methyl viologen.

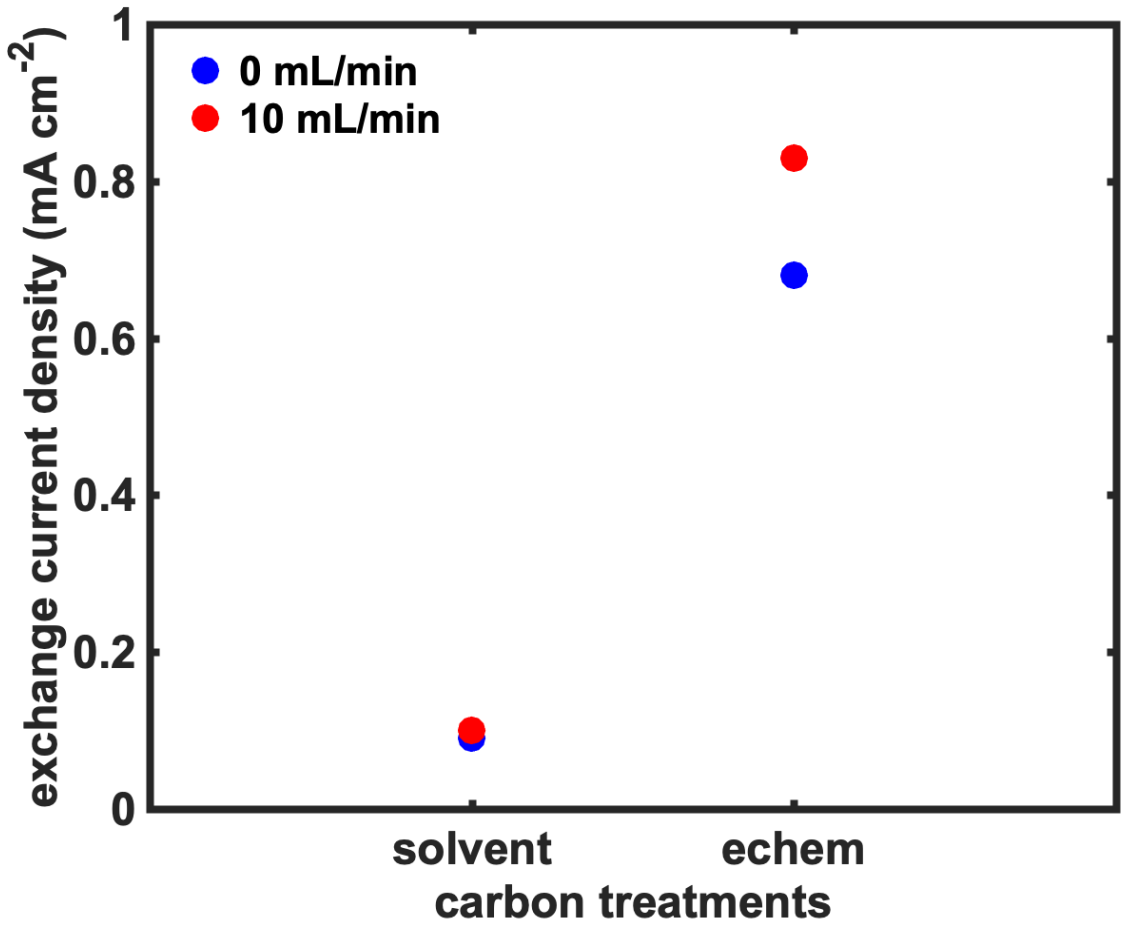

Figure 33: Exchange current densities obtained on solvent and electrochemically treated carbon under static (0 mL/min) and flowing conditions (10 mL/min) of the electrolyte (5 mM $FeCl_2$ and 5 mM $FeCl_3$ in 0.5 M HCl).

2.4.3 Future Outlook for Developing Flow Batteries–Opportunities to Leverage Catalysis Science

Continued efforts to improve the performance of RFBs can greatly benefit from developing insights and adopting design strategies from the field of electrochemical catalysis. Recent advances in the theoretical and experimental aspects of this field have resulted in a set of design principles that can be used to develop efficient electrocatalysts by way of stabilization or destabilization of surface bound intermediates [251–254]. When these principles are applied to RFBs, it leads to the conclusion that RFB electrolytes should only require one surface bound intermediate since they generally consist of only one or two electron transfer reactions. Thus, it should be possible to accelerate the adsorption and desorption of this surface bound intermediate by designing interfaces with optimal binding energies—similar to that obtained at the surface of a Pt electrode for the hydrogen evolution reaction (HER). Hence, it should be possible to design electrocatalysts for RFBs that completely eliminate kinetic losses for all electrolytes with $\leq$2 electron transfer reactions. Nonetheless, much work remains in this field to successfully develop design principles for efficient catalysts in RFBs.

Complexities associated with electron-transfer in VRFBs provide a representative case study illustrating the need to develop better electrocatalysts. Although both positive and negative half cells reactions of a vanadium RFB involve only one electron transfer, they still suffer from sluggish kinetics at unmodified carbon electrodes [128, 255]. While a variety of pre-treatment procedures are conducted on the electrode surfaces to accelerate the kinetics, these strategies are mainly based on trial and error methods and these have not yet been successful at completely eliminating kinetic losses in these systems [137, 256–259]. Additionally, there is still an active debate regarding the molecular basis of enhanced catalysis at pretreated carbon electrodes as well as whether the positive or negative vanadium redox couple exhibits faster kinetics [139, 148, 168, 255, 260]. Finally, the stability of these surface treatments over extended battery operation remain poorly understood. Thus, renewed efforts to understand the mechanism of electron transfer in vanadium RFBs can provide valuable insights into the development of efficient and stable electrocatalysts.

Quinone based chemistries provide an interesting contrast to vanadium systems in that they exhibit fast electron transfer kinetics even at bare, unmodified carbon electrodes despite the fact that they exhibit two electron-two proton transfer reactions [72, 132, 142, 261]. Thus, untreated carbon electrodes appear to be excellent electrocatalysts for this chemistry by coincidence. This is consistent with the self-catalytic mechanism reported in the literature for quinone based redox couples wherein the surface adsorbed quinone stabilizes the transition state associated with proton coupled electron transfer to solution phase quinones, but this possibility has not been addressed directly in the RFB research literature [236]. Further work to understand the mechanism of quinone redox catalysis alongside their ability to possess long-term stability at the surface of carbon under practical RFB conditions can be extremely valuable in enabling the use of these electrodes in next-generation commercial systems.

An increasingly popular strategy adopted in the field of RFB electrocatalysis is to design and develop novel molecules (generally, organics and organometallics) that exhibit inherently fast kinetics. These molecules are desirable since they possess the ability to undergo minimal changes in bonding and structure during a reaction, which eliminates the need to undergo specific interactions with the electrode surfaces to stabilize the transition states [197, 262–264]. However, this molecular design strategy also has several key limitations. First, it is difficult to achieve fast kinetics with redox couples which undergo more than one electron transfer reactions. But using a single-electron transfer redox couple significantly limits the ability to achieve energy-dense RFBs. Second, facile electron-transfer kinetics may also lead to side reactions with solvent, impurities and stack components that are susceptible to corrosion. Thus, using kinetically facile redox couples can lead to high voltage efficiencies at the cost of reduced battery life. This consideration is especially important for emerging nonaqueous RFBs, which are touted for their potential to achieve very large cell voltages—on the order of 3 V or larger. This goal is often rationalized by analogy to the use of nonaqueous solvents in Li-ion battery systems [52, 183, 265]. However, Li-ion batteries are generally stabilized by formation of passivation layers on the electrode from decomposition of solvent or the supporting electrolytes, a trait that cannot be readily adapted for RFBs [266–271]. In fact, kinetically facile redox couples that readily transfer electrons to or from solvent species will likely degrade rapidly in this type of environment.

Based on the strategies discussed above, an ideal RFB redox couple should exhibit multi-electron transfer reaction with extreme redox potentials to avoid solvent or supporting electrolyte degradation and only undergo acceleration in kinetics in the presence of a good catalyst. Interestingly, VRFB electrolytes satisfy this description well if improved electrocatalysts could be developed. Water-soluble quinones also satisfy most of these requirements, which helps explain why they are among the most promising contenders for next-generation RFB active materials [72, 143, 272, 273]. Nonetheless, there exist a vast range of materials that can be used in RFBs that need to be carefully designed and evaluated to achieve control over interfacial electron transfer. Working toward this goal will require research strategies that consider electrode and electrolyte materials together. This increases the complexity of experimental design for RFB materials discovery, but it also enables a higher degree of tuneability via modifications of the electrode and electrolyte in tandem.

2.5 Summary, Impact and Recommended Future Work

In summary, this chapter comprised detailed studies aimed at improving RFB performance. We worked towards two broad objectives of improving analytical methods for characterization of electron-transfer kinetics and developing efficient electrode materials to improve electrocatalysis in RFBs. Successful completion of this work has offered a valuable resource to the RFB community: a new method to measure RFB kinetics that is specifically tailored to technologically relevant conditions. This tool has improved the precision of kinetics measurements and has resulted in obtaining reproducible kinetics under practical RFB conditions. We also demonstrated several treatment protocols to fabricate high performance carbon electrodes and provided a mechanistic understanding of the associated electron-transfer process. These insights have helped motivate improved surface functionalization strategies that can be applied to technologically relevant carbon electrodes in the interest of minimizing energy efficiency losses attributable to kinetics in practical flow batteries. While specific recommendations are provided within individual sections; overall, future work should be directed at validating these advances by demonstrating high-performing RFBs within our own lab.

3.0 Dynamics of Zircaloy Corrosion in Nuclear Reactors

The focus of this chapter is on studies related to the corrosion resistance of cladding materials that are widely used in light water nuclear reactors. The Boiling Water Reactor (BWR) and Pressurized Water Reactor (PWR) are two of the common types of nuclear reactors employed in the world [274]. Fission of the enriched uranium dioxide nuclear fuel, UO_2 form the primary reaction that leads to the generation of heat in these reactors. This heat generated from nuclear fission is used to convert water into steam, which then drives turbines to generate electricity. While in a BWR, the steam is generated within the reactor vessel itself; in a PWR, the heat from nuclear fission is first transferred to a secondary water loop where the water gets converted into steam. Typical operating conditions of these light water reactors are summarized in Table 4 [275].

3.1 Significance of Zircaloy corrosion

Zirconium based alloys (collectively referred to as Zircaloys) are routinely employed in light water nuclear reactors as cladding materials owing to their numerous desirable properties, such as low thermal neutron cross-section, good mechanical strength, high thermal conductivity, and excellent corrosion resistance in high temperature aqueous environments [276–278]. The key property of any corrosion-resistant Zr alloy is its ability to form a chemically stable, tightly adherent zirconium-oxide (ZrO_x) passivation layer that protects the underlying alloy from further corrosion [279, 280]. This was one of the primary features responsible for the adoption of Zircaloys as cladding materials in the early history of the nuclear industry. Zirconium-tin based system (Zr-1.5% Sn) formed the composition of the first Zircaloy cladding developed in the United States [43, 281]. Unlike many other alloy systems, the corrosion performance of zirconium alloys deteriorates with decreasing content of the alloying elements, where highly purified crystal bar Zr exhibits unpredictable and often unstable corrosion behavior. Accordingly, industrially relevant Zircaloys generally

Table 4: Typical operating conditions in light water nuclear reactors (Individual datapoints extracted from Allen et al. [275])

	Boiling Water Reactor (BWR)	**Pressurized Water Reactor (PWR)**
Pressure (MPa)	~ 7	~ 15
Temperature (°C)	270 - 300	270-330
Coolant	water	water
Coolant composition		
oxygen (ppb)	~ 200	< 0.05
hydrogen (ppm)	~ 0.03	2-5
H_3BO_3 (ppm)	-	0-2200
LiOH (ppm)	-	0.5-5

comprise $> 95\%$ zirconium with trace quantities of Fe, Cr, Ni and/or Sn to further improve their physicochemical properties [282]. Zircaloy-2 and Zircaloy-4 are the 2 major types of cladding materials routinely employed in the commercial nuclear reactors. Typical compositions of these alloys alongside two other, more pure forms of Zr alloys are presented in Table 5.

Although Zircaloys readily form passivating oxide layers, the thickness and overall morphology of the layer is controlled by the respective rates of oxide formation and dissolution, and the dynamics of these processes are complex [44, 283]. Zircaloy corrosion proceeds via the formation of a sparingly soluble Zr rich oxide layer, so corrosion is generally monitored by measuring the net weight gain of a Zr coupon as a function of time that the sample has been exposed to the relevant environment. The net rate of oxide growth on Zircaloys in aqueous environments is generally found to fall into pre- and post-transition regimes, as schematized in Figure 34 [284, 285]. This transition is associated with growth of the oxide layer beyond a threshold thickness of ~ 2 μm along with a characteristic increase in the oxide porosity and the overall corrosion rate.

Table 5: Typical compositions of four Zr-based alloys (via Stanford Advanced Materials)

Alloy	**"crystal bar" Zr**	**Zr 702**	**Zircaloy-2**	**Zircaloy-4**
% purity	99.95	99.5	98	98
Element	**Composition (%)**			
Sn	0.0016	/	1.2-1.7	1.2-1.7
Fe	0.0051	<0.05	0.07-0.2	0.07-0.2
Cr	0.0003	<0.05	0.05-0.15	0.05-0.15
Ni	0.0003	/	0.03-0.08	0.007
Hf	0.025	1-2.5	<0.02	<0.02
Nb	0.0017	/	/	/

During the pre-transition period, Zr oxide formation is understood to be governed by primarily diffusive processes, which leads to the expectation of a parabolic rate law for corrosion. However, the governing rate law is instead found to be cubic, and the reason for this behavior has not yet been elucidated. During the post-transition period, corrosion rates are generally accelerated and tend to converge toward a linear rate law, implying a constant (e.g., reaction rate limited) rate of oxidation and minimal mass transfer limitations. This acceleration of the corrosion rate has been attributed broadly to environmental conditions that disrupt the conformal oxide coating or the underlying metal layer. The oxide that develops after transition consists of an outer porous layer and an inner dense layer that is referred to as the *barrier layer* [286]. This barrier layer is typically characterized with a threshold thickness of 2-5 nm, not significantly different from the thickness of a naturally formed oxide under atmospheric conditions [278]. The thickness and integrity of the barrier layer is often thought to govern the rate of further corrosion. Accordingly, factors that degrade the protective nature of the barrier layer have a major impact on the passivity of the surface oxide. Under the extremely harsh conditions of nuclear reactors—which include temperatures on the order of 300 °C along with a constant flux of subatomic particles and high-energy radiation—the post-transition rates of Zircaloy corrosion are further accelerated.

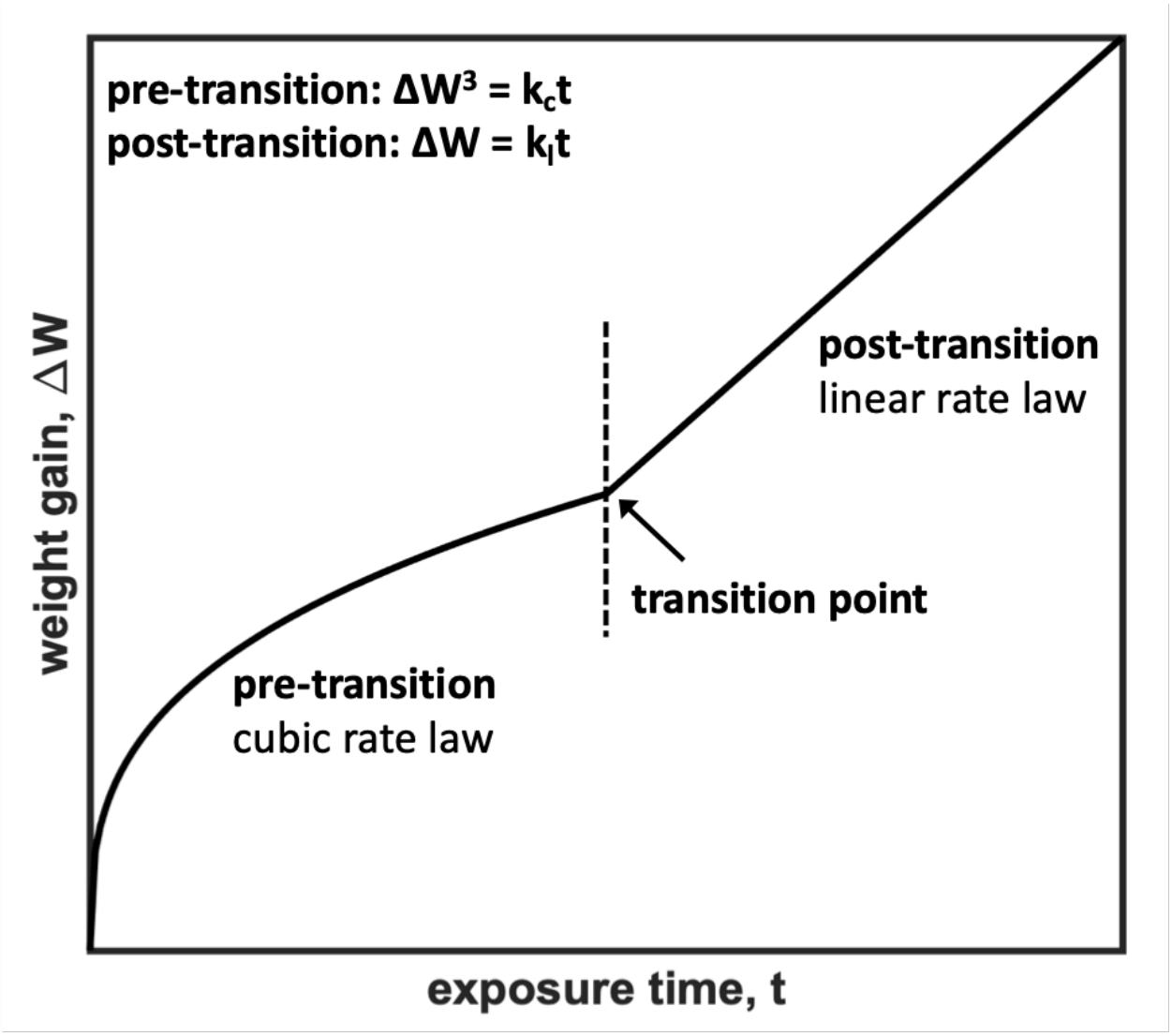

Figure 34: Schematic representation of corrosion rates of Zircaloy. Variables k_c and k_l represent cubic and linear rate constants for the pre- and post-transition regions, respectively. (Adapted from Hillner et al. [45])

This result is generally attributed to rapid attack of the rate-controlling barrier layer. These observations suggest that substantial dissolution of the passivating oxide may occur despite the net positive rate of weight gain.

Some of the primary reasons for the breakdown of Zr oxide reported in literature are cracking of oxide from differential stress due to formation of new oxide, sudden changes in pressure due to the propagation of cracks at the oxide/metal interface, dissolution in water and LiOH environments, increase in oxidation rate due to hydride formation and degradation through the dissolution of secondary phase precipitates [287–292]. The effect of irradiation on the breakdown of Zr oxide has also been extensively studied [46, 293, 294]. Neutrons are widely considered to be the primary reason for radiation induced change in corrosion behavior of Zr alloys since they induce direct changes to the chemical composition of the substrate and/or the oxide, resulting in poor physical and mechanical properties after radiation [295, 296]. However, other radiation types cannot be ruled out for contributing to accelerated corrosion. For instance, photons with a wide range of energies from the visible (>3 eV) to the gamma (> 100 keV) region are also prevalent in the reactor. These photons result from several processes, including spontaneous fission reactions, fission product decay, nuclear fuel decay, capture process in the fuel or other reactor components and several others [297].

Prior observations of corrosion behavior under operating conditions of a pressurized water reactor (PWR) show enhanced corrosion rates in environments with radiation compared to non-irradiated corrosion rates [293, 298]. While prior work has focused mainly on the influence of neutrons, it has been proposed that a mechanism related to photochemical dissolution may be responsible for at least part of the acceleration of corrosion. A key element of the proposed mechanism is that the absorption of gamma and other high-energy radiation in the zirconia film produces excited electrons and holes [46, 47, 299]. Based on analogy to the established physics of transition metal oxide photoelectrodes in contact with water, the photo-induced flux may induce the migration of charge carriers (electrons and/or holes) to the oxide/solution interface [300]. The capture of holes in particular at surface sites leads to the localization of the hole on a surface oxygen atom, thereby progressively weakening the associated bonds and ultimately forming species that are soluble in the coolant. In

this context, photoanodic oxide dissolution may result in degradation of the barrier layer and acceleration of the corrosion kinetics. Reaction R1 shows the net reaction occurring in aqueous environments, which exhibits a positive Gibbs free energy of reaction ∼526.4 kJ/mol at 25 °C and 1 atm [301]. This Gibb's free energy can be converted to an equilibrium potential, E^0 of 1.36 V vs. RHE using Equation 3.1.

$$ZrO_2 + 4\,H_2O \longrightarrow Zr(OH)_4 + O_2 + 2\,H_2 \tag{R1}$$

$$\Delta G^\circ = -nFE^\circ \tag{3.1}$$

where ΔG° is the standard Gibbs free energy of reaction, n is the number of electrons transferred in the reaction, F is Faraday's constant and E° is the standard equilibrium potential of the reaction vs. RHE.

A principal cause of concern to the integrity of an operating nuclear reactor is the failure of Zircaloy cladding due to this accelerated corrosion in the post-transition regime, which remains poorly understood to date. To this end, there is a pressing need to understand the underlying mechanisms of in-reactor corrosion of Zr alloys in the broader pursuit of developing advanced cladding materials that are still more corrosion resistant. Moreover, the rate at which Zircaloy cladding materials must be replaced in practical nuclear environments greatly exceeds what would be expected from the same materials outside of the reactor environment under otherwise identical conditions. Thus, there is significant economic and operational impetus to understand the electrochemistry of Zircaloy corrosion under high-energy irradiation.

3.2 Assessing the Semiconducting Behavior of Zr and Zircaloy Surface Oxides

We sought to critically evaluate the hypothesis that accelerated Zircaloy corrosion can be attributed to the influence of gamma (γ) radiation. In general, γ-radiation comprises extremely energetic (>100 keV) photons that readily interact with reactor components to generate excited states, which can further re-emit radiation in the γ energy range or below

(e.g., X-rays, ultraviolet, etc.). This high-energy photon flux could be expected to generate excited electronic states in Zr oxides, despite their characteristically large bandgaps (on the order of 5 eV). This leads to the possibility that oxide passivation layers on Zircaloys do not obey classical corrosion dynamics and are better represented as semiconductor photo-electrodes. To address this possibility, our work was directed at building insights into the semiconducting properties of zirconium oxides using the tools of applied electroanalysis and semiconductor photo-physics.

3.2.1 Identifying the Effect of Illumination on Photoelectrochemical Behavior of the Oxides

Our initial studies were directed at evaluating the hypothesis that the naturally forming passivating surface oxides on Zircaloy under reactor conditions behave as n-type photoanodes by inducing surface oxidation reactions upon illumination. To evaluate the semiconducting properties of Zr oxides, we used Zircaloy-4 samples along with pure Zr (99.95% purity) to independently assess the effects of alloy corrosion arising from impurities. Zircaloy-4 samples were prepared by our research partners at the Fluor Marine Propulsion Naval Nuclear Laboratory (NNL) using standard autoclave techniques, whereas we prepared pure Zr oxide samples by heating in a muffle furnace under aerobic conditions to obtain desired oxide thickness using the relationship between oxide thickness and weight gain as found from Per Kofstad [302]. Figure 35(a) presents a SEM cross-sectional image of a representative Zr—ZrO_x sample after thermal oxidation in air. The thermal treatment resulted in the formation of a surface oxide with a thickness of roughly 254 ± 31 nm. Deviation is reported as a 95% confidence interval taken over a set of ten measurements of oxide thicknesses at randomly selected locations from the micrograph. The Zr—ZrO_x interface shows a characteristic roughness as compared to the ZrO_x—air layer, which we attribute to the polishing of bare metal Zr samples. We also found that the heat treatment approximately doubled the polarization resistance from "bare" Zr to ZrO_x sample (See Figure 35(b) and (c)). While the bare Zr is expected to have a small, non-negligible oxide thickness occurring from atmospheric oxidation of the surface, the difference in observed polarization resistance is quite

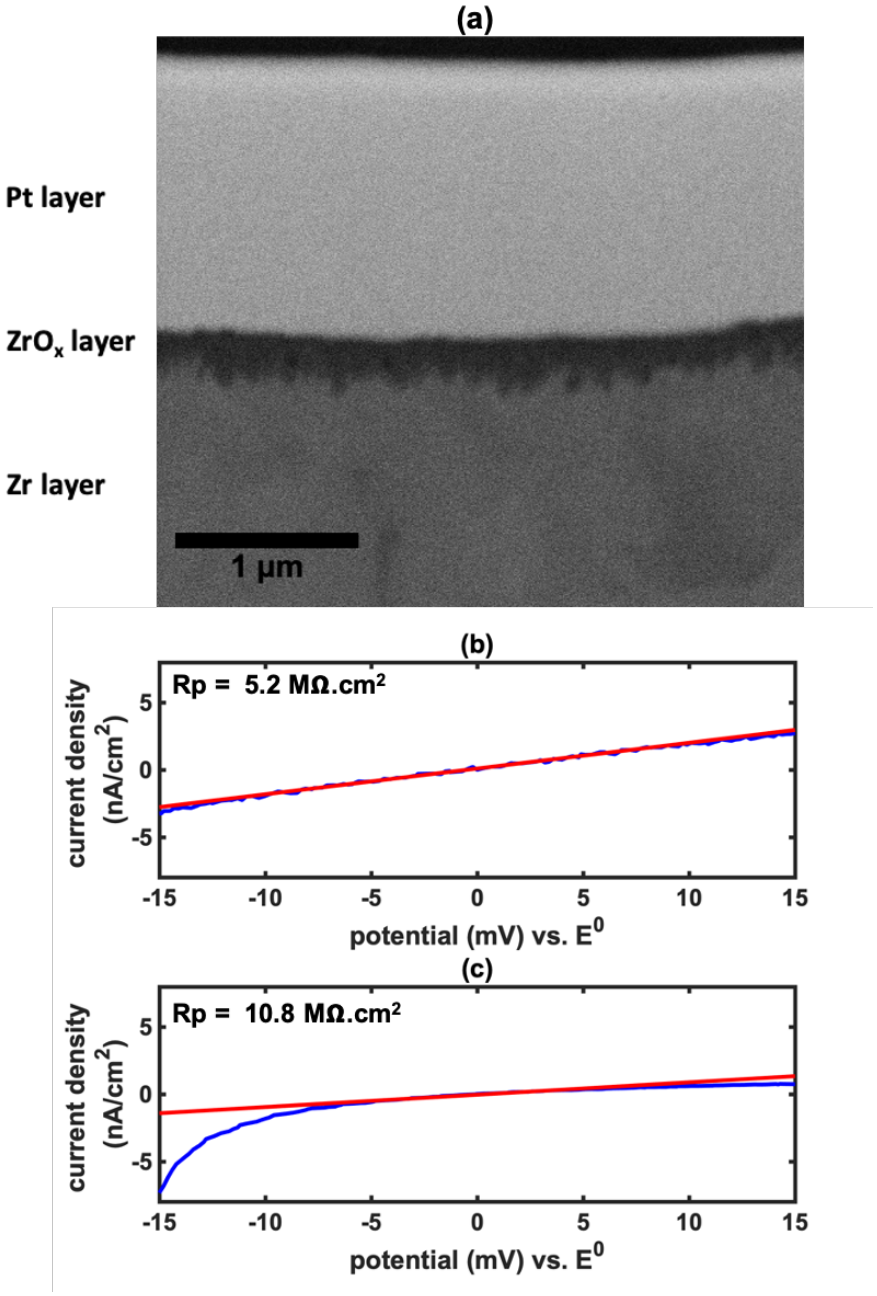

Figure 35: (a) SEM micrograph of a representative Zr sample after thermal oxidation in air at 400 ^{o}C for 5 min; Plot of potential vs. current density obtained in pH 13 LiOH using linear polarization method for (b) Zr and (c) Zr heat treated to obtain 240 nm of oxide thickness. Blue lines represent the experimental data and red lines indicate tangents drawn at open circuit conditions.

small as compared to the total growth in the oxide thickness. Moreover, the oxide layer was dense, with no significant cracks/pores propagating to the oxide—metal interface, suggesting that the surface oxide films formed from our heat treatments resemble the oxide passivation films formed under nuclear reactor conditions, only thinner. These results strongly suggest that our thermal treatment resulted in a thin but protective oxide coating on the surface of the Zr sample.

In the interest of safety, cost, and convenience, we used deep-UV illumination as a proxy for the high-energy radiation that is present in nuclear reactors. The intensity of above bandgap photons incident on our samples using the UVC light source was $\sim 10^{19}$ photons cm^{-2} s^{-1} (flux = 8.5 W/cm^2) which is comparatively higher than the maximum expected γ flux in a PWR type nuclear reactor is $\sim 10^{13}$–10^{14} γ cm^{-2} s^{-1} (flux = 1.6 W/cm^2) [46]. Thus, we expect our samples to be subjected to a somewhat harsher radiation environment as compared to that in a nuclear reactor, but nevertheless both these types of high energy radiation can lead to generation of electron-hole pairs in the oxide upon illumination. We used a unique electrolytic cell made from fused quartz and Teflon to be able to withstand the high intensity illumination. Figure 36 presents a schematic and photograph of this experimental setup. To approximate the composition of the PWR coolant, the electrolyte used in this case was pure deionized (>18 MΩ) water adjusted to pH 10 with LiOH, which is the base formulation for aqueous coolants in practical nuclear reactors. This low supporting electrolyte concentration results in very high series resistance in the electrochemical cell, which in turn decreases the time constant associated with equilibration of the sample to the electrolyte. We used platinum as the counter electrode and a Ag/AgCl reference electrode which had extremely small leak rate to avoid chloride contamination in the system. The working electrode connection was made by abrading the back side of the electrode and applying a conductive silver paint, which was used to secure a connection using a brass pin to the potentiostat.

We carried out a series of photo-electrochemistry experiments to assess the ability of the thermally generated Zr oxide to generate photovoltage and photocurrent under UV illumination. Representative results of open circuit potential measurements in pH 10 LiOH are compiled in Figure 37(a). Open circuit potential measurements were performed over

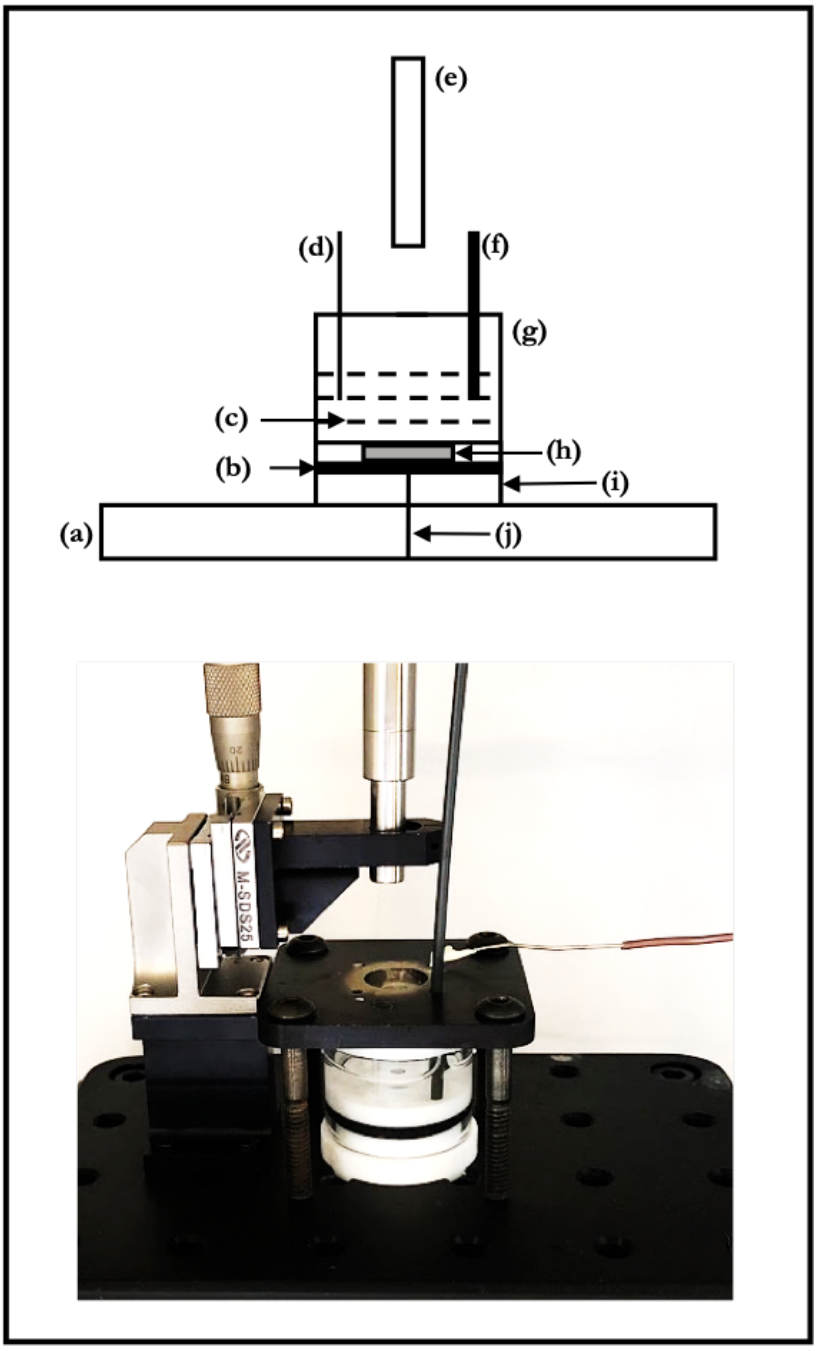

Figure 36: Schematic (top) and photograph (bottom) of the experimental setup used for photoelectrochemistry measurements. Components labeled in the schematic are as follows: (a) stand, (b) o-ring, (c) electrolyte, (d) counter electrode (platinum), (e) light guide, (f) reference electrode (Ag/AgCl), (g) quartz glass cell, (h) sample, (i) teflon housing and (j) brass pin for back contact.

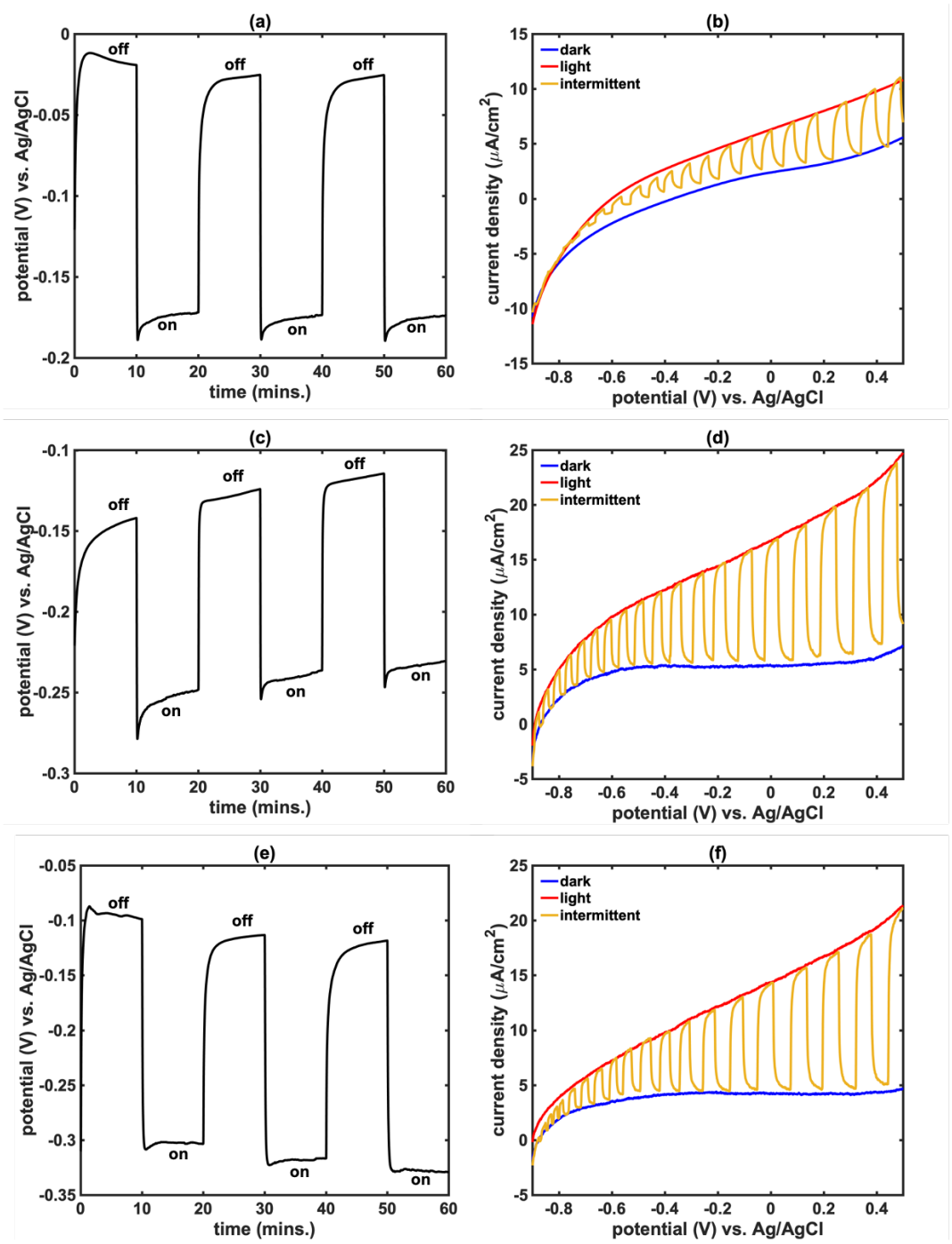

Figure 37: Electrochemical measurements taken on a representative Zr—ZrO_x sample over a range of electrolyte and illumination conditions. (a) Open circuit potential in pH 10 LiOH (aq.), (b) linear sweep voltammetry in pH 10 LiOH (aq.), (c) open circuit potential in pH 13 LiOH (aq.), (d) linear sweep voltammetry in pH 13 LiOH (aq.), (e) open circuit potential in 0.5 M Na_2SO_3(aq.) and (f) linear sweep voltammetry in 0.5 M Na_2SO_3(aq.).

a 1-hour timeframe with intermittent chopping of light to observe differences under dark and illuminated conditions. Under intermittent illumination with a period of 10 mins, the open-circuit voltage of the sample was found to shift in the negative direction by ∼150 mV. This is consistent with a classical picture of an n-type semiconductor photoanode, wherein the oxide forms a depletion region and illumination by above-bandgap photons increases the steady-state concentration of holes at the oxide-electrolyte interface. This increase in hole concentration results in an oxidizing photovoltage that must be opposed by the potentiostat to maintain zero net current flow, which results in a negative shift in the open-circuit potential.

These OCP data show that UV illumination under open-circuit conditions clearly perturbs the quasi-equilibrium condition associated with Zr corrosion. While the OCP change is modest compared to, e.g., the overall driving force (-2.4 V) for Zr corrosion by water at pH 10, the thermodynamic implication of this photovoltage is significant. For example, a similar change in the equilibrium electrochemical potential at an oxide surface would require an increase in oxygen partial pressure by several orders of magnitude. However, these data alone do not indicate whether illumination stabilizes or destabilizes the surface oxide—indeed, given the highly protective nature of the surface oxide, increased oxidizing potential under illumination may be expected to further passivate a Zr—ZrO_x sample.

Figure 37 (b) compiles polarization measurements carried out in pH 10 LiOH electrolyte. We observed clear evidence for anodic photocurrent in the potential range above -0.6 V vs. Ag/AgCl in LiOH electrolytes at pH 10. Figure 37 (c) and (d) presents the open circuit potential and polarization measurements carried out in pH 13 LiOH electrolyte. The magnitude of the photocurrent was ∼3-fold greater in pH 13 as compared to pH 10, which suggests that series resistance associated with electrolyte conductivity limits the photocurrent at pH 10. Moreover, the onset of photoanodic response was found to occur above -0.6 V vs. Ag/AgCl in pH 10 as compared to -0.9 V vs. Ag/AgCl in pH 13 electrolyte.

Based on analogies to the well-established photo-electrochemistry of n-type transition metal oxide photoanodes (e.g., TiO_2), we postulate that the holes present in the Zr oxide valence band are highly oxidizing and thus, the primary Faradaic reaction occurring in these alkaline electrolytes is oxygen evolution (Reaction R2) [300].

$$4\,OH^- \longrightarrow O_2 + 2\,H_2O + 4\,e^- \tag{R2}$$

However, oxygen evolution is a kinetically sluggish process on most oxides, which complicates the analysis as to whether the onset and shape of the photoanodic response results from the intrinsic photophysics of the oxides or the reaction kinetics. Thus, we also measured the photoresponse of the Zr—ZrO_x samples in the presence of sodium sulfite, Na_2SO_3, a commonly used molecular hole acceptor. Representative results are shown in Figure 37 (e) and (f). Notably, the photocurrent response in 0.5 M Na_2SO_3 was substantially similar to that in 0.1 M LiOH, which implies that the rate at which surface holes are captured by the electrolyte is not the primary bottleneck in the photoanodic process. These data together clearly demonstrate that thermal oxides synthesized at modest temperatures on Zr metal behave as defective n-type semiconducting photoanodes whose properties are broadly analogous to that of nanocrystalline TiO_2.

Photoelectrochemical measurements on Zircaloy-4 samples with 700 nm of oxide formed by exposure to water at elevated temperature and pressure show broadly similar photoanodic response in all three electrolytes, but with characteristically lower photovoltages and photocurrents. Representative data are depicted in Figure 38. Given the improved corrosion resistance of Zircaloy-4 compared to pure Zr, it is plausible that the alloying elements introduce additional mid-gap states to the surface oxide, thereby increasing the rate of charge-carrier recombination and decreasing the negative impact of photoexcitation. These results broadly indicate that pure Zr oxide and Zircaloy-4 indeed behave as n-type semi-conducting photoanodes, which confirms our hypothesis that these cladding materials engage in photochemical reactions under nuclear reactor conditions. This further supports the possibility of oxidative photo-degradation of the passivation layer over extended periods of illumination in an operating nuclear reactor.

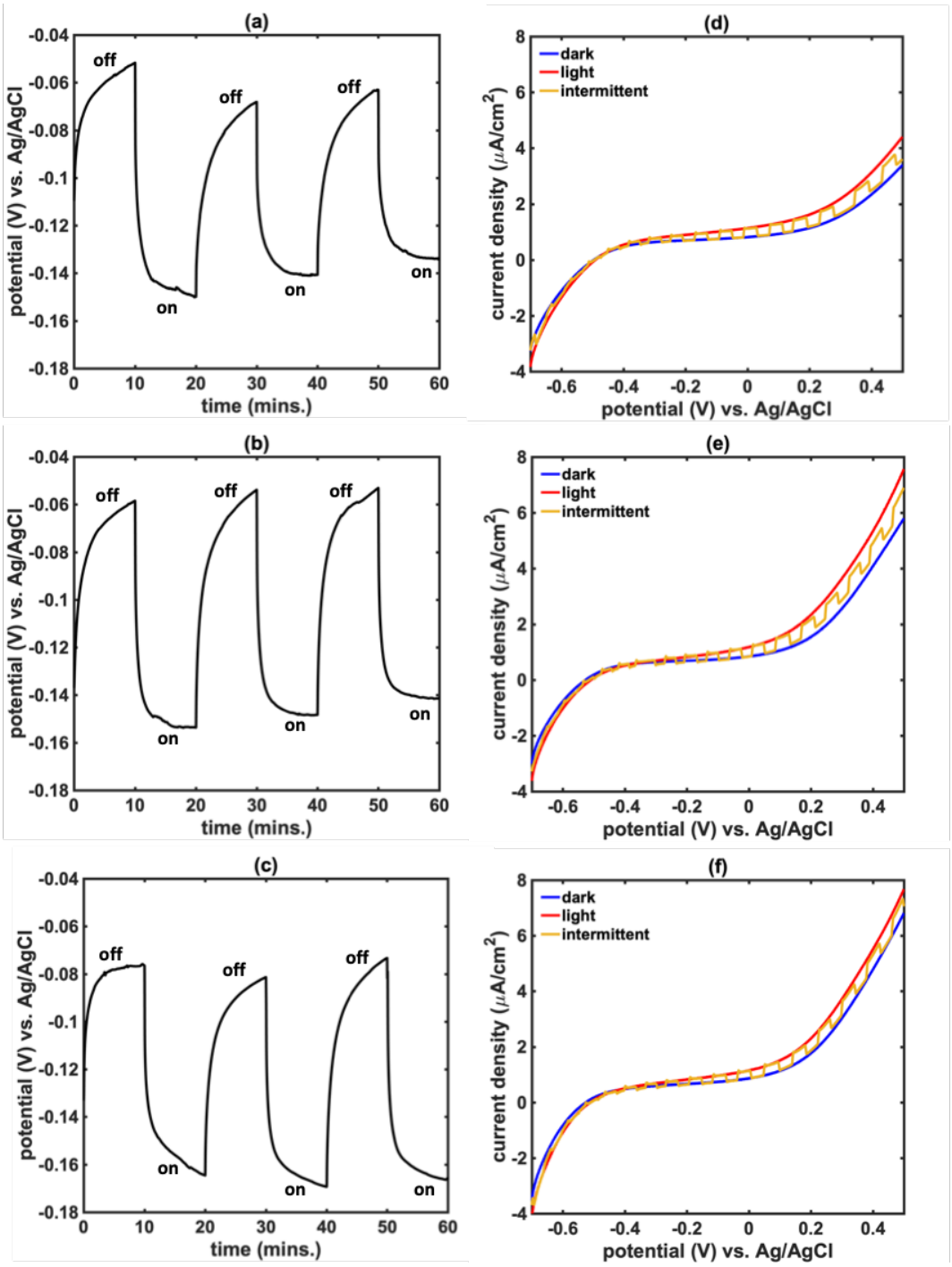

Figure 38: Electrochemical measurements taken on a representative Zircaloy-4 sample over a range of electrolyte and illumination conditions. Open circuit potential measurements in (a) pH 10 LiOH (aq.), (b) pH 13 LiOH (aq.) and (c) 0.5 M Na_2SO_3(aq.); Linear sweep voltammetry measurements in (d) pH 10 LiOH (aq.), (e) pH 13 LiOH (aq.) and (f) 0.5 M Na_2SO_3(aq.).

3.2.2 Elucidating the Semiconducting Properties using Band Energy Diagrams

Building on our results indicating that passivating ZrO_x layers behave as n-type semiconductors, we sought to formulate accurate band energy diagrams (depicting the relative energies of valence band, conduction band and Fermi level) for Zr and Zircaloy oxides. Our working hypothesis was that alloying elements dope the oxide, resulting in widely variable band interfacial energetics associated with the formation of Helmholtz and depletion regions at the ZrO_x—solution interface [303]. Thus, understanding the band energetics of these metal oxides will aid in understanding how each element dopes the oxide grown on Zr and how it influences the oxygen anion vacancy as well as the electron-hole populations under equilibrium and under illumination.

Initial efforts to build band-energy diagrams were based on performing Mott-Schottky (MS) measurements of pure Zr oxides [304–307]. This technique is commonly used to find the flatband potentials (V_{fb}) and doping densities of oxide semiconductors, which in turn enables the assignment of the Fermi energy referenced to the electrochemical scale. For an n-type semiconductor, a plot of inverse square of capacitance (C^{-2}) vs. DC bias (E) should yield a straight line with a positive slope, where the slope relates to the doping density and the intercept on the x-axis represents the flat-band potential, as shown in Figure 39 (a). However, the interfacial capacitance values extracted from pure Zr passivating oxides did not exhibit the linear C^{-2} vs. E relationship expected for the MS model. Representative Mott Schottky data for pure Zr sample is shown in Figure 39 (b). Possibilities for the unexpected MS behavior include:

1. Contributions to the total capacitance from the Helmholtz layer, the back contact (metal-oxide interface), or the electrochemical cell (i.e., stray capacitance) may obscure the capacitance of the desired oxide—solution interface.
2. The oxide—solution interface may exhibit such a high degree of compositional heterogeneity so that there does not exist a single well-defined depletion region.
3. Conditions under which the data were collected may result in transient changes in the oxide surface chemistry over the course of the measurements.

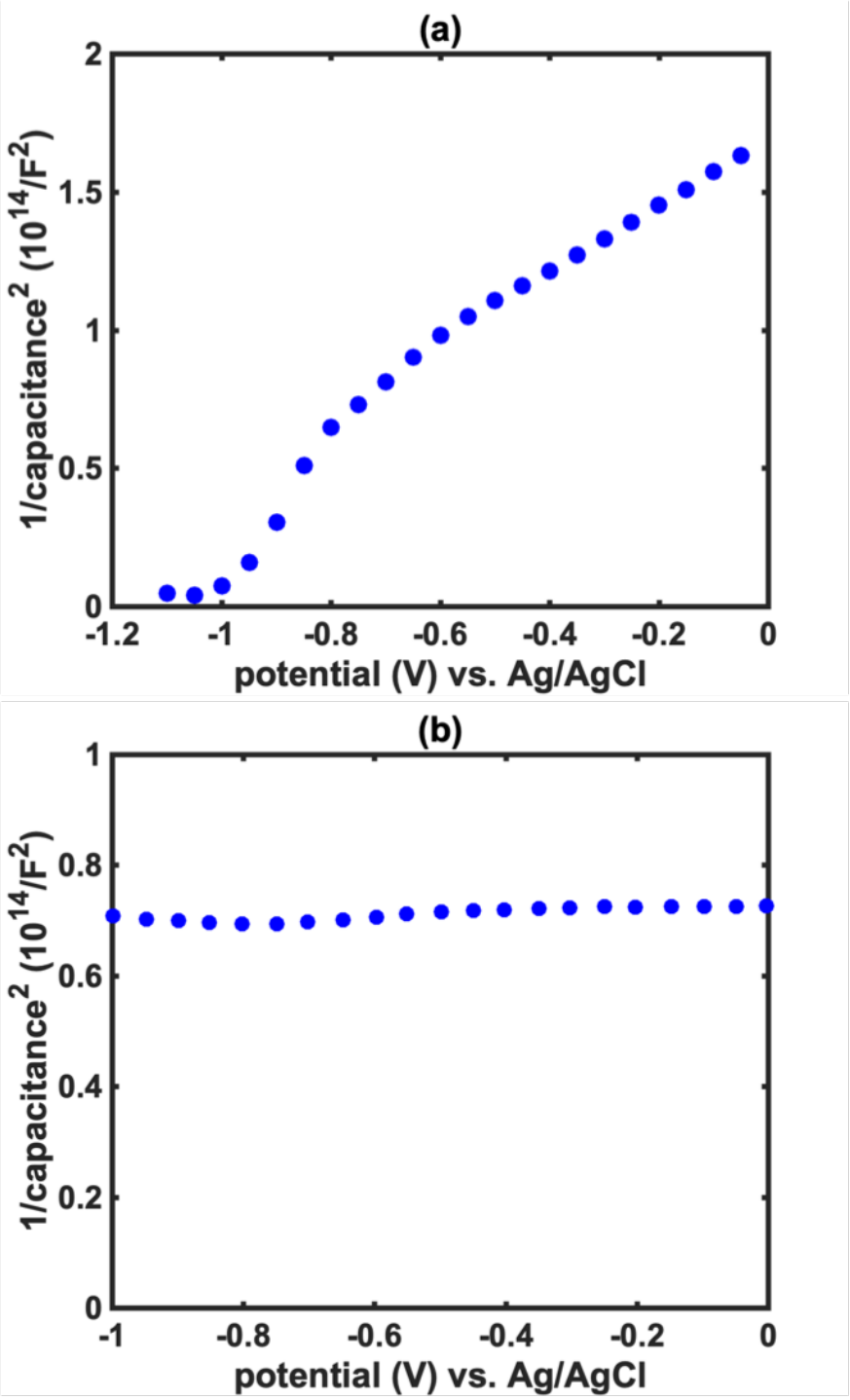

Figure 39: Mott Schottky plot depicting C^{-2} vs. E for (a) TiO_2 single crystal electrode and (b) pure Zr oxide electrode in pH 13 electrolyte.

Since Zr oxides did not provide an adequate MS relationship, we evaluated another technique called the chopped illumination method to find the flatband potentials. In a recent article that critically assessed methods for V_{fb} determination in oxide semiconductors, Hankin et al. argued that chopped-photocurrent measurements are considerably more reliable than EIS measurements [308]. This alternative approach involves identifying the potential associated with the change in the direction of photocurrent (from photoanodic to photocathodic) under intermittent illumination conditions. This potential can be regarded as the flatband potential on the basis that the change in photocurrent direction corresponds to the transition between majority-carrier depletion and accumulation in the near-surface of the semiconductor (i.e. changes the direction of the band bending as shown in Figure 40). This method would be expected to fail only for semiconductors that are very highly doped (and therefore cannot be driven into accumulation) or those that exhibit ill-defined equilibria with the electrolyte (where V_{fb} in turn would not be well defined).

To that end, we carried out a series of chopped photocurrent experiments on several Zr and alloy samples using Pt as the counter and Ag/AgCl as the reference electrodes in the Teflon cell setup shown in Figure 36. Table 6 summarizes the compositional details and presents the associated naming convention for all Zr oxide samples. Complete elemental compositions of samples Zr240 and Zry-4 are presented in Table 5 as Zr702 and Zircaloy-4 respectively. Only Zr240 was synthesized in McKone lab using heat treatment. All other samples were provided by our NNL partners. These experiments were carried out at a scan rate of 10 mV/s in six different electrolytic conditions:

- pH 10 LiOH to simulate reactor environment
- pH 13 LiOH to improve electronic conductivity and minimize contributions from Helmholtz capacitance
- 1% Na_2SO_3 in pH 13 LiOH where sodium sulfite was added as a hole scavenger
- 1% H_2O_2 in pH 13 LiOH where hydrogen peroxide was added as a hole scavenger
- H_2 saturated pH 13 LiOH to evaluate effect of presence of hydrogen
- pH 1 $HClO_4$ to evaluate effect of pH

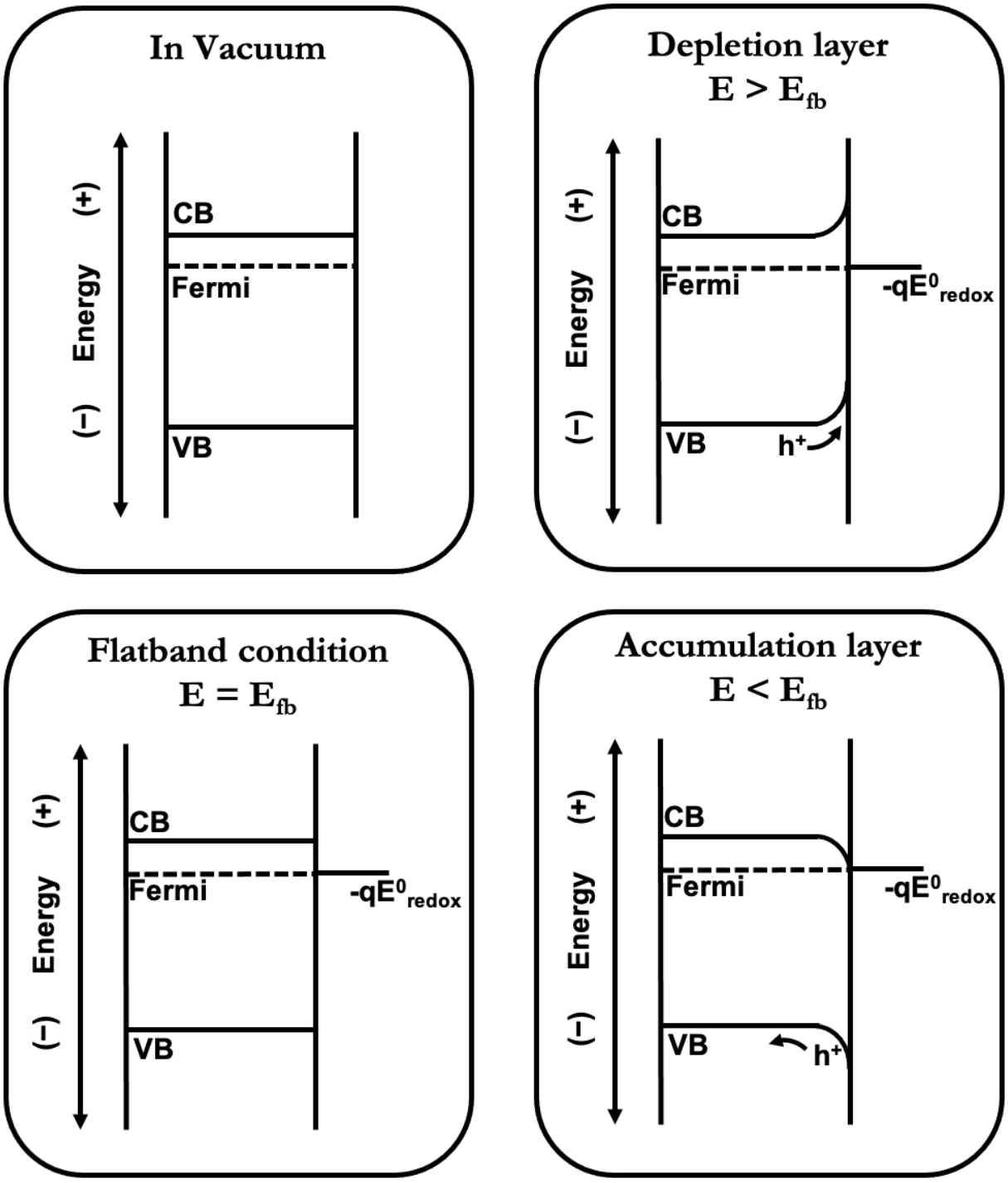

Figure 40: Schematic representation of the band energy diagram of an n-type semiconductor under vacuum, depletion, flatband and accumulation conditions.

Table 6: Composition details and naming convention for various Zr oxides samples

type	**name**	**oxide thickness (nm)**
pure Zr	Zr240	240
Zircaloy-4	Zry-4	700
Zr sponge	Z1	700
Zr-0.1% Cr	C1	700
Zr-0.2% Sn	S1	700
Zr-0.4% Sn	S2	700
Zr-0.2% Fe	F1	700

A representative dataset obtained in pH 10 LiOH in air atmosphere on Zr240 sample is presented in Figure 41. Alongside these measurements, we also performed open circuit potential measurements on these samples to evaluate the photovoltages obtained under the various electrolytic conditions.

A comparative bar chart of flatband potentials referenced to Ag/AgCl and RHE scales, obtained on the seven Zr samples is presented in Figure 42. As seen from the figure, the magnitude of V_{fb} varied in the order: C1 $\sim$ Z1$\sim$ S1 $>$ F1 $>$ Zr240 $>$ S2 $>$ Zry-4. The flat band potentials obtained for each individual sample over the range of alkaline conditions (pH 10-13) were found to be roughly constant, whereas a more positive V_{fb} was obtained under acidic conditions (pH 1). This trend is expected due to the pH dependence of the surface charge in transition metal oxides, but the precise magnitude of the shift did not exactly agree with the 59 mV per pH unit shift expected from the Nernst equation. Finally, for all samples, the addition of hole scavenger did not cause any appreciable change in the flatband potential, as was expected from Hankin et al. [308].

For all samples in all electrolytic conditions, the open circuit potential shifted negative upon illumination. Figure 43 presents a bar chart of the shift in open circuit potential upon illumination for the Zr samples. The photovoltage obtained for Zr240, Zry-4 and S2 samples

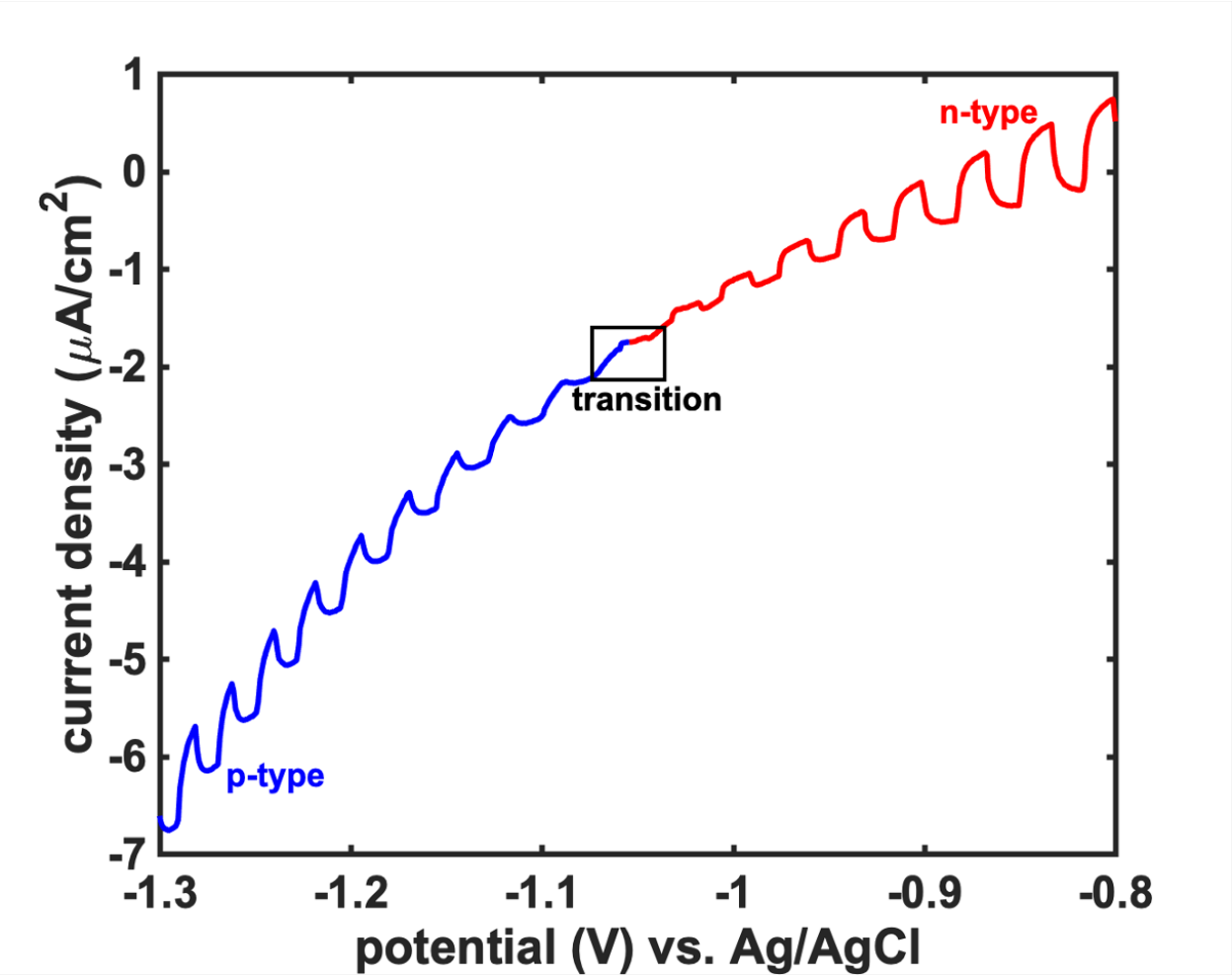

Figure 41: Transient photocurrent response in pH 10 LiOH saturated with air on pure Zr sample heat treated to obtain 240 nm of oxide thickness. (V_{fb} = -1.05 V vs. Ag/AgCl).

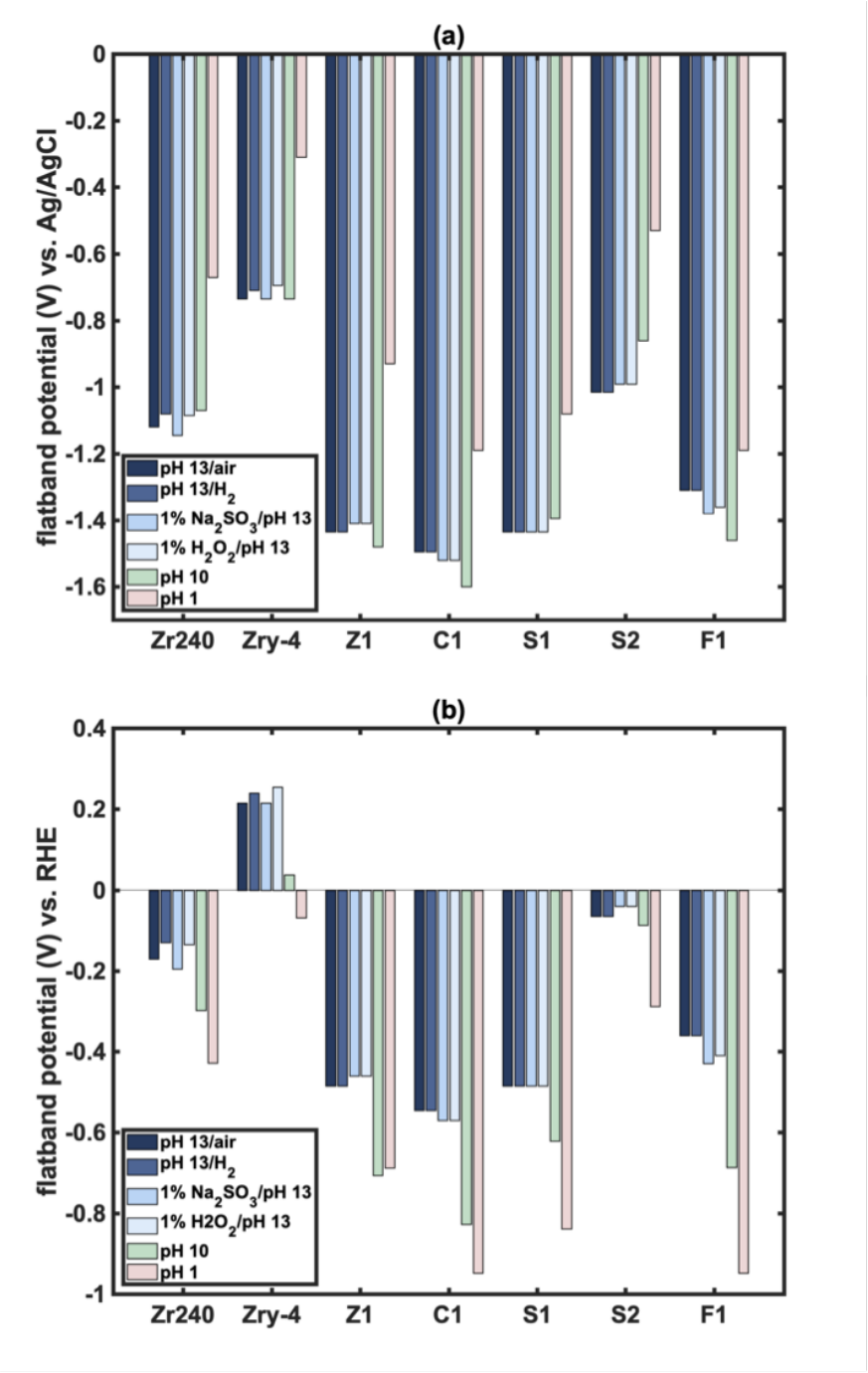

Figure 42: Bar chart presenting the flatband potentials referenced to (a) Ag/AgCl and (b)RHE scales obtained in various electrolytic conditions on different Zr samples [Zr240, Zircaloy-4 (Zry-4), Zr sponge (Z1), Zr-0.1%Cr (C1), Zr-0.2%Sn (S1), Zr-0.4%Sn (S2) and Zr-0.2%Fe (F1)].

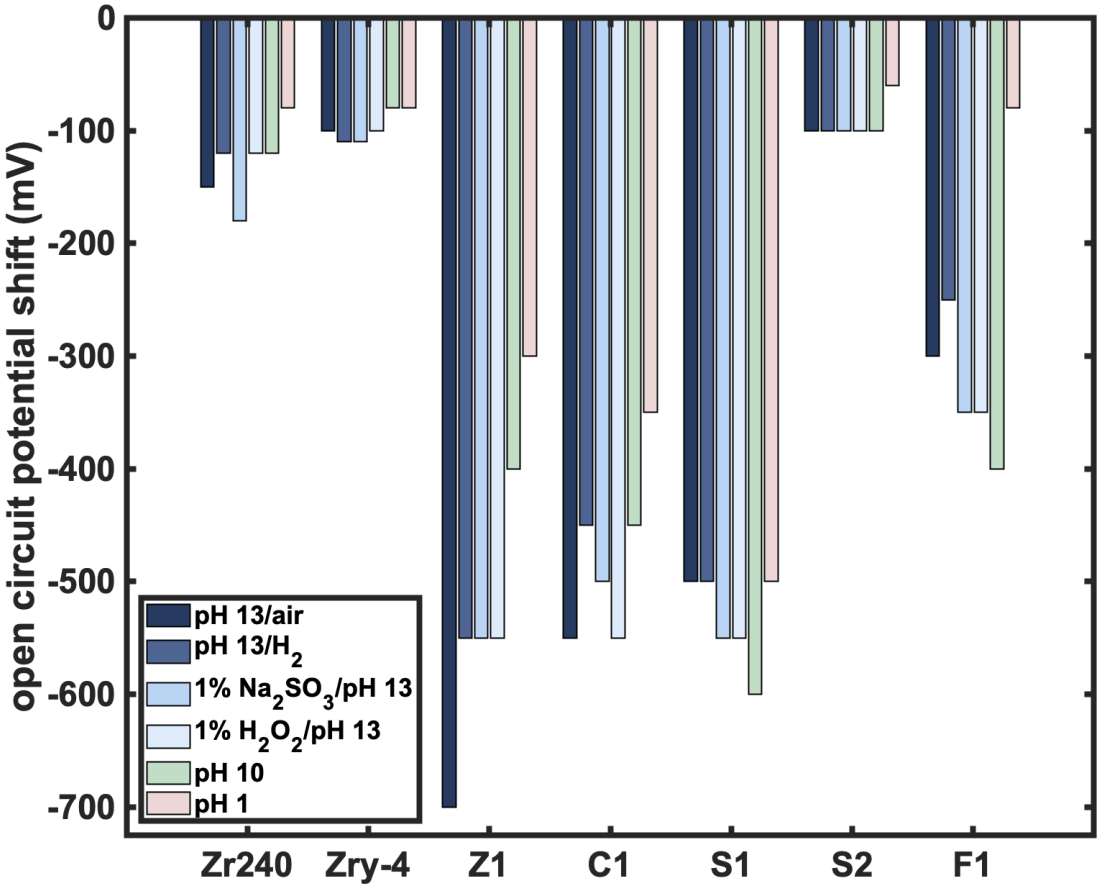

Figure 43: Bar chart presenting the open circuit potential shift obtained in various electrolytic conditions on different Zr samples [Zr240, Zircaloy-4 (Zry-4), Zr sponge (Z1), Zr-0.1%Cr (C1), Zr-0.2%Sn (S1), Zr-0.4%Sn (S2) and Zr-0.2%Fe (F1)].

was on the order of -150 mV whereas that for sample F1 was 2-3 times larger and that for samples Z1, C1 and S1 was 5-7 times larger. Moreover, we observed a smaller negative shift in OCP in pH 1 $HClO_4$ electrolyte upon illumination for all seven samples. We also observed that an addition of 0.1% Cr and 0.2% Sn does not cause a significant change in these metrics as compared to Zr sponge. However, addition of 0.2% Fe and 0.4% Sn lead to significantly smaller photovoltages. Additionally, Zry-4 results in the smallest photovoltages; as discussed previously, this conceptually agrees with the notion that the magnitude of the photovoltage scales inversely with corrosion resistance.

While knowing the value of V_{fb} is useful as a general indicator of the doping type of a semiconductor as well as the magnitude of its built-in potential in contact with a redox-active electrolyte, this value alone does not provide the necessary information to determine the electronically active doping density. Accordingly, we worked to estimate the n-type doping density (n) in our samples using the well-known relationships between n and the energetic difference between the conduction band edge and the Fermi level(Equation 3.2):

$$E_{CB} - E_F = kTln(\frac{n}{N_C}) \tag{3.2}$$

where E_F and E_{CB} are the energies of Fermi level and conduction bands in eV, k is the Boltzmann constant, T is temperature, and N_C is the effective density of states in the conduction band. Equation 3.2 can be rewritten as:

$$n = N_C \exp(\frac{E_{CB} - E_F}{kT}) \tag{3.3}$$

where the numerator in the exponential expressed on the right-hand side can be taken as the product of the difference between V_{fb} and the conduction band minimum on an electrochemical scale and the unsigned electronic charge, q, which converts from V to eV.

Prior literature reports indicate that E_{CB} for ZrO_2 on the electrochemical scale is approximately -1.1 V vs NHE (at pH 0) [309, 310]. This value can then be further inferred to be -1.1 V vs. RHE over the full range of pH values under the assumption that the band edge positions shift at 59 mV per pH unit, as has been clearly demonstrated for refractory oxides like TiO_2 over an extremely wide range of pH values [311]. The final unknown in

Equation 3.3 is N_C, the effective density of states in the conduction band. This value can be estimated from the electron effective mass, m_e using Equation 3.4:

$$N_C = 2(\frac{2\pi m_e kT}{h^2})^{2/3} \tag{3.4}$$

where m_e for ZrO_2 has been reported in the range from 0.6–2m_0 (where m_0 is the free electron mass) [312]. This gives the upper bound value of N_C for ZrO_2 as 10^{25} m^{-3} or 10^{19} cm^{-3}. Notably, doping densities exceeding this value would imply a degenerately doped semiconductor, which would be unlikely to exhibit significant photovoltage and photocurrent. Hence, n=10^{19} cm^{-3} can be treated as a rough upper bound of n-type doping density in photoactive Zr oxides, and this would require a V_{fb} value on the order of -1.1 V vs. RHE. In practice, V_{fb} values measured by the transient photocurrent method fell in the range from -0.7 to -1.6 V vs. Ag/AgCl in pH 13 electrolyte (See Figure 42 (a)), which corresponds to the range from 0.25 to -0.65 V vs. RHE. These results imply an electroactive dopant concentration far below N_C.

Note also that the intrinsic dopant density n_i obeys the following relation:

$$n_i = \sqrt{N_C N_V} exp(\frac{-E_g}{kT}) \tag{3.5}$$

where the very wide bandgap (E_g) of ZrO_2 ($\sim$5 eV) results in $n_i \sim 0$. Moreover, impurities would only be expected to result in electroactive n-type dopants if they introduce electronic states with energies that are near to the conduction band edge. Hence, it is plausible that many Zr-oxide passivation films exhibit extremely low electroactive dopant densities.

Figure 44 presents a comparison of calculated doping densities for the seven Zr samples. Because the conduction band energy obtained from the literature is referenced to only one value of pH and our measurements showed that V_{fb} does not vary linearly with pH, we cannot confidently extract one single doping density for these samples. Therefore, each horizontal line on the bar represents the doping density evaluated from the V_{fb} obtained in the different electrolytic conditions. Thus, the bars enclose the full range of apparent doping densities extracted from the available data.

Based on these results, the apparent doping density varies in the order: Z1 $\sim$ C1 $\sim$ S1 $\sim$ F1 $>$ Zr240 $>$ S2 $>$ Zry-4. A notable difference is observed with proportion of tin in

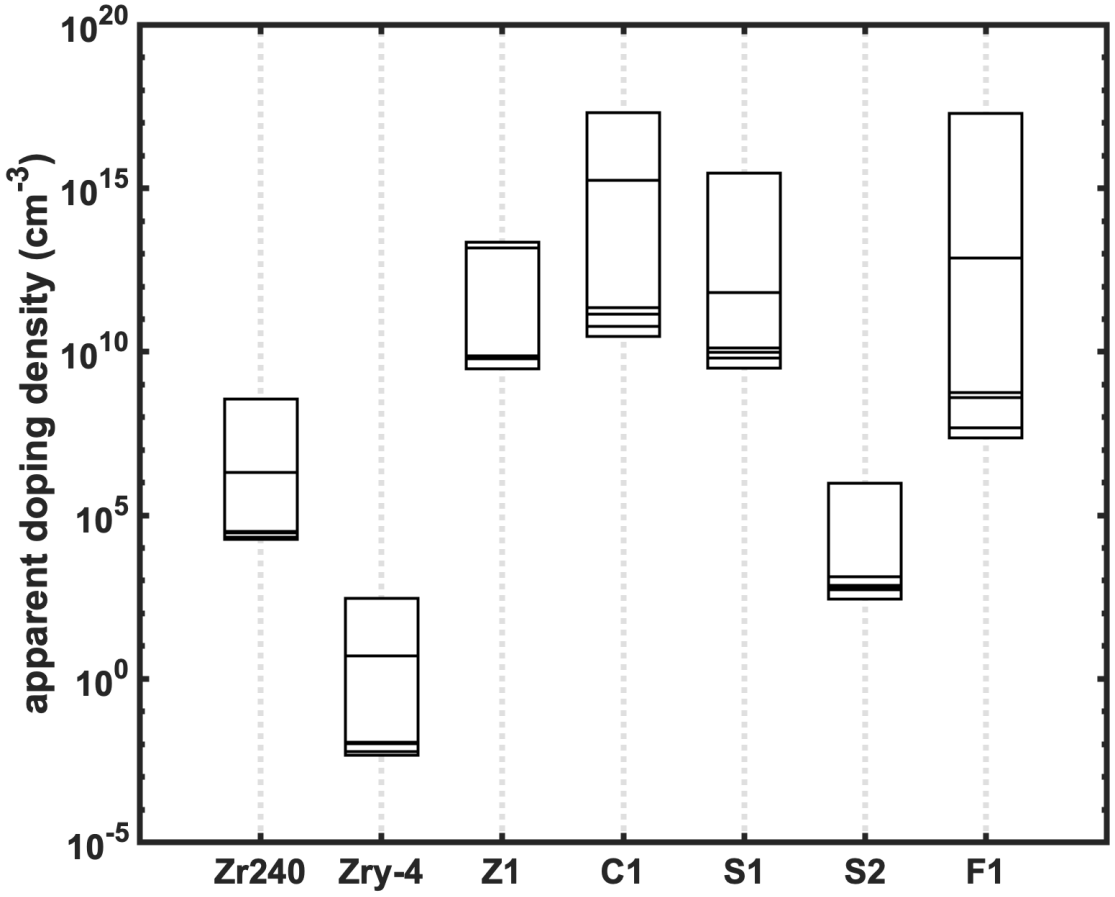

Figure 44: Plot depicting the doping density for various Zr samples [Zr240, Zircaloy-4 (Zry-4), Zr sponge (Z1), Zr-0.1%Cr (C1), Zr-0.2%Sn (S1), Zr-0.4%Sn (S2) and Zr-0.2%Fe (F1)].

the sample, where the apparent doping density decreases drastically as the Sn content is increased from 0.2 to 0.4%. Additionally, Zr240, S2 and Zry-4 samples exhibited V_{fb} values that are consistent with negligible apparent doping densities. We speculate that for Zr240 this may be attributable to the fact that we prepared the oxides by thermal oxidation in air, which may lead to a very low concentration of electronically active n-type dopants like oxygen vacancies, Zr interstitials, or H interstitials. By contrast, all other samples were prepared in autoclave environments under elevated temperature in aqueous electrolytes with an overpressure of H_2 (g).

The low value of n in Zry-4 is especially intriguing, since these samples were prepared under nominally similar "pre-filming" conditions as Z1 samples. Hence, we postulate that alloying elements (particularly Fe and high proportions of Sn) may in fact introduce a high degree of n-type dopant compensation. This would be expected to decrease the magnitude of the photoresponse by (a) decreasing the magnitude of the built-in potential, and (b) introducing a high density of recombination centers. This effect is similar to what we observed for the "high-tin" alloy S2, which is unsurprising considering that Zry-4 contains 1.2 to 1.7% Sn. These results also have significant implications for Mott-Schottky analysis, because essentially undoped semiconductors would not be expected to exhibit the type of well-defined depletion behavior that is required for the Mott-Schottky model.

Finally, we can correlate flatband potential, doping density and photovoltages as a function of the alloying elements. Figure 45 shows a representative correlation plot in air saturated pH 13 LiOH electrolyte. These results clearly demonstrate that increasing photovoltage can be correlated to a more negative flatband potential and a higher doping density. All of these are indicative of n-type semiconducting materials. Future work in this area should be directed at experimentally evaluating the conduction band edge position as a function of pH of the electrolyte. This will help in elucidating accurate doping densities for various alloys across a range of pH conditions as well as in understanding the effect of alloying elements on the band energetics of Zr.

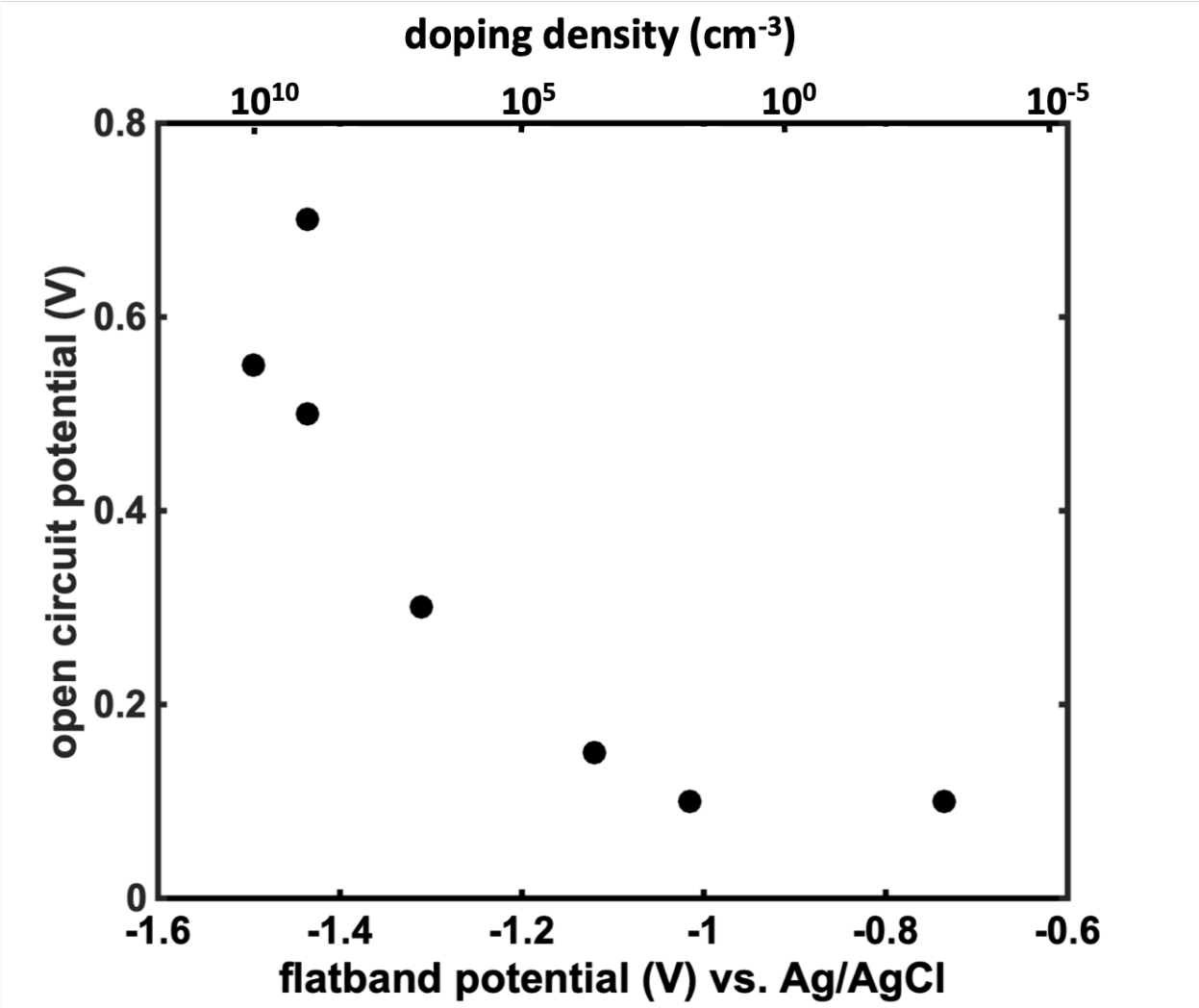

Figure 45: Representative plot depicting the correlation between flatband potential, doping density and photovoltages obtained in air saturated pH 13 LiOH electrolyte.

3.3 Conditions of Oxide Growth/Dissolution

To further probe the stability of Zr-based passivating oxides, we undertook experiments directed at identifying conditions under which Zircaloy oxide dissolution/growth is accelerated using benchtop electroanalytical tools. Specifically, we attempted to deliberately induce oxide dissolution using various chemical reagents under the expectation that these dissolution processes may then be accelerated or inhibited with high intensity illumination. We hypothesized that the passivating oxide could be dissolved (Reaction R3) and redeposited (Reaction R4) via the following the following mechanism:

$$ZrO_2 + 4\,h^+ \longrightarrow Zr^{4+} + O_2 \tag{R3}$$

$$Zr^{4+} + 4\,OH^- \longrightarrow Zr(OH)_4 \longrightarrow ZrO_2 + 2\,H_2O \tag{R4}$$

where h^+ refers to an oxidizing equivalent and Zr^{4+} represents soluble Zr species. Based on this mechanism, strong chemical oxidants or reagents that stabilize the Zr^{4+} cation would accelerate reaction (2), thereby increasing the rate of dissolution and ultimately leading to significant restructuring of the passivating oxide.

3.3.1 Efforts to Induce Oxide Growth/Dissolution under Lab-scale Conditions

Our initial efforts to induce oxide restructuring were based on using chemical reagents to accelerate the process of oxide dissolution. These experiments involved incubating pre-oxidized Zr and Zircaloy samples in strong acid (1 M nitric acid) and base (5 M potassium hydroxide). We expected these conditions to accelerate the dissolution of the passivating oxide by stabilizing the Zr^{4+} cation under highly acidic and alkaline conditions [313]. We then used scanning electron microscopy to assess changes in the oxide structure. However, preliminary experiments resulted in essentially unchanged morphology of Zr oxide for an oxide thickness of 240 nm over several weeks with the use of strong acids and bases.

We then evaluated the effect of illumination on pure Zr oxide sample (240 nm oxide thickness) by subjecting it to 48 hours of UVC illumination in DI water. Representative

SEM micrographs are shown in Figure 46. As seen from the figure, an increase in roughness of the sample was obtained upon illumination. However, the results obtained over multiple reproductions of the same experiment were inconsistent. Upon careful review of these results, we concluded that the only unambiguous morphology changes that resulted in increase in sample roughness were obtained when the sample was placed in a teflon (perfluorinated ethylene) experimental apparatus (as shown in Figure 36). Additionally, EDS analysis suggested the presence of fluoride based contamination on the sample surface. This led us to hypothesize that solution-based impurities occurring from UV induced degradation of the cell housing were likely responsible for the observed morphology changes. For instance, UV-based degradation of Teflon may release fluoride ions, which could go on to induce or accelerate oxide (photo)etching via transient formation of highly corrosive hydrofluoric acid, HF(aq) [314].

To that end, we developed a new, simplified experimental apparatus to minimize contamination in the system. Figure 47 shows a schematic and photograph of this setup, in which the only wetted components are composed of fused silica (quartz) glass. We then deliberately introduced a fluoride-containing electrolyte—100 ppm LiF in DI water—and subjected a pure Zr (with a 240 nm oxide) sample to 48 hours of UV illumination. Figure 48 shows representative SEM micrographs of this sample. Indeed, addition of fluoride-based impurities resulted in an increase in the roughness of the sample, which is further evidence that prior results of oxide morphology changes were attributable to contamination associated with the fluoropolymer housing. All subsequent studies were therefore executed using the "all-quartz" apparatus without added LiF.

We then evaluated the effect of illumination on morphology of the oxide using reactor relevant pH 10 LiOH electrolyte. To maintain charge neutrality, electrons generally migrate from one Zr to other, leading to a change in oxidation state of Zr. They can also lead to the formation of hydrogen and subsequent absorption of hydrogen in the Zr oxide layers. Thus, electron migration and/or hydrogen evolution/absorption form the cathodic half-cell reactions on these metal oxides [315]. As noted above, the primary faradaic photo-anodic reaction in LiOH electrolytes is likely to be oxygen evolution occurring from photogenerated holes. In principle, this reaction may accelerate the corrosion of Zr and Zircaloys indirectly

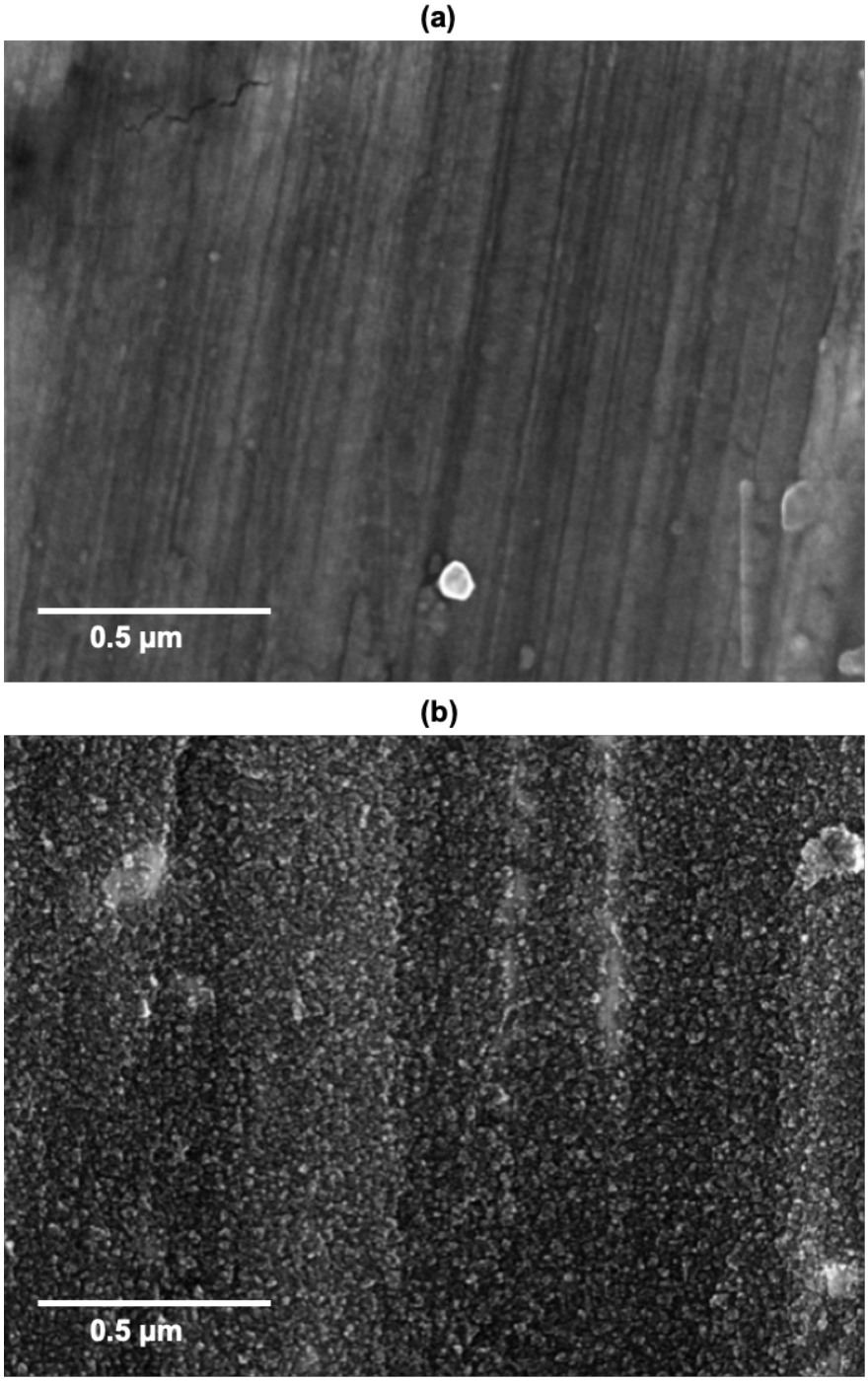

Figure 46: SEM micrographs of Zr samples with 240 nm of oxide thickness subjected to 48 hours of UV illumination in DI water; (a) non-illuminated region, (b) illuminated region of the sample.

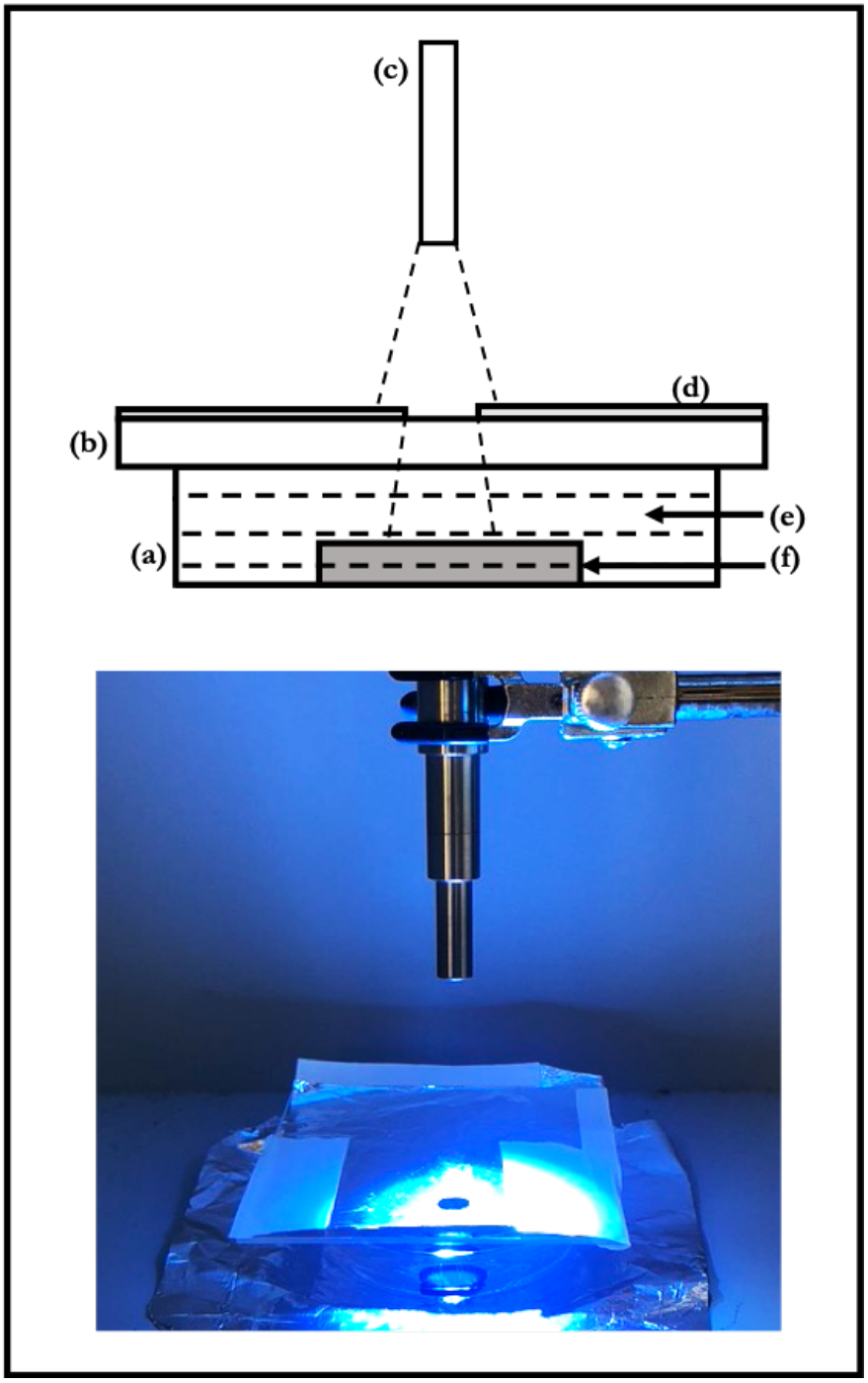

Figure 47: Schematic (top) and photograph (bottom) of the 'all quartz' experimental setup. Components labeled in the schematic are as follows: (a) quartz petri dish, (b) quartz plate, (c) light guide, (d) aluminum foil, (e) electrolyte and (f) sample.

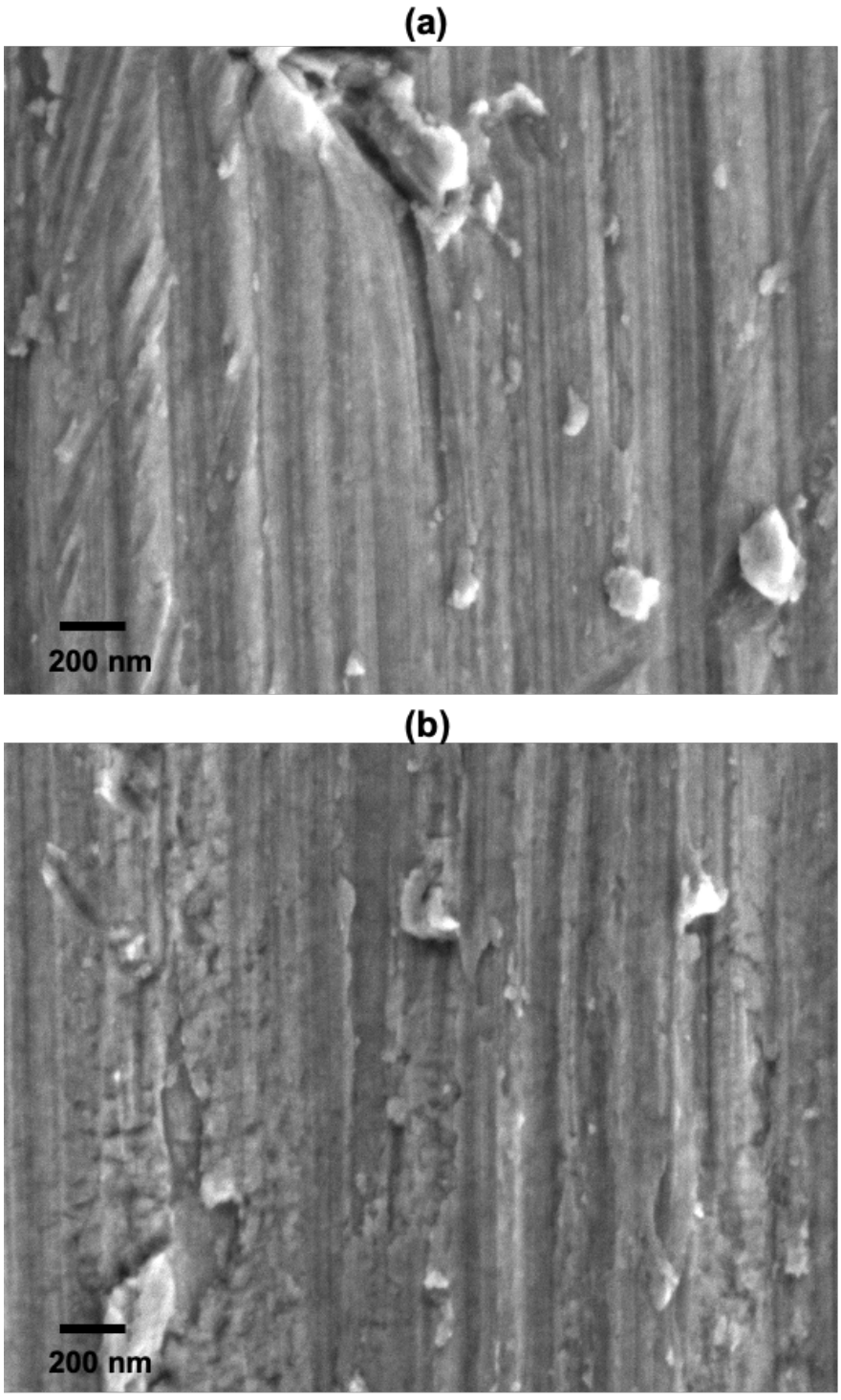

Figure 48: SEM micrographs of Zr samples with 240 nm of oxide thickness subjected to 48 hours of UV illumination in 100 ppm LiF in DI water; (a) non-illuminated region, (b) illuminated region of the sample.

by decreasing the local pH in the near vicinity of the oxide surface, thereby inducing transient dissolution or gellation of the passivation layer. We further evaluated, using a simple transport model over a range of current densities, that a pH change of roughly several units can result from water oxidation of an unbuffered pH 10 LiOH solution at current densities of a few tens of $\mu A/cm^2$ (See Figure 49). Nonetheless, Zr oxides are known to be highly refractory over a broad range of pH and applied potential, and the aforementioned measurements involving strong acid treatments further suggest that dissolution does not proceed at an appreciable rate due to decreased pH alone. We again independently confirmed this by exposing thermally oxidized Zr—ZrO_x samples to aqueous solutions containing pH 4 $HClO_4$ under illumination, and we found no evidence for oxide dissolution observable by SEM. Representative SEM micrographs are presented in Figure 50. We also observed no evidence by SEM for oxide dissolution as a result of UV illumination for extended periods in air-saturated DI water (pH ∼5.5), which we would also expect to be more corrosive than LiOH(aq) at pH 10 (See Figure 51).

Another possible source of photo-induced oxide destabilization is not driven by pH but instead involves direct photoanodic dissolution of the oxide itself via so-called oxygen redox reactions of the form shown in Reaction R3. The hallmark of these reactions is oxidative Zr−O bond breaking, which would likely proceed primarily at the reactive dangling bonds on the oxide surface. This type of reactivity is also broadly consistent with the initial formation of hydoxyl radicals at the surface of wide-bandgap photoanodes like TiO_2, which is well precedented in the prior research literature [316, 317]. Moreover, this type of surface bond breaking was previously reported as the physical basis of decreased water contact angle (WCA) on TiO_2 crystal surfaces upon extended UV illumination. Thus, we set out to determine whether similar WCA changes occur in Zr—ZrO_x passivating oxides.

Figure 52 depicts the results of a set of time-dependent WCA measurements on Zr—ZrO_x samples that were incubated in DI water for 24 hrs with and without UV illumination. The initial contact angle for a clean sample was ∼20° in all cases. This rather small value is consistent with the high degree of hydrophilicty expected of a clean transition metal oxide. Upon UV illumination, we found that the contact angle dropped to 7° over a period of 1 hour and remained relatively constant between 6 and 9° over the remaining 23 hrs of illumination.

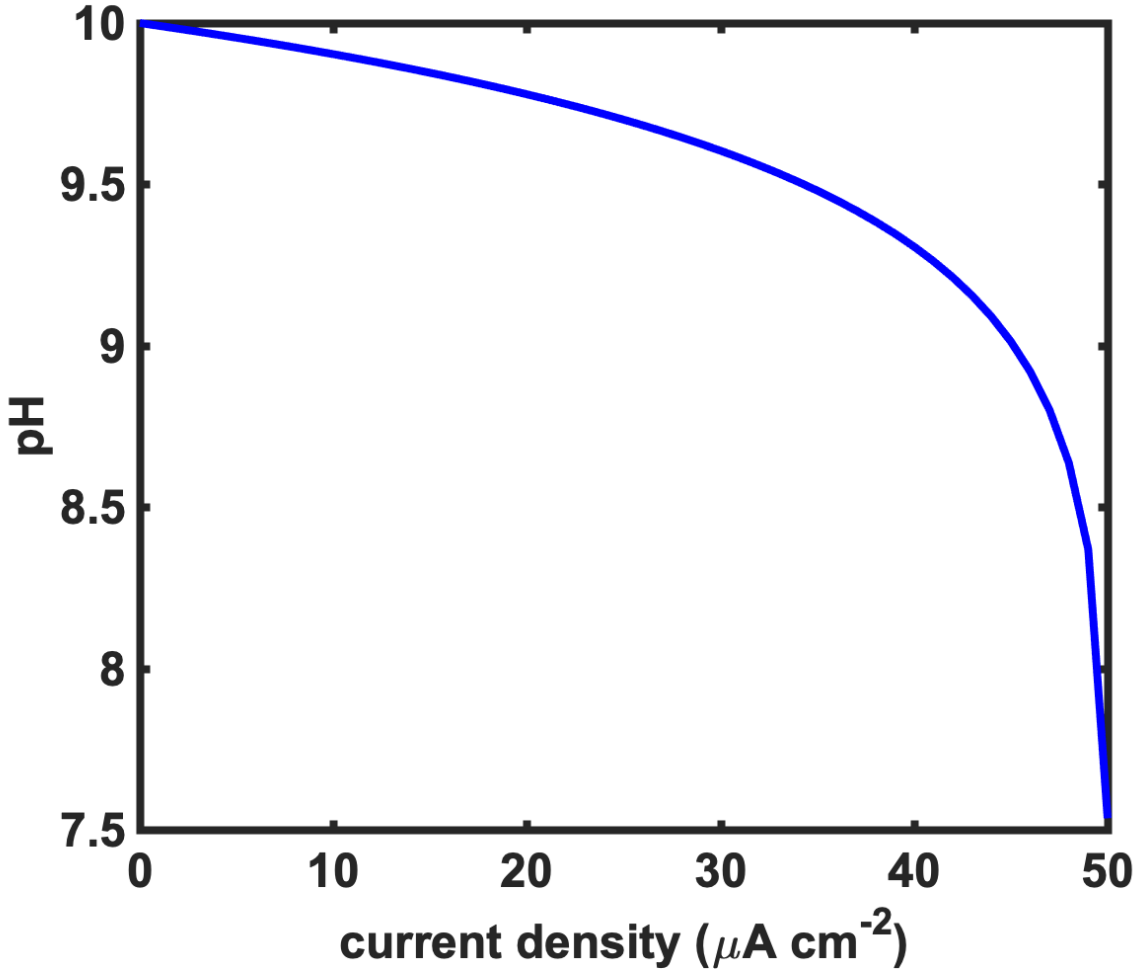

Figure 49: Simulated pH as a function of current density for water oxidation reaction occurring on the surface of Zr oxide sample. Bulk electrolyte was assumed to be 10^{-4} M and the diffusion boundary layer thickness was set to 100 μm.

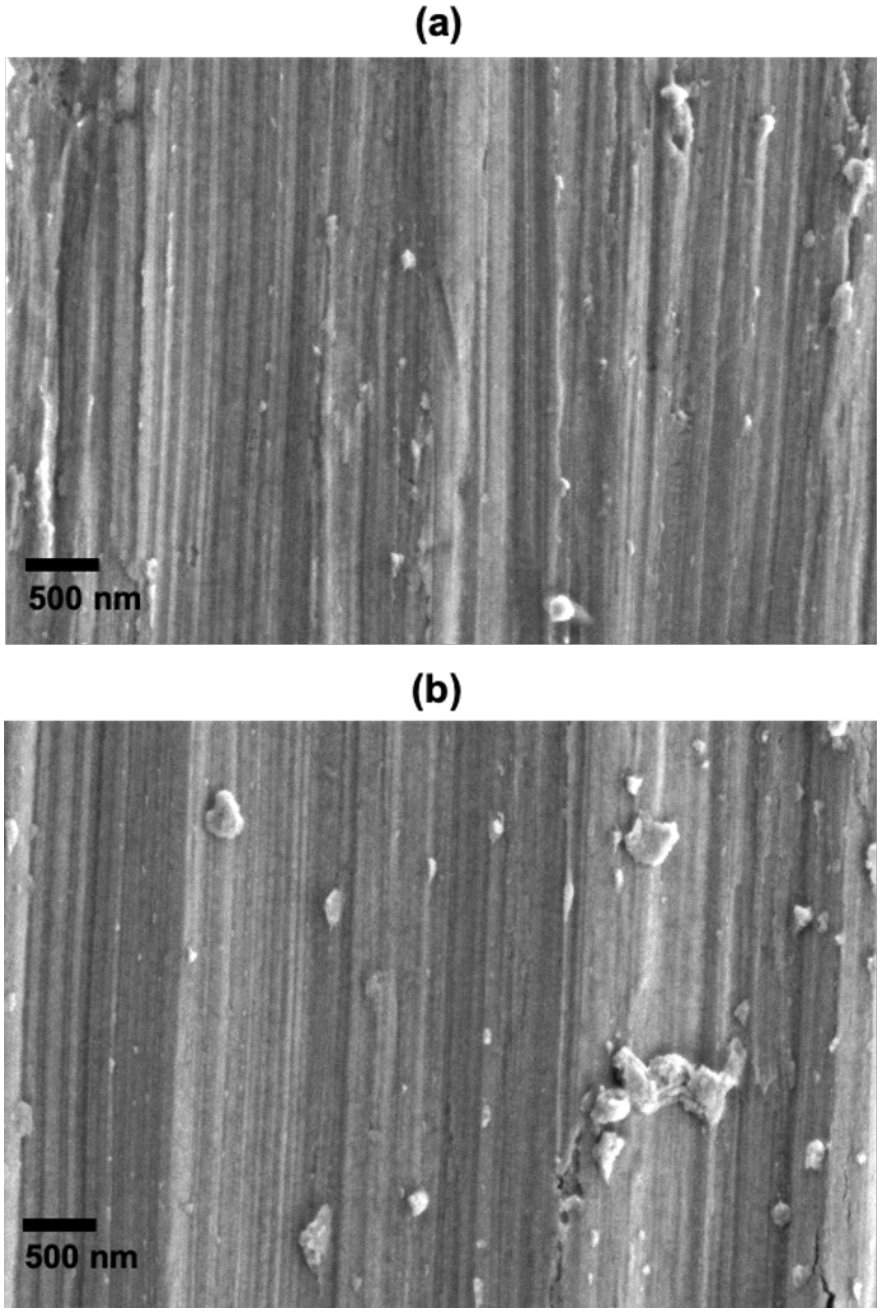

Figure 50: SEM micrographs of Zr samples with 240 nm of oxide thickness subjected to 24 hours of UV illumination in pH 4 $HClO_4$ electrolyte; (a) non-illuminated region, (b) illuminated region of the sample.

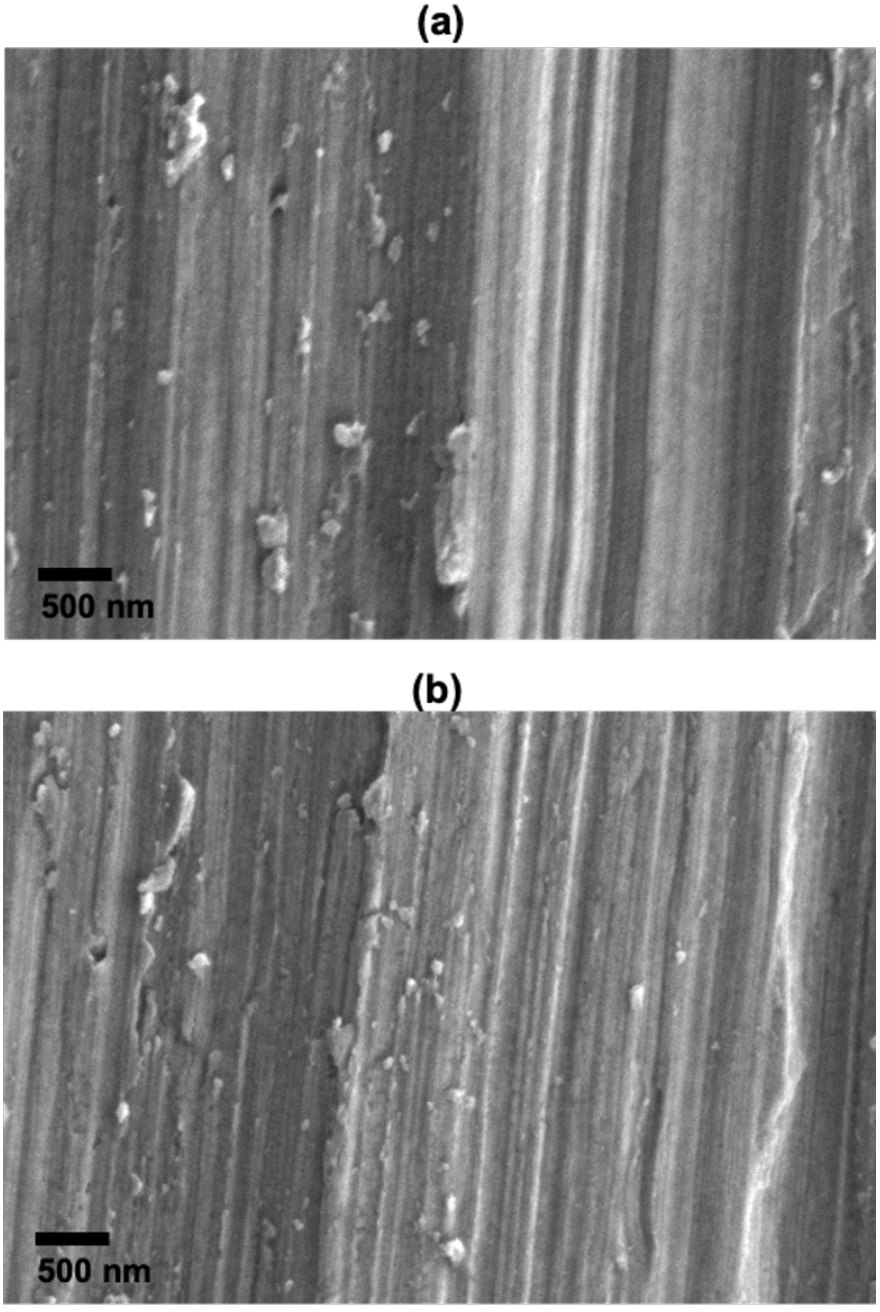

Figure 51: SEM micrographs of Zr samples with 240 nm of oxide thickness subjected to 24 hours of UV illumination in DI water; (a) non-illuminated region, (b) illuminated region of the sample.

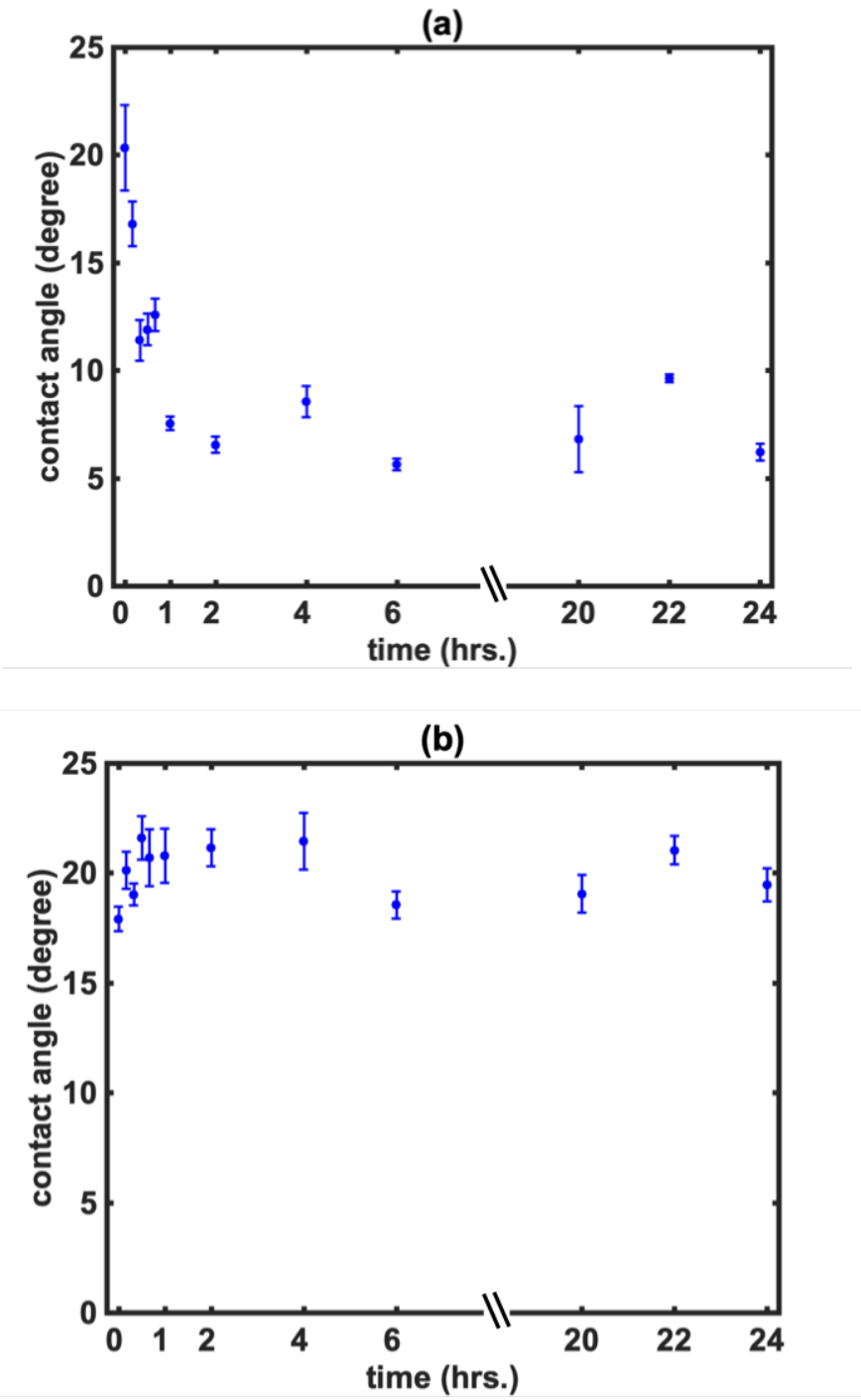

Figure 52: Plot of contact angle vs. time for pure Zr sample in DI water under (a) illuminated and (b) non-illuminated conditions. Error bars are reported at 95% confidence interval over a set of 6 measurements at each time point.

Control experiments under the same conditions but in the absence of illumination show that the contact angle instead remained constant at ∼20°. Thus, we conclude that UV illumination indeed results in a change in the wetting properties of Zr oxide. Moreover, SEM imaging of representative samples prior and after UV illumination (See Figure 51) showed no discernible change in oxide morphology, which means changes in contact angle is unlikely to result from an increase in surface roughness.

Similar results were observed on autoclave-passivated Zircaloy-4 samples with 700 nm of oxide thickness, where the WCA decreased by ∼45° under illumination and remained roughly constant under dark conditions without a discernible change in surface morphology. Representative data on Zry-4 sample are shown in Figure 53. These results are strikingly similar to prior work on crystalline Ti oxides, which were also found to become more hydrophilic upon above-bandgap illumination in aqueous environments [316]. In those studies, the proposed mechanism involved oxidative removal of O_2 from the TiO_2 lattice, followed by water hydrolysis to generate two new hydroxyl groups that increased the net hydrophilicity of the sample. Dehydration of adjacent surface hydroxyls over time ultimately regenerates the stable surface termination (as shown in Figure 54) whereupon the sample recovers its initial WCA. This reaction mechanism corresponds to net photoanodic water oxidation via a Mars Van Krevelen type mechanism.

Based on the results described above, and by analogy to the well-established physics and chemistry of transition metal oxide photoanodes, Figure 55 depicts a postulated band energy diagram for Zr—ZrO_x under illumination with above-bandgap photons [318]. Bandgap excitation results in the generation of minority carriers (holes) that can engage in at least four different processes. First, holes can recombine with electrons in the bulk or on the surface of the oxide via radiative or nonradiative pathways. Second, holes can oxidize water to evolve $O_{2(g)}$ along with a concomitant reduction reaction (e.g., hydrogen evolution, oxygen reduction) at a proximal location on the oxide surface. Third, charge carriers can fill long-lived shallow trap states, where holes can be trapped at terminal Zr-OH or Zr-O-Zr sites (Reactions R5 and R6) and electrons can be trapped at defective sites (ds) of Zr^{4+} (Reaction R7) [319].

$$\mathrm{Zr{-}OH} + \mathrm{h^+} \longrightarrow \mathrm{Zr{-}OH^+} \tag{R5}$$

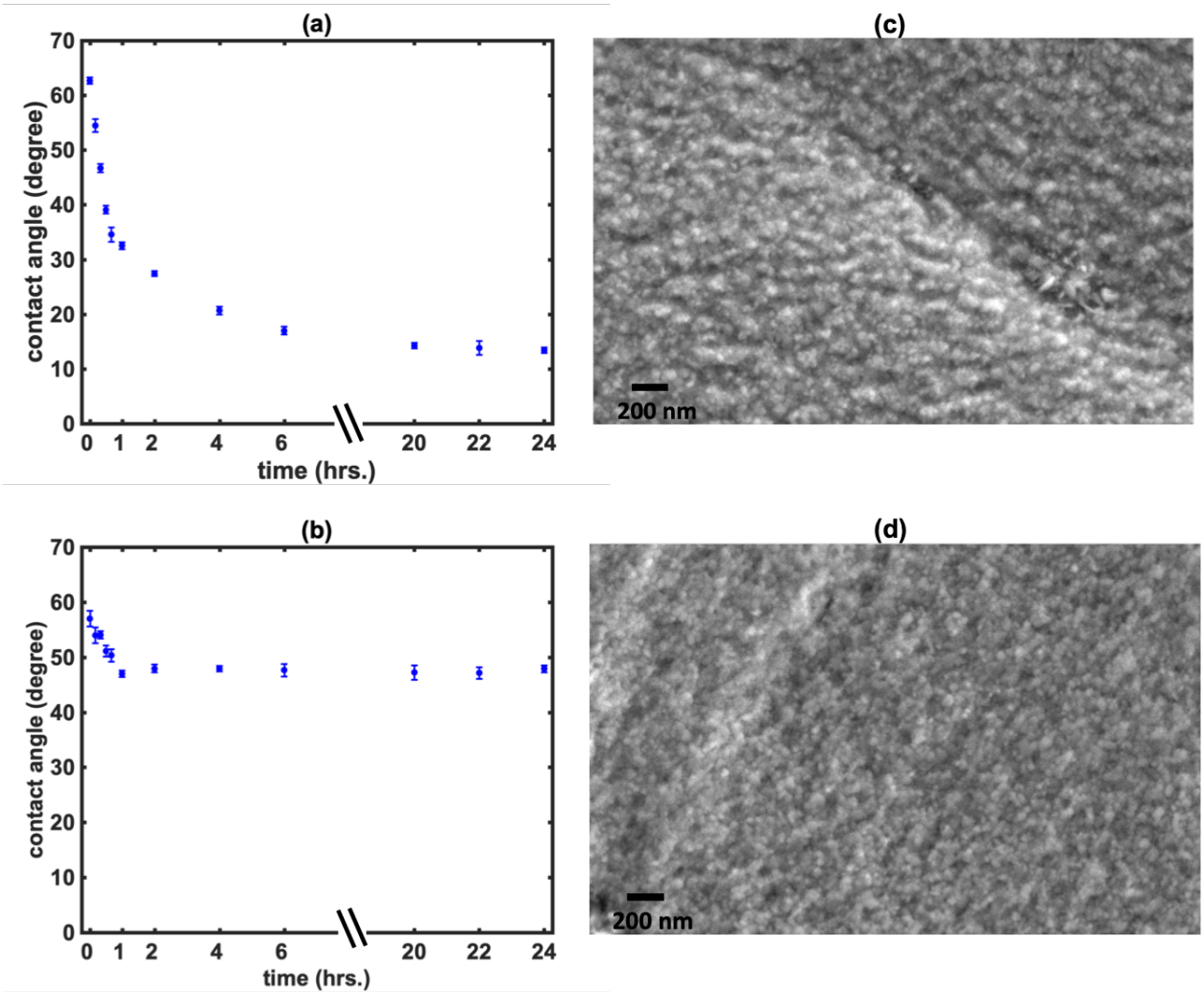

Figure 53: Plot of contact angle vs. time for Zry-4 sample in DI water under (a) illuminated and (b) non-illuminated conditions. Error bars are reported at 95% confidence interval over a set of 6 measurements at each time point; SEM micrographs of Zry-4 subjected to 24 hours in DI water under (c) illuminated and (d) non-illuminated conditions.

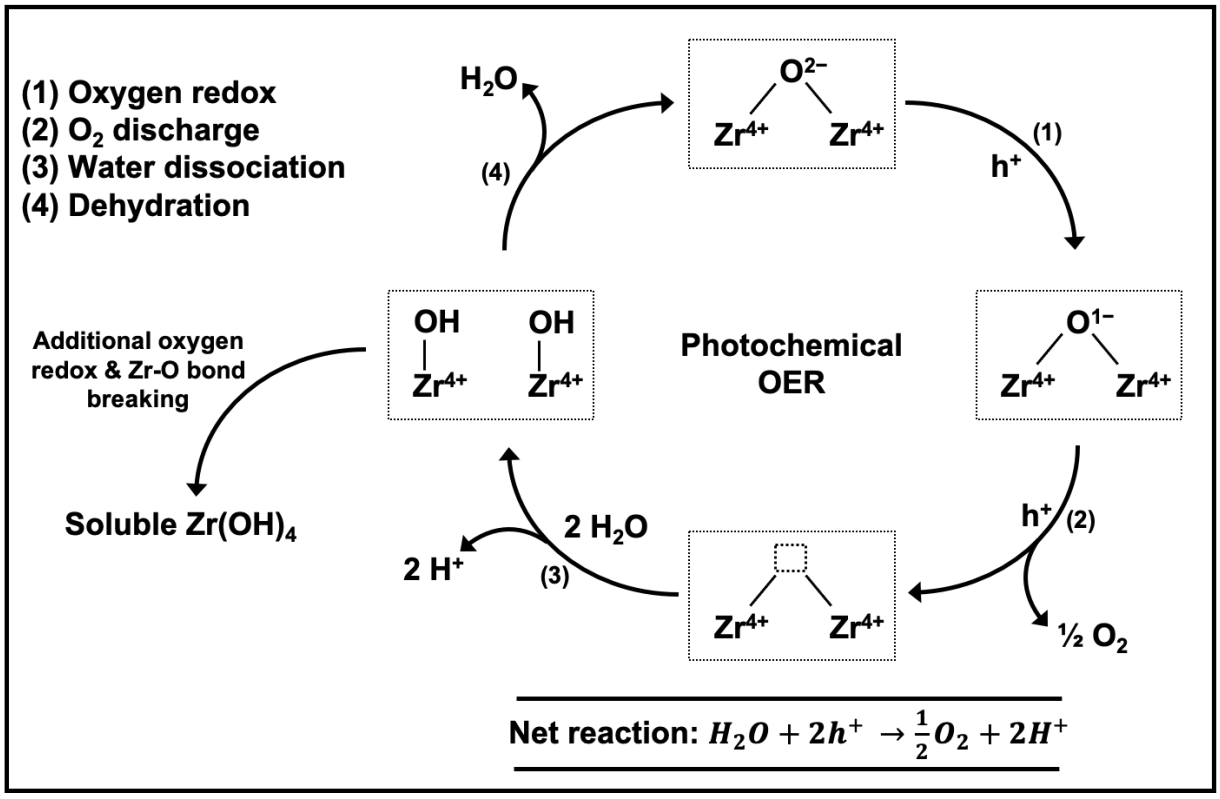

Figure 54: Schematic representation of the metal-oxide bond breaking process occurring on the surface of the oxide.

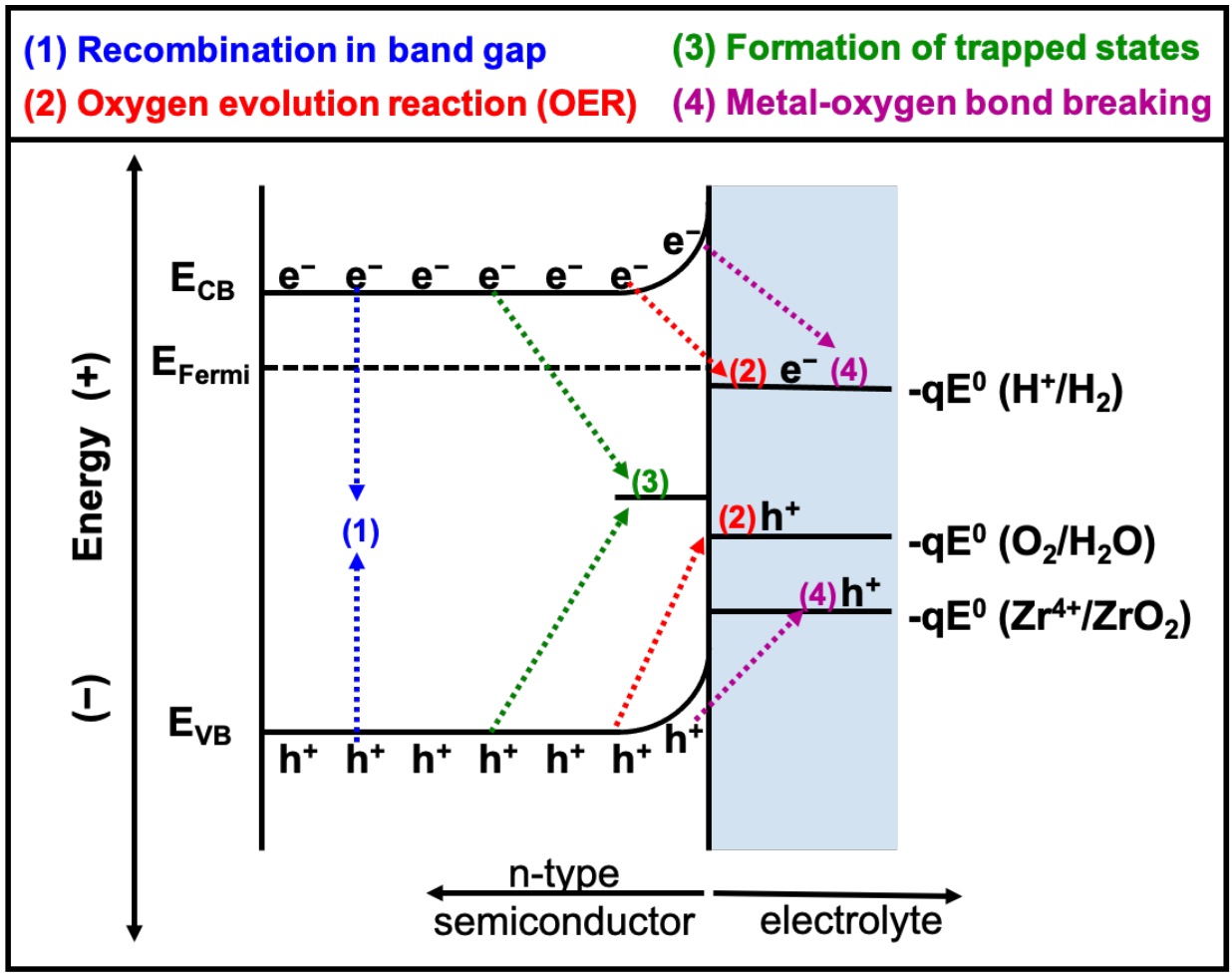

Figure 55: Schematic representation of postulated photo-chemical processes under open-circuit conditions in n-type Zr oxide.

$$Zr{-}O{-}Zr + h^{+} \longrightarrow ZrO^{+}{-}Zr \tag{R6}$$

$$Zr_{ds}{}^{4+} + e^{-} \longrightarrow Zr_{ds}{}^{3+} \tag{R7}$$

And lastly, holes can act as oxidizing equivalents that accumulate on surface O atoms and ultimately break metal-oxygen bonds. Each of these photochemical processes would be expected to proceed in parallel with the net oxidation of the underlying Zr by water in the reactor coolant.

We further postulate that there are three possible pathways for dissolution/restructuring in ZrO_x: (1) Zr^{4+} dissolves and remains in solution, (2) Zr^{4+} dissolves, diffuses and reprecipitates in a new location and (3) Zr-oxygen bonds break and instantaneously form Zr hydroxides in the same location. While all three mechanisms could result in an increase in sample hydrophilicity (via an increase in surface roughness and/or density of surface hydroxyl groups), only the formation of soluble oxide species would result in a morphology change that is observable through SEM. Thus, we tentatively attribute our observations of increase in hydrophilicity without a change in oxide morphology to bond breaking and near-instantaneous formation of Zr hydroxide at the same location. These results lead us to believe that Zr-O bond breaking represents a minor contribution to the overall interfacial oxidative photocurrent. However, currents as low as tens of nA/cm^2 would be sufficient to dissolve a few nm of fully dense Zr oxide over a timescale of hours. Notably this reaction rate is three orders of magnitude lower than the oxidative photocurrents we observed in illumination studies, implying that even if only a minute fraction of the holes captured at the ZrO_x surface resulted in *irreversible* $Zr{-}O$ bond breaking, this would be sufficient to significantly erode the barrier layer over technologically relevant timescales. Furthermore, irreversible oxide dissolution would not be necessary to destabilize the Zr-oxide passivation layer; even transient dissolution followed by redeposition (e.g., of hydrous Zr oxides) could result in increased porosity and reduced passivity of the barrier oxide. Hence, we argue that the processes discussed above, and directly evidenced by our photoelectrochemical and WCA measurements, provide a plausible mechanistic rationale for reduced Zr-oxide passivity in nuclear reactors. Future work in this effort should be directed at evaluating the effect

of increased temperature and pressure alongside illumination on the dissolution/growth dynamics of Zr oxides. Further efforts should then be targeted towards quantifying the rate of oxide growth/dissolution under illumination. Finally, the effect of illumination on various oxide thicknesses, dopant types and concentrations should be studied in the pursuit of developing more corrosion resistant alloys.

3.4 Summary, Impact and Recommended Future Work

In summary, this dissertation chapter presented the body of work I undertook to improve our understanding of the degradation mechanisms of Zr and Zircaloy oxides under high energy radiation. It was divided into two broad topics of understanding the implications of photoelectrochemical behavior of Zr alloys on corrosion performance and evaluating the conditions of oxide growth/dissolution on a laboratory scale. Successful completion of this work has led to the development of key insights into the importance of photoelectrochemistry in dictating the long-term stability of nuclear reactors. Our work also resulted in the development of a new mechanistic understanding of the dynamics of Zircaloy corrosion which can be used to predict the maintenance requirements for current generation alloy materials. Additionally, our results can be used to direct the development of better corrosion resistant materials by increasing the proportion of Fe and Sn in the alloys and/or by introducing a readily oxidizable/reducible redox couple to decrease the probability of hole transfer to the surface and thus improve corrosion performance. Overall future work in this area should be targeted towards developing quantitative rate laws for oxide growth/dissolution as a function of various alloying elements to design the next generation of Zircaloy cladding with increased lifetimes.

4.0 Summary and Conclusions

The last four years marked the beginning of my efforts in contributing to the development of a sustainable energy future. These efforts were directed at making progress in the field of two carbon-free energy technologies that can store and produce clean energy. The first involved improving large-scale energy storage by understanding electrocatalysis in redox flow batteries and the second involved developing corrosion resistant cladding materials for nuclear reactors.

In the field of RFBs, our work has resulted in the development of novel electroanalytical tools for characterization of interfacial electron-transfer kinetics that bridge the gap between lab-scale and practical RFB conditions. Additionally, it has facilitated the design of highly catalytic carbon electrodes for use in commercial devices. In the nuclear energy domain, our work has demonstrated the role of photoelectrochemistry in influencing the corrosion performance of Zr oxides and has greatly increased our understanding of Zircaloy corrosion under the unique conditions of nuclear fission. It has further allowed us to develop strategies to improve corrosion performance of Zr and Zircaloy oxides under reactor relevant conditions.

Overall, our work has demonstrated the importance of considering technologically relevant conditions when developing characterization tools to enable direct translation of obtained results to practical RFB systems. It has further motivated the need to understand electrocatalysis to design efficient and cost-effective materials for RFBs. It has also provided considerable impetus to develop more corrosion resistant alloys for use as cladding materials in nuclear reactors, thus advancing the path toward a carbon-free energy supply.

I hope this work serves as a valuable resource to enable further advancements in the field of redox flow batteries to develop novel electrocatalysts that can be adapted into commercial RFB systems and to drive the development of next-generation alloy materials for nuclear reactors. I am eager to see what the future looks like for these two research fields.

Appendix A Electrocatalysis in Redox Flow Batteries

A.1 Simulation Details for Figure 9

The simulations in Figure 9 were performed using the MATLAB software suite to solve a series of coupled algebraic equations accounting for overpotential contributions associated with reaction kinetics, series resistance, and mass transfer. We simulated the charge-discharge performance of a prototypical vanadium redox flow battery at 50% state of charge–Figure 9 (a)–using the parameters tabulated in Table 7. The total overpotential of the system was calculated as the sum of the overpotentials due to kinetics, electrical resistance, and mass transport losses. These losses were calculated using the Butler-Volmer equation for kinetics (Equation A.1), ohms law for resistance (Equation A.2) and concentration overpotential for mass transport (Equation A.3):

$$i = i_0 \left[c_{\text{ox}} \exp\left(\frac{(1-\alpha) n F \eta_k}{RT} \right) - c_{\text{red}} \exp\left(\frac{-\alpha n F \eta_k}{RT} \right) \right] \tag{A.1}$$

$$\eta_r = i \times \mathcal{R} \tag{A.2}$$

$$\eta_t = \frac{RT}{nF} \ln \frac{i_L}{i - i_L} \tag{A.3}$$

where i is the current; i_0 is the exchange current; c_{ox} and c_{red} are the concentrations of the species to be oxidized and to be reduced, respectively; α is the symmetry factor; n is the number of electrons transferred; F is Faraday's constant; R is the universal gas constant; T is temperature, $\mathcal{R}$ is the potential-independent series resistance; i_L is the limiting current; η_k is overpotential associated with kinetics; η_r is overpotential associated with resistance; and η_t is overpotential associated with transport in the system.

Figure 9 (b) depicts polarization curves—current density vs. potential—simulated over a range of heterogeneous electron-transfer rate constants between 10^{-2} cm/s and 10^{-6} cm/s. All other parameters used to obtain the polarization curves were the same as reported in

Table 7: Parameters used for simulating the effect of electron-transfer kinetics on voltage and coulombic efficiencies, Figures 9 and 10 respectively.

Parameter	**Notation**	**Value**	**Units**
Theoretical voltage	Vth	1.26	V
Universal gas constant	R	8.314	J/mol K
Temperature	T	298	K
Number of electrons transferred	n	1	
Symmetry factor	alpha	0.5	
Faraday's constant	F	96485	C/mol
Area specific resistance	ASR	0.65	Ωcm^2
Concentration	c	1	molar
State of charge	SOC	50	%
Limiting current density	jL	500	mA/cm^2
Area	Area	5	cm^2
Intrinsic reaction rate constant	k0	10^{-4}	cm/s

Table 7. We further simulated the voltage efficiency as a function of power density—shown in Figure 9 (c)–with heterogeneous electron-transfer rate constants ranging from 10^{-2} cm/s to 10^{-6} cm/s. To do so, we first simulated the charge-discharge performance of the battery as shown in Figure 9 (a). We then obtained the discharge power density of the system by finding the product of discharge voltage and the associated current density. The voltage efficiency of the system was then calculated as the ratio of the discharge voltage to the charge voltage, $\frac{V_{discharge}}{V_{charge}}$ at that current density. Voltage efficiency was then plotted as a function of power density. This procedure was repeated for each of the simulated rate constants and again after removing the kinetic contributions entirely (by eliminating the kinetic overpotential term) as well as the contributions from kinetics and series resistance (by eliminating both of these terms) to obtain the associated data.

A.2 Simulation Details for Figure 10

We simulated steady-state polarization curves for the electron-transfer reactions shown in Figure 10 (a) using a simplifying approximation that treats the coulombic efficiency (CE) for a full charge-discharge cycle as equal to the value that is simulated (using steady-state current/voltage calculations) at 50% state of charge at a fixed operating current density (50 mA/cm^2 in this case). We then iteratively decreased the capacity of the cell by an amount equal to $1 - CE$, which is the fraction of the current attributable to the parasitic "over-oxidation" process. This is accomplished with the following mathematical relationships:

$$CE_{\mathrm{n}} = \frac{J_{\mathrm{ox1,n}}}{J_{\mathrm{tot,n}}} \tag{A.4}$$

$$C_{\mathrm{tot,n+1}} = CE_{\mathrm{n}} \cdot C_{\mathrm{tot,n}} \tag{A.5}$$

$$C_{\mathrm{ox,n}} = C_{\mathrm{red,n}} = 0.5 C_{\mathrm{tot,n}} \tag{A.6}$$

where n is an index that refers to the cycle number; J_{ox1} is the partial current density of the desired oxidation reaction; J_{tot} is the total current density; C_{tot} is the total concentration of the redox couple in the electrolyte; and C_{ox} and C_{red} are the concentrations of the oxidized and reduced forms of the redox couple, respectively. The first electron transfer process occurs at $E_1 = 0$ V vs. an arbitrary reference point E_0 and the second electron transfer reaction occurs at a potential of $E_2 = 0.3$ V vs. E_0. The heterogeneous electron-transfer rate constants for each oxidation step was initially taken to be 10^{-3} cm/s. All other parameters used for the simulation are identical to those in Table 7.

The Butler-Volmer (Equation A.1) and the Koutecky-Levich (Equation A.7) relationship were used to obtain the observed current density as a function of potential for each reaction.

$$\frac{1}{J} = \frac{1}{J_{lim}} + \frac{1}{J_k} \tag{A.7}$$

where J is the observed current density, J_{lim} is the limiting current density and J_k is the kinetic current density (calculated from the Butler-Volmer equation). To obtain steady-state current vs. overpotential relationships for the desired and undesired oxidation reactions, the electrolyte concentrations were initialized at the values shown in Table 7 and then incremented down using Equations A.4 to A.6. This simulation was then repeated for two cases in which (1) the rate constant of the second oxidation step was reduced by a factor of 10, and (2) the equilibrium potential of the second oxidation step was shifted positive by 0.1 V.

A.3 Analytical Protocol for Measurement of Kinetics using Ultramicroelectrodes (UMEs)

A brief description of the experimental and analysis protocol to obtain electron-transfer kinetics using ultramicroelectrodes is presented here. The flow cell, graphite counter and Ag/AgCl reference electrodes were first thoroughly rinsed with copious amounts of water and the cell itself was dried before use. The microelectrode (BASi, 10-11 μm diameter) was prepared by polishing with 5, 1, and 0.05 μm alumina slurries with 30 seconds of sonicating between each polishing step. Next, depending on the type of electrode to be tested, it was

pretreated to obtain the desired electrode surface using the same protocol established for RDE. Once the electrode was completely prepared, an o-ring was inserted near its tip and it was then introduced into the flow cell (channel dimensions 40 x 1 x 0.5 mm^3) using the respectively sized teflon threaded plug. Similarly, the counter and reference electrodes were inserted into the flow cell, where the counter electrode was placed downstream relative to the direction of flow. At each end of the cell, Masterflex pump tubing was attached by using luer style couplings and the pump was connected to the inlet side of the tube. The two free ends of the tubing were placed in a 100 mL beaker containing the electrolyte, which was left open to the ambient air. An initial test of the system seal was performed by running DI water through the setup. Once the absence of any leaks was confirmed, the electrolyte was pumped at a linear flow velocities of few tens of cm/s. Cyclic voltammetry was then carried out at a scan rate of 30 mV/s in a potential range of roughly 0 to 0.9 V vs. Ag/AgCl, which was chosen to facilitate observation of limiting anodic and cathodic currents for the $Fe^{3+/2+}$ redox couple.

Similar to RDE data analysis, we used Butler-Volmer fits to obtain the exchange current densities in our flow platform. However, because UMEs are not amenable to Koutecky-Levich analysis to account for the influence of mass transfer, we instead developed an analytical approach that involves using only the overpotential range corresponding to nearly pure kinetic control. Note that the same analysis can be achieved using RDE voltammetry, but UMEs exhibit characteristically larger mass-transfer limited current densities, which increases the available potential range for this kinetically limited regime.

We empirically evaluated the overpotential range over which the current-voltage data at UME can be treated as kinetically limited. To illustrate, Figure 56 presents simulated current densities as a function of the range of overpotentials used to perform Butler Volmer fits, where the transport limited current density was assumed to be 2.5 mA/cm^2 corresponding roughly to j_{lim} obtained at the surface of carbon UMEs and carbon rotating disk electrodes at 1600 rpm in a 10 mM total Fe concentration. This plot clearly illustrates that as the range of overpotential used to perform Butler-Volmer fits decreases, the j_0 value approaches the true exchange current density of that system. In other words, as long as the exchange current density is considerably smaller than the limiting current density, a larger range

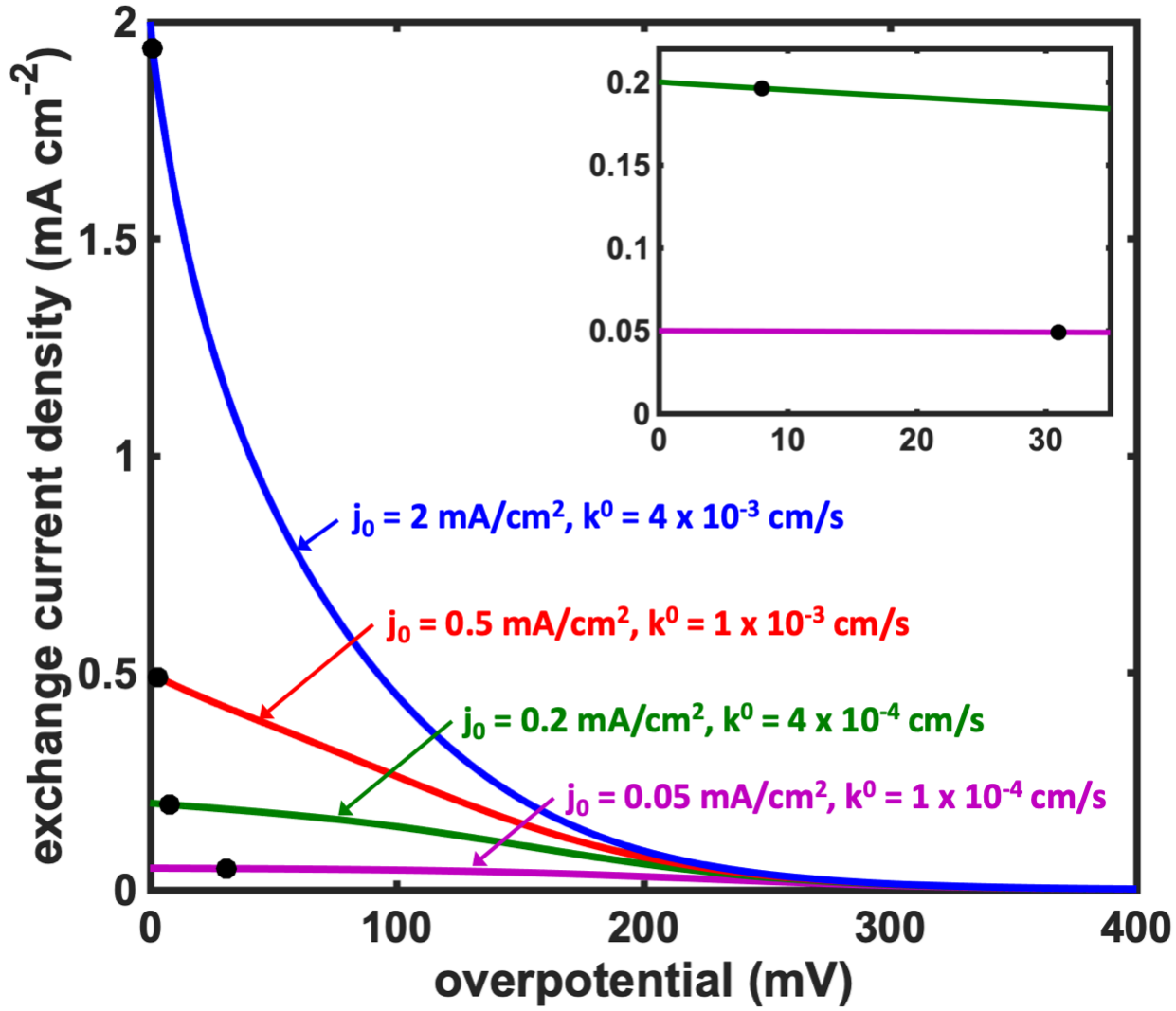

Figure 56: Simulated exchange current density as a function of overpotential range used in Butler-Volmer fit where the transport limited current density was 2.5 mA/cm^2. Inset represents the same data over a narrow overpotential range and filled black markers indicate the maximum overpotential range that can be used to obtain j_0 with an error less than 3%. Hypothetical k^0 values are extracted using a concentration of 5 mM.

of overpotential can be used to perform BV fits. This is particularly important as a lower overpotential range corresponds to a smaller number of data points, which can lead to a lower precision in analysis. Thus, we converged on using a range of overpotentials corresponding to $\pm$ 5% of the apparent limiting current density to perform Butler-Volmer fits, and to obtain exchange current densities and apparent reaction rate constants. Using this protocol, we found that a maximum error of $\sim$3% is introduced in j_0 even when the exchange current density is 80% of the limiting current density.

A.4 Simulation Details for Figure 21

We simulated the current density as a range of potential for varying values of electron-transfer kinetics for our RDE and microelectrode flow platforms. Simulations for the RDE data in Figure 21(a) were performed in an software package called DigiElch, which uses finite difference methods to numerically solve the coupled kinetic and transport equations. In this case, a single electron-transfer redox reaction was specified to correspond to $Fe^{3+/2+}$ chemistry and the concentration of the system was maintained at 10 mM total with a 50% state-of-charge. Hydrodynamic conditions were established by performing the simulations at 1600 rpm. Simulated cyclic voltammograms were obtained over a range of potential from -0.6 to 0.6 V vs. E^0 where the equilibrium potential, E^0 was maintained at 0 V and the interfacial electron transfer kinetics were varied from 10^{-5} to 1 cm/s.

The COMSOL multiphysics application was used to perform the simulations for Figure 21(b) using finite element techniques. First, a 3D geometry was established with the dimensions of 1 mm x 0.5 mm x a few cms to replicate the dimensions of our flow platform (See Figure 57). A volumetric flow at the inlet was maintained at 10 mL/min and was used to calculate the flux of reduced species, Fe^{2+} to the micro electrode surface, which was placed on one of the 1 mm faces, halfway down the length of the flow field. The COMSOL electrochemistry module containing the Butler-Volmer equation was used to calculate the current at each discretized point on the microelectrode surface. This current also described the change in concentration of reduced to oxidized species, Fe^{3+}, which was recorded by the

species flux module. Integrating spatially over the microelectrode surface gave a total current for the microelectrode as a function of applied potential which was then used to generate the cyclic voltammogram. This process was repeated for a range of interfacial electron transfer kinetics from 10^{-5} to 1 cm/s.

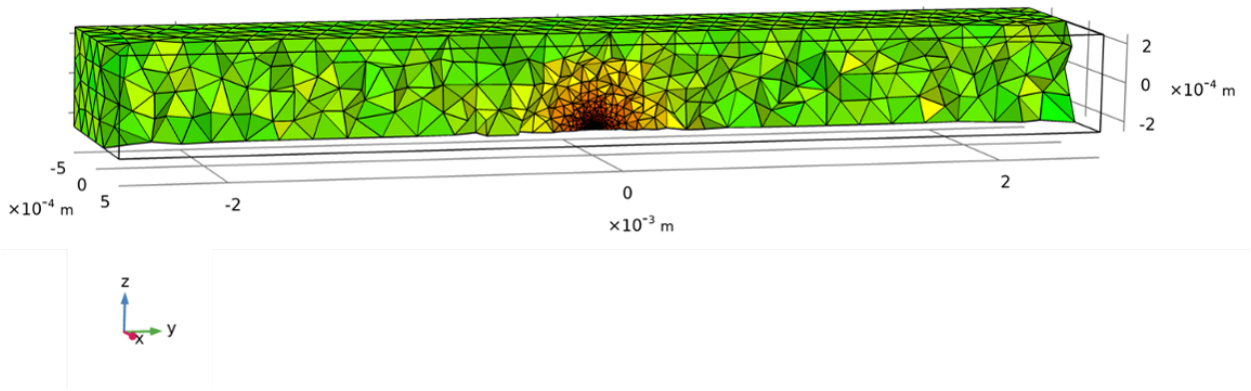

Figure 57: Representative image of the geometry used in COMSOL to simulate cyclic voltammograms in our microelectrode flow platform.

Bibliography

[1] Z. Chen and G. Chen, "An overview of energy consumption of the globalized world economy," *Energy Policy*, vol. 39, p. 5920–5928, 2011.

[2] "Sustainable Energy for All (SE4ALL) Database, World Bank, International Energy Agency and Energy Sector Management Assistance Program." http://data.worldbank.org/data-catalog/world-development-indicators (accessed on 2020-11-17).

[3] "IEA, IRENA, UNSD, World Bank, WHO. Tracking SDG 7: The Energy Progress Report. World Bank, Washington DC., License: Creative Commons Attribution—NonCommercial 3.0 IGO (CC BY-NC 3.0 IGO), 2020." https://irena.org/ (accessed on 2020-11-17).

[4] "U.S. Census Bureaus' International Database, 2018." https://www.census.gov/data-tools/demo/idb/informationGateway.php (accessed on 2020-11-17).

[5] V. Smil, "Energy Transitions: Global and National Perspectives." second ed., 2017.

[6] "BP Statistical Review of World Energy, 2020." https://www.bp.com/ (accessed on 2020-11-17).

[7] "Annual Energy Outlook 2019 with projections to 2050, U.S. Energy Information Administration, AEO2019." https://www.eia.gov/ (accessed on 2020-11-17).

[8] F. L. Toth and H.-H. Rogner, "Oil and nuclear power: Past, present, and future," *Energy Economics*, vol. 28, no. 1, pp. 1–25, 2006.

[9] P. M. Jackson and L. K. Smith, "Exploring the undulating plateau: the future of global oil supply," *Philosophical Transactions of the Royal Society A: Mathematical, Physical and Engineering Sciences*, vol. 372, no. 2006, p. 20120491, 2014.

[10] "Monthly Energy Review (April 2019), U.S. Energy Information Administration, DOE/EIA-0035(2019/04)." https://www.eia.gov/ (accessed on 2020-11-17).

[11] "IRENA 2020, Renewable Power Generation Costs in 2019, International Renewable Energy Agency, Abu Dhabi." www.irena.org/publications (accessed on 2020-11-17).

[12] K. Menyah and Y. Wolde-Rufael, "CO_2 emissions, nuclear energy, renewable energy and economic growth in the US," *Energy Policy*, vol. 38, no. 6, pp. 2911–2915, 2010.

[13] "Inventory of US Greenhouse Gas Emissions and Sinks (1990-2018), United States Environmental Protection Agency, EPA 430-R-20-002, 2020." https://www.epa.gov/ghgemissions/inventory-us-greenhouse-gas-emissions-and-sinks (accessed on 2020-11-17).

[14] T. B. Johansson, H. Kelly, A. K. N. Reddy, and R. H. Williams, "Renewable fuels and electricity for a growing world economy: Defining and achieving the potential.," *Energy Studies Review*, vol. 4, pp. 201–212, 1992.

[15] I. Dincer, "Renewable energy and sustainable development: a crucial review," *Renewable and Sustainable Energy Reviews*, vol. 4, no. 2, pp. 157–175, 2000.

[16] C. Karakosta, C. Pappas, V. Marinakis, and J. Psarras, "Renewable energy and nuclear power towards sustainable development: Characteristics and prospects," *Renewable and Sustainable Energy Reviews*, vol. 22, no. C, pp. 187–197, 2013.

[17] A. Adamantiades and I. Kessides, "Nuclear power for sustainable development: Current status and future prospects," *Energy Policy*, vol. 37, no. 12, pp. 5149–5166, 2009.

[18] N. Apergis, J. Payne, K. Menyah, and Y. Wolde-Rufael, "On the causal dynamics between emissions, nuclear energy, renewable energy, and economic growth," *Ecological Economics*, vol. 69, no. 11, pp. 2255–2260, 2010.

[19] S. Chu and A. Majumdar, "Opportunities and challenges for a sustainable energy future," *Nature*, vol. 488, p. 294–303, 2012.

[20] "Monthly Energy Review (April 2020), U.S. Energy Information Administration, DOE/EIA-0035(2020/04)." https://www.eia.gov/ (accessed on 2020-11-17).

[21] "Monthly Energy Review (June 2011), U.S. Energy Information Administration, DOE/EIA-0035(2011/06)." https://www.eia.gov/ (accessed on 2020-11-17).

[22] K. Moslehi and R. Kumar, "A reliability perspective of the smart grid," *IEEE Transactions on Smart Grid*, vol. 1, no. 1, pp. 57–64, 2010.

[23] X. Luo, J. Wang, M. Dooner, and J. Clarke, "Overview of current development in electrical energy storage technologies and the application potential in power system operation," *Applied Energy*, vol. 137, pp. 511 – 536, 2015.

[24] B. Tarroja, F. Mueller, J. D. Eichman, J. Brouwer, and S. Samuelsen, "Spatial and temporal analysis of electric wind generation intermittency and dynamics," *Renewable Energy*, vol. 36, no. 12, pp. 3424 – 3432, 2011.

[25] "National Solar Radiation Data Base 2018, The National Renewable Energy Laboratory." https://rredc.nrel.gov/solar/old_data/nsrdb/ (Accessed on 2020-11-17).

[26] J. Cho, S. Jeong, and Y. Kim, "Commercial and research battery technologies for electrical energy storage applications," *Progress in Energy and Combustion Science*, vol. 48, pp. 84 – 101, 2015.

[27] "Energy storage — a key technology for global energy sustainability," *Journal of Power Sources*, vol. 100, no. 1, pp. 2 – 17, 2001.

[28] F. Klumpp, "Comparison of pumped hydro, hydrogen storage and compressed air energy storage for integrating high shares of renewable energies—Potential, cost-comparison and ranking," *Journal of Energy Storage*, vol. 8, pp. 119 – 128, 2016.

[29] H. Liu and J. Jiang, "Flywheel energy storage—An upswing technology for energy sustainability," *Energy and Buildings*, vol. 39, no. 5, pp. 599 – 604, 2007.

[30] S. M. G, F. Faraji, A. Majazi, and K. Al-Haddad, "A comprehensive review of Flywheel Energy Storage System technology," *Renewable and Sustainable Energy Reviews*, vol. 67, pp. 477 – 490, 2017.

[31] S. Rehman, L. M. Al-Hadhrami, and M. M. Alam, "Pumped hydro energy storage system: A technological review," *Renewable and Sustainable Energy Reviews*, vol. 44, pp. 586 – 598, 2015.

[32] H. Lund and G. Salgi, "The role of compressed air energy storage (CAES) in future sustainable energy systems," *Energy Conversion and Management*, vol. 50, no. 5, pp. 1172 – 1179, 2009.

[33] X. Hu, C. Zou, C. Zhang, and Y. Li, "Technological Developments in Batteries: A Survey of Principal Roles, Types, and Management Needs," *IEEE Power and Energy Magazine*, vol. 15, no. 5, pp. 20–31, 2017.

[34] C. A. Hill, M. C. Such, D. Chen, J. Gonzalez, and W. M. Grady, "Battery Energy Storage for Enabling Integration of Distributed Solar Power Generation," *IEEE Transactions on Smart Grid*, vol. 3, no. 2, pp. 850–857, 2012.

[35] B. Dunn, H. Kamath, and J.-M. Tarascon, "Electrical Energy Storage for the Grid: A Battery of Choices," *Science*, vol. 334, no. 6058, pp. 928–935, 2011.

[36] J. Noack, N. Roznyatovskaya, T. Herr, and P. Fischer, "The Chemistry of Redox-Flow Batteries," *Angewandte Chemie International Edition*, vol. 54, no. 34, pp. 9776–9809, 2015.

[37] T. Nguyen and R. F. Savinell, "Flow Batteries," *The Electrochemical Society Interface*, vol. 19, no. 3, pp. 54–56, 2010.

[38] "The Ultimate Fast Facts Guide to Nuclear Energy, US Department of Energy, Office of Nuclear Energy, DOE/NE-0150." https://www.energy.gov/ne/ (accessed on 2020-11-17).

[39] "Power Plant Operations, US Energy Information Administration, Form EIA-923, 2020." https://www.eia.gov/ (accessed on 2020-11-17).

[40] "Annual Electric Generator Report, US Energy Information Administration, Form EIA-860, 2020." https://www.eia.gov/ (accessed on 2020-11-17).

[41] "Nuclear Costs in Context, Nuclear Energy Institute, 2020." https://www.nei.org/resources/reports-briefs/nuclear-costs-in-context (accessed on 2020-11-17).

[42] "Assessment of Disposal Options for DOE-Managed High-Level Radioactive Waste and Spent Nuclear Fuel, US Department of Energy, Office of Nuclear Energy, 2014." https://www.energy.gov/ne/downloads/assessment-disposal-options-doe-managed-high-level-radioactive-waste-and-spent-nuclear (accessed on 2020-11-17).

[43] "The Development of the Zircaloys," *Corrosion of Zirconium Alloys, ASTM International*, pp. 3 – 27, 1964.

[44] B. Cox, "Some thoughts on the mechanisms of in-reactor corrosion of zirconium alloys," *Journal of Nuclear Materials*, vol. 336, no. 2, pp. 331 – 368, 2005.

[45] "Corrosion of Zirconium-Base Alloys–An Overview," *Zirconium in the Nuclear Industry, ASTM International*, pp. 211 – 235, 1977.

[46] "The Role of Gamma Radiation on Zircaloy-4 Corrosion," *Zirconium in the Nuclear Industry, 18th International Symposium, ASTM International*, pp. 555 – 595, 2018.

[47] Y. Nishino, M. Endo, E. Ibe, and T. Yasuda, "Formation and dissolution of oxide film on zirconium alloys in 288°C pure water under γ-ray irradiation," *Journal of Nuclear Materials*, vol. 248, pp. 292 – 298, 1997.

[48] T. M. Gür, "Review of electrical energy storage technologies, materials and systems: challenges and prospects for large-scale grid storage," *Energy Environmen. Sci.*, vol. 11, no. 10, pp. 2696–2767, 2018.

[49] Z. Yang, J. Zhang, M. C. W. Kintner-Meyer, X. Lu, D. Choi, J. P. Lemmon, and J. Liu, "Electrochemical Energy Storage for Green Grid," *Chem. Rev.*, vol. 111, no. 5, pp. 3577–3613, 2011.

[50] I. Hadjipaschalis, A. Poullikkas, and V. Efthimiou, "Overview of current and future energy storage technologies for electric power applications," *Renew. Sust. Energ. Rev.*, vol. 13, no. 6, pp. 1513–1522, 2009.

[51] K. W. Beard, "Linden's Handbook of Batteries," *Fifth ed., McGraw-Hill Education*, p. 1456, 2019.

[52] G. E. Blomgren, "The Development and Future of Lithium Ion Batteries," *J. Electrochem. Soc.*, vol. 164, no. 1, pp. A5019–A5025, 2016.

[53] A. Yoshino, "The Birth of the Lithium-Ion Battery," *Angew. Chem. Int. Ed.*, vol. 51, pp. 5798–5800, 6 2012.

[54] J. B. Goodenough and K.-S. Park, "The Li-Ion Rechargeable Battery: A Perspective," *J. Am. Chem. Soc.*, vol. 135, pp. 1167–1176, 1 2013.

[55] M. Beaudin, H. Zareipour, A. Schellenberglabe, and W. Rosehart, "Energy storage for mitigating the variability of renewable electricity sources: An updated review," *Energy Sustain. Dev.*, vol. 14, no. 4, pp. 302–314, 2010.

[56] A. J. Cavallo, "Energy Storage Technologies for Utility Scale Intermittent Renewable Energy Systems," *J. Sol. Energy Eng.*, vol. 123, pp. 387–389, 7 2001.

[57] A. Castillo and D. F. Gayme, "Grid-scale energy storage applications in renewable energy integration: A survey," *Energ. Convers. Manage.*, vol. 87, pp. 885–894, 2014.

[58] A. Z. Weber, M. M. Mench, J. P. Meyers, P. N. Ross, J. T. Gostick, and Q. Liu, "Redox Flow Batteries: A Review," *J. Appl. Electrochem.*, vol. 41, no. 10, pp. 1137–1164, 2011.

[59] M. Skyllas-Kazacos, M. H. Chakrabarti, S. a. Hajimolana, F. S. Mjalli, and M. Saleem, "Progress in Flow Battery Research and Development," *J. Electrochem. Soc.*, vol. 158, no. 8, p. R55, 2011.

[60] W. Wang, Q. Luo, B. Li, X. Wei, L. Li, and Z. Yang, "Recent Progress in Redox Flow Battery Research and Development," *Adv. Funct. Mater.*, vol. 23, pp. 970–986, 2 2013.

[61] P. Leung, X. Li, C. Ponce de León, L. Berlouis, C. T. J. Low, and F. C. Walsh, "Progress in Redox Flow Batteries, Remaining Challenges and their Applications in Energy Storage," *RSC Adv.*, vol. 2, no. 27, pp. 10125–10156, 2012.

[62] L. H. Thaller, "Electrically Rechargeable Redox Flow Cell," 1976. United States Patent 3,996,064.

[63] J.Giner, L.Swette, and K.Cahill, "Screening of Redox Couples and Electrode Materials," *National Aeronautics and Space Administration, U S Dept. of Energy*, no. NAS3-19760, 1976.

[64] N. Hagedorn and L. Thaller, "Redox Storage Systems for Solar Applications," 1980. NASA TM 81464, National Aeronautics and Space Administration, U S Dept. of Energy.

[65] M. A. Reid and R. F. Gahn, "Factors affecting the open-circuit voltage and electrode kinetics of some iron/titanium redox flow cells," *National Aeronautics and Space Administration, U S Dept. of Energy*, no. NASA-TM-X-73669, 1977.

[66] M. Skyllas-Kazacos, "New All-Vanadium Redox Flow Cell," *J. Electrochem. Soc.*, vol. 133, no. 5, p. 1057, 1986.

[67] M. Skyllas-Kazacos, "Efficient Vanadium Redox Flow Cell," *J. Electrochem. Soc.*, vol. 134, no. 12, p. 2950, 1987.

[68] M. Rychcik and M. Skyllas-Kazacos, "Evaluation of Electrode Materials for Vanadium Redox Cell," *J. Power Sources*, vol. 19, no. 1, pp. 45–54, 1987.

[69] M. Rychcik and M. Skyllas-Kazacos, "Characteristics of a new all-vanadium redox flow battery," *J. Power Sources*, vol. 22, no. 1, pp. 59–67, 1988.

[70] B. Sun and M. Skyllas-Kazacos, "Modification of graphite electrode materials for vanadium redox flow battery application—I. Thermal treatment," *Electrochim. Acta.*, vol. 37, no. 7, pp. 1253–1260, 1992.

[71] B. Sun and M. Skyllas-Kazacos, "Chemical Modification of Graphite Electrode Materials for Vanadium Redox Flow Battery Application-Part II. Acid Treatments," *Electrochim. Acta.*, vol. 37, no. 13, pp. 2459–2465, 1992.

[72] B. Huskinson, M. P. Marshak, C. Suh, S. Er, M. R. Gerhardt, C. J. Galvin, X. Chen, A. Aspuru-Guzik, R. G. Gordon, and M. J. Aziz, "A metal-free organic-inorganic aqueous flow battery," *Nature*, vol. 505, no. 7482, pp. 195–198, 2014.

[73] J. Yuan, C. Zhang, Y. Zhen, Y. Zhao, and Y. Li, "Enhancing the performance of an all-organic non-aqueous redox flow battery," *J. Power Sources*, vol. 443, p. 227283, 2019.

[74] K. Lin, R. Gomez-Bombarelli, E. S. Beh, L. Tong, Q. Chen, A. W. Valle, A. Aspuru-Guzik, R. G. Gordon, and M. J. Aziz, "A redox flow battery with an alloxazine-based organic electrolyte," *Nature Energy*, vol. 1, no. 16102, 2016.

[75] T. Liu, X. Wei, Z. Nie, V. Sprenkle, and W. Wang, "A Total Organic Aqueous Redox Flow Battery Employing a Low Cost and Sustainable Methyl Viologen Anolyte and 4-HO-TEMPO Catholyte," *Adv. Energy Mater.*, vol. 6, p. 1501449, 2 2016.

[76] B. Hu, C. DeBruler, Z. Rhodes, and T. L. Liu, "Long-Cycling Aqueous Organic Redox Flow Battery (AORFB) toward Sustainable and Safe Energy Storage," *J. Am. Chem. Soc*, vol. 139, no. 3, pp. 1207–1214, 2017.

[77] Y. Ding, C. Zhang, L. Zhang, Y. Zhou, and G. Yu, "Molecular engineering of organic electroactive materials for redox flow batteries," *Chem. Soc. Rev.*, vol. 47, pp. 69–103, 2018.

[78] J. Winsberg, T. Hagemann, T. Janoschka, M. D. Hager, and U. S. Schubert, "Redox-Flow Batteries:From Metals to Organic Redox-Active Materials," *Angew. Chem. Int. Ed*, vol. 56, pp. 686–711, 2017.

[79] X. Wei, W. Pan, W. Duan, A. Hollas, Z. Yang, B. Li, Z. Nie, J. Liu, D. Reed, W. Wang, and V. Sprenkle, "Materials and Systems for Organic Redox Flow Batteries: Status and Challenges," *ACS Energy Lett.*, vol. 2, no. 9, p. 2187–2204, 2017.

[80] M. Kazacos and M. Skyllas-Kazacos, "Performance Characteristics of Carbon Plastic Electrodes in the All-Vanadium Redox Cell," *J. Electrochem. Soc.*, vol. 136, pp. 2759–2760, 1989.

[81] "Review of electrical energy storage technologies and system of their potential for the UK," *EA technology*, vol. DTI report contract no.- DG/ DTI/00055/00/00, URN no-041876, 2004.

[82] M. Skyllas-Kazacos, D. Kasherman, D. R. Hong, and M. Kazacos, "Characteristics and performance of 1 kW UNSW vanadium redox battery," *J. Power Sources*, vol. 35, no. 4, pp. 399–404, 1991.

[83] P. Zhao, H. Zhang, H. Zhou, J. Chen, S. Gao, and B. Yi, "Characteristics and performance of 10kW class all-vanadium redox-flow battery stack," *J. Power Sources*, vol. 162, no. 2, pp. 1416–1420, 2006.

[84] Y. K. Zeng, X. L. Zhou, L. An, L. Wei, and T. S. Zhao, "A high-performance flow-field structured iron-chromium redox flow battery," *J. Power Sources*, vol. 324, pp. 738–744, 2016.

[85] K. Li and K. J. Tseng, "Energy efficiency of lithium-ion battery used as energy storage devices in micro-grid," *IECON 2015 - 41st Annual Conference of the IEEE Industrial Electronics Society*, pp. 5235–5240, 2015.

[86] L. Ahmadi, M. Fowler, S. B. Young, R. A. Fraser, B. Gaffney, and S. B. Walker, "Energy efficiency of Li-ion battery packs re-used in stationary power applications," *Sustain. Energy Techn.*, vol. 8, pp. 9–17, 2014.

[87] C. Ponce de León, A. Frías-Ferrer, J. González-García, D. A. Szánto, and F. C. Walsh, "Redox flow cells for energy conversion," *J. Power Sources*, vol. 160, no. 1, pp. 716–732, 2006.

[88] T. Shigematsu, "Redox Flow Battery for Energy Storage," *SEI Tech Rev*, vol. 73, 2011.

[89] V. Viswanathan, A. Crawford, D. Stephenson, S. Kim, W. Wang, B. Li, G. Coffey, E. Thomsen, G. Graff, P. Balducci, M. Kintner-Meyer, and V. Sprenkle, "Cost and performance model for redox flow batteries," *J. Power Sources*, vol. 247, pp. 1040–1051, 2014.

[90] S. Ha and K. G. Gallagher, "Estimating the system price of redox flow batteries for grid storage," *J. Power Sources*, vol. 296, pp. 122–132, 2015.

[91] R. M. Darling, K. G. Gallagher, J. A. Kowalski, S. Ha, and F. R. Brushett, "Pathways to low-cost electrochemical energy storage: a comparison of aqueous and nonaqueous flow batteries," *Energy Environ. Sci.*, vol. 7, no. 11, pp. 3459–3477, 2014.

[92] K. Mongird, V. Fotedar, V. Viswanathan, V. Koritarov, P. Balducci, B. Hadjerioua, and J. Alam, "Energy storage technology and cost characterization report," Tech. Rep. July, 2019.

[93] R. Dmello, J. D. Milshtein, F. R. Brushett, and K. C. Smith, "Cost-driven materials selection criteria for redox flow battery electrolytes," *J. Power Sources*, vol. 330, pp. 261–272, 2016.

[94] J. Noack, L. Wietschel, N. Roznyatovskaya, K. Pinkwart, and J. Tübke, "Techno-Economic Modeling and Analysis of Redox Flow Battery Systems," *Energies*, vol. 9, no. 8, 2016.

[95] J. D. Milshtein, R. M. Darling, J. Drake, M. L. Perry, and F. R. Brushett, "The Critical Role of Supporting Electrolyte Selection on Flow Battery Cost," *J. Electrochem. Soc.*, vol. 164, no. 14, pp. A3883–A3895, 2017.

[96] T. Lüth, S. König, M. Suriyah, and T. Leibfried, "Passive components limit the cost reduction of conventionally designed vanadium redox flow batteries," *Energy Procedia*, vol. 155, pp. 379–389, 2018.

[97] S. M. Laramie, J. D. Milshtein, T. M. Breault, F. R. Brushett, and L. T. Thompson, "Performance and cost characteristics of multi-electron transfer, common ion exchange non-aqueous redox flow batteries," *J. Power Sources*, vol. 327, pp. 681–692, 2016.

[98] World Energy Council, "Energy Storage Monitor," tech. rep., 2019.

[99] Z. González, A. Sánchez, C. Blanco, M. Granda, R. Menéndez, and R. Santamaría, "Enhanced performance of a Bi-modified graphite felt as the positive electrode of a vanadium redox flow battery," *Electrochemistry Communications*, vol. 13, no. 12, pp. 1379 – 1382, 2011.

[100] W. H. Wang and X. D. Wang, "Investigation of Ir-modified carbon felt as the positive electrode of an all-vanadium redox flow battery," *Electrochim. Acta.*, vol. 52, no. 24, pp. 6755–6762, 2007.

[101] D. Aaron, Z. Tang, A. B. Papandrew, and T. A. Zawodzinski, "Polarization Curve Analysis of All-Vanadium Redox Flow Batteries," *J. Appl. Electrochem.*, vol. 41, pp. 1175–1182, 8 2011.

[102] M. Skyllas-Kazacos, C. Menictas, and T. Lim, *12 - Redox flow batteries for medium- to large-scale energy storage*. Woodhead Publishing, 2013.

[103] D. S. Aaron, Q. Liu, Z. Tang, G. M. Grim, A. B. Papandrew, A. Turhan, T. A. Zawodzinski, and M. M. Mench, "Dramatic Performance Gains in Vanadium Redox Flow Batteries through Modified Cell Architecture," *J. Power Sources*, vol. 206, pp. 450–453, 2012.

[104] Q. H. Liu, G. M. Grim, A. B. Papandrew, A. Turhan, T. A. Zawodzinski, and M. M. Mench, "High Performance Vanadium Redox Flow Batteries with Optimized Electrode Configuration and Membrane Selection," *J. Electrochem. Soc.*, vol. 159, no. 8, pp. A1246–A1252, 2012.

[105] X. L. Zhou, T. S. Zhao, L. An, Y. K. Zeng, and L. Wei, "Critical transport issues for improving the performance of aqueous redox flow batteries," *J. Power Sources*, vol. 339, pp. 1–12, 2017.

[106] N. Gurieff, D. Keogh, M. Baldry, V. Timchenko, D. Green, I. Koskinen, and C. Menictas, "Mass Transport Optimization for Redox Flow Battery Design," *Appl. Sci.*, vol. 10, p. 2801, 2020.

[107] J. D. Milshtein, K. M. Tenny, J. L. Barton, J. Drake, R. M. Darling, and F. R. Brushett, "Quantifying Mass Transfer Rates in Redox Flow Batteries," *J. Electrochem. Soc.*, vol. 164, pp. E3265–E3275, 2017.

[108] J. D. Milshtein, A. P. Kaur, M. D. Casselman, J. A. Kowalski, S. Modekrutti, P. L. Zhang, N. Harsha Attanayake, C. F. Elliott, S. R. Parkin, C. Risko, F. R. Brushett, and S. A. Odom, "High current density, long duration cycling of soluble organic active species for non-aqueous redox flow batteries," *Energy Environ. Sci.*, vol. 9, no. 11, pp. 3531–3543, 2016.

[109] J. S. Lawton, A. Jones, and T. Zawodzinski, "Concentration Dependence of VO2+Crossover of Nafion for Vanadium Redox Flow Batteries," *J. Electrochem. Soc.*, vol. 160, no. 4, pp. A697–A702, 2013.

[110] N. Roznyatovskaya, J. Noack, K. Pinkwart, and J. Tübke, "Aspects of electron transfer processes in vanadium redox-flow batteries," *Curr. Opin. Electrochem.*, vol. 19, pp. 42–48, 2020.

[111] C.-H. Bae, E. P. L. Roberts, and R. A. W. Dryfe, "Chromium redox couples for application to redox flow batteries," *Electrochim. Acta.*, vol. 48, no. 3, pp. 279–287, 2002.

[112] A. Tang, J. Bao, and M. Skyllas-Kazacos, "Thermal modelling of battery configuration and self-discharge reactions in vanadium redox flow battery," *J. Power Sources*, vol. 216, pp. 489–501, 2012.

[113] A. Tang, J. Bao, and M. Skyllas-Kazacos, "Dynamic modelling of the effects of ion diffusion and side reactions on the capacity loss for vanadium redox flow battery," *J. Power Sources*, vol. 196, no. 24, pp. 10737–10747, 2011.

[114] D. You, H. Zhang, C. Sun, and X. Ma, "Simulation of the self-discharge process in vanadium redox flow battery," *J. Power Sources*, vol. 196, no. 3, pp. 1578–1585, 2011.

[115] Z. Wei, A. Bhattarai, C. Zou, S. Meng, T. M. Lim, and M. Skyllas-Kazacos, "Real-time monitoring of capacity loss for vanadium redox flow battery," *J. Power Sources*, vol. 390, pp. 261–269, 2018.

[116] B. Jiang, L. Wu, L. Yu, X. Qiu, and J. Xi, "A comparative study of Nafion series membranes for vanadium redox flow batteries," *J. Membr. Sci.*, vol. 510, pp. 18–26, 2016.

[117] X. Wei, B. Li, and W. Wang, "Porous Polymeric Composite Separators for Redox Flow Batteries," *Polym. Rev.*, vol. 55, pp. 247–272, 4 2015.

[118] D. Chen, M. A. Hickner, E. Agar, and E. C. Kumbur, "Selective anion exchange membranes for high coulombic efficiency vanadium redox flow batteries," *Electrochem. Commun.*, vol. 26, pp. 37–40, 2013.

[119] P. K. Leung, Q. Xu, T. S. Zhao, L. Zeng, and C. Zhang, "Preparation of silica nanocomposite anion-exchange membranes with low vanadium-ion crossover for vanadium redox flow batteries," *Electrochim. Acta.*, vol. 105, pp. 584–592, 2013.

[120] M.-A. Goulet, L. Tong, D. A. Pollack, D. P. Tabor, S. A. Odom, A. Aspuru-Guzik, E. E. Kwan, R. G. Gordon, and M. J. Aziz, "Extending the Lifetime of Organic Flow Batteries via Redox State Management," *J. Am. Chem. Soc.*, vol. 141, pp. 8014–8019, 5 2019.

[121] F. R. Brushett, M. J. Aziz, and K. E. Rodby, "On Lifetime and Cost of Redox-Active Organics for Aqueous Flow Batteries," *ACS Energy Lett.*, vol. 5, pp. 879–884, 2020.

[122] M.-A. Goulet and M. J. Aziz, "Flow Battery Molecular Reactant Stability Determined by Symmetric Cell Cycling Methods," *J. Echem. Soc.*, vol. 165, no. 7, pp. A1466–A1477, 2018.

[123] A. Paulenova, S. E. Creager, J. D. Navratil, and Y. Wei, "Redox potentials and kinetics of the Ce3+/Ce4+ redox reaction and solubility of cerium sulfates in sulfuric acid solutions," *J. Power Sources*, vol. 109, no. 2, pp. 431–438, 2002.

[124] Y. H. Wen, H. M. Zhang, P. Qian, H. T. Zhou, P. Zhao, B. L. Yi, and Y. S. Yang, "A study of the Fe(III)/Fe(II)–triethanolamine complex redox couple for redox flow battery application," *Electrochim. Acta.*, vol. 51, no. 18, pp. 3769–3775, 2006.

[125] S. Ranganathan, T.-C. Kuo, and R. L. McCreery, "Facile Preparation of Active Glassy Carbon Electrodes with Activated Carbon and Organic Solvents," *Anal. Chem.*, vol. 71, pp. 3574–3580, 8 1999.

[126] T. C. Kuo and R. L. McCreery, "Surface chemistry and electron-transfer kinetics of hydrogen-modified glassy carbon electrodes," *Anal. Chem.*, vol. 71, no. 8, pp. 1553–1560, 1999.

[127] X. W. Wu, T. Yamamura, S. Ohta, Q. X. Zhang, F. C. Lv, C. M. Liu, K. Shirasaki, I. Satoh, T. Shikama, D. Lu, and S. Q. Liu, "Acceleration of the redox kinetics of VO(2+)/VO2(+) and V(3+)/V(2+) couples on carbon paper," *J. Appl. Electrochem.*, vol. 41, no. 10, pp. 1183–1190, 2011.

[128] E. Sum and M. Skyllas-Kazacos, "A study of the V(II)/V(III) redox couple for redox flow cell applications," *J. Power Sources*, vol. 15, no. 2, pp. 179–190, 1985.

[129] G. Oriji, Y. Katayama, and T. Miura, "Investigations on V(IV)/V(V) and V(II)/V(III) redox reactions by various electrochemical methods," *J. Power Sources*, vol. 139, no. 1-2, pp. 321–324, 2005.

[130] T.-M. Tseng, R.-H. Huang, C.-Y. Huang, K.-L. Hsueh, and F.-S. Shieu, "A Kinetic Study of the Platinum/Carbon Anode Catalyst for Vanadium Redox Flow Battery," *J. Electrochem. Soc.*, vol. 160, no. 4, pp. A690–A696, 2013.

[131] D. Aaron, C.-N. Sun, M. Bright, A. B. Papandrew, M. M. Mench, and T. A. Zawodzinski, "In Situ Kinetics Studies in All-Vanadium Redox Flow Batteries," *ECS Electrochem. Lett.*, vol. 2, no. 3, pp. A29–A31, 2013.

[132] B. Yang, A. Murali, A. Nirmalchandar, B. Jayathilake, G. K. S. Prakash, and S. R. Narayanan, "A Durable, Inexpensive and Scalable Redox Flow Battery Based on Iron Sulfate and Anthraquinone Disulfonic Acid," *J. Electrochem. Soc.*, vol. 167, no. 6, p. 60520, 2020.

[133] C. A. McDermott, "Electron Transfer Kinetics of Aquated Fe(+3/+2), Eu(+3/+2), and V(+3/+2) at Carbon Electrodes," *J. Electrochem. Soc.*, vol. 140, no. 9, p. 2593, 1993.

[134] F. Štulíková, M.; Vydra, "Voltammetry with Disk Electrodes and its Analytical Application: IV. The Voltammetry of Iron(III) at the Glassy Carbon Rotating Disk Electrode in Acid Media," *J. Electroanal. Chem. Interf. Electrochem.*, vol. 38, pp. 349–357, 1972.

[135] L. G. Ateya, B. G.; Austin, "The Kinetics of Fe(2+)/ FeCl(2+)/ HCI (aq) on Pyrolytic Graphite Electrodes," *J. Electrochem. Soc.*, vol. 120, p. 1216–1219, 1973.

[136] E. Hollax and D. Cheng, "The influence of oxidative pretreatment of graphite electrodes on the catalysis of the Cr(3+)/Cr(2+) and Fe(3+)/Fe(2+) redox reactions," *Carbon*, vol. 23, no. 6, pp. 655–664, 1985.

[137] A. Bourke, M. A. Miller, R. P. Lynch, X. Gao, J. Landon, J. S. Wainright, R. F. Savinell, and D. N. Buckley, "Electrode Kinetics of Vanadium Flow Batteries: Contrasting Responses of V(II)-V(III) and V(IV)-V(V) to Electrochemical Pretreatment of Carbon," *J. Electrochem. Soc.*, vol. 163, no. 1, pp. A5097–A5105, 2015.

[138] Y. Li, J. Parrondo, S. Sankarasubramanian, and V. Ramani, "Impact of Surface Carbonyl- and Hydroxyl-Group Concentrations on Electrode Kinetics in an All-Vanadium Redox Flow Battery," *J. Phys. Chem. C*, vol. 123, pp. 6370–6378, 3 2019.

[139] E. Agar, C. R. Dennison, K. W. Knehr, and E. C. Kumbur, "Identification of performance limiting electrode using asymmetric cell configuration in vanadium redox flow batteries," *J. Power Sources*, vol. 225, pp. 89–94, 2013.

[140] J. Friedl, C. M. Bauer, A. Rinaldi, and U. Stimming, "Electron transfer kinetics of the VO(2+)/VO2(1+) – Reaction on multi-walled carbon nanotubes," *Carbon*, vol. 63, pp. 228–239, 2013.

[141] T. Yamamura, N. Watanabe, T. Yano, and Y. Shiokawa, "Electron-Transfer Kinetics of Np(3+)/Np(4+), NpO2(1+)/NpO2(2+), V(2+)/V(3+), and VO(2+)/VO2(1+) at Carbon Electrodes," *J. Electrochem. Soc.*, vol. 152, no. 4, p. A830, 2005.

[142] B. Yang, L. Hoober-Burkhardt, F. Wang, G. K. Surya Prakash, and S. R. Narayanan, "An Inexpensive Aqueous Flow Battery for Large-Scale Electrical Energy Storage Based on Water-Soluble Organic Redox Couples," *J. Electrochem. Soc.*, vol. 161, no. 9, pp. A1371–A1380, 2014.

[143] A. W. Lantz, S. A. Shavalier, W. Schroeder, and P. G. Rasmussen, "Evaluation of an Aqueous Biphenol- and Anthraquinone-Based Electrolyte Redox Flow Battery," *ACS Appl. Energy Mater.*, vol. 2, pp. 7893–7902, 11 2019.

[144] N. C. Hung and Z. Nagy, "Kinetics of the Ferrous/Ferric Electrode Reaction in the Absence of Chloride Catalysis," *J. Electrochem. Soc.*, vol. 134, p. 2215–2220, 1987.

[145] D. H. Angell and T. Dickinson, "The Kinetics of the Ferrous/Ferric and Ferro/Ferricyanide Reac- tions at Platinum and Gold Electrodes: Part I. Kinetics at Bare-Metal Surfaces," *J. Electroanal. Chem. Interfacial Electrochem.*, vol. 35, pp. 55–72, 1972.

[146] R. S. Nicholson, "Theory and Application of Cyclic Voltammetry for Measurement of Electrode Reaction Kinetics," *Anal. Chem.*, vol. 37, no. 11, pp. 1351–1355, 1965.

[147] L. E. VanGelder, A. M. Kosswattaarachchi, P. L. Forrestel, T. R. Cook, and E. M. Matson, "Polyoxovanadate-alkoxide clusters as multi-electron charge carriers for symmetric non-aqueous redox flow batteries," *Chemical Science*, vol. 9, no. 6, pp. 1692–1699, 2018.

[148] E. Sum, M. Rychcik, and M. Skyllas-kazacos, "Investigation of the V(V)/V(IV) System for use in the Positive Half-Cell of a Redox Battery," *J. Power Sources*, vol. 16, no. 2, pp. 85–95, 1985.

[149] H. Kaneko, K. Nozaki, Y. Wada, T. Aoki, A. Negishi, and M. Kamimoto, "Vanadium redox reactions and carbon electrodes for vanadium redox flow battery," *Electrochim. Acta.*, vol. 36, no. 7, pp. 1191–1196, 1991.

[150] A. Bourke, M. A. Miller, R. P. Lynch, J. S. Wainright, R. F. Savinell, and D. N. Buckley, "Effect of Cathodic and Anodic Treatments of Carbon on the Electrode Kinetics of V(IV)/V(V) Oxidation-Reduction," *J. Electrochem. Soc.*, vol. 162, no. 8, pp. A1547–A1555, 2015.

[151] J. Langner, M. Bruns, D. Dixon, A. Nefedov, C. Wöll, F. Scheiba, H. Ehrenberg, C. Roth, and J. Melke, "Surface properties and graphitization of polyacrylonitrile based fiber electrodes affecting the negative half-cell reaction in vanadium redox flow batteries," *J. Power Sources*, vol. 321, pp. 210–218, 2016.

[152] B. Fang, S. Iwasa, Y. Wei, T. Arai, and M. Kumagai, "A study of the Ce(III)/Ce(IV) redox couple for redox flow battery application," *Electrochim. Acta.*, vol. 47, no. 24, pp. 3971–3976, 2002.

[153] L. Yue, W. Li, F. Sun, L. Zhao, and L. Xing, "Highly hydroxylated carbon fibres as electrode materials of all-vanadium redox flow battery," *Carbon*, vol. 48, no. 11, pp. 3079–3090, 2010.

[154] Z. González, A. Sánchez, C. Blanco, M. Granda, R. Menéndez, and R. Santamaría, "Enhanced performance of a Bi-modified graphite felt as the positive electrode of a vanadium redox flow battery," *Electrochem. Commun.*, vol. 13, no. 12, pp. 1379–1382, 2011.

[155] T. Yamamura, Y. Shiokawa, H. Yamana, and H. Moriyama, "Electrochemical investigation of uranium β-diketonates for all-uranium redox flow battery," *Electrochim. Acta.*, vol. 48, no. 1, pp. 43–50, 2002.

[156] J. A. Suttil, J. F. Kucharyson, I. L. Escalante-Garcia, P. J. Cabrera, B. R. James, R. F. Savinell, M. S. Sanford, and L. T. Thompson, "Metal acetylacetonate complexes for high energy density non-aqueous redox flow batteries," *J. Mater. Chem. A*, vol. 3, no. 15, pp. 7929–7938, 2015.

[157] J. T. Davies and J. J. Tummino, "High-Performance Vanadium Redox Flow Batteries with Graphite Felt Electrodes," *C — Journal of Carbon Research*, vol. 4, no. 1, 2018.

[158] R. A. Elgammal, Z. Tang, C.-N. Sun, J. Lawton, and T. A. Zawodzinski, "Species Uptake and Mass Transport in Membranes for Vanadium Redox Flow Batteries," *Electrochim. Acta.*, vol. 237, pp. 1–11, 2017.

[159] J. D. Milshtein, J. L. Barton, T. J. Carney, J. A. Kowalski, R. M. Darling, and F. R. Brushett, "Towards Low Resistance Nonaqueous Redox Flow Batteries," *J. Electrochem. Soc.*, vol. 164, no. 12, pp. A2487–A2499, 2017.

[160] Y. K. Zeng, T. S. Zhao, X. L. Zhou, L. Zeng, and L. Wei, "The effects of design parameters on the charge-discharge performance of iron-chromium redox flow batteries," *Appl. Energy*, vol. 182, pp. 204–209, 2016.

[161] L. F. Arenas, F. C. Walsh, and C. P. de León, "The Importance of Cell Geometry and Electrolyte Properties to the Cell Potential of Zn-Ce Hybrid Flow Batteries," *J. Electrochem. Soc.*, vol. 163, no. 1, pp. A5170–A5179, 2015.

[162] H. S. Yang, J. H. Park, H. W. Ra, C.-S. Jin, and J. H. Yang, "Critical rate of electrolyte circulation for preventing zinc dendrite formation in a zinc–bromine redox flow battery," *J. Power Sources*, vol. 325, pp. 446–452, 2016.

[163] M. Al-Yasiri and J. Park, "A novel cell design of vanadium redox flow batteries for enhancing energy and power performance," *Appl. Energy*, vol. 222, pp. 530–539, 2018.

[164] D. Reed, E. Thomsen, B. Li, W. Wang, Z. Nie, B. Koeppel, and V. Sprenkle, "Performance of a low cost interdigitated flow design on a 1 kW class all vanadium mixed acid redox flow battery," *J. Power Sources*, vol. 306, pp. 24–31, 2016.

[165] J. Houser, J. Clement, A. Pezeshki, and M. M. Mench, "Influence of architecture and material properties on vanadium redox flow battery performance," *J. Power Sources*, vol. 302, pp. 369–377, 2016.

[166] K. Zhang, J. Xiong, C. Yan, and A. Tang, "In-situ measurement of electrode kinetics in porous electrode for vanadium flow batteries using symmetrical cell design," *Appl. Energy*, vol. 272, p. 115093, 2020.

[167] P. Leuaa, D. Priyadarshani, D. Choudhury, R. Mauryaa, and M. Neergat, "Resolving charge-transfer and mass-transfer processes of VO^{2+}/VO_2^+ redox species across the electrode/electrolyte interface using electrochemical impedance spectroscopy for vanadium redox flow battery," *RSC Adv.*, vol. 10, p. 30887–30895, 2020.

[168] H. Agarwal, J. Florian, B. R. Goldsmith, and N. Singh, "V(2+)/V(3+) Redox Kinetics on Glassy Carbon in Acidic Electrolytes for Vanadium Redox Flow Batteries," *ACS Energy Lett.*, vol. 4, p. 23682377, 2019.

[169] K. Amini and M. D. Pritzker, "In situ polarization study of zinc–cerium redox flow batteries," *J. Power Sources*, vol. 471, p. 228463, 2020.

[170] A. M. Pezeshki, "Impedance-Resolved Performance and Durability in Redox Flow Batteries," *PhD diss., University of Tennessee*, 2016.

[171] A. Bourke, M. A. Miller, R. P. Lynch, J. S. Wainright, R. F. Savinell, and D. N. Buckley, "Electrode Kinetics in All-Vanadium Flow Batteries: Effects of Electrochemical Treatment," *ECS Transactions*, vol. 66, no. 8, pp. 181–211, 2015.

[172] H. Wang, S. Y. Sayed, E. J. Luber, B. C. Olsen, S. M. Shirurkar, S. Venkatakrishnan, U. M. Tefashe, A. K. Farquhar, E. S. Smotkin, R. L. McCreery, and J. M. Buriak, "Redox Flow Batteries: How to Determine Electrochemical Kinetic Parameters," *ACS Nano*, vol. 14, pp. 2575–2584, 3 2020.

[173] X. L. Zhou, T. S. Zhao, Y. K. Zeng, L. An, and L. Wei, "A highly permeable and enhanced surface area carbon-cloth electrode for vanadium redox flow batteries," *J. Power Sources*, vol. 329, pp. 247–254, 2016.

[174] J. Houser, A. Pezeshki, J. T. Clement, D. Aaron, and M. M. Mench, "Architecture for improved mass transport and system performance in redox flow batteries," *J. Power Sources*, vol. 351, pp. 96–105, 2017.

[175] S. Kumar and S. Jayanti, "Effect of flow field on the performance of an all-vanadium redox flow battery," *J. Power Sources*, vol. 307, pp. 782–787, 2016.

[176] K. M. Lisboa, J. Marschewski, N. Ebejer, P. Ruch, R. M. Cotta, B. Michel, and D. Poulikakos, "Mass transport enhancement in redox flow batteries with corrugated fluidic networks," *J. Power Sources*, vol. 359, pp. 322–331, 2017.

[177] X. Ke, J. M. Prahl, J. I. D. Alexander, J. S. Wainright, T. A. Zawodzinski, and R. F. Savinell, "Rechargeable redox flow batteries: flow fields, stacks and design considerations," *Chem. Soc. Rev.*, vol. 47, no. 23, pp. 8721–8743, 2018.

[178] Q. Xu, T. S. Zhao, and C. Zhang, "Performance of a vanadium redox flow battery with and without flow fields," *Electrochim. Acta.*, vol. 142, pp. 61–67, 2014.

[179] R. M. Darling and M. L. Perry, "The Influence of Electrode and Channel Configurations on Flow Battery Performance," *J. Electrochem. Soc.*, vol. 161, no. 9, pp. A1381–A1387, 2014.

[180] C.-N. Sun, F. M. Delnick, D. S. Aaron, A. B. Papandrew, M. M. Mench, and T. A. Zawodzinski, "Probing Electrode Losses in All-Vanadium Redox Flow Batteries with Impedance Spectroscopy," *ECS Electrochem. Lett.*, vol. 2, no. 5, pp. A43–A45, 2013.

[181] A. M. Pezeshki, J. T. Clement, G. M. Veith, T. A. Zawodzinski, and M. M. Mench, "High performance electrodes in vanadium redox flow batteries through oxygen-enriched thermal activation," *J. Power Sources*, vol. 294, pp. 333–338, 2015.

[182] J. D. Milshtein, J. L. Barton, R. M. Darling, and F. R. Brushett, "4-acetamido-2,2,6,6-tetramethylpiperidine-1-oxyl as a model organic redox active compound for nonaqueous flow batteries," *J. Power Sources*, vol. 327, pp. 151–159, 2016.

[183] F. R. Brushett, J. T. Vaughey, and A. N. Jansen, "An All-Organic Non-aqueous Lithium-Ion Redox Flow Battery," *Adv. Energy Mater.*, vol. 2, pp. 1390–1396, 11 2012.

[184] K. B. Oldham, J. C. Myland, C. G. Zoski, and A. M. Bond, "Kinetic parameters from steady-state voltammograms at microdisc electrodes," *J. Electroanal. Chem. Interf. Electrochem.*, vol. 270, no. 1, pp. 79–101, 1989.

[185] K. B. Oldham and C. G. Zoski, "Comparison of voltammetric steady states at hemispherical and disc microelectrodes," *J. Electroanal. Chem. Interf. Electrochem.*, vol. 256, no. 1, pp. 11–19, 1988.

[186] J. Kim and A. J. Bard, "Application of the Koutecký-Levich Method to the Analysis of Steady State Voltammograms with Ultramicroelectrodes," *Anal. Chem.*, vol. 88, pp. 1742–1747, 2 2016.

[187] J. O. Howell and R. M. Wightman, "Ultrafast voltammetry and voltammetry in highly resistive solutions with microvoltammetric electrodes," *Anal. Chem.*, vol. 56, pp. 524–529, 3 1984.

[188] J. V. Macpherson, N. Simjee, and P. R. Unwin, "Hydrodynamic ultramicroelectrodes: kinetic and analytical applications," *Electrochim. Acta.*, vol. 47, no. 1, pp. 29–45, 2001.

[189] J. E. Baur and R. Wightman, "Diffusion coefficients determined with microelectrodes," *J. Electroanal. Chem. Interfac. Electrochem.*, vol. 305, no. 1, pp. 73–81, 1991.

[190] R. M. Wightman, "Voltammetry with Microscopic Electrodes in New Domains," *Science*, vol. 240, no. 4851, pp. 415–420, 1988.

[191] R. J. Forster, "Microelectrodes: New Dimensions in Electrochemistry," *Chem. Soc. Rev.*, vol. 23, pp. 289–297, 1994.

[192] J. Heinze, "Ultramicroelectrodes in Electrochemistry," *Angew. Chem. Int. Ed. Engl.*, vol. 32, pp. 1268–1288, 1993.

[193] C. P. Andrieux, P. Hapiot, and J. Saveant, "Ultramicroelectrodes for Fast Electrochemical Kinetics," *Electroanalysis*, vol. 2, pp. 183–193, 1990.

[194] K. Aoki, "Theory of Ultramicroelectrodes," *Electroanalysis*, vol. 5, pp. 627–639, 1993.

[195] A. A. Shinkle, A. E. S. Sleightholme, L. D. Griffith, L. T. Thompson, and C. W. Monroe, "Degradation mechanisms in the non-aqueous vanadium acetylacetonate redox flow battery," *J. Power Sources*, vol. 206, pp. 490–496, 2012.

[196] M. A. Miller, A. Bourke, N. Quill, J. S. Wainright, R. P. Lynch, D. N. Buckley, and R. F. Savinell, "Kinetic Study of Electrochemical Treatment of Carbon Fiber Microelectrodes Leading to In Situ Enhancement of Vanadium Flow Battery Efficiency," *J. Electrochem. Soc.*, vol. 163, pp. A2095–A2102, 1 2016.

[197] B. Hwang, M.-S. Park, and K. Kim, "Ferrocene and Cobaltocene Derivatives for Non-Aqueous Redox Flow Batteries," *Chem Sus Chem*, vol. 8, pp. 310–314, 1 2015.

[198] N. Nioradze, J. Kim, and S. Amemiya, "Quasi-Steady-State Voltammetry of Rapid Electron Transfer Reactions at the Macroscopic Substrate of the Scanning Electrochemical Microscope," *Anal. Chem.*, vol. 83, pp. 828–835, 2 2011.

[199] J. Kwak and A. J. Bard, "Scanning electrochemical microscopy. Theory of the feedback mode," *Anal. Chem.*, vol. 61, pp. 1221–1227, 6 1989.

[200] G. Nagarjuna, J. Hui, K. J. Cheng, T. Lichtenstein, M. Shen, J. S. Moore, and J. Rodríguez-López, "Impact of Redox-Active Polymer Molecular Weight on the Electrochemical Properties and Transport Across Porous Separators in Nonaqueous Solvents," *J. Am. Chem. Soc.*, vol. 136, pp. 16309–16316, 11 2014.

[201] N. L. Ritzert, J. Rodríguez-López, C. Tan, and H. D. Abruña, "Kinetics of Interfacial Electron Transfer at Single-Layer Graphene Electrodes in Aqueous and Nonaqueous Solutions," *Langmuir*, vol. 29, pp. 1683–1694, 2 2013.

[202] M. J. Baran, M. N. Braten, E. C. Montoto, Z. T. Gossage, L. Ma, E. Chénard, J. S. Moore, J. Rodríguez-López, and B. A. Helms, "Designing Redox-Active Oligomers for Crossover-Free, Nonaqueous Redox-Flow Batteries with High Volumetric Energy Density," *Chemistry of Materials*, vol. 30, pp. 3861–3866, 6 2018.

[203] Y. Garsany, O. A. Baturina, K. E. Swider-Lyons, and S. S. Kocha, "Experimental Methods for Quantifying the Activity of Platinum Electrocatalysts for the Oxygen Reduction Reaction," *Analytical Chemistry*, vol. 82, no. 15, pp. 6321–6328, 2010.

[204] H. A. Gasteiger, S. S. Kocha, B. Sompalli, and F. T. Wagner, "Activity benchmarks and requirements for Pt, Pt-alloy, and non-Pt oxygen reduction catalysts for PEMFCs," *Applied Catalysis B: Environmental*, vol. 56, no. 1, pp. 9 – 35, 2005.

[205] C. C. L. McCrory, S. Jung, J. C. Peters, and T. F. Jaramillo, "Benchmarking Heterogeneous Electrocatalysts for the Oxygen Evolution Reaction," *Journal of the American Chemical Society*, vol. 135, no. 45, pp. 16977–16987, 2013.

[206] C. C. L. McCrory, S. Jung, I. M. Ferrer, S. M. Chatman, J. C. Peters, and T. F. Jaramillo, "Benchmarking Hydrogen Evolving Reaction and Oxygen Evolving Reaction Electrocatalysts for Solar Water Splitting Devices," *Journal of the American Chemical Society*, vol. 137, no. 13, pp. 4347–4357, 2015.

[207] T. V. Sawant and J. R. McKone, "Flow Battery Electroanalysis: Hydrodynamic Voltammetry of Aqueous Fe(III/II) Redox Couples at Polycrystalline Pt and Au," *ACS Appl. Energy Mater.*, vol. 1, pp. 4743–4753, 9 2018.

[208] M. Pournaghi-Azar and R. Ojani, "Electrode kinetic parameters of the ferrocene oxidation at platinum, gold and glassy carbon electrodes in chloroform," *Electrochimica Acta*, vol. 39, no. 7, pp. 953 – 955, 1994.

[209] K. M. Rosso, D. M. A. Smith, and M. Dupuis, "Aspects of Aqueous Iron and Manganese (II/III) Self-Exchange Electron Transfer Reactions," *The Journal of Physical Chemistry A*, vol. 108, no. 24, pp. 5242–5248, 2004.

[210] J. Silverman and R. W. Dodson, "The Exchange Reaction between the Two Oxidation States of Iron in Acid Solution," *The Journal of Physical Chemistry*, vol. 56, no. 7, pp. 846–852, 1952.

[211] J. Suzuki, "Hydrodynamic Voltammetry with the Convection Electrode. IV. The Measurements of the Kinetic Parameters of the Electrode Reaction. Part II," *Bulletin of the Chemical Society of Japan*, vol. 43, no. 3, pp. 755–758, 1970.

[212] "The effect of anion adsorption on the kinetics of the Fe3+/Fe2+ reaction on Pt and Au electrodes in $HClO_4$," *Journal of Electroanalytical Chemistry and Interfacial Electrochemistry*, vol. 89, no. 2, pp. 271 – 288, 1978.

[213] A. A. Shah, R. Tangirala, R. Singh, R. G. A. Wills, and F. C. Walsh, "A Dynamic Unit Cell Model for the All-Vanadium Flow Battery," *J. Electrochem. Soc.*, vol. 158, no. 6, pp. A671–A677, 2011.

[214] T. Sukkar and M. Skyllas-Kazacos, "Water transfer behaviour across cation exchange membranes in the vanadium redox battery," *J. Membr. Sci.*, vol. 222, p. 235–247, 2003.

[215] M. Skyllas-Kazacos and M. Kazacos, "State of charge monitoring methods for vanadium redox flow battery control," *J. Power Sources*, vol. 196, p. 8822– 8827, 2011.

[216] W. Zhang, L. Liu, and L. Liu, "An on-line spectroscopic monitoring system for the electrolytes in vanadium redox flow batteries," *RSC Adv.*, vol. 5, p. 100235, 2015.

[217] C. Petchsingh, N. Quill, J. T. Joyce, D. N. Eidhin, D. Oboroceanu, C. Lenihan, X. Gao, R. P. Lynch, and D. N. Buckley, "Spectroscopic Measurement of State of

Charge in Vanadium Flow Batteries with an Analytical Model of V(IV)-V(V) Absorbance," *J. Electrochem. Soc.*, vol. 163, no. 1, pp. A5068–A5083, 2016.

[218] E. Martin and K. Bentley, "Spectrophotometric Investigation of Vanadium(II),Vanadium(III), and Vanadium(IV) in Various Media," *Anal. Chem.*, vol. 34, no. 3, pp. 354–358, 1962.

[219] D. N. Buckley, X. Gao, R. P. Lynch, N. Quill, and M. J. Leahy, "Towards Optical Monitoring of Vanadium Redox Flow Batteries (VRFBs): An Investigation of the Underlying Spectroscopy," *J. Electrochem. Soc.*, vol. 161, no. 4, pp. A524–A534, 2014.

[220] Z. Tang, D. S. Aaron, A. B. Papandrew, and J. Thomas A. Zawodzinski, "Monitoring the State of Charge of Operating Vanadium Redox Flow Batteries," *ECS Trans.*, vol. 41, no. 23, pp. 1–9, 2012.

[221] L. Tong, Q. Chen, A. A. Wong, R. Gomez-Bombarelli, A. Aspuru-Guzik, R. G. Gordon, and M. J. Aziz, "UV-Vis spectrophotometry of quinone flow battery electrolyte for in situ monitoring and improved electrochemical modeling of potential and quinhydrone formation," *Phys.Chem.Chem.Phys.*, vol. 19, p. 31684, 2017.

[222] D. G. Kwabi, A. A.Wong, and M. J. Aziz, "Rational Evaluation and Cycle Life Improvement of Quinone-Based Aqueous Flow Batteries Guided by In-Line Optical Spectrophotometry," *J. Electrochem. Soc.*, vol. 165, no. 9, pp. A1770–A1776, 2018.

[223] M. Chakrabarti, N. Brandon, S. Hajimolana, F. Tariq, V. Yufit, M. Hashim, M. Hussain, C. Low, and P. Aravind, "Application of carbon materials in redox flow batteries," *Journal of Power Sources*, vol. 253, pp. 150 – 166, 2014.

[224] R. L. McCreery, "Advanced Carbon Electrode Materials for Molecular Electrochemistry," *Chemical Reviews*, vol. 108, no. 7, pp. 2646–2687, 2008.

[225] M. Yazici, D. Krassowski, and J. Prakash, "Flexible graphite as battery anode and current collector," *Journal of Power Sources*, vol. 141, no. 1, pp. 171 – 176, 2005.

[226] R. C. Engstrom and V. A. Strasser, "Characterization of electrochemically pretreated glassy carbon electrodes," *Analytical Chemistry*, vol. 56, no. 2, pp. 136–141, 1984.

[227] P. Chen, M. A. Fryling, and R. L. McCreery, "Electron Transfer Kinetics at Modified Carbon Electrode Surfaces: The Role of Specific Surface Sites," *Analytical Chemistry*, vol. 67, no. 18, pp. 3115–3122, 1995.

[228] K. Kim, "Carbon: Electrochemical and Physicochemical Properties," *Wiley, New York*, 1988.

[229] R. L. McCreery and K. K. Cline, "Laboratory Techniques in Electroanalytical Chemistry," 1996.

[230] R. J. Rice, N. M. Pontikos, and R. L. McCreery, "Quantitative correlations of heterogeneous electron-transfer kinetics with surface properties of glassy carbon electrodes," *Journal of the American Chemical Society*, vol. 112, no. 12, pp. 4617–4622, 1990.

[231] R. Rice, C. Alfred, and R. McCreery, "Fast Heterogeneous Electron Transfer Rates for Glassy Carbon Electrodes without Polishing or Activation Procedures," *J. Electroanal. Chem. Interf. Electrochem.*, vol. 263, p. 163–169, 1989.

[232] M. Poon and R. L. McCreery, "In Situ Laser Activation of Glassy Carbon Electrodes," *Anal. Chem.*, vol. 58, p. 2745–2750, 1986.

[233] L. Eifert, R. Banerjee, Z. Jusys, and R. Zeis, "Characterization of Carbon Felt Electrodes for Vanadium Redox Flow Batteries: Impact of Treatment Methods," *Journal of The Electrochemical Society*, vol. 165, no. 11, pp. A2577–A2586, 2018.

[234] Y. Yi, G. Weinberg, M. Prenzel, M. Greiner, S. Heumann, S. Becker, and R. Schlögl, "Electrochemical corrosion of a glassy carbon electrode," *Catalysis Today*, vol. 295, pp. 32 – 40, 2017.

[235] R. Bowling, R. T. Packard, and R. L. McCreery, "Mechanism of electrochemical activation of carbon electrodes: role of graphite lattice defects," *Langmuir*, vol. 5, no. 3, pp. 683–688, 1989.

[236] S. H. DuVall and R. L. McCreery, "Self-catalysis by Catechols and Quinones during Heterogeneous Electron Transfer at Carbon Electrodes," *Journal of the American Chemical Society*, vol. 122, no. 28, pp. 6759–6764, 2000.

[237] Z. He, Y. Jiang, W. Meng, F. Jiang, H. Zhou, Y. Li, J. Zhu, L. Wang, and L. Dai, "HF/H2O2 treated graphite felt as the positive electrode for vanadium redox flow battery," *Applied Surface Science*, vol. 423, pp. 111 – 118, 2017.

[238] Park, Minjoon and Jeon, In-Yup and Ryu, Jaechan and Baek, Jong-Beom and Cho, Jaephil, "Exploration of the Effective Location of Surface Oxygen Defects in

Graphene-Based Electrocatalysts for All-Vanadium Redox-Flow Batteries," *Advanced Energy Materials*, vol. 5, no. 5, p. 1401550, 2015.

[239] N. Pour, D. G. Kwabi, T. Carney, R. M. Darling, M. L. Perry, and Y. Shao-Horn, "Influence of Edge- and Basal-Plane Sites on the Vanadium Redox Kinetics for Flow Batteries," *The Journal of Physical Chemistry C*, vol. 119, no. 10, pp. 5311–5318, 2015.

[240] T. V. Sawant and J. R. McKone, "Flow Battery Electroanalysis. 2. Influence of Surface Pretreatment on Fe(III/II) Redox Chemistry at Carbon Electrodes," *J. Phys. Chem. C*, vol. 123, no. 1, pp. 144–152, 2019.

[241] A. J. Bard and L. R. Faulkner, "Electrochemical Methods: Fundamentals and Applications," *2nd ed., John Wiley and Sons, Inc.*, vol. 18, 1980.

[242] W. Zhang, J. Xi, Z. Li, H. Zhou, L. Liu, Z. Wu, and X. Qiu, "Electrochemical activation of graphite felt electrode for VO2+/VO2+ redox couple application," *Electrochimica Acta*, vol. 89, pp. 429 – 435, 2013.

[243] R. Taylor and A. Humffray, "Electrochemical studies on glassy carbon electrodes: II. Oxygen reduction in solutions of high pH (pH¿10)," *Journal of Electroanalytical Chemistry and Interfacial Electrochemistry*, vol. 64, no. 1, pp. 63 – 84, 1975.

[244] G. Zhang, S. Sun, D. Yang, J.-P. Dodelet, and E. Sacher, "The surface analytical characterization of carbon fibers functionalized by H2SO4/HNO3 treatment," *Carbon*, vol. 46, no. 2, pp. 196 – 205, 2008.

[245] P. K. Chu and L. Li, "Characterization of amorphous and nanocrystalline carbon films," *Materials Chemistry and Physics*, vol. 96, no. 2-3, pp. 253–277, 2006.

[246] Y. Wang, D. C. Alsmeyer, and R. L. McCreery, "Raman spectroscopy of carbon materials: structural basis of observed spectra," *Chemistry of Materials*, vol. 2, no. 5, pp. 557–563, 1990.

[247] L. G. Cançado, A. Jorio, E. H. Ferreira, F. Stavale, C. A. Achete, R. B. Capaz, M. V. Moutinho, A. Lombardo, T. S. Kulmala, and A. C. Ferrari, "Quantifying defects in graphene via Raman spectroscopy at different excitation energies," *Nano letters*, vol. 11, no. 8, p. 3190–3196, 2011.

[248] J. G. M and K. K., "Structure of glassy carbon," *Nature*, vol. 175, no. 5299, pp. 175–176, 1971.

[249] P. J. F. Harris, "Fullerene-related structure of commercial glassy carbons," *Philosophical Magazine*, vol. 84, no. 29, pp. 3159–3167, 2004.

[250] H. Shinotsuka, S. Tanuma, C. J. Powell, and D. R. Penn, "Calculations of Electron Inelastic Mean Free Paths. X. Data for 41 Elemental Solids over the 50 eV to 200 keV Range with the Relativistic Full Penn Algorithm. ," *Surf. Interface Anal.*, vol. 47, p. 871–888, 2015.

[251] J. K. Nørskov, J. Rossmeisl, A. Logadottir, L. Lindqvist, J. R. Kitchin, T. Bligaard, and H. Jónsson, "Origin of the Overpotential for Oxygen Reduction at a Fuel-Cell Cathode," *J. Phys. Chem. B*, vol. 108, no. 46, p. 17886–17892, 2004.

[252] J. Greeley, "Theoretical Heterogeneous Catalysis: Scaling Relationships and Computational Catalyst Design," *Annu. Rev. Chem. Biomol. Eng.*, vol. 7, pp. 605–635, 2016.

[253] Z. W. Seh, J. Kibsgaard, C. F. Dickens, I. Chorkendorff, J. K. Nørskov, and T. F. Jaramillo, "Combining theory and experiment in electrocatalysis: Insights into materials design," *Science*, vol. 355, no. 6321, 2017.

[254] J. K. Nørskov, F. Studt, F. Abild-Pedersen, and T. Bligaard, "Fundamental Concepts in Heterogeneous Catalysis," *Wiley-Blackwell*, p. 196, 2014.

[255] S. Zhong and M. Skyllas-Kazacos, "Electrochemical behaviour of vanadium(V)/vanadium(IV) redox couple at graphite electrodes," *J. Power Sources*, vol. 39, no. 1, pp. 1–9, 1992.

[256] V. Haddadi-Asl, M. Kazacos, and M. Skyllas-Kazacos, "Conductive carbon-polypropylene composite electrodes for vanadium redox battery," *J. Appl. Electrochem.*, vol. 25, no. 1, pp. 29–33, 1995.

[257] M. Kazacos, M. Cheng, and M. Skyllas-Kazacos, "Vanadium redox cell electrolyte optimization studies," *J. Appl. Electrochem.*, vol. 20, no. 3, pp. 463–467, 1990.

[258] Y. Liu, X. Xia, and H. Liu, "Studies on cerium Ce(4+)/Ce(3+)–vanadium V(2+)/V(3+) redox flow cell—cyclic voltammogram response of Ce(4+)/Ce(3+) redox couple in H2SO4 solution," *J. Power Sources*, vol. 130, no. 1, pp. 299–305, 2004.

[259] A. Mukhopadhyay, Y. Yang, Y. Li, Y. Chen, H. Li, A. Natan, Y. Liu, D. Cao, and H. Zhu, "Mass Transfer and Reaction Kinetic Enhanced Electrode for High-Performance Aqueous Flow Batteries," *Adv. Funct. Mater.*, vol. 29, p. 1903192, 2019.

[260] H. Fink, J. Friedl, and U. Stimming, "Composition of the Electrode Determines Which Half-Cell's Rate Constant is Higher in a Vanadium Flow Battery," *J. Phys. Chem. C*, vol. 120, no. 29, pp. 15893–15901, 2016.

[261] W. Wang, W. Xu, L. Cosimbescu, D. Choi, L. Li, and Z. Yang, "Anthraquinone with tailored structure for a nonaqueous metal–organic redox flow battery," *Chem. Commun.*, vol. 48, no. 53, pp. 6669–6671, 2012.

[262] X. Wei, W. Xu, M. Vijayakumar, L. Cosimbescu, T. Liu, V. Sprenkle, and W. Wang, "TEMPO-Based Catholyte for High-Energy Density Nonaqueous Redox Flow Batteries," *Adv. Mater.*, vol. 26, pp. 7649–7653, 12 2014.

[263] C. DeBruler, B. Hu, J. Moss, X. Liu, J. Luo, Y. Sun, and T. L. Liu, "Designer Two-Electron Storage Viologen Anolyte Materials for Neutral Aqueous Organic Redox Flow Batteries," *Chem.*, vol. 3, no. 6, pp. 961–978, 2017.

[264] J. Luo, B. Hu, C. Debruler, and T. L. Liu, "A π-Conjugation Extended Viologen as a Two-Electron Storage Anolyte for Total Organic Aqueous Redox Flow Batteries," *Angew. Chem. Int. Ed.*, vol. 57, pp. 231–235, 1 2018.

[265] Y. Matsuda, K. Tanaka, M. Okada, Y. Takasu, M. Morita, and T. Matsumura-Inoue, "A rechargeable redox battery utilizing ruthenium complexes with non-aqueous organic electrolyte," *J. Appl. Electrochem.*, vol. 18, no. 6, pp. 909–914, 1988.

[266] E. Barsoukov, "Effect of Low-Temperature Conditions on Passive Layer Growth on Li Intercalation Materials," *J. Electrochem. Soc.*, vol. 145, no. 8, p. 2711, 1998.

[267] M. Broussely, P. Biensan, F. Bonhomme, P. Blanchard, S. Herreyre, K. Nechev, and R. J. Staniewicz, "Main aging mechanisms in Li ion batteries," *J. Power Sources*, vol. 146, no. 1, pp. 90–96, 2005.

[268] X.-B. Cheng, R. Zhang, C.-Z. Zhao, F. Wei, J.-G. Zhang, and Q. Zhang, "A Review of Solid Electrolyte Interphases on Lithium Metal Anode," *Adv. Sci.*, vol. 3, p. 1500213, 3 2016.

[269] K. Xu, "Electrolytes and Interphases in Li-Ion Batteries and Beyond," *Chemical Reviews*, vol. 114, pp. 11503–11618, 12 2014.

[270] B. P. Balbuena and W. Y. Xuan, "Lithium-ion Batteries: Solid-electrolyte Interphase," *World Scientific Publishing Company*, p. 424, 2004.

[271] S. J. An, J. Li, C. Daniel, D. Mohanty, S. Nagpure, and D. L. Wood, "The state of understanding of the lithium-ion-battery graphite solid electrolyte interphase (SEI) and its relationship to formation cycling," *Carbon*, vol. 105, pp. 52–76, 2016.

[272] B. Yang, L. Hoober-Burkhardt, S. Krishnamoorthy, A. Murali, G. K. S. Prakash, and S. R. Narayanan, "High-Performance Aqueous Organic Flow Battery with Quinone-Based Redox Couples at Both Electrodes," *J. Electrochem. Soc.*, vol. 163, no. 7, pp. A1442–A1449, 2016.

[273] W. Lee, A. Permatasari, B. W. Kwon, and Y. Kwon, "Performance evaluation of aqueous organic redox flow battery using anthraquinone-2,7-disulfonic acid disodium salt and potassium iodide redox couple," *Chem. Eng. J.*, vol. 358, pp. 1438–1445, 2019.

[274] "Quadrennial Technology Review 2015, Advancing Clean Electric Power Technologies–Technological Assessments, US Department of Energy." https://www.energy.gov/ (accessed on 2020-11-18).

[275] T. R. Allen, R. Konings, and A. T. Motta, "Corrosion of Zirconium Alloys," *Comprehensive Nuclear Materials, Elsevier Ltd*, vol. 5, pp. 49–68, 2012.

[276] "Waterside Corrosion of Zirconium Alloys in Nuclear Power Plants." Int. At. Energy Agency IAEATEC DOC-996 (1998).

[277] A. T. Motta, A. Couet, and R. J. Comstock, "Corrosion of Zirconium Alloys Used for Nuclear Fuel Cladding," *Annual Review of Materials Research*, vol. 45, no. 1, pp. 311–343, 2015.

[278] "Corrosion of Zirconium Alloys in Nuclear Power Plants," *Int. At. Energy Agency, TECDOC Series*, no. 684, 1992.

[279] B. Cox and J. Pemsler, "Diffusion of oxygen in growing zirconia films," *Journal of Nuclear Materials*, vol. 28, no. 1, pp. 73 – 78, 1968.

[280] D. D. Macdonald, "Passivity–the key to our metals-based civilization," *Pure Appl. Chem.*, vol. 71, no. 6, pp. 951–978, 1999.

[281] H. G. Rickover, L. D. Geiger, and B. Lustman, "History of the development of zirconium alloys for use in nuclear reactors," *Energy Research and Development Administration, Div. of Naval Reactors*, 1975.

[282] S. J. Mardon JP, Charquet D, "Development of new zirconium alloys for PWR fuel rod cladding," *In Proceedings of International Conference on Light Water Reactor Fuel Performance*, p. 643–49.

[283] A. T. Motta, "Mechanistic Understanding of Zirconium Alloy Fuel Cladding Performance," *Zirconium in the Nuclear Industry: 18th International Symposium, ASTM STP1597*, p. 19–51.

[284] B. Cox, "Processes occurring during the breakdown of oxide films on zirconium alloys," *Journal of Nuclear Materials*, vol. 29, no. 1, pp. 50 – 66, 1969.

[285] A. T. Motta, M. J. G. da Silva, A. Yilmazbayhan, R. J. Comstock, Z. Cai, , and B. Lai, "Microstructure and growth mechanism of oxide layers formed on Zr alloys studied with micro-beam synchrotron radiation," *In 14th International Symposium on Zirconium in the Nuclear Industry*, vol. ASTM STP 1467, p. 205–32, 2008.

[286] K. N. Nikitin and V. N. Shishov, "Behavior of a Barrier Layer of Corrosion Films on Zirconium Alloys," *Protection of Metals and Physical Chemistry of Surfaces*, vol. 46, no. 2, p. 261–266, 2010.

[287] A. M. C. Lemaignan, "Zirconium Alloys in Nuclear Applications," *Materials Science and Technology, Nuclear Materials Pt. 2*, vol. 10B, 1995.

[288] "Pellet-clad interaction (PCI) failures of zirconium alloy fuel cladding — A review," *Journal of Nuclear Materials*, vol. 172, no. 3, pp. 249 – 292, 1990.

[289] H. A. K. Takeda, "Mechanisms of Corrosion Rate Degradation due to Tin," *Proceedings of 12th International Symposium on Zr in the Nuclear Industry*, vol. ASTM-STP-1354, p. 592, 1995.

[290] "Hydrothermal degradation mechanism of tetragonal Zirconia," *Journal of Materials Science*, vol. 36, no. 15, pp. 3737–3744, 2001.

[291] M. Oskarsson, E. Ahlberg, and K. Pettersson, "Phase transformation of stabilised zirconia in water and 1.0 M LiOH," *Journal of Nuclear Materials*, vol. 295, no. 1, pp. 126 – 130, 2001.

[292] B. Cox and W. Chenguang, "Dissolution of zirconium oxide films in 300 °C LiOH," *Journal of Nuclear Materials*, vol. 199, no. 3, pp. 272 – 284, 1993.

[293] B. Cox, "Effects of irradiation on the oxidation of zirconium alloys in high temperature aqueous environments: A review," *Journal of Nuclear Materials*, vol. 28, no. 1, pp. 1 – 47, 1968.

[294] C. Yan, R. Wang, Y. Wang, X. Wang, and G. Bai, "Effects of ion irradiation on microstructure and properties of zirconium alloys—A review," *Nuclear Engineering and Technology*, vol. 47, no. 3, pp. 323 – 331, 2015.

[295] M. Griffiths, R. Gilbert, and G. Carpenter, "Phase instability, decomposition and redistribution of intermetallic precipitates in Zircaloy-2 and -4 during neutron irradiation," *Journal of Nuclear Materials*, vol. 150, no. 1, pp. 53 – 66, 1987.

[296] H. Nifenecker and J. A. Pinston, "High Energy Photon Production in Nuclear Reactions," *Annual Review of Nuclear and Particle Science*, vol. 40, no. 1, pp. 113–144, 1990.

[297] O. W. Hermann and C. W. Alexander, "Review of spent-fuel photon and neutron source spectra," *Oak Ridge National Lab*, vol. ORNL/CSD/TM–205, 1986.

[298] W. G. Wang, P., "Oxidation of Zircaloy-4 during in situ proton irradiation and corrosion in PWR primary water," *Journal of Materials Research*, vol. 30, p. 1335–1348, 2015.

[299] P. Harrop, N. Wilkins, and J. Wanklyn, "The effect of gamma dose on oxide films on zirconium and zircaloy-2 and its relevance to corrosion," *Journal of Nuclear Materials*, vol. 16, no. 3, pp. 290 – 297, 1965.

[300] P. Salvador, "Influence of pH on the Potential Dependence of the Efficiency of Water Photooxidation at n - TiO_2 Electrodes," *J. Electrochem. Soc.*, vol. 128, p. 1895–1900, 1981.

[301] F. Mompean, J. Perrone, and M. Illemassène, "Chemical Thermodynamics of Zirconium," *Elsevier Science*, 2005.

[302] P. Kofstad, "High Temperature Corrosion," *Elsevier Applied Science*, 1988.

[303] M. Inagaki, M. Kanno, and H. Maki, "Effect of Alloying Elements in Zircaloy on Photo-Electrochemical Characteristics of Zirconium Oxide Films," *Zirconium in the Nuclear Industry: Ninth International Symposium*, vol. ASTM International 978-0-8031-5177-2, pp. 437–460, 1991.

[304] V. Renčiuková, J. Macák, P. Sajdl, R. Novotný, and A. Krausová, "Corrosion of zirconium alloys demonstrated by using impedance spectroscopy.," *J. Nucl. Mater.*, vol. 510, p. 312–321, 2018.

[305] J. Ai, Y. Chen, M. Urquidi-Macdonald, and D. D. Macdonald, "Electrochemical Impedance Spectroscopic Study of Passive Zirconium In High-Temperature , Deaerated Aqueous Solutions.," *The Electrochemical Society*, vol. 154, pp. C43–51, 2007.

[306] K. Gelderman, L. Lee, and S. W. Donne, "Flat-Band Potential of a Semiconductor: Using the Mott–Schottky Equation," *Journal of Chemical Education*, vol. 84, no. 4, p. 685, 2007.

[307] Y. Chen, M. Urquidi-Macdonald, and D. D. Macdonald, "The electrochemistry of zirconium in aqueous solutions at elevated temperatures and pressures," *Journal of Nuclear Materials*, vol. 348, no. 1, pp. 133 – 147, 2006.

[308] A. Hankin, F. E. Bedoya-Lora, J. C. Alexander, A. Regoutz, and G. H. Kelsall, "Flat band potential determination: avoiding the pitfalls," *J. Mater. Chem. A*, vol. 7, pp. 26162–26176, 2019.

[309] Y. Xu and M. A. Schoonen, "The absolute energy positions of conduction and valence bands of selected semiconducting minerals," *American Mineralogist*, vol. 85, no. 3-4, pp. 543–556, 2000.

[310] J. Li and N. Wu, "Semiconductor-based photocatalysts and photoelectrochemical cells for solar fuel generation: a review," *Catal. Sci. Technol.*, vol. 5, pp. 1360–1384, 2015.

[311] L. A. Lyon and J. T. Hupp, "Energetics of the Nanocrystalline Titanium Dioxide/Aqueous Solution Interface: Approximate Conduction Band Edge Variations between H0 = 10 and H- = +26," *The Journal of Physical Chemistry B*, vol. 103, no. 22, pp. 4623–4628, 1999.

[312] A. V. Shaposhnikov, D. V. Gritsenko, I. P. Petrenko, O. P. Pchelyakov, V. A. Gritsenko, S. B. Érenburg, N. V. Bausk, A. M. Badalyan, Y. V. Shubin, T. P. Smirnova, H. Wong, and C. W. Kim, "The atomic and electron structure of ZrO_2," *Journal of Experimental and Theoretical Physics*, vol. 102, no. 5, pp. 799–809, 2006.

[313] M. Pourbaix, "Atlas of electrochemical equilibria in aqueous solutions," 1974.

[314] K. R. Mikeska, S. J. Bennison, and S. L. Grise, "Corrosion of Ceramics in Aqueous Hydrofluoric Acid," *Journal of the American Ceramic Society*, vol. 83, no. 5, pp. 1160–1164, 2000.

[315] A. T. Motta and L.-Q. Chen, "Hydride Formation in Zirconium Alloys," *JOM*, vol. 64, no. 12, pp. 1403–1408, 2012.

[316] N. Sakai, A. Fujishima, T. Watanabe, and K. Hashimoto, "Enhancement of the Photoinduced Hydrophilic Conversion Rate of TiO2 Film Electrode Surfaces by Anodic Polarization,"

[317] N. Sakai, A. Fujishima, T. Watanabe, and K. Hashimoto, "Quantitative Evaluation of the Photoinduced Hydrophilic Conversion Properties of TiO2 Thin Film Surfaces by the Reciprocal of Contact Angle," *The Journal of Physical Chemistry B*, vol. 107, no. 4, pp. 1028–1035, 2003.

[318] N. S. Lewis, "Chemical Control of Charge Transfer and Recombination at Semiconductor Photoelectrode Surfaces," *Inorg. Chem.*, vol. 44, pp. 6900–6911, 2005.

[319] S. Kohtani, A. Kawashima, and H. Miyabe, "Reactivity of Trapped and Accumulated Electrons in Titanium Dioxide Photocatalysis," *Catalysts*, vol. 7, p. 303, 2017.